

Diss. ETH Nr. 21274

# Colours in thin metallic films based on precious metals and their intermetallic phases

A dissertation submitted to the

**ETH ZURICH**

for the degree of

**Doctor of Sciences**

presented by

**Angela Furrer**

**MSc in Materials Science, ETH Zurich**

born on October 23<sup>rd</sup> 1983

citizen of Aesch, LU

accepted on the recommendation of

**Prof. Dr. Ralph Spolenak, examiner**

**Prof. Dr. Peter J. Uggowitzer, co-examiner**

**Dr. Ulrich E. Klotz, co-examiner**

**Prof. Dr. Andreas Mortensen, co-examiner**

2013



*You have brains in your head.  
You have feet in your shoes.  
You can steer yourself any direction you choose.  
— Dr. Seuss*





## Acknowledgements

Famous people around us are more and more often stripped of their doctor titles, accused of not having produced their work autonomously. Nevertheless, I admit without hesitation that during the time I was working on the following thesis, there were many people who helped me out in many different ways. Before I begin with science, I would like to take the opportunity to give them a big thank you.

First of all I would like to thank the supervisor of my thesis, Prof. Ralph Spolenak, who accompanied me during the last few years. As well as supporting my scientific work and supplying me with food for thought and ideas, his tireless optimism always managed to let me see the bright side when things, at least from my perspective, did not look all that good. I learned a lot, not only about science, and enjoyed working with you very much.

Secondly, a big thank you is due to Prof. Peter J. Uggowitzer, Dr. Ulrich E. Klotz and Prof. Andreas Mortensen who kindly agreed to co-referee my thesis.

I am much obliged to the CCMX, the *'centre de competence des materiaux'*, and the industrial partners who financially supported my work and gave helpful input during numerous meetings.

The last years would have not been as enjoyable if it had not been for the great company I have had with the current and former members of the fantastic LNM. All the lunchtimes and coffee breaks spent with intelligent or pointless but entertaining discussions were a perfect counter balance to everyday work. And whenever there was a problem, work-related or not, somebody was there to help out.

Special thanks go to Dr. Alla Sologubenko who taught me a great deal about FIB and TEM, and also Dr. Christian Solenthaler, who helped me a lot with TEM experiments. I also want to thank Dr. Elisabeth Müller and Dr. Fabian Gramm who introduced me to the fascinating world of electron microscopy, and Philippe Gasser, keeper of the FIB, who was always a great help and a good laugh.

The newest addition to the group, Franziska Schlich, performed all the reflectivity calculations in chapter 3, and together with Daniel Bernoulli, the AFM measurements of the same chapter. To both of them I am very grateful.

A big thank you deserve Dr. Matteo Seita, Daniel Muff, André Röthlisberger and Huan Ma who carried out the ion irradiations reported in chapter 4. Dr. Seita also performed the EBSD measurements and evaluations, and in long and fruitful discussions contributed a large part to the paper that was published based on subchapter 4.2.

My office mates, Dr. Matteo Seita, Matthias Schamel and the just recently arrived Martin Süess deserve a special mention. They had to put up with my ups and downs, my temperature- and noise sensitivity and the smell of the rice cakes very directly and frequently. They served as

shrinks, personal motivators and fashion advisors simultaneously. You were a great help and much, much fun. I hope whoever takes my desk will appreciate you as much as I did.

For their support not only during my PhD years, but my whole life, I want to thank my family. While I might have brought them trouble explaining to their friends what exactly I am doing, (something I occasionally struggle with myself) I would have never made it without them.

If I am still well-fed, in clean clothes and at least partially at mental health, it is thanks to Terry, who has taken great care of me during the last few months. I hope sometime within the next 60 years I will get the chance to give it back.

## Summary

Since the technology is available to produce materials in smaller and smaller dimensions, it has been noticed that along with the size also the material properties change, once a certain limit is reached. These so-called *size effects* have been discovered for many different properties, such as the electrical resistivity of metal films or the fracture toughness of nano-sized particles. The resistivity increases due to a growing amount of scattering sites, such as interfaces and grain boundaries, which divert the electrons from their path. The number of defects that are present within nanoparticles decreases with their size, which improves their mechanical strength. Also the optical properties of metal films have been found to change as the thickness is reduced. When the thickness falls below a critical value, the reflectivity decreases continuously and the layer becomes transparent. This *critical thickness* is material dependent and was investigated for three different metals (Au, Pt and Al) and an intermetallic phase ( $\text{AuAl}_2$ ) during the course of this thesis. It became clear that the amount of free electrons determines the film thickness at which the optical properties start to deviate from the bulk material.

The design of alloys on small scales such as thin films can be very beneficial when materials are investigated that are cost-intensive, such as precious metals. The possibility to upscale the optical properties of sputter-deposited layers to bulk material was investigated. Several well-known alloys were produced with thicknesses above the critical value: three Au-Ag alloys with different compositions and the binary intermetallic phases  $\text{AuAl}_2$ ,  $\text{PtAl}_2$  and  $\text{AuIn}_2$ . While the optical properties of the Au-Ag alloys, which form solid solutions over the whole composition range, corresponded nicely to the bulk materials, differences were found for the intermetallics. Common features of the three phases are their crystal structure (fluorite) and the display of special colours. The origin of the colours is a so-called *pseudo-gap* in their density of electronic states, which inhibits the absorption of light with certain wavelengths that would otherwise occur due to interband transitions of electrons. The reflected wavelengths add up to create a purple ( $\text{AuAl}_2$ ), yellow ( $\text{PtAl}_2$ ) or blue ( $\text{AuIn}_2$ ) colour. When produced as thin films by means of magnetron sputter deposition, only the blue colour of the  $\text{AuIn}_2$  is visible. The other two phases are initially grey and require a heat treatment for the colour to appear. It seems that depending on the mobility of the atoms during the deposition process, a significant amount of defects is integrated in the structure. When the distance between these defects, which can be point defects, line defects or grain boundaries, is too small, the band structure is smeared out. As a consequence the possible electron transitions change and lead to a lack of colour.

In final experiments, ternary samples were produced consisting of Au, Pt and Al. The Al content was kept at a constant 66.6 at.%, while the ratio of Au to Pt was altered. The resulting phases still crystallised in the fluorite structure and, after a suitable heat treatment, displayed colours that varied linearly from purple to yellow with increasing Pt content. The variation of the colour is attributed to a changing electron density within the material. Pt contributes one electron less than Au, meaning that with increasing Pt content the Fermi level is shifted towards lower values while the band structure remains roughly the same, due to the persistent crystal

structure. The energies at which the electron interband transitions are possible are thus shifted to different wavelengths of the visible spectrum, leading to a change in the perceived colour. We hence achieved to produce an intermetallic phase with an easily tuneable colour that can be applied for decorative purposes.

## Zusammenfassung

Seit Materialien in immer kleineren Dimensionen produziert werden können wurde festgestellt, dass sich auch die Eigenschaften der Materialien ändern, wenn die Grösse unter einen bestimmten Wert sinkt. Solche *Grösseneffekte* sind für verschiedene Eigenschaften bekannt, beispielsweise für den elektrischen Widerstand dünner Metallfilme oder die mechanische Festigkeit kleiner Metallsäulen. Der Widerstand der dünner werdenden Schichten nimmt zu wegen der steigenden Anzahl von Streuzentren für die Elektronen, wie die Filmoberfläche oder Korngrenzen. Wenn das Volumen der Säulen abnimmt, enthalten sie immer weniger Versetzungen, bis sie ab einer bestimmten Grösse praktisch defektfrei sind. Die Festigkeit, die mit sinkendem Volumen steigt, entspricht dann dem theoretischen Wert. Auch die optischen Eigenschaften ändern sich mit der Grösse, so zum Beispiel die Reflektivität von dünnen Metallschichten. Wird eine bestimmte *kritische Dicke* unterschritten sinkt die Reflektivität kontinuierlich, gleichzeitig werden die Filme zunehmend transparent. Diese kritische Dicke ist materialabhängig und wurde für drei verschiedene Metalle (Au, Pt, Al) und eine intermetallische Phase ( $\text{AuAl}_2$ ) untersucht. Die Messungen zeigten, dass die Anzahl freier Elektronen bestimmt, ab welcher Dicke die optischen Eigenschaften sich von denen eines massiven Materials zu unterscheiden beginnen.

Die Entwicklung von neuen Legierungen in der Form von Dünnschichten ist vorteilhaft, wenn kostspielige Materialien verwendet werden, wie zum Beispiel Edelmetalle. Die Möglichkeit des hochskalierens der optischen Eigenschaften von dünnen metallischen Filmen zu massiven Metallen wurde untersucht. Die Filme wurden durch Magnetron Sputter Deposition hergestellt, mit Dicken oberhalb des kritischen Wertes. Drei verschiedene Au-Ag Legierungen und die binären intermetallischen Phasen  $\text{AuAl}_2$ ,  $\text{PtAl}_2$  und  $\text{AuIn}_2$  wurden untersucht. Während die Farben der Au-Ag Legierungen, die über den gesamten Zusammensetzungsbereich einen Mischkristall bilden, gut mit denen der massiven Metalle übereinstimmen, wurden bei den intermetallischen Phasen gewisse Unterschiede gefunden. Den drei Phasen ist gemeinsam, dass sie die Fluorit Struktur besitzen und spezielle Farben aufweisen. Die Herkunft der Farben beruht auf einer so genannten *Pseudo-Lücke* in der Zustandsdichte der Elektronen. Diese Lücke verunmöglicht die Interbandübergänge der Elektronen, die normalerweise zu einer Absorption des Lichts führen. Die aus diesem Grund reflektierten Wellenlängen erzeugen die Farben violett ( $\text{AuAl}_2$ ), gelb ( $\text{PtAl}_2$ ) und blau ( $\text{AuIn}_2$ ). In den Dünnschichten die mittels Sputter Deposition hergestellt wurden ist jedoch lediglich die blaue Farbe des  $\text{AuIn}_2$  zu erkennen. Die ändern beiden Phasen sind anfänglich grau und benötigen eine Wärmebehandlung um die gewünschten Farben erscheinen zu lassen. Abhängig von der Mobilität der Atome während der Abscheidung des Films, wird eine grosse Menge von Defekten in die Filme eingebaut. Wenn die Distanz zwischen diesen Defekten, welche Punkt-, Liniendefekte oder Korngrenzen sein können, zu klein wird, wird die normalerweise ausgeprägte Bandstruktur verschmiert und die möglichen Elektronenübergänge ändern sich, was ein Fehlen der Farbe zur Folge hat.

In abschliessenden Experimenten wurden ternäre Proben aus Au, Pt and Al hergestellt. Der Al Gehalt wurde konstant bei 66.6 at.% gehalten, während das Verhältnis von Au zu Pt geändert wurde. Die resultierenden intermetallischen Phasen besaßen immer noch die Fluorit Struktur und zeigten, nach adäquater Wärmebehandlung, mit dem Pt Gehalt linear variierende Farben zwischen violett und gelb. Die Farbänderung kommt durch die wechselnde Elektronendichte im Material zustande: Da Pt ein Elektron weniger enthält als Au wird die Fermi Energie mit steigendem Pt Gehalt zu niedrigeren Werten verschoben, während die Bandstruktur wegen der gleich bleibenden Kristallstruktur nahezu unverändert bleibt. Der Energiebereich, in dem Interbandübergänge möglich sind, verschiebt sich, was eine Farbänderung zur Folge hat. Auf diese Weise wurde es erreicht Phasen herzustellen, deren Farben sich auf einfache Weise einstellen lassen und Anwendungen als dekorative Schichten erlauben könnte.

# Table of Contents

1. Introduction.....	13
1.1 Colours.....	13
Colour due to the scattering of light.....	13
Colour in dyes and pigments.....	14
Colour in metals.....	15
Structural colours.....	17
Colour measurements.....	19
CIE - Commission internationale de l'éclairage.....	19
1.2 Gold.....	23
Gold alloys.....	23
1.3 Size Effects.....	29
1.4 Aim of the project.....	31
2. Materials and methods.....	33
2.1 Sample production.....	33
2.2 Sample treatment.....	34
2.3 Investigation methods.....	36
3. Film thickness dependence of colour.....	41
3.1 Gold (Au).....	41
3.2 Platinum (Pt).....	45
3.3 Aluminium (Al).....	48
3.4 Gold-aluminide (AuAl <sub>2</sub> ).....	51
3.5 Comparison of thin films of different materials.....	60
4. Colours due to electronic band structures.....	63
4.1 Au-Ag.....	63
4.2 Au-Al.....	69
4.3 Pt-Al.....	84
4.4 Au-In.....	92
4.5 Comparison of AuAl <sub>2</sub> , PtAl <sub>2</sub> and AuIn <sub>2</sub> .....	99
4.6 Au-Pt-Al.....	101

5. Final discussion and conclusions .....	117
6. Outlook .....	121
6.1 Layer thickness dependence of colour .....	121
6.2 Colours due to electronic band structures.....	121
7. References .....	125
8. Appendices .....	129
9. Curriculum Vitae.....	162



# 1. Introduction

## 1.1 Colours

When we get up in the morning, look out the window and see a blue sky, we decide to wear our red shorts. If the sky is grey, we try not to forget our yellow umbrella. Then we have breakfast and pour white milk over our brown müesli and drink a cup of black tea. By the time we leave the house, we have seen tens of different colours and probably did not even take notice. Technically speaking, ‘colour’ is only a perception – something our brain creates when the cone-shaped receptors in our eyes are struck by electromagnetic radiation with a wavelength between roughly 380 nm to 780 nm [1]. But how materials interact with light and thus determine what portion of the visible spectrum is reflected back and enters our eyes is a fascinating subject. In his book, Nassau [2] summed up 15 different causes of colour, describing how light is selectively absorbed, reflected, refracted, scattered or diffracted by matter. Often treated as a side effect with minor importance, maybe even with a slightly feminine touch, the physical and chemical features behind the creation of colour are numerous, diverse and intriguing. While treating them all exceeds the scope of this introduction, a few of the most commonly encountered will be mentioned here.

### *Colour due to the scattering of light*

The blue sky, but also the grey sky we see are both caused by the scattering of sunlight in our atmosphere. The blue colour is produced by *Rayleigh scattering*, which is scattering at particles that are small compared to the wavelength of light, such as air molecules. Rayleigh found that the intensity of scattering depends on the wavelength and is proportional to  $\lambda^{-4}$ , meaning that light with shorter wavelengths, hence violet and blue colour, is scattered more strongly than the longer, reddish wavelengths (illustrated in Figure 1). To us, the sky is blue and not violet because the sensitivity of our eyes to radiation with very short wavelengths is reduced. In the evening, when the light has to travel a long way through the atmosphere, most of the blue wavelengths are filtered out of the light before it reaches our eyes; hence a setting sun appears red.

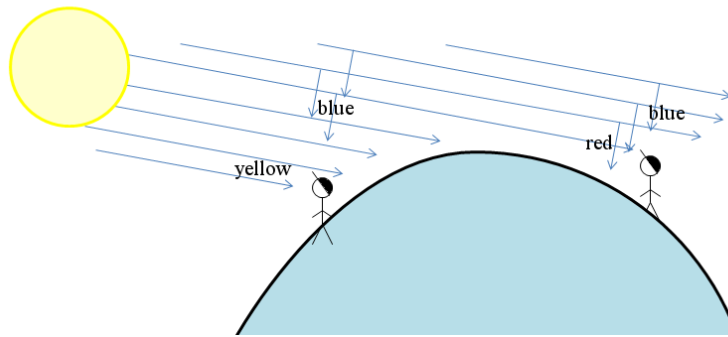


Figure 1: Schematic illustration of the scattering in the atmosphere and the perceived colour of the light. While during the day the light that comes directly from the sun appears yellow, in the evening it is red, due to the longer distance it travels through the atmosphere, which scatters the light with blue wavelengths.

The white colour of the sky is produced by the scattering of light at the little water droplets in the clouds. When the scattering particles are of a size comparable with or larger than the wavelength of light, the process is termed *Mie scattering*. When all particles are roughly the same size, Mie scattering can also produce colours [3]. This is usually not the case in a cloud; hence the produced colour is white or grey, depending on the thickness. The same scattering is responsible for the white colour of milk; there it is the small droplets of fat in watery solution that serve as scattering centres.

### *Colour in dyes and pigments*

Most of the artificially produced objects that surround us owe their colour to dyes or pigments. The fabric of our clothes has been dyed, our houses and cars painted. The difference between dyes and pigments is that the former generally are water soluble, while the latter require a binder [2]. What they have in common is that the mechanism that produces the colour is based on the preferential absorption of a certain part of the visible spectrum. For example, a pair of red shorts has been dyed with a substance that preferentially absorbs the blue, green and yellow light from the sun. The molecules used for dyes and pigments are very diverse; the absorption of the light is normally based on the transition of electrons into higher lying molecular orbitals. Apart from synthetically produced colorants, there are many natural pigments, such as chlorophyll, which is responsible for the green colour in plants, or melanin that is found in the skin, hair and eyes of animals.

## Colour in metals

Probably the most obvious property of metals is their shiny appearance, or ‘metallic lustre’. This lustre is simply a very high reflectivity, which is mostly due to the free electrons. The exact nature of the interaction of light with metals is rather complicated and different theories have been advanced to explain it.

The electron theory of metals developed by *P. Drude* in 1900 treats a metal as consisting of a lattice of positive ion cores, surrounded by a gas of free, negative electrons [4], disregarding any electron-electron or electron-ion interaction apart from the occasional collision and assuming the Maxwell-Boltzmann distribution for the electron velocity distribution. Despite its simplicity several physical phenomena, for example the electrical and thermal conductivity or the Hall Effect could be explained with it quite satisfactorily. According to the Drude theory, when the surface of a metal is hit by electromagnetic radiation, such as a light wave, the free electrons begin to oscillate with the same frequency as the incoming wave. Thus, being a moving electric charge, the electrons themselves become the origin of an electromagnetic wave, reflecting all incident light with the original wavelength. This can occur similarly for all wavelengths of light up to the point where the plasma frequency is reached - the frequency at which collective oscillations of the electron gas set in and absorb the incoming energy. For simple, monovalent elements like Na or K, the Drude theory holds rather well [5], however the behaviour of more complicated metals requires different approaches.

The *theory of electron bands* describes how the electrons in a solid are distributed in bands of different allowed energy states. It is derived from the discrete energy states of a single atom, which for a solid containing around  $10^{23}$  atoms become indistinguishably close and form near-continuous regions of allowed energies, separated by regions of forbidden energy states, the band gaps. Conductors, semiconductors and insulators can be readily described using the band theory (Figure 2). In a conductor the Fermi Energy  $E_F$  - the highest filled electron energy level at zero K - lies within a band of allowed states and the electrons in the outermost band are able to travel freely through the material. The Fermi Energy of a semiconductor and an insulator lies within a band gap, the valence bands are filled and their electrons tied to the ionic cores. While the energy gap between the highest filled band and the lowest unfilled band is rather high in an insulator ( $>2\text{eV}$ ), it requires only little energy ( $<2\text{eV}$ ) to promote an electron from the valence band across the gap into the conduction band in a semiconductor. This promotion can be done, for example, by a light wave

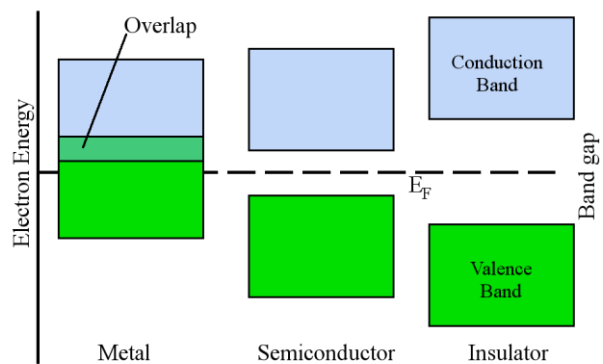


Figure 2: Schematic drawing of the band structures of different types of materials. While the valence and conduction band in a metal overlap, a band gap is present in semiconductors and insulators.

impinging on the surface. The energy is absorbed by the excitation and not reflected; as a consequence semiconductors usually have a black or dark grey appearance. In insulators on the other hand, the energy that is required to promote an electron from the valence into the conduction band is so high that the corresponding wavelengths lie outside the visible spectrum. Thus, no light is absorbed and a perfect insulator is transparent. If it contains imperfections, such as pores, the light is scattered and the material appears white.

For a metal the colour that is perceived strongly depends on its band structure. Different types of electron transitions can occur, depending on the energy of the incoming light. Figure 3 (left) shows a strongly simplified section of a band structure of a metal, describing the first Brillouin zone (from [6]). The transitions requiring the least energy are so-called *intra*band transitions, where an electron from around the Fermi Energy is promoted to a previously empty energy level within the same band. As no gap has to be overcome, no minimum energy is needed. These intraband transitions correspond to the oscillations of the free conduction electrons as described by the Drude theory.

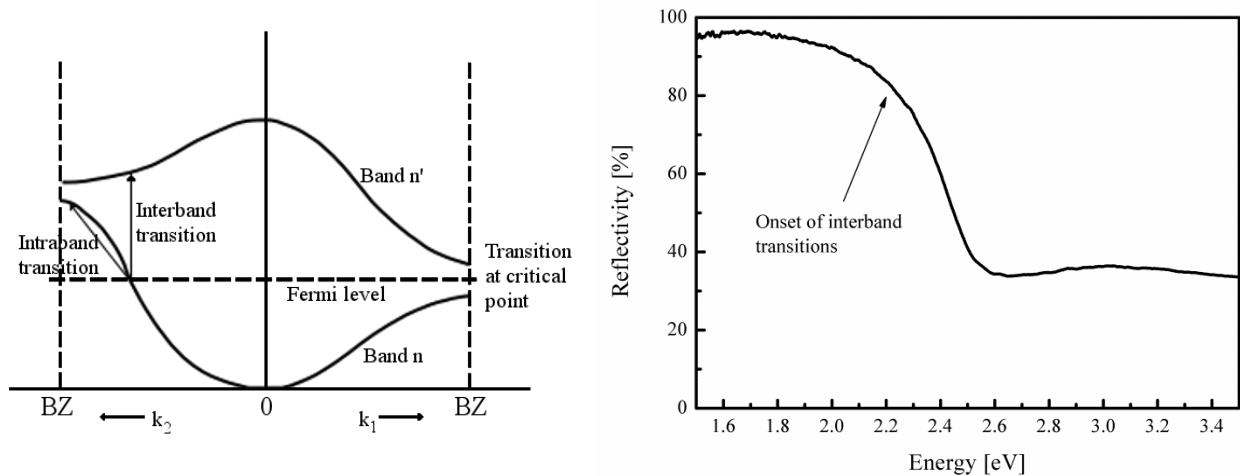


Figure 3: Left: Simplified band structure of a metal showing possible transitions (from [6]). Next to intraband transitions that occur within the same electron band, interband promotions of electrons to a different energy band can happen once a certain energy is reached. Right: Reflectivity spectrum of Au showing the onset of interband transitions around 2 eV by a sharp drop in the curve (own data, right).

When an electron is promoted from one energy band into a higher energetic one, it is called an *interband transition*. This can happen when an electron from the valence band is raised into an energy level above the Fermi Energy, or when electrons from around the Fermi Energy are promoted into higher lying bands. Interband transitions require a minimum energy which is at least the energy difference between the involved bands. The light that enables the interband transition is absorbed and thus missing in the spectrum. The onset of such transitions is easy to observe in the reflectivity spectra of the metal, which drops noticeably when the threshold is reached, as for example in the spectrum of gold (Figure 3, right). The selective absorption of light with wavelengths higher than around 550 nm (the green and blue part of the visible spectrum), renders the metal its famous yellow colour. The red colour of copper is also due to

interband transitions, here the energy difference between the bands is slightly smaller and light of longer wavelengths is able to transport electrons across. A large part of the yellow light is also absorbed, leaving the reddish wavelengths to create the colour.

Apart from intra- and interband transitions a third type of interaction can occur between light and a metal, the *plasma oscillation*. When the frequency of the light corresponds to the plasma frequency, the frequency at which the collective oscillations of the conduction electrons set in, the metal loses its high reflectivity and suddenly becomes transparent to the radiation. Depending on the electronic structure of the material, the plasma frequency is reached in the visible [5] or ultraviolet [7] part of the spectrum.

### *Structural colours*

Regular geometric structures in the same dimensions as the wavelengths of visible light can interact with incoming rays and lead to selective absorption and reflection and give colour to an object. The responsible geometric structures can have numerous different build ups. Just a few will be mentioned here.

#### - Interference colours

A simple example is the interference of light reflected by the front and the back surface of a thin, transparent medium. The phenomenon was thoroughly described by Newton, experimenting with a convex and a flat surface of glass [9]. He discovered that the thickness difference of the air gap between flat and round surface leads to the occurrence of a series of rings (now termed Newton's rings, [8], bottom) on the surface - dark and bright rings when a monochromatic light source is used, and a sequence of colours when white light is employed. The reason for this is the constructive and destructive interference of light waves that are reflected from the front and backside of the air gap. This happens under defined conditions, namely when the path difference  $\Delta = AB + BC$  between the two rays corresponds to  $m \cdot \lambda$  (constructive), or  $1.5m \cdot \lambda$  (destructive), where  $m$  is an integer number and  $\lambda$  the wavelength in air. One important thing to note is that when light is reflected at an interface with a higher refractive index  $n$  than the medium it has been travelling through, a phase shift of  $\pi/2$  will occur. In the case of an air gap between two glass objects, a phase shift occurs at the air-glass interface (B) but not the glass-air interface (C). For different wavelengths of light, these criteria are fulfilled at different

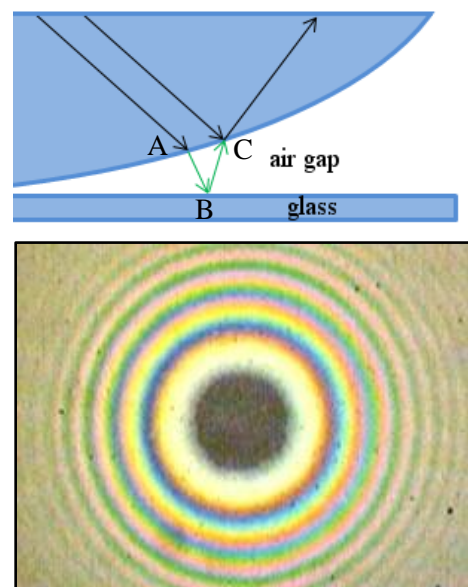


Figure 4: Newton's experiment with a convex and flat glass surface (top) and the resulting Newton's rings (bottom) from [8].

thicknesses of the gap, which is why the different colours are observed at different positions on the surface. The same phenomenon can be seen on oily patches on the street on a rainy day, soapy bubbles or even the wings of a house fly [2].

Interference colours are also a well-known occurrence in metals. When, after a heat treatment or conditioning with chemicals, a formerly grey metal suddenly displays a colour, it is normally due to interference colours produced by a thin dielectric film on the metal surface. The colour is uniform when the thickness of the film is homogeneous over the sample, but changes with the angle of observation. The so-called *temper colours* on steel or copper were even a means of determining the achievement of a desired heat treatment [10]. Today, interference colours are applied as decorative coatings on all different types of surfaces, from jewellery to art or architecture, or even as a means of fraud prevention on bank notes, when small metallic particles with interference coatings are printed on the paper [11]. A metallic shimmer with slightly shifting characteristic interference colours is obtained that is very difficult to imitate.

- Diffraction gratings

More complicated structures are diffraction gratings, where the light waves are reflected from small, periodical structures. Each feature of the grating becomes the origin of a spherical wavelet and depending on the wavelength of the light they constructively interfere with each other in very specific directions, as schematically drawn in Figure 6. The condition of constructive interference is the fulfilment of the Bragg equation,  $n\lambda = 2d\sin\theta$ , where  $\lambda$  is the wavelength of the light,  $d$  the period of the grating and  $\theta$  the angle under which the radiation leaves the surface. Diffraction gratings are often

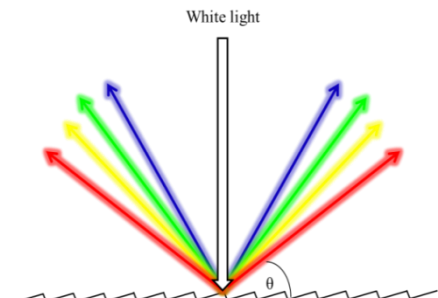


Figure 6: Schematic drawing of the splitting of colours at a diffraction grating.

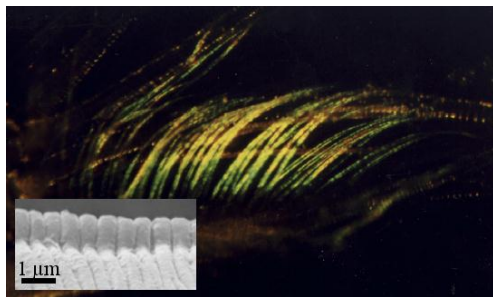


Figure 5: Image of a seed shrimp (*Azygocypridina lowryi*), displaying colours due to a diffraction grating (SEM image in the insert), from [12].

found in nature, where they render conspicuous colours to their bearer, as for example seed shrimp in Figure 5 (*Azygocypridina lowryi*) [12]. The brilliant colours on the bottom of a CD are an accidental consequence of the data containing pits, which are arranged in a regular fashion. Other man-made diffraction gratings find application for example as monochromators, where their ability to divert light according to its wavelength is used.

### Colour measurements

The colour of a reflecting or transmitting object is not a physical property; therefore it cannot be easily quantified. Depending on the illuminant, the surface roughness, the angle of observation and the observer, the perception might be quite different. Early colour determination was therefore based on the direct comparison of two objects. Colours were arranged in so-called *colour spaces*, as for example the one developed by A. Munsell in 1905 [13]. His system categorised colour by means of their hue (the shade of colour), chroma (the intensity) and value (the brightness) (Figure 7). Even today, the method of comparison is still in use, for example in architecture, art or the food industry [14].

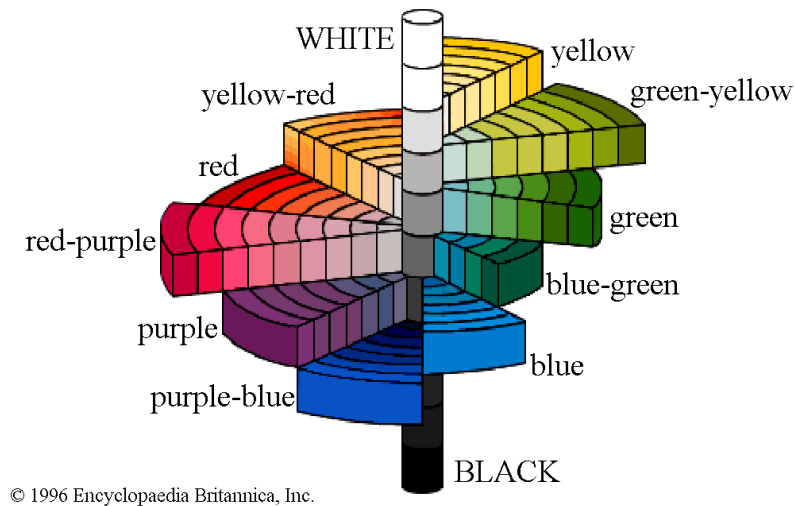


Figure 7: The Munsell colour space, with the three axes hue, chroma (intensity) and value (brightness), from [15].

### CIE - Commission internationale de l'éclairage

By the beginning of the 20<sup>th</sup> century a significant amount of research in the field of colours had been made but there was need for a quantitative measure of the colour perception of the human eye, so that a more scientific method for colour measurements could be developed. In 1931, based on the research of J. Guild [16] and W.D. Wright [17], the *CIE 1931 standard colorimetric observer* was defined. From a series of experiments where a number of test subjects had to match a given test stimulus by mixing three primary colours, the so-called *colour matching functions (CMFs)* were determined, which reflect the spectral sensitivity of the human eye to light of different wavelengths. As primary colours spectral light sources ('spectral' meaning of only one wavelength) of red, green and blue colours were used. The resulting CMFs, called  $\bar{r}$ ,  $\bar{g}$  and  $\bar{b}$  are shown in Figure 8 (left). The disadvantage of using that set of colour matching functions is that the curves contain negative values, which complicate further calculations. To solve the problem, they were linearly transformed into functions which would only have positive values, resulting in the  $\bar{x}$ ,  $\bar{y}$ ,  $\bar{z}$  CMFs (Figure 8, right). The same linear

transformation also instated that  $\bar{y}(\lambda)$  equals the photopic luminous efficiency of the standard observer - the perception of the brightness of light depending on its wavelength [18].

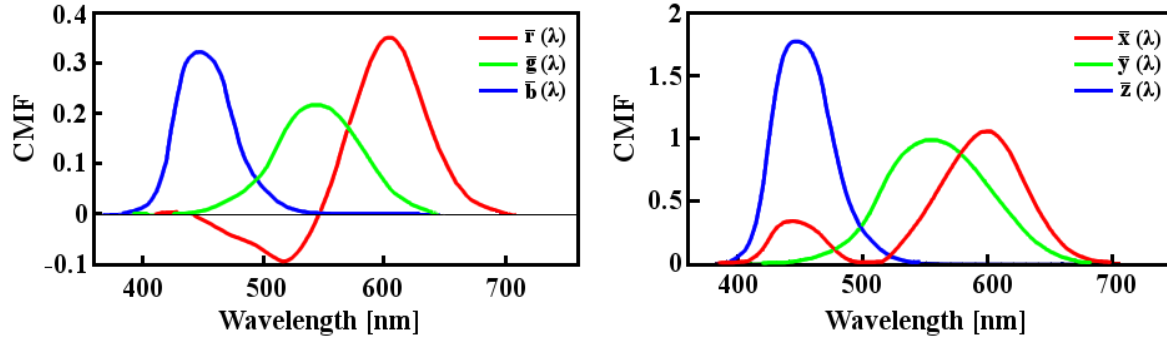


Figure 8: Colour matching functions (CMFs)  $\bar{r}$ ,  $\bar{g}$ ,  $\bar{b}$  (left) and  $\bar{x}$ ,  $\bar{y}$ ,  $\bar{z}$  (right) of the CIE 1931 standard observer. While  $\bar{r}$ ,  $\bar{g}$ ,  $\bar{b}$  contain negative values,  $\bar{x}$ ,  $\bar{y}$ ,  $\bar{z}$  have been transformed in a way that only positive values remain.

By means of these CMFs the colour of a light source can be numerically determined in the XYZ colour space by means of its spectral intensity distribution  $\phi(\lambda)$ .

$$X = k \int_{380 \text{ nm}}^{780 \text{ nm}} \phi(\lambda) \bar{x}(\lambda) d\lambda, Y = k \int_{380 \text{ nm}}^{780 \text{ nm}} \phi(\lambda) \bar{y}(\lambda) d\lambda, Z = k \int_{380 \text{ nm}}^{780 \text{ nm}} \phi(\lambda) \bar{z}(\lambda) d\lambda$$

The determination of the colour of a non-self-luminous object, an object that does not itself produce light but solely reflects or transmits light from a source, requires knowledge of the reflectivity spectrum of the object  $R(\lambda)$ , and of the spectral intensity of the light source  $S(\lambda)$ , giving  $\phi(\lambda) = R(\lambda) * S(\lambda)$ . The value k, which is defined in a way that the value Y becomes 100 for objects with  $R(\lambda)$ , or  $T(\lambda) = 1$ , is given by  $k = \frac{100}{\sum_{\lambda} S(\lambda) * \bar{y}(\lambda) d\lambda}$  [19].

More commonly used for the illustration of a colour than these basic colour coordinates are the chromaticity coordinates x, y and z, where

$$x = \frac{X}{X+Y+Z}, y = \frac{Y}{X+Y+Z}, z = \frac{Z}{X+Y+Z}.$$

From the definition it follows that  $x+y+z = 1$ , making it sufficient to determine x and y. However, the value Y, which is the luminance of the colour, is generally required, too. The x/y plot is the well-known chromaticity diagram in Figure 9. On the outer curve of the horseshoe lie the spectral colours - colours containing only a single wavelength of light, on the straight line connecting red and blue lie the purple colours, which do not correspond to a single wavelength. The colours within the horseshoe can be produced by combination of the right proportions of spectral colours.



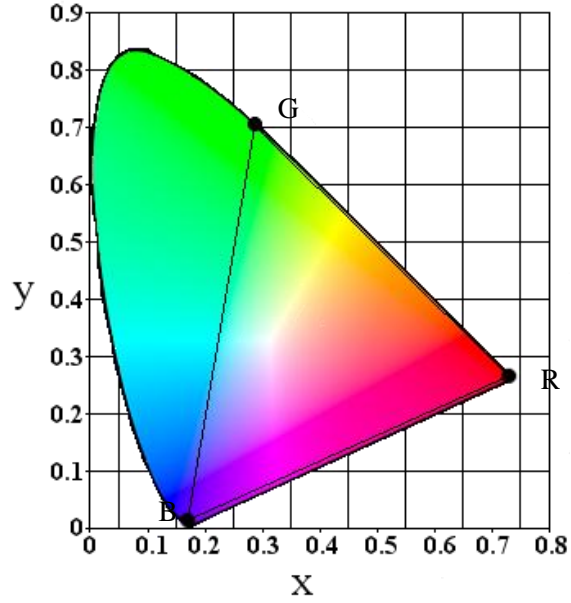


Figure 9: Chromaticity diagram based on the 1931 standard observer; the spectral colours are located along the horseshoe line; the inscribed triangle is the range of the CIE RGB colour space.

Based on the 1931 XYZ colour space, numerous other colour spaces were developed. For example, the CIE  $L^*a^*b^*$  which, in contrast to the XYZ space is a uniform colour space, meaning that the difference between the values of two colours always corresponds to the same difference in colour perception. The conversion is carried out using the following calculations.

$$L^* = 116 * f(Q_y) - 16,$$

$$a^* = 500 * [f(Q_x) - f(Q_y)],$$

$$b^* = 200 * [f(Q_y) - f(Q_z)],$$

Where  $Q_x = X/X_n$ ,  $Q_y = Y/Y_n$  and  $Q_z = Z/Z_n$ ,  $f(Q) = Q^{1/3}$  if  $Q > (6/29)^3$  and  $f(Q) = (841/108) * Q + 4/29$  if  $Q < (6/29)^3$ . The values  $X_n$ ,  $Y_n$  and  $Z_n$  are the XYZ values of a perfectly white object [20].

The 1931 colorimetric standard observer holds certain flaws, namely the fact that it measured the response of the eye under an angle of  $2^\circ$ . This narrow angle lies completely within the fovea of the eye, the central point of the visual field, where the concentration of the colour-sensing cone cells is highest. It has been found that the colour response at higher angles, extending to the region of the eye where the density of cones is lower, leads to a somewhat different colour perception [21]. Therefore, in 1964 a new standard observer, the 1964  $10^\circ$  standard observer was introduced, whose colour matching functions are termed  $\bar{x}_{10}$ ,  $\bar{y}_{10}$  and  $\bar{z}_{10}$  to enable distinction from the 1931 observer. Both observers are still in use and the appropriate one is chosen depending on the application.

The CIE RGB colour space is one of many different RGB spaces. They all have in common that they are based on the three primary colours red, green and blue and are able to reproduce all the colours contained in the triangle defined by them. The CIE RGB colour space, which is inscribed in the chromaticity diagram in Figure 9, is directly derived from the  $\bar{r}$ ,  $\bar{g}$  and  $\bar{b}$  values by means of

$$\begin{aligned} \mathbf{R} &= \int_0^{\infty} I(\lambda) \bar{r}(\lambda) d\lambda \\ \mathbf{G} &= \int_0^{\infty} I(\lambda) \bar{g}(\lambda) d\lambda \\ \mathbf{B} &= \int_0^{\infty} I(\lambda) \bar{b}(\lambda) d\lambda. \end{aligned}$$

RGB spaces are widely used in displays, where each pixel of the screen consists of a red, green and blue light filter, creating the required colour by applying the correct mixture of the three colours. It is employed for computer screens, video cameras, mobile phones, colour television and many more.

## 1.2 Gold

The first archaeological findings of gold date back to as early as 4000 B.C. [22]; gold was since used all over the world by nearly every culture in history. There are several reasons for this continuous fascination: due to its nobility, gold occurs naturally in its elemental form and does not have to be tediously extracted from ores. Furthermore, it is highly ductile and can therefore be shaped with simplest techniques. Additionally, its persistent yellow colour is unique among metals and its rarity makes it a valuable trade article. Already around 3600 B.C. the Egyptians were producing cast gold objects [23] and also managed to beat gold into leaf. For a long time, the main applications were ornamental or ceremonial objects until the Chinese started using little squares of gold as a form of money, slightly before 1000 B.C.



Figure 10: Lydian gold coin from around 600 BC, from [24].

Formerly, one gold coin weighed 24 carats [26] while in today's terminology, 24 carat signifies 100% pure gold. To define the carat of an alloy, the weight per cent of the contained gold is expressed in  $\frac{1}{24}$ . For example, an alloy containing 75 wt.% is termed as 18 carat gold.

About 500 years later, the first gold coins were employed as currency in Lydia, a kingdom of Asia Minor under the reign of King Croesus - known for his enormous wealth [25]. From then on, coins became the preferred currency, some made of pure gold but more commonly of gold alloys. The grading of gold alloys is based on the carat system. The name carat originates from the Greek word *κεράτιον* (*kerátion*), "fruit of the carob tree" whose seeds were used as weight standard due to their uniform weight.

The use of gold has long ceased to be limited to jewellery and coins. In medieval times, gold was considered to have healing powers, mainly based on the belief that something so pure and special could only be good for someone's health [27]. Later, it was found that gold, or more precisely gold complexes really are a valuable aid in the treatment of rheumatoid arthritis [28]. Today, gold is applied in areas ranging from microelectronics to dentistry, from catalysts to nanostructures and medical applications. It is even employed in slightly eccentric food [29] and luxury cosmetic products [30].

### *Gold alloys*

Despite numerous other applications, gold is still one of the preferred metals for luxury watches and jewellery. Yet, the research dedicated to gold for such applications has, in comparison with other fields, been rather small. A big part of the research in the last 30 years about alloying of bulk gold has been performed with the focus on the binary and ternary alloys of gold, silver and

copper [31, 32]. A variety of different colours can be obtained with the three elements, ranging from yellow to red towards the copper-rich side, and over a slightly greenish tinge to the white of the silver (Figure 11, left). However, not all the alloys are equally suited for an application. While gold and silver, as well as gold and copper are soluble in each other over the whole composition range, silver and copper form a eutectic phase diagram, showing very little solubility at room temperature. For the ternary phase diagram this means that a solubility gap reaches into the system from the silver-copper side (Figure 11, right). As a consequence of this solubility gap, it is possible to differentiate between three different alloy types in the system [31]. Type I alloys are in the solid solution range and therefore rather soft and easily workable. Type II alloys are in a two-phase region, but can be solution annealed at high temperatures. They can be worked in the resulting soft state and subsequently age-hardened. In contrast, it is very hard to quench alloys from type III, as they are located in the middle of the solubility gap, where the solid solution is only stable at very high temperatures. Their processing is accordingly difficult.

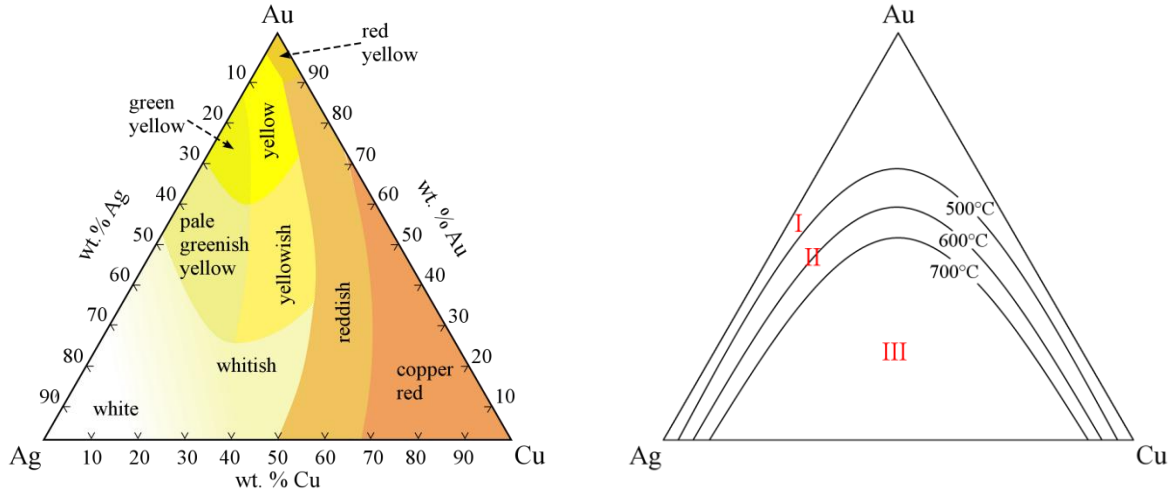


Figure 11: Colour areas [33] and miscibility gap [31] in the ternary Au-Ag-Cu diagram.

Next to yellow and red gold, the most widely known variation is white gold. Initially, it was developed to replace Pt, which grew more and more expensive but quickly became very popular. White gold alloys can contain platinum, palladium, nickel or several other elements. Often, they require a rhodium coating, as the sole addition of whitening alloys does not reach the desired colour.

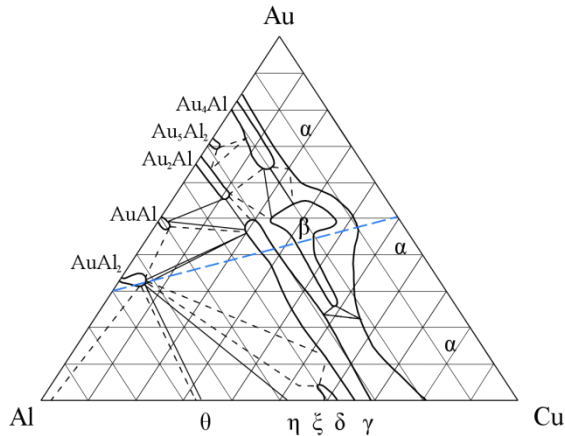


Figure 12: Au-Cu-Al ternary phase diagram, from [34].

original structure, the atoms ‘remembering’ their position and restoring the initial shape of the work piece. Due to their high gold content, these shape memory alloys are only rarely used in industry. Only one of them is occasionally used for jewellery, a composition that has been termed and trademarked ‘Spangold’ [35]. The decorative effect of the spangling surface is utilised, which occurs due to the tilting of the grains after the martensitic transformation. An example is shown in Figure 13. The Au-Cu-Al phase diagram also contains a few differently coloured alloys. Along the binary Au-Cu line, the  $\alpha$ -phase forms, displaying the typical red colour of copper-rich gold alloys (see Figure 11). The alloys of the  $\beta$ -phase are apricot coloured, while the  $\gamma$ -phase that forms along the 30 at. % Al line is whitish-grey. Perhaps the most notable colour has the deep purple  $\text{AuAl}_2$  phase, formed in a small region around 66 at.% aluminium, which will be more closely described in the next section.

An alloy system which only recently attracted interest is the gold-copper-aluminium system [34], shown in Figure 12. The area in which the  $\beta$ -phase is present is probably the most interesting region. Within this area, several of the alloys exhibit a shape-memory effect. When cooled to lower temperatures, they undergo a martensitic phase transformation, meaning that the structure changes from body-centred (bcc) to face-centred (fcc) cubic by diffusionless shear transformation. Upon reheating, the alloy switches back to the

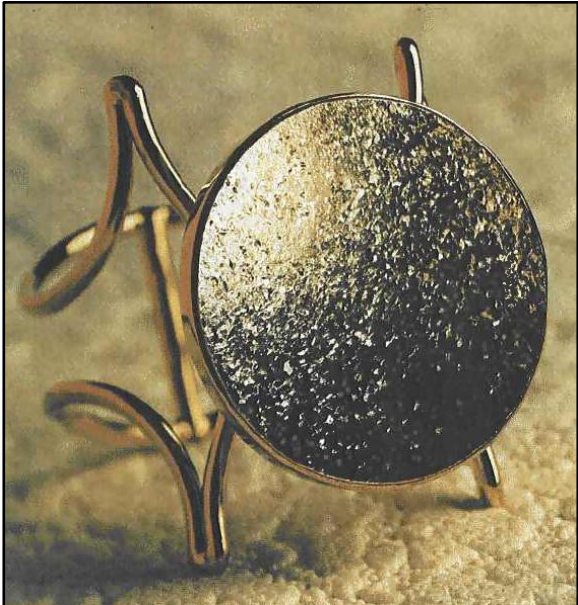


Figure 13: Example of Spangold - the spangling surface is obtained by a martensitic transformation of a previously polished surface (from [35]).

In 1892, an intermetallic phase of gold and aluminium was discovered [36], which displays a striking purple colour (Figure 14). The  $\text{AuAl}_2$  phase forms at 33 at.% Au and 66 at.% Al, crystallises in the fluorite structure (Figure 15) and, because the carat system is based on weight and not atomic per cent, still qualifies as an 18 carat gold alloy. The purple colour has its origin in the selective absorption of light with wavelengths around 530 nm, in the region of yellow and green light. The remaining light from the blue and the red ends of the spectrum is reflected and combined creates the purple colour perception. The selective absorption was traditionally attributed solely to interband transitions from Au s-p bands (1-2 eV below  $E_F$ ) to the Au p-d/Al p band (1-2 eV above  $E_F$ ) [37]. These transitions are possible for a certain energy range, above which a so-called *pseudo gap* in the density of states (DOS) reduces them (Figure 16, from [37]) and the reflectivity increases again, until at higher energies the transitions resume. In addition to the electron interband transitions, it was recently found that the excitation of a bulk plasmon around 2 eV enhances the effect and thus intensifies the colour [38]. Despite its stunning colour, the purple phase is rarely used due to its inherent brittleness and low corrosion resistance, which makes the production and application difficult.



Figure 14: Example of the purple  $\text{AuAl}_2$  phase, used as pseudo-gem stone (from [33]).

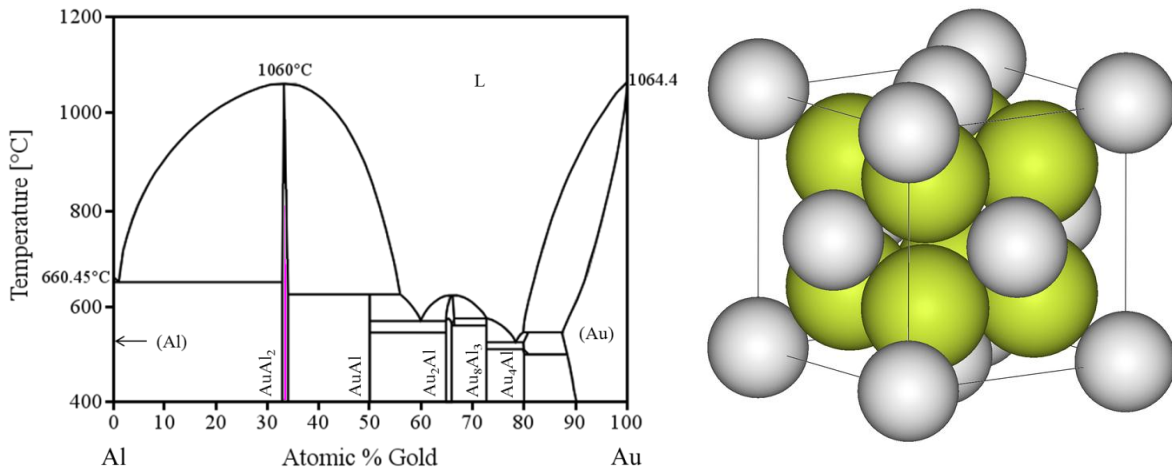


Figure 15: Phase diagram of Al and Au (left) and schematic of the fluorite structure (right), where the Au atoms (grey) form an fcc lattice and the Al atoms (yellow) fill the tetrahedron gaps.



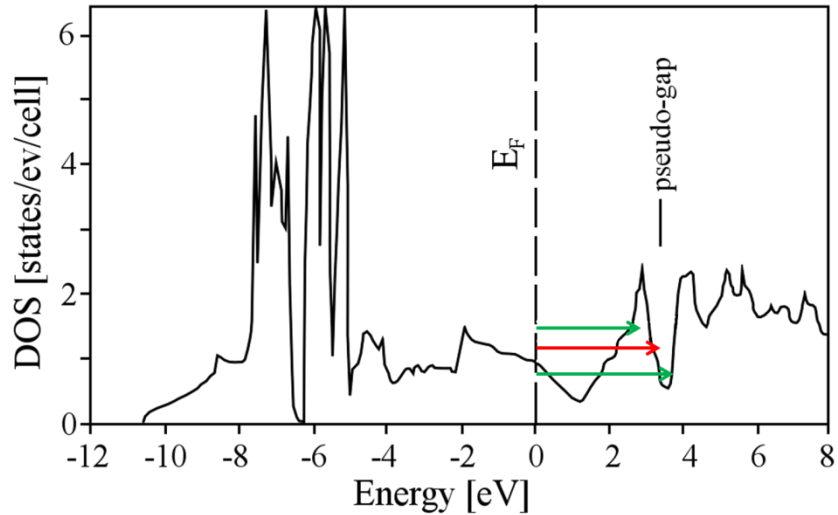


Figure 16: Density of states (DOS) of AuAl<sub>2</sub>, displaying the pseudo gap between 3 and 4 eV (from [37]). The allowed electron transitions are indicated with a green, the forbidden ones with a red arrow.

Two very similar intermetallic phases of gold were discovered with the same crystalline structure as AuAl<sub>2</sub>. AuGa<sub>2</sub> and AuIn<sub>2</sub> both display a shade of blue colour, which is not as intense as the purple of AuAl<sub>2</sub>, probably because they lack the plasmon excitation in the visible range [38]. The two phases are not quite as brittle as AuAl<sub>2</sub>; still they are rarely applied as bulk metals. A large amount of research has been carried out with the aim of improving the mechanical



Figure 17: Blue gold (AuIn<sub>2</sub>), produced by fem Schwäbisch Gmünd / Janine Rall.

properties of the three phases and enabling an application, for example as jewellery. By means of microalloying an improvement of the crack resistance could be achieved without affecting the optical properties of the materials [39]. Investment casting of those alloys was successfully performed but the mechanical properties still complicate an application as bulk materials. However, design strategies were suggested, where by means of bi-metal casting technologies the brittle phase is protected by a ductile matrix. A different approach is the application of the materials as coatings. Several techniques have been tried out: sputter deposition [40], electroplating with subsequent annealing, surface cladding and liquid-metal dip coating [41]. The

latter reference also performed metal release tests and concluded that an invisible protective coating is required as the corrosion resistance of all the three phases is rather low. The possible applications of the intermetallic phases go further than just jewellery: Research has been carried out with an application as architectural coatings on glass [40] or as transparent electrode material in mind [42], and even as coating for cutting tools [43] which would facilitate the detection of an overused blade.

The display of special colours is a property that is common to a lot of intermetallic phases; roughly 100 of them are known [44]. It was found that a prerequisite for colour is the formation of a crystal structure with a high symmetry. This leads to distinct band structures and potentially the required pseudo-gaps in the density of states curve, which leads to a selective reflection of certain wavelengths [44, 45]. Examples are  $\text{CoSi}_2$ ,  $\text{NiSi}_2$  (both blue),  $\text{PtAl}_2$ ,  $\text{PtGa}_2$  (both yellow) or  $\text{PtIn}_2$  (apricot), all crystallising in the fluorite structure, or  $\text{PdIn}$  (brown-rose) and  $\text{NiAl}$  (bluish), which both have the caesium chloride crystal structure.

From the viewpoint of colour development with precious metals, the intermetallic phases of Pt with Al, Ga and In are especially interesting. Like their gold counterparts, they crystallise in the fluorite structure, with a Pt content of 33 at.% and 66 at.% of Al, Ga or In, respectively. Due to this similarity, the production of a ternary phase seems possible, even though no ternary phase diagrams are available.

Klotz *et al.* [41] and Fischer-Bühner *et al.* [39] manufactured such ternary alloys. The former produced alloys of Au, Pt and In by casting and found that the colour continuously changes from blue to apricot as the Pt content is increased. However, a close investigation of the microstructure revealed that the material does not consist of a single, ternary phase but a mixture of binary phases. The intermediate colour is then produced by combining the light reflected from all of them. Similar results were obtained by the latter reference, exchanging the aluminium in  $\text{AuAl}_2$  gradually by gallium, aiming for the production of a ternary  $\text{Au}(\text{Al}/\text{Ga})_2$  phase. While a smooth colour shift was received from purple to blue with increasing gallium content, the material again consisted of a mixture of binary phases.



### 1.3 Size Effects

As mentioned above, metals can not only be produced as bulk materials but also in the form of thin films. While the fabrication of such films had been possible for a while [46], the development of the technology has reduced the achievable dimensions further and further, into the nanometre regime. Subsequently, it has been discovered that the properties of materials change once a critical size limit has been reached. These so-called *size effects* have been found for all different types of properties, for example the mechanical ones [47], where suddenly the strength or hardness increases largely. Another example is the electrical properties, where the conductivity of a metal depends on the size of a sample due to the increased importance of surface or interface scattering contribution [48, 49]. Also the optical properties are subject to size effects. Below a critical value, which depends on the material [46], the reflectivity of a metal thin film decreases with the film thickness. Under a certain value, the layer becomes transparent and can display a different colour in transmission and reflection. A thin silver film, for example, obtains a blue colour in the counter light, while the light transmitted through a thin gold layer becomes green [46].

Thin films that are produced by the condensation of a vapour phase (such as sputter deposition or thermal evaporation) do not form a continuous layer at the initial stage of film growth, but separate islands that grow and coalesce when the deposition continues (termed *Volmer-Weber growth*). Again, the film thickness required to form a continuous film depends on the material, the deposition method and the temperature of the substrate. At room temperature, the condensed atoms are mobile enough to move from their initial position to energetically more favourable places and a longer deposition is required until the film is continuous. Such structures lead to yet other optical effects and can be described as colloids.

A colloid is per definition a two-phase system, consisting of a disperse phase of particles in a matrix. Those particles, typically with sizes between 1 nm and 1  $\mu\text{m}$ , scatter and absorb light selectively, according to their dimension and shape. Famous colloids are, for example, gold or silver nanoparticles immersed in solution [50]. When the size and aspect ratio of the particle is changed, surface plasmons are excited at different wavelengths and light of specific colours is absorbed, creating colloidal solutions with a colour that is adjustable over the whole visible range of the spectrum [51]. When films are so thin that they form separate islands, the optical properties are also determined by their size and shape. Norrman *et al.* [52] investigated gold films of thicknesses between 1 nm and 4 nm and found that the discontinuous layers lead to absorption phenomena that differ from the bulk properties. Kaiser



Figure 18: Colloidal solutions display a different colour, dependent on the size and shape of the Au particles they contain (from [50]).

Kaiser

[53] reported that the plasmon frequency of isolated particles depends on the electronic structure of the metal, the size and shape of the particles and the substrate. He also found that after the percolation threshold is reached, metal films behave optically similarly to the corresponding bulk materials.

## 1.4 Aim of the project

The aim of the project was to design noble metal-based alloys that display novel colours for a possible application in watches and jewellery. While the final application in mind was bulk materials, the alloys in this thesis were produced in the form of magnetron sputter-deposited thin films. This allowed the production of multiple different compositions with minimal material expenditure. Another advantage of the technique is that the produced films are rather far from an equilibrium state, which allows the production of phases and phase compositions that cannot be obtained by conventional casting techniques [54].

A first series of experiments examined the film-thickness dependence of the optical properties of selected materials, three elements (Au, Al and Pt) and one intermetallic phase ( $\text{AuAl}_2$ ). As the designed alloys were required to display bulk behaviour, size-effects due to the layer thickness needed to be excluded.

A further study investigated a range of well-known noble metal alloys and intermetallic phases, namely Au-Ag alloys with different compositions,  $\text{AuAl}_2$ ,  $\text{PtAl}_2$  and  $\text{AuIn}_2$ . The film thickness of all samples was well within the bulk-behaviour range. Differences and similarities in the optical and electrical properties were studied between the thin films and literature values of bulk materials.

In final experiments, the production of ternary alloys based on noble metals was attempted. The purpose was to obtain an intermetallic phase with tuneable colours. While maintaining the abovementioned fluorite structure, a change of colour can be induced in two different ways. When atoms are added that have a very similar size as the ones they are replacing, as for example Pt to  $\text{AuAl}_2$ , the lattice parameter, and hence the band structure remains the same (the unit cell of  $\text{AuAl}_2$  measures 0.5997 nm compared to 0.591 nm for  $\text{PtAl}_2$ ). What changes is the number of electrons, as Pt has only 78 compared to the 79 of Au. As a consequence, the position of the Fermi Level is shifted to lower energies, causing the light-absorbing interband transitions to occur at higher energies. If, in contrast, the added atoms have an equivalent electronic configuration as the ones they are replacing, but a rather different size (such as In to  $\text{AuAl}_2$ , where  $\text{AuIn}_2$  has a lattice constant of 0.65 nm), a change of the band structure would occur, also resulting in a change of the colour. Due to technical reasons, only the first option was chosen, and ternary alloys consisting of 66.6 at.% Al and different Au to Pt ratios were produced.

In a parallel doctoral thesis by D. Keçik, efforts were made to establish a way to model the optical constants and thus reflectivity of an arbitrary alloy composition by *ab initio* simulations. This thesis has already been successfully defended [55].



## 2. Materials and methods

### 2.1 Sample production

All samples were produced by means of magnetron sputter deposition in a tool that allowed simultaneous deposition of up to four different materials (PVD products, Inc.), the target diameter of all materials being 3 inches. The magnetrons were normally aimed at the centre of the substrate ( $0^\circ$ ) but could be tilted away to up to  $15^\circ$  to reduce the deposition rate. The base pressure in the sputter chamber was less than  $5 \cdot 10^{-6}$  mTorr and for the sputter process an argon pressure of 2, 5 or 10 mTorr was introduced. Different substrate materials were employed: Si wafers with a (100) orientation, coated with a diffusion barrier of 50 nm of  $\text{SiO}_2$ , Si wafers with 50 nm of  $\text{SiO}_2$  and 50 nm of  $\text{Si}_3\text{N}_4$  as a diffusion barrier, Cu grids (2 mm in diameter), coated with an amorphous carbon film and standard laboratory glass slides. Before deposition, the glass slides were cleaned in an ultrasonic bath in acetone for five to ten minutes, then rinsed with water and dried with pressurised air. To obtain thin films with homogeneous composition the substrates were rotated during the deposition; to produce samples with a concentration gradient, the substrate was kept static.

The exact sputter parameters are found in appendix A; in the following a short description of the samples produced for the different chapters will be given.

#### *Chapter 3 - Thickness dependence of colour*

To investigate the influence of the layer thickness on the colour, samples of four different materials, Au, Al, Pt and  $\text{AuAl}_2$ , were deposited with a number of different thicknesses, nominally 5, 10, 50, 100 and 200 nm. Glass slides were used as substrate for the reflectivity measurements, and pieces of Si wafers with a size around  $2 \text{ cm}^2$  were employed for the exact thickness determination by AFM. The films with a thickness of 5 nm, 10 nm and 50 nm were also deposited on carbon-coated Cu grids, for the examination of the film continuity in the transmission electron microscope (TEM).

#### *Chapter 4 - Colours due to electronic band structures*

A sample with a composition gradient of Au and Ag was deposited on a 3 inch wafer by keeping the substrate still during the production, with a film thickness of roughly 500 nm. Three different homogeneous Au-Ag alloys were produced with an targeted composition of 20, 50 and 80 at.% Ag and a film thickness of about 300 nm. Also a pure Ag film was produced at a thickness of roughly 300 nm and an Au layer with a thickness of 950 nm.

A sample with a composition gradient of Au and Al was obtained on a 3 inch wafer, with a thickness of roughly 500 nm. The homogeneous  $\text{AuAl}_2$  films were deposited with an Au to Al ratio of 1:2 and also a thickness of 500 nm. A Pt-Al gradient sample was deposited on a 3 inch wafer with a thickness of 500 nm. The homogeneous  $\text{PtAl}_2$  samples were aimed at a thickness of

800 nm, having a Pt to Al ratio of 1:2. The AuIn<sub>2</sub> films, having an Au to In ratio of 1:2 were produced with a thickness of 200 nm. The sputter power of the In target had to be kept very low (<50 W) and deposition was interrupted twice in order to prevent the melting of the target.

Different ternary (Au/Pt)Al<sub>2</sub> samples were produced, with a constant Al content of 66 at. % and a varying Au to Pt ratio. Due to technical issues, some of the samples were deposited at an argon pressure of 10 mTorr.

## 2.2 Sample treatment

### *Heat treatment*

Two different ovens were used for the heat treatments. One of them was a circulating air oven (750/1, Heraeus). To reduce oxidation during the heat treatments, the samples to be treated in this oven were placed in quartz tubes and flushed with argon several times. Then the argon was adjusted to a pressure corresponding to 1 bar at the temperature of the heat treatment and sealed off by melting the tubes with a gas burner. The second oven was a vacuum oven (RTA-1000-3-P, SY116, CreaTec Fischer & Co. GmbH), that was operated at a pressure of  $2.5 \cdot 10^{-8}$  bar. Heat treatments were carried out at different temperatures and for different durations depending on the material/system that was investigated.

### *Chapter 3 - Thickness dependence of the colour*

The pure Au, Al and Pt films were not heat treated, but the AuAl<sub>2</sub> films required a heat treatment of 30 min at 350°C (RTA oven) to obtain the purple colour.

### *Chapter 4 - Colours due to electronic band structures*

The gradient sample of Au-Ag was not heat treated. Despite displaying the expected colours, the homogeneous Au-Ag alloys and the pure Au and Ag layers were treated for 5 h at 350°C in the RTA oven to investigate a possible change of the properties.

The gradient sample of Au-Al was broken into two halves, one of which was annealed for 5 h at 400°C in the RTA oven. The homogeneous AuAl<sub>2</sub> films were annealed for varying times at 350°C to examine the colour development from the initial grey to intense purple over time. Samples were treated for 2 min, 10 min, 30 min, 60 min and 300 min in the circulating air oven.

One half of the produced Pt-Al gradient sample was heat treated for 1 h at 400°C. The homogeneous PtAl<sub>2</sub> were heat treated at 100°C, 200°C, 300°C and 350°C for 30 min. Additionally, a series of treatments was made at 200°C for 1 h, 3 h, 6 h and 24 h, all in the RTA oven.

The AuIn<sub>2</sub> film displayed a shade of blue colour already after the deposition. To investigate a possible intensification of the colour, heat treatments at 300°C were carried out for 30 min and 12 h in the RTA oven.

The ternary Au-Pt-Al sample with the lowest Pt content (Au89Pt11) was heat treated for 1 h at 250 °C as it was found that higher temperatures led to strong hillock formation and delamination. The other Au-Pt-Al samples were heat treated for 30 min at 350°C in the RTA oven. Longer heat treatments of 24 h at 350°C were carried out on the four samples with the highest Pt contents, to gain more information about their stability over longer terms.

### *Ion irradiation*

The ion irradiations of chapter 4.2 were carried out with 3.5 MeV Au<sup>+</sup> ions using a Van de Graaff EN tandem accelerator (High Voltage Inc.) at an angle normal to the sample surface. Different ion fluences listed in Table 1 were used while the ion current ranged between 1 and 50 nA. The sample temperature during most irradiations was monitored by a thermocouple and kept at about -196°C by circulating liquid nitrogen through a custom made cooler. In one irradiation, the temperature of the sample was kept at room temperature. All the samples irradiated had been previously heat treated for 5 h at 350°C.

Table 1: Fluences and temperatures of the irradiations

Sample	Temperature [°C]	Fluence [ions/cm <sup>2</sup> ]	Substrate
AuAl <sub>2</sub> 10 <sup>12</sup>	-196	10 <sup>12</sup>	Si-SiO <sub>2</sub> -Si <sub>3</sub> N <sub>4</sub> wafer
AuAl <sub>2</sub> 10 <sup>13</sup>	-196	10 <sup>13</sup>	Si-SiO <sub>2</sub> -Si <sub>3</sub> N <sub>4</sub> wafer
AuAl <sub>2</sub> 10 <sup>15</sup>	-196	10 <sup>15</sup>	Si-SiO <sub>2</sub> -Si <sub>3</sub> N <sub>4</sub> wafer
AuAl <sub>2</sub> 5 * 10 <sup>15</sup>	-196	5 * 10 <sup>15</sup>	Si-SiO <sub>2</sub> -Si <sub>3</sub> N <sub>4</sub> wafer
AuAl <sub>2</sub> 5 * 10 <sup>15</sup> RT	25	5 * 10 <sup>15</sup>	Si-SiO <sub>2</sub> -Si <sub>3</sub> N <sub>4</sub> wafer
AuAl <sub>2</sub> 5 * 10 <sup>15</sup> glass	-196	5 * 10 <sup>15</sup>	SiO <sub>2</sub> glass

## 2.3 Investigation methods

### *Optical methods*

Images of all samples were taken with a Nikon D80 equipped with a 200 mm macro objective. As most of the samples were specularly reflective, the images were taken at a small angle (roughly 5°) and a white paper was used as a reflector to be able to properly capture their colour. For chapter 3, images were taken of the thin films in counter light, to examine their transparency. For this purpose, a lamp was covered with a patterned piece of paper and placed underneath the samples. Again, the images were taken from a small angle.

A Polyvar-MET microscope (Reichert) was used for light microscopy, to determine the presence of large second phases and detect areas of delamination and hillocks.

Reflectivity measurements were performed with a fibre spectrometer (USB2000+, OceanOptics), equipped with a deuterium/halogen light source (DH-2000-BAL, OceanOptics) and operated by SpectraSuite software (OceanOptics). The measurements were performed at an angle of 0° incidence. A sputter-deposited Al film of 500 nm thickness was used for the calibration measurement and a non-unity correction file was employed.

The reflectivity of the semi-transparent films was measured by placing the glass slide on top of a black, absorbing layer of foam rubber that ensured that the light that had been transmitted would not be reflected at the back interface. The internal reflection in the glass slid was assumed to be negligible.

The reflectivity data were converted into colour coordinates of the XYZ colour space using a standard procedure [20], according to the description in the introduction on page 16. Based on that, the CIE L\*a\*b\*, and the xyY were determined. For ease of display, the colours were mapped in the xy chromaticity diagram.

The reflectivity of the semi-transparent films on SiO<sub>2</sub> was modelled according to the method specified in [56]. The reflection coefficient is described as

$$\tilde{r} = \frac{\tilde{r}_{12} + \tilde{r}_{23}e^{2i\beta}}{1 + \tilde{r}_{12}\tilde{r}_{23}e^{2i\beta}}$$

Where  $\tilde{r}_{mn} = (\tilde{p}_m - \tilde{p}_n)/(\tilde{p}_m + \tilde{p}_n)$ ,  $\tilde{p}_m = \tilde{n} \cos(\tilde{\theta}_m)$ ,  $\tilde{\beta} = \left(\frac{2\pi}{\lambda}\right) \tilde{n}_2 h \cos(\tilde{\theta}_2)$  and  $\tilde{\theta}_m = \sin^{-1}(\sin\left(\frac{\theta_1}{\tilde{n}_m}\right))$ , which is the complex form of Snell's law. The refractive indices references were taken from [57].



### *Electron microscopy*

Scanning electron microscopy (SEM) investigations were carried out in a SU-70 instrument (Hitachi), equipped with a secondary (SE) and a backscattered electron (BSE) detector and an energy-dispersive X-ray (EDX) detector operated by the Inca program (Oxford Instruments, UK). Next to the composition of the films, their topography and phase uniformity was investigated.

The samples for the transmission electron microscopy (TEM) investigations were either directly deposited on carbon coated copper grids (for very thin films), or cross-sectional lamellae were prepared by means of focused ion beam (FIB) (NVision 40, Zeiss) (for films of any thickness).

The transmission electron microscopy (TEM) measurements were carried out in a field emission gun (FEG) TEM (Tecnai F30, FEI) operated at 300 kV. The morphology of the films in bright and dark field was investigated as well as the crystal structure by means of diffraction analysis. High-resolution images were taken and their fast Fourier transformed (FFT) images used as additional source of phase information. In certain cases the machine was operated in Scanning-TEM mode (STEM) and an energy dispersive X-ray (EDX) mapping was performed to gain information about the distribution of the elements in the film.

Electron backscatter diffraction (EBSD) was employed to investigate the texture of selected samples from chapter 4.2 using a FEI Quanta 200 FEG microscope.

### *Electrical resistivity*

Electrical resistivity measurements were performed on the samples of chapters 4.1 and 4.2 to gain information about the defect content in the films. The four-point technique developed by Van der Pauw [58] was employed, using a Jandel probe head. The pins on the probe were arranged in a square geometry and had a spacing of 0.51 mm. A direct current of 0.1 A was applied and the resulting voltage was measured (National Instruments PXI-8187). For every sample an average of 200 measurements was made and the sample size was between 1 cm<sup>2</sup> and 2 cm<sup>2</sup>. The evaluation was done using LabView 8.2 software and the results were compared with calculated values, obtained from the combined Fuchs-Sondheimer/Mayadas-Shatzkes models, which will be described in the following.

#### Modelling of the resistivity

The resistivity of the samples was modelled using the combined Fuchs-Sondheimer (FS) and Mayadas-Shatzkes (MS) method [59], which takes into account the reflection of the electrons at the surface and interface (FS) and at the grain boundaries (MS). The formula after which the resistivity is calculated is:

$$\rho = \rho_0 \left[ \left( \frac{3}{8} * \frac{\lambda}{d} * (1 - p) \right) + \frac{1}{3} / \left( \frac{1}{3} - \frac{\alpha}{2} + \alpha^2 - \alpha^3 * \ln \left( 1 + \frac{1}{\alpha} \right) \right) \right]$$

Where  $\alpha = \lambda/D * (R/(1-R))$ ,  $\rho_0$  being the bulk resistivity,  $\lambda$  the electron mean free path,  $d$  the film thickness,  $p$  the surface scattering parameter,  $D$  the grain size and  $R$  the grain boundary reflection coefficient.

**AuAl<sub>2</sub>** The bulk resistivity of AuAl<sub>2</sub> at room temperature  $\rho_0$  is 8  $\mu\Omega\text{cm}$  [42] and  $d$  was 500 nm as determined from TEM images. The mean free path length  $\lambda$  has been calculated to be 13 nm by means of its Hall coefficient  $A$ , which is  $1.56 * 10^{-4} \text{ cm}^3/\text{C}$  [60]. From the Hall coefficient, the electron density can be determined using  $n = 1/(A * e)$ , which is used to obtain the Fermi velocity  $v_F$  following  $v_F = \hbar/m * (3\pi^2 n)^{1/3}$ . With the help of the relaxation time, which depends on the electrical conductivity and the electron density according to  $\tau = \chi m/(e^2 n)$ ,  $\lambda$  can be calculated using  $\lambda = v_F * \tau$  [61].

The surface scattering parameter  $p$  takes values between 0 and 1, and describes whether the electrons at the surface are scattered diffusely ( $p = 0$ ) or specularly ( $p = 1$ ). As the film thickness is rather large,  $p$  was found to have little influence on the modelled resistivity. It was set to 0.5, as no reference value could be retrieved.  $R$  was chosen such that the modelled resistivity matched the measured resistivity of the sample temperature treated for 5 h at 350°C, as it was assumed that for this sample the defect concentration was reduced to a minimum level. This was the case at  $R = 0.74$ .

**AuIn<sub>2</sub>** The bulk resistivity  $\rho_0$  of AuIn<sub>2</sub> is with is 8  $\mu\Omega\text{cm}$  the same as the one of AuAl<sub>2</sub>. From its Hall coefficient of  $1.14 * 10^{-4} \text{ cm}^3/\text{C}$  [60] the mean free path length is calculated, as described above, to be 7.49 nm [61]. The film thickness  $d$  measured from TEM images is 245 nm. The value  $p$  was again set to 0.5 and  $R$  was set to match the measurement of the sample heat treated for 12 h at 300°C, which was the case at  $R = 0.75$ .

No reference value for the bulk resistivity or the Hall coefficient could be found for PtAl<sub>2</sub>; therefore no resistivity calculations could be performed.

### *X-Ray diffraction (XRD)*

To determine the phases present in the samples X-ray diffraction (XRD) measurements were performed. An X'Pert PRO-MPD X-ray diffractometer (PANalytical) with an Eulerian cradle was used. As source a Cu  $K_{\alpha}$  tube with Ni filter and mono-capillary was employed, the detector was an X'celerator semiconductor detector (PANalytical). The  $2\theta$ -angle ranges for the measurements of the different investigated materials are listed in Table 2. The  $\psi$ -angle was kept at  $5^{\circ}$  to avoid the strong signal from the Si wafer. For chapter 4.2 measurements were conducted with varying  $\psi$ -angle from  $0^{\circ}$  to  $45^{\circ}$ , to obtain information about the texture of the films and macrostrains. Stress analyses were carried out by means of the  $\sin^2\psi$  method [62].

Table 2: Measured  $2\theta$  range of the different sample materials

Samples	$2\theta$ [°]
AuAl <sub>2</sub>	25 - 100
PtAl <sub>2</sub>	30-100
AuIn <sub>2</sub>	30 - 90
(Au/Pt)Al <sub>2</sub>	25 - 100

A rough estimation was made of the grain sizes of the as-deposited PtAl<sub>2</sub> sample by means of the Scherrer Formula, which calculates the minimum diffracting grain sizes by the peak broadening:

$$\beta_{\tau} = \frac{\lambda}{\tau \cos\theta},$$

where  $\beta_{\tau}$  is the peak broadening,  $\lambda$  the wavelength of the X-ray source,  $\tau$  the grain size and  $\theta$  the diffraction angle. Included in  $\beta_{\tau}$  are the full width at half maximum (FWHM) of the measured peak and the instrumental peak broadening. For the latter value, the peak width of the heat treated PtAl<sub>2</sub> sample was employed.

### *Atomic force microscopy (AFM)*

Atomic force microscopy (AFM) in tapping mode was carried out to determine the film thickness of the samples in chapter 3 on a Cypher Scanning Probe Microscope (Asylum Research, USA).



### 3. Film thickness dependence of colour

#### 3.1 Gold (Au)

##### Thickness evaluation

The film thickness of the produced gold layers as determined by AFM is listed in Table 3. The measured values do not perfectly correspond to the aimed-for layer thicknesses, especially for the thinnest sample, which was supposed to be 5 nm thick. For the following presentation of results and discussion the samples will be named after their nominal thickness and not the exact values.

Table 3: Layer thickness of the Au films as measured by AFM

Sample	Thickness [nm]
Au 5	16
Au 10	18
Au 50	60
Au 100	109
Au 200	189
Au 300	291

##### Macroscopic appearance and reflectivity

While the films of 200 nm and 300 nm thickness are opaque, the thinner films are transparent and display a greenish colour when held against a light source (Figure 19, the left part of the image is covered with the thin films on a glass substrate, the right part is the underlying paper background). Surprisingly, the 50 nm layer is still transparent. At a thickness of 100 nm and more the films become completely opaque. The film thickness at which opacity is reached is dependent on the used light source and might vary with its brightness. For all images in this chapter the same light source was used, which allows a comparison between the investigated materials, but not necessarily to literature.

On the reflectivity measurements of the thin films in Figure 20 the development of the reflectivity curve of gold can be nicely observed. While the 5 nm thin film transmits most of the incoming light to the same degree, a clear dip is visible in the curve of the 10 nm thick sample. The typical shape of the Au reflectivity curve,



Figure 19: Images of thin Au films (left part), in counter light. After a thickness of 100 nm is reached, the films are opaque.

with the absorption edge around 500 nm, is clearly recognisable when the sample reaches a thickness of 50 nm. The sharp absorption edge is intensified in the 100 nm thick film and does not change any further when the film thickness increases to 200 nm and 300 nm. It is therefore assumed that the bulk reflectivity is reached. Comparing the measured reflectivity curves with the calculated ones reveals that they fit nicely for the thicker films. The calculated reflectivity of the 10 nm film is slightly higher than the measured one and deviates quite strongly for the 5 nm film.

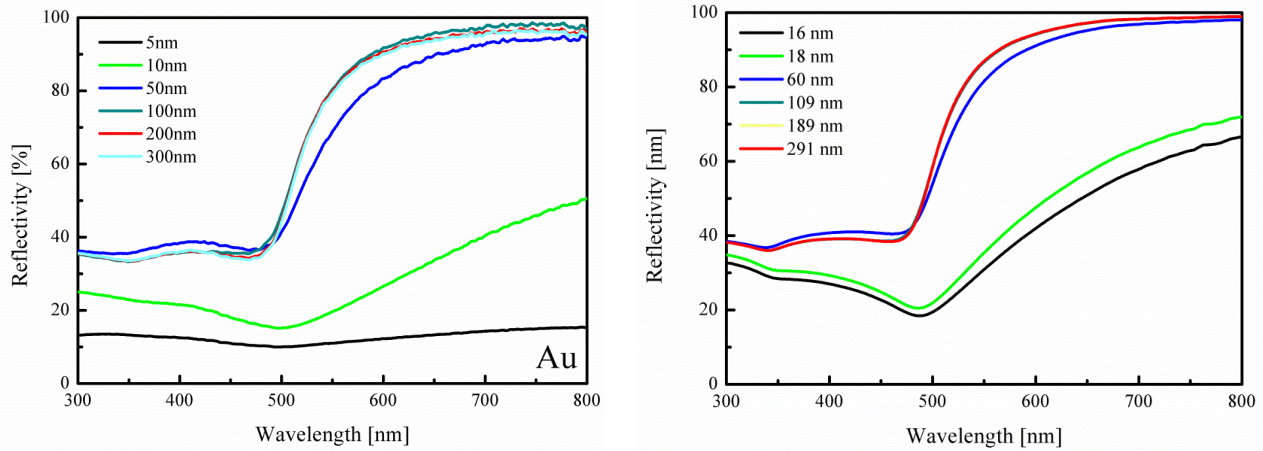


Figure 20: Measured reflectivity curves of the Au thin films (left) and their calculated counterparts (right). The initially very low reflectivity of the samples increases with the film thickness and reaches a stable shape at 100 nm. The calculations were performed for films with the exact thickness as determined by AFM measurements.

### Microstructure studies

The transmission electron microscopy (TEM) investigations of the 5 nm thick film (Figure 21, left) shows that while the layer is not completely continuous yet, only few grooves are present between the covered areas. Diffraction patterns and high-resolution images (appendix B) show that the film is already crystalline. With 10 nm thickness the substrate is completely covered and grains of sizes around 10 nm are visible. The 50 nm thick film displays larger grains with sizes between 50 nm and 100 nm. Taking high resolution images was no longer possible at this thickness.

It has to be noted that the films that were used for reflectivity measurements were deposited on laboratory glass slides, while an amorphous carbon film was employed as substrate for the TEM investigations. While both samples were produced simultaneously, it is possible that during the initial stages of the deposition the film formation is slightly different for the two. Yet, comparing the reflectivity and morphology of thin metal films deposited on laboratory glass substrates and Formvar® resin substrates, Sennet *et al.* [63] found no notable difference. This suggests that no major influence of the substrate is to be expected in our case, either.

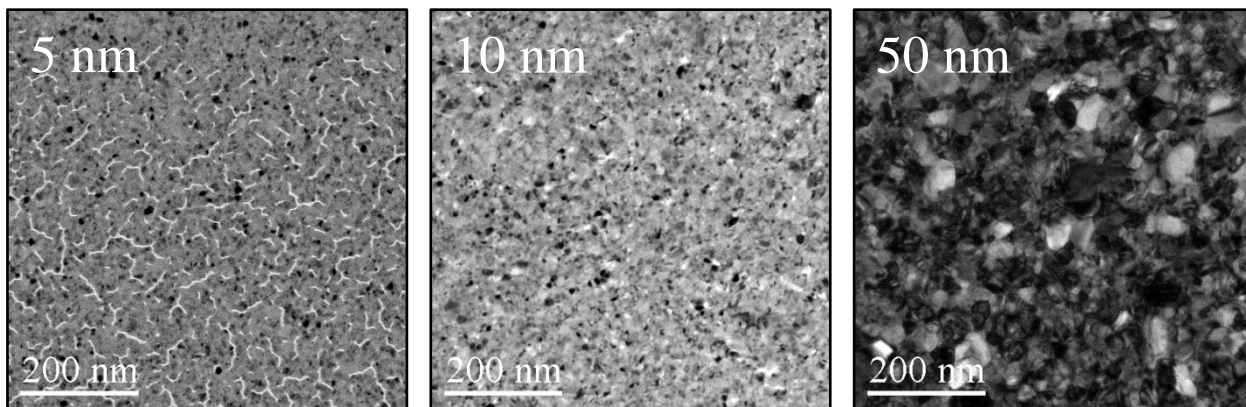


Figure 21: TEM BF images of thin Au films with different thicknesses. Grooves are present in the 5 nm thick sample; the 10 nm film is already continuous, with grains around 10 nm in size. In the 50 nm sample an increased grain size can be observed.

### *Discussion*

The produced thickness, as measured by AFM, differs rather strongly from the aimed-for values, especially for the thinnest two films. The reason is probably that the layers are not formed as smooth, continuous layer from the beginning of the film growth, but start off as separate islands on the substrate. With increasing layer thickness the islands grow, coalesce and form a continuous film. This kind of film growth is also referred to as Volmer-Weber growth and occurs when a material is deposited on a substrate it does not wet.

The sputter rate was measured on a relatively thick film (around 100 nm) which would have been continuous already, and the required deposition time calculated for each layer thickness. While the amount of material of the thinnest film probably corresponds to a 5 nm thick film if it was spread out continuously, the islands can reach higher thicknesses, as illustrated in Figure 22.

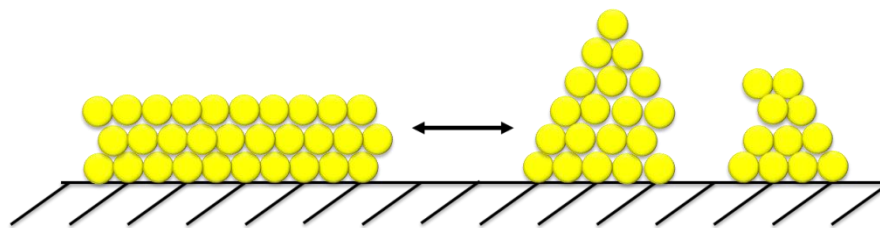


Figure 22: Schematic of the thickness of a continuous layer compared to Volmer-Weber growth.

This discrepancy is also likely to be the reason for the large difference between the measured and calculated reflectivities of the thinnest layers. For the calculations a continuous, smooth film is assumed, which is not the case, as was shown by the TEM images.

The thickness required for thin Au layers to display the same optical properties as the bulk material lies in between 60 and 109 nm. After this value is reached, the films are completely opaque, dense and crystalline.



## 3.2 Platinum (Pt)

### Results

#### Thickness evaluation

Again, AFM measurements reveal that the produced films differ from the intended thickness. The nominally 5 nm and 10 nm thick layers appear to have the same effective thickness. The same effects at the initial stage of film formation as were described above are likely to be the reason for the discrepancy.

Table 4: Layer thickness of the Pt films as measured by AFM

Sample	Thickness [nm]
Pt 5	9
Pt 10	9
Pt 50	51
Pt 100	85
Pt 200	225

#### Macroscopic appearance and reflectivity

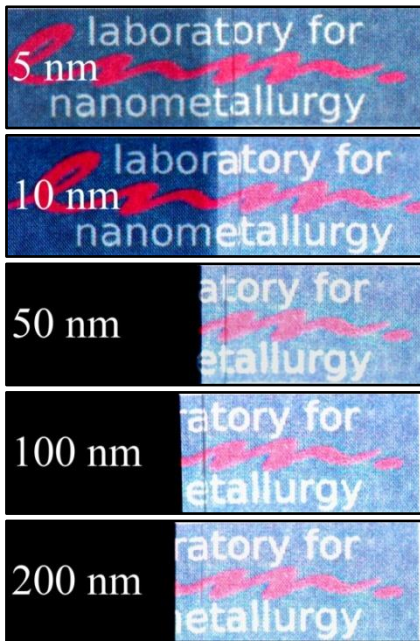


Figure 23: Images of thin Pt films (left part), lit from the back. Already at a thickness of 50 nm the sample is not transparent anymore.

The platinum films with 5 nm and 10 nm thickness are transparent, but do not display a specific colour in the counter-light as the Au films in the previous section (Figure 23). Already the film with a thickness of 50 nm is fully opaque and has the expected grey colour of Pt. Hence, the minimum thickness for bulk properties seems to be smaller than in the case of Au. The reflectivity of the thinnest layer is very low but increases with increasing film thickness (Figure 24). The curve of the 50 nm thick layer already has roughly the same progression as the reflectivity of the samples with 100 nm and 200 nm thickness, also suggesting that the minimum thickness for bulk properties is lower than in the case of Au. There is a bump in the measured reflectivity around 430 nm in all films. Its origin is not entirely clear as it has not been reported in literature [64, 65]. While the formation of an oxide can be excluded, a contamination during the deposition could be the reason. The calculations fit quite well; the reflectivity of all films is only slightly lower than the measured ones.

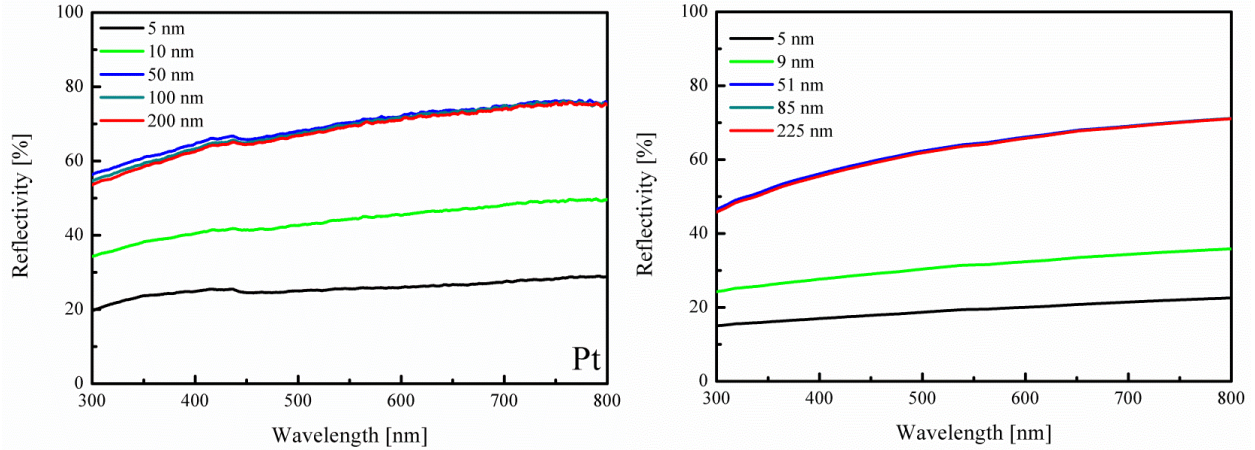


Figure 24: Reflectivity curves of the Pt thin films, measured (left) and calculated (right). Again, the reflectivity increases with film thickness. Already at a thickness of 50 nm the shape and position of the curve remain constant in the measured as well as the calculated curves.

### Microstructure studies

The TEM BF images (Figure 25) show that the thinnest Pt layer is nearly continuous and only contains small grooves in very few places. The 10 nm film looks very similar, with only marginally larger grains. No more grooves were found and the film is fully continuous. Further grain growth can be seen on the 50 nm thick sample and again the thickness was too large for high-resolution images.

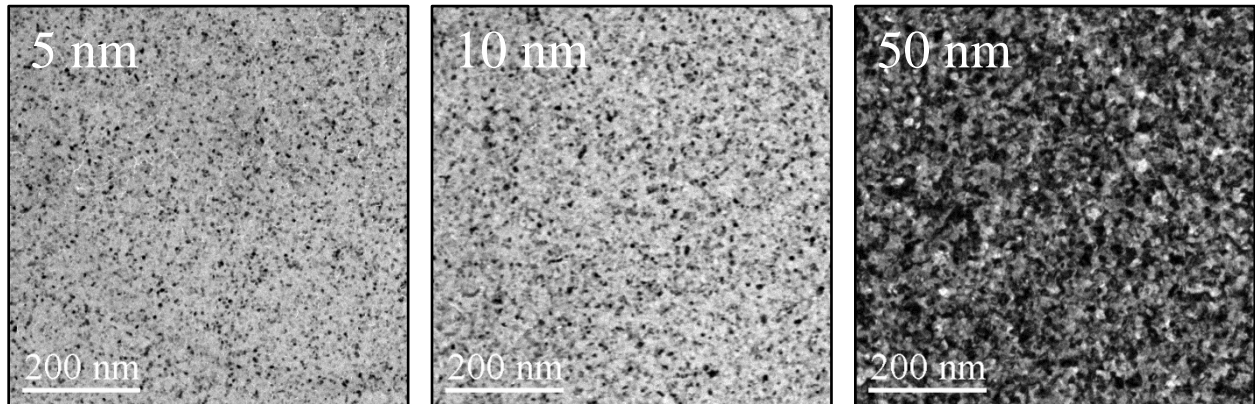


Figure 25: TEM BF images of thin Pt films with different thicknesses. The 5 nm thick film is nearly continuous, with only slightly smaller grains than the 10 nm thick film. A small increase in the grain size is visible in the 50 nm thick sample.

### *Discussion*

The discrepancies between the intended and real film thicknesses for the very thin films are probably due to the same reasons mentioned before: The film does not form as a homogeneous, continuous layer from the very early stages of film formation, but initially forms separate islands that coalesce during further film growth.

The film that was supposed to be 100 nm is thinner; the one intended to be 200 nm is thicker than the aimed-for value. An inaccurately determined sputter rate could be the reason or miscalculations of the required sputter times.

The minimum film thickness to produce optical properties which correspond to the bulk material is smaller than was the case in Au - at 50 nm the films are already completely opaque and their reflectivity remains constant for increasing layer thicknesses.

### 3.3 Aluminium (Al)

#### *Results*

##### Thickness evaluation

The film thickness measurements by means of AFM indicate that the thin Al films are quite close to the intended film thickness. A notable discrepancy is only visible for the 5 nm thick sample, and here again, it is probably due to non-continuous layer formation at the initial stages of film growth.

Table 5: Layer thickness of the Al films as measured by AFM

Sample	Thickness [nm]
Al 5	8
Al 10	12
Al 50	51
Al 100	102
Al 200	192

##### Macroscopic appearance and reflectivity

The films of 5 nm and 10 nm Pt are transparent when held against a light source, as can be seen in Figure 26. The films of 50 nm and higher thickness are completely opaque and display the typical light grey colour of aluminium. Also the reflectivity measurements (Figure 27) reveal that the three thickest films behave very similarly, with values constantly between 80 and 90 % over the whole visible spectrum, comparing well to literature [66]. The 10 nm and 5 nm films have a reduced reflectivity, as was expected considering their partial transparency. The semi-transparent films do not display a special colour when viewed in back light. The calculated reflectivities do not fit very well to the measurements. They are much lower for all film thicknesses and the values seem to increase with increasing wavelength while the measured ones are slightly reduced (Figure 27).

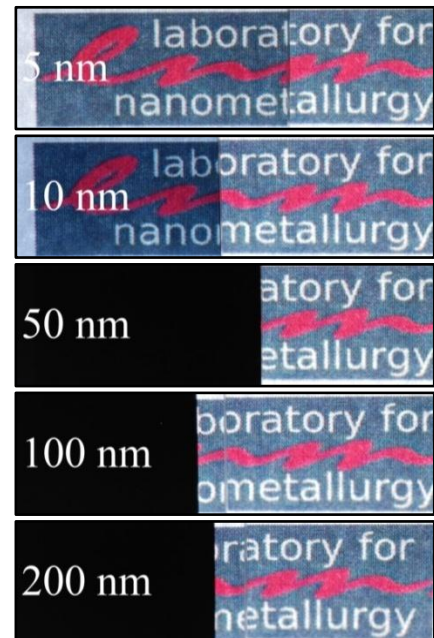


Figure 26: Images of thin Al films (left part), lit from the back. A 50 nm thick layer of Al is sufficient to lead to optical bulk properties.



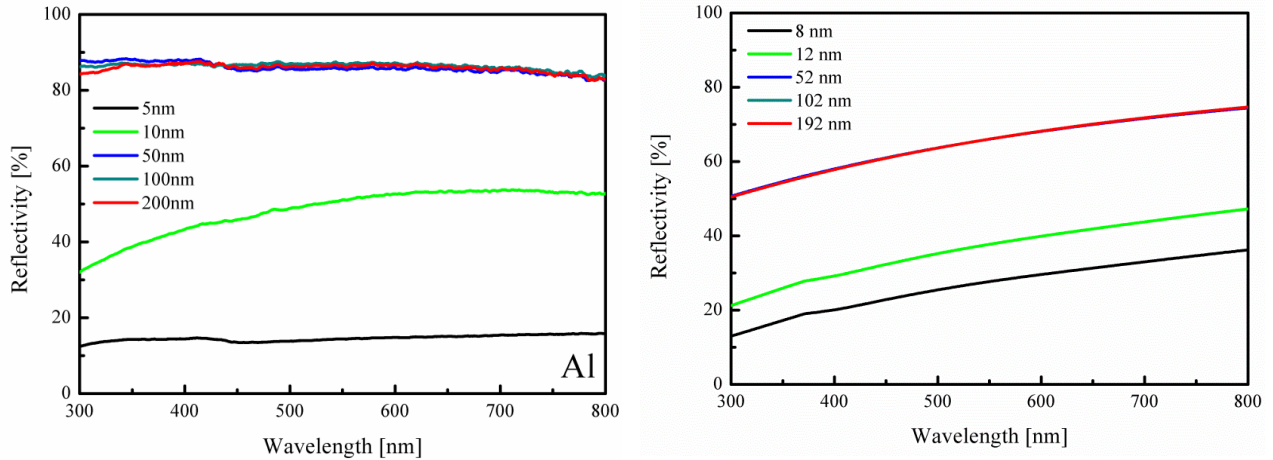


Figure 27: Reflectivity curves of the Al thin films, measured (left) and calculated (right). The measured reflectivity of the thinnest film is rather low and increases with the film thickness. Already at 50 nm the bulk reflectivity is obtained. The reflectivity calculations do not match very well, possibly due to a faulty refractive index used for the calculation.

### Microstructure studies

The TEM BF images of the 5 nm Al film show a structure of islands separated by grooves (Figure 28, left). The diffraction pattern of the sample shows clearly defined, continuous rings, without sharp reflexes. At 10 nm thickness a continuous film has formed, with grains of sizes around 10 nm. Nicely defined grains between 50 and 100 nm are found on the 50 nm thick film of aluminium. The diffraction pattern has changed into rings consisting of separate sharp reflexes. Notable is that in the BF image several twin bands (parallel twin boundaries) appear to be present. Aluminium has a rather high stacking fault energy and does not usually form twins [67]. This indicates that a small amount of impurities are present in the film.

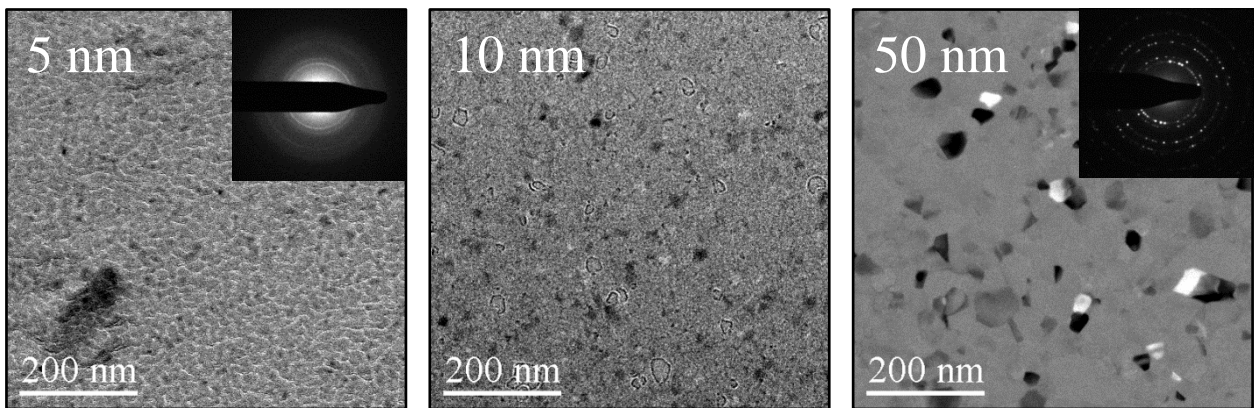


Figure 28: TEM BF images of thin Al films with different thicknesses. The 5 nm film contains grooves, but already at 10 nm the layer is continuous. In the images of the 50 nm thick film, with rather large grains, twin bands can be observed, suggesting that there are impurities present.

### *Discussion*

The AFM measurements reveal that the film thickness of the Al films corresponds rather nicely to the intended values. The reflectivity of the films increases with the film thickness and reaches a stable value when a thickness of 50 nm is reached. The reason for the poor agreement of measured and calculated reflectivity could be an inaccurate reference for the refractive index.

The presence of the oxide layer that forms on the surface of aluminium when it is exposed to air has been neglected for all considerations as it is expected to be transparent and much too thin to produce interference colours.

### 3.4 Gold-aluminide (AuAl<sub>2</sub>)

#### Results

##### Thickness determination

As was the case in all previously examined materials, the thinnest AuAl<sub>2</sub> film has a higher thickness than the intended 5 nm (Table 6). While the 10 nm sample appears to have the correct film thickness, the values of the thicker films are all thinner than the target thickness. The measured sputter rate might have been slightly too low.

Table 6: Layer thickness of the AuAl<sub>2</sub> films (as-deposited) by AFM

Sample	Thickness [nm]
AuAl <sub>2</sub> 5	8
AuAl <sub>2</sub> 10	10
AuAl <sub>2</sub> 50	38
AuAl <sub>2</sub> 100	75
AuAl <sub>2</sub> 200	185

##### Macroscopic appearance and reflectivity

When viewed in reflection the AuAl<sub>2</sub> samples display a shade of pink in the as-deposited state as soon as a thickness of 50 nm is reached (Figure 29). After a heat treatment of 30 min at 350°C, those samples appear in the expected purple colour. While no specific colour is visible on the 5 nm sample, a slightly bluish shade can be observed on the 10 nm thick sample. The heat treatment does not have a big influence on the colour of these two films.

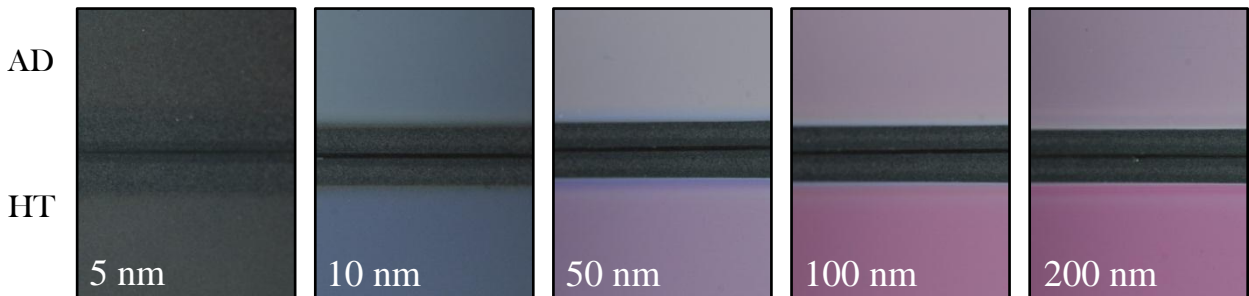


Figure 29: Images of the thin films on a dark background. The top half of the image is as-deposited (AD), the bottom half heat treated for 30 min at 350°C (HT). After a thickness of 50 nm is reached, a purple colour is visible, however in a slightly paler shade. Only the 200 nm thick film displays the expected intense colour.

The images in Figure 30 show that the AuAl<sub>2</sub> films are transparent until a thickness of 200 nm is reached, in the as-deposited as well as the heat treated state. The heat treatment even appears to lead to an increase of the transparency.

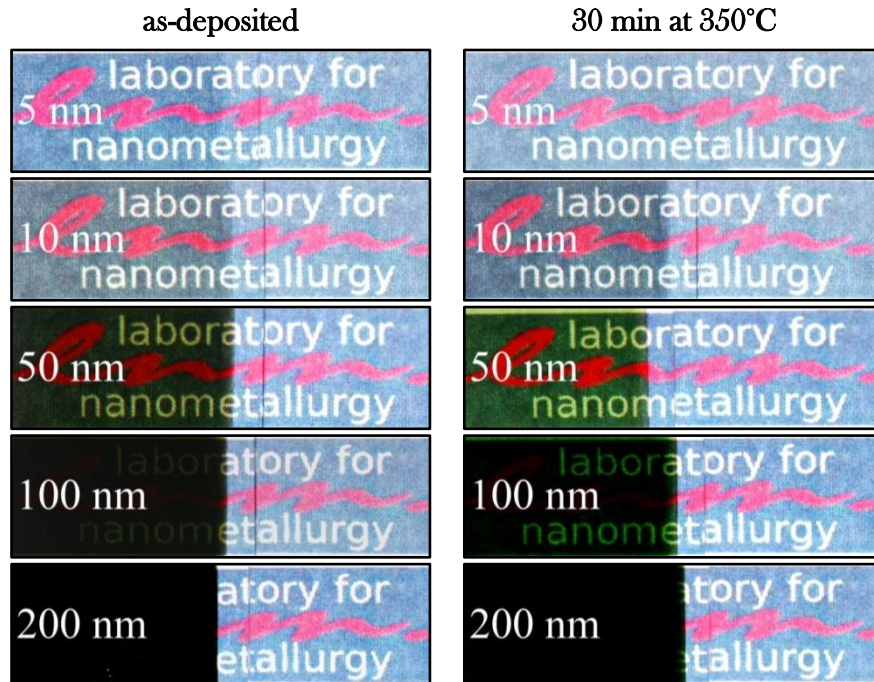


Figure 30: Images of thin AuAl<sub>2</sub> films (left part), lit from the back, in the as-deposited (left) and heat treated state (right). It seems like the heat treatment for 30 min at 350°C increases the transmission of the light.

The reflectivity curve (Figure 31) of the as-deposited sample at a thickness of 5 nm is very low, mirroring the high transparency that is perceived. The slightly thicker sample has an increased reflectivity at shorter wavelengths, a feature that is enhanced with growing film thickness. At 50 nm thickness the dip in the reflectivity curve around 540 nm, which is responsible for the pink shade, is already clearly visible. It becomes deeper as the film thickness increases.

The heat treatment does not largely affect the reflectivity of the 5 nm thick sample and slightly increases the values of the 10 nm sample for medium wavelengths. The dip in the reflectivity curve is intensified for the samples with a thickness of 50 nm, 100 nm and 200 nm. For comparison, the reflectivity data of a sample with 500 nm thickness has been added to the data. It can be seen that the 200 nm and 500 nm sample are very similar, but the thicker sample is shifted to slightly lower reflectivity values. This could be due to an increased roughness as a consequence of the longer duration of the deposition. The different features of the curve do not change anymore, which leads to the assumption that at 200 nm the bulk properties are achieved.



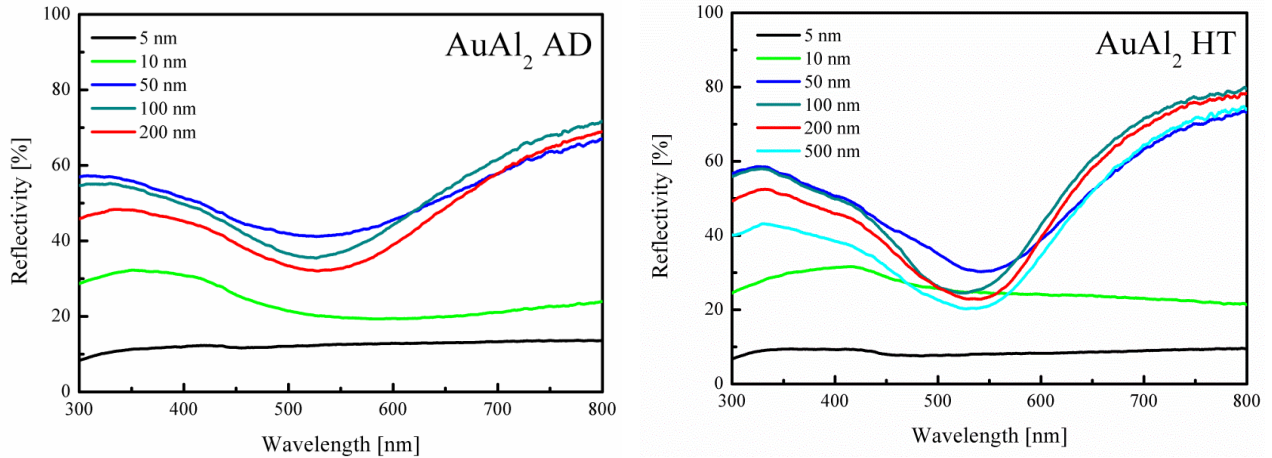


Figure 31: Reflectivity curves of the  $\text{AuAl}_2$  thin films, as-deposited (left) and heat treated for 30 min at  $350^\circ\text{C}$  (right). To the spectra of the heat treated samples, the reflectivity of a 500 nm thick sample has been added for comparison.

Optical microscopy investigations showed that in the heat treated specimens of the 50 nm, 100 nm and 200 nm thick films the precipitation of a second phase had occurred. The second phase, most likely the binary intermetallic phase  $\text{AuAl}$ , has a grey colour, but is not expected to influence the optical properties strongly, as the precipitates are rather small. The films with a thickness of 5 nm and 10 nm did not contain any second phases; however, they also did not display the purple colour.

## Microstructure studies

### Sample 5 nm

The TEM BF images in Figure 32 of the thinnest sample show features that resemble dendritic structure. Diffraction analysis of the two phases indicate that the brighter areas consist of pure Au or Al (the crystal structure and dimensions of the unit cells of the two materials are so similar that it is not possible to distinguish them by means of electron diffraction). The bright contrast in the BF image suggests that it consists of the lighter Al. Due to the broadness and the low number of diffraction rings that were collected from the dark area it is not possible to say what they might consist of, but the shape of the rings suggest that a nanocrystalline phase is at hand.

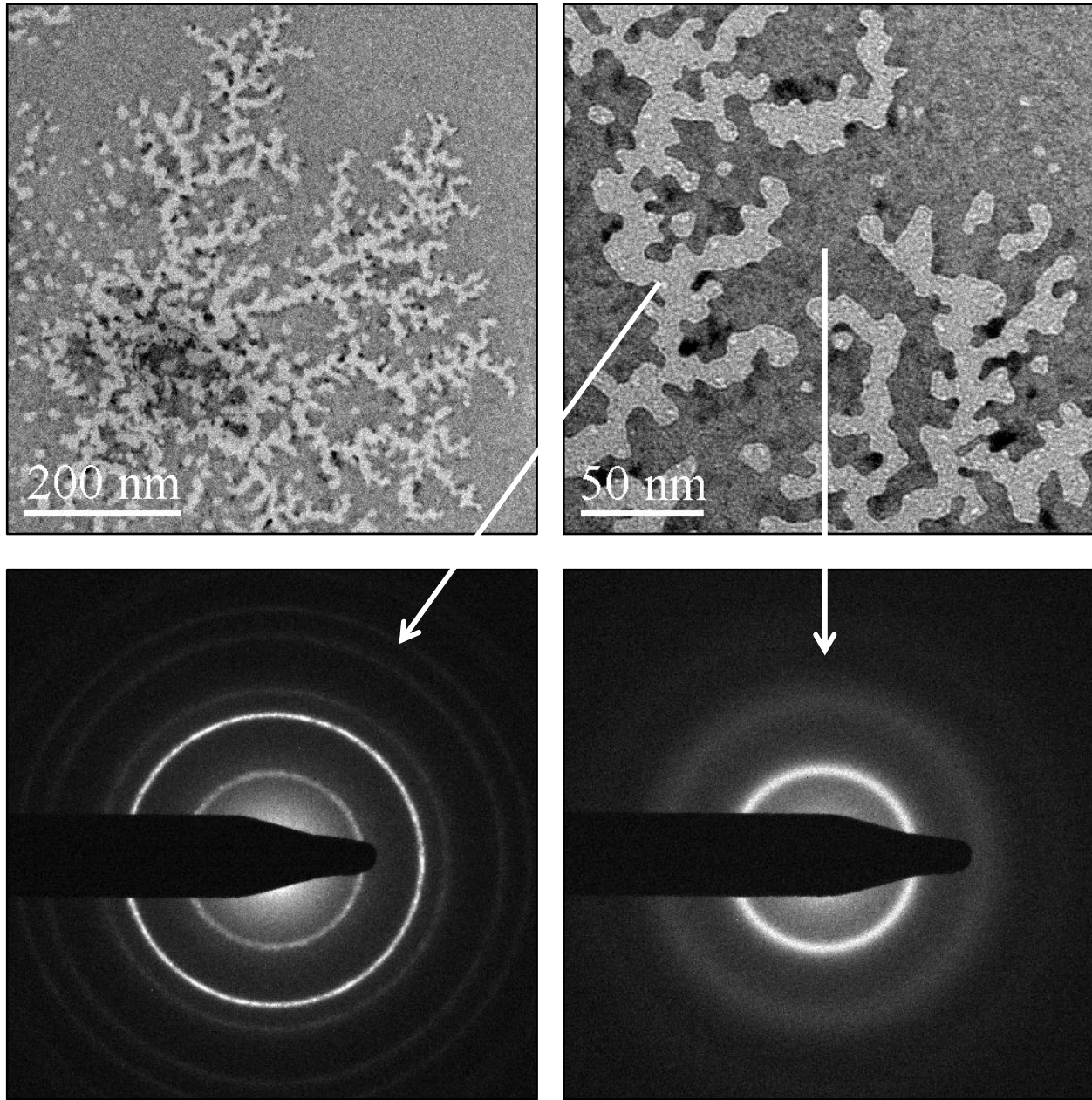


Figure 32: TEM BF images (top) and diffraction patterns of the 5 nm thick AuAl film. A two-phased microstructure appears to be present. The arrows indicate the type of area the diffraction patterns were taken from. The evaluation suggests that the bright areas consist of Au and/or Al, while the rings produced from the dark area are too broad and too few to be attributed to a specific phase.

After the heat treatment, the features of the film have coarsened but the two-phased, dendritic-looking morphology remains (Figure 33, left). The diffraction pattern, taken from a mixture of both phases (insert Figure 33) leads to only one diffraction pattern, which again can be attributed to either Au or Al. It could be suggested that a mixture of pure Au and Al are present. Both phases seem to be crystalline with moderately sized grains, as no broad rings or diffuse background were recorded.

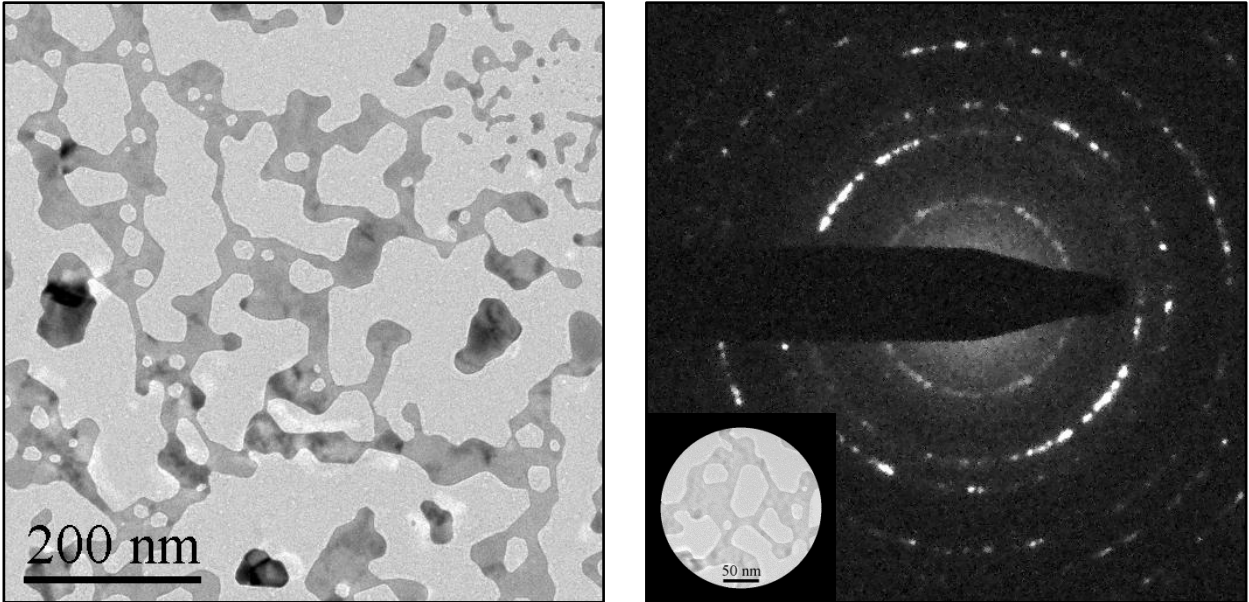


Figure 33: TEM BF image (left) and diffraction pattern of either the Au and/or the Al phase, the area where the pattern was taken from is shown in the insert. No broad rings indicating a nanocrystalline phase were recorded.

#### Sample 10 nm

The TEM BF image of the 10 nm thick sample reveals very fine grains of a size around 5 nm to 10 nm (Figure 34, left). No dendritic structures are visible and the diffraction pattern (Figure 34, right) displays clear rings that can all be attributed to the intermetallic  $\text{AuAl}_2$  phase. The film is also fully continuous and does not show grooves or areas that seem to have a comparably lower thickness.

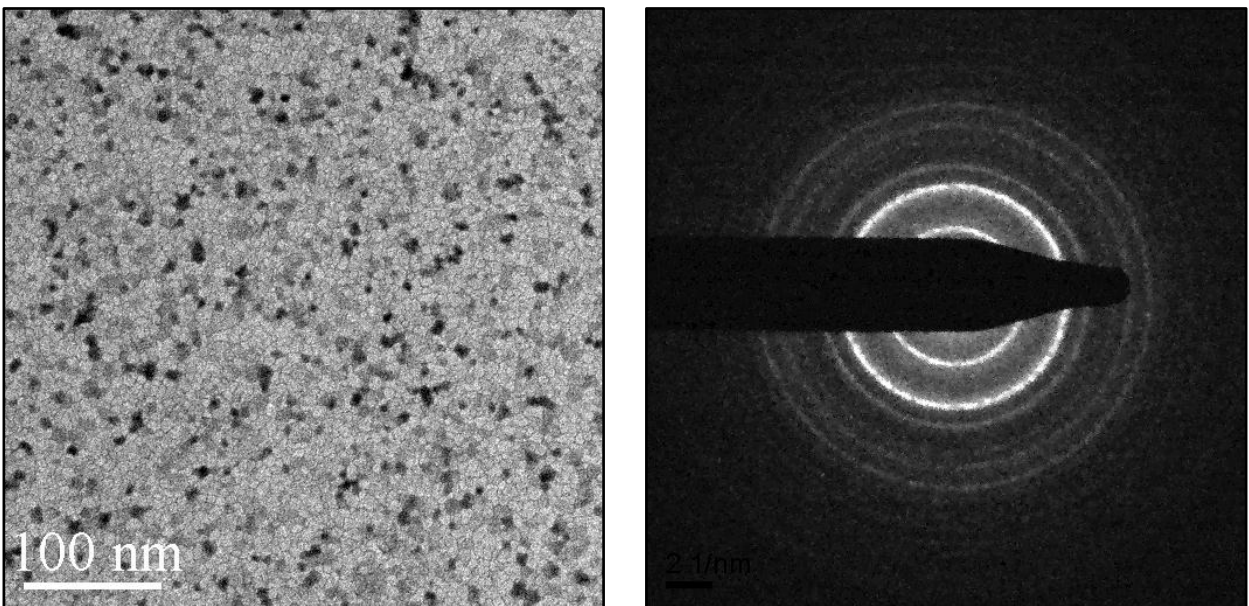


Figure 34: TEM BF image (left) and diffraction pattern (right) of the 10 nm thick sample. Small but defined grains of a size around 5 nm are visible. The diffraction rings can all be attributed to the intermetallic  $\text{AuAl}_2$  phase.

A rather significant grain growth takes place during the heat treatment for 30 min at 350°C (Figure 35). The grain size has a bimodal distribution, some being around 100 nm in size, others reaching up to 500 nm and more. The sample appears to have been under a considerable amount of mechanical strain, as numerous bending contours and stacking faults are observed. The diffraction pattern (appendix B) implies that the sample consists mainly of AuAl<sub>2</sub> but also contains a certain amount of the intermetallic phase AuAl.

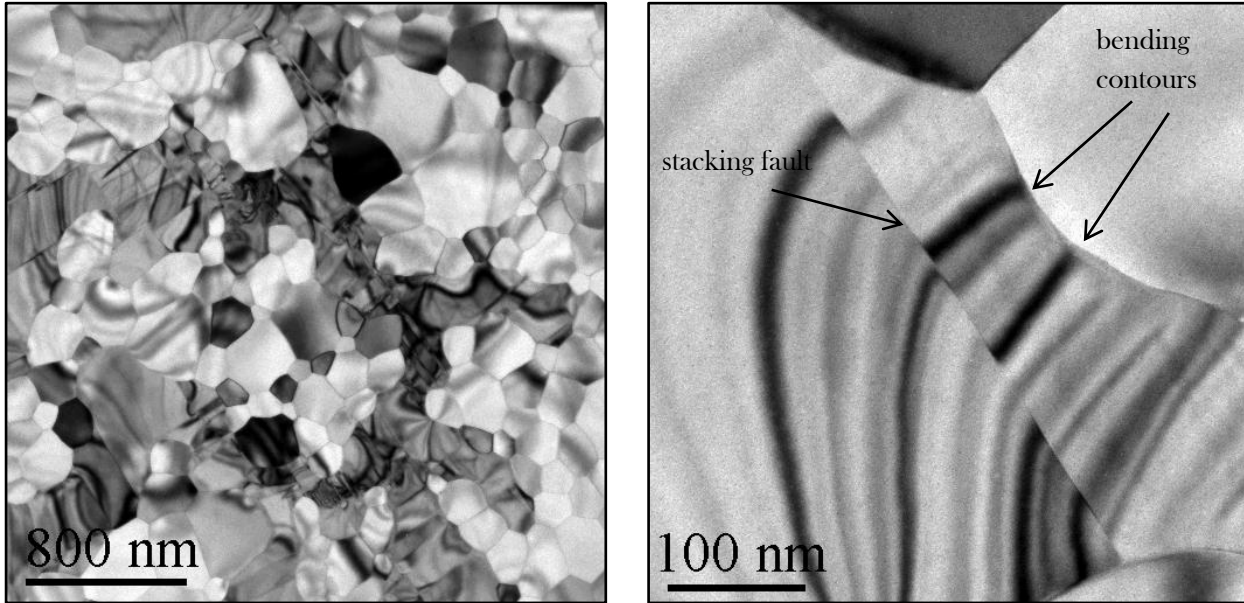


Figure 35: TEM BF images of the heat treated 10 nm thick film. The grains have grown and a bimodal size distribution has appeared. Due to mechanical strains numerous bending contours and stacking faults (arrows) can be seen.

#### Sample 50 nm

The as-deposited film with 50 nm thickness has clearly defined grains of sizes around 20 nm (Figure 36, left). The diffraction pattern as well as the Fourier transformation of the high-resolution images (Figure 36, right) suggest that the only phase present is the fluorite AuAl<sub>2</sub> phase and no traces of nanocrystalline or amorphous phase are found.

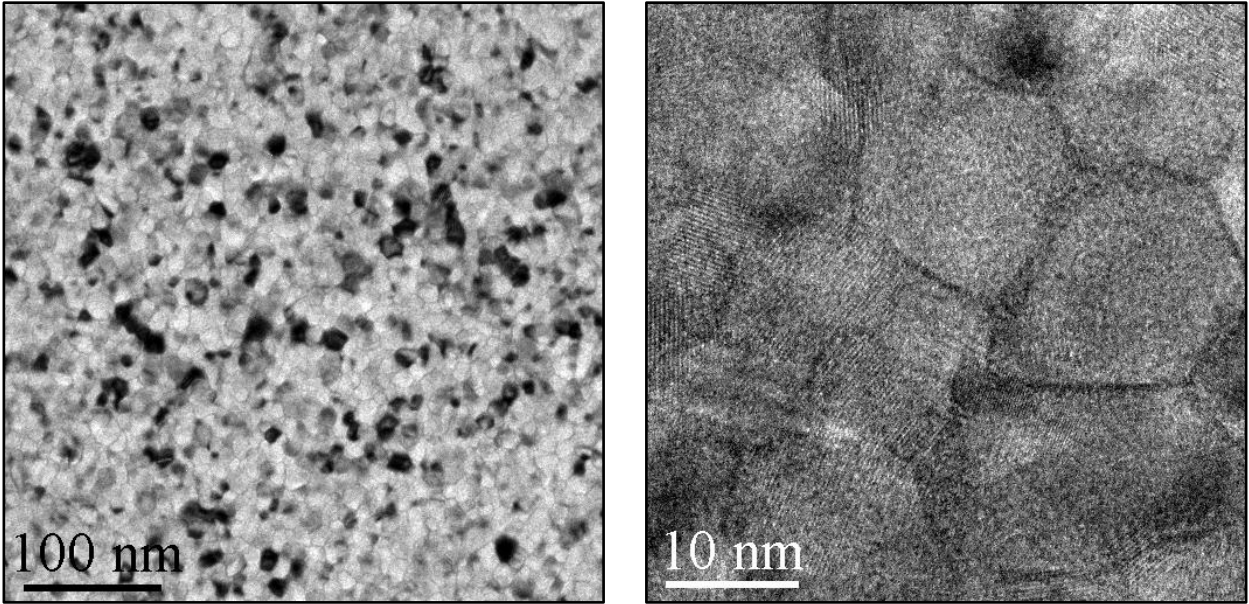


Figure 36: TEM BF (left) and high-resolution (right) images of the as-deposited 50 nm thick film. The grain sizes are around 20 nm and the Fourier-transforms of the high resolution images show that they consist of the intermetallic phase AuAl<sub>3</sub>.

After the heat treatment, the images look rather different. As can be seen in Figure 37, the continuous, homogeneous film has disappeared and is replaced by large, dark particles on a bright background. The particles are full of stacking faults and bending contours and each particle seems to be single-crystalline. The diffraction pattern of one of the particles (Figure 37, right) shows a crystal structure that could not be matched by any of the considered binary phases of Au and Al (AuAl<sub>2</sub>, AuAl), and neither by Al<sub>2</sub>O<sub>3</sub>.

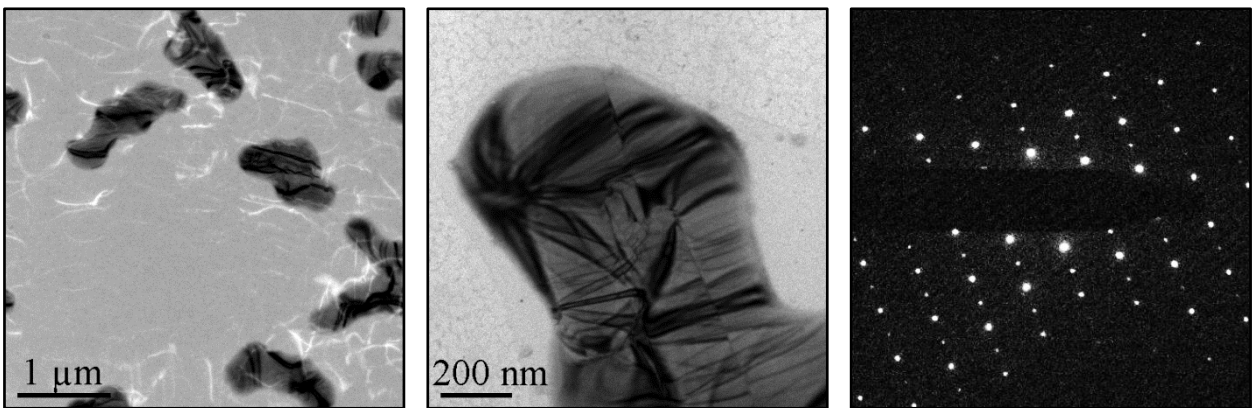


Figure 37: TEM BF images (left and middle) and diffraction pattern (right) of the heat treated thin film of 50 nm thickness. Large particles have formed that are full of stacking faults and bending contours, and appear to be single crystalline. The diffraction pattern could not be matched with any of the expected phases.

Therefore, TEM EDX mappings were performed on the particle shown in Figure 38 and it was found that they not only consist of Au and Al, but also contain a significant amount of Cu. The crystalline phase is therefore ternary and their identification exceeds the scope of this thesis.



The origin of the copper is most likely the copper grid over which the carbon film is suspended, serving as a substrate for the deposition of the TEM samples.

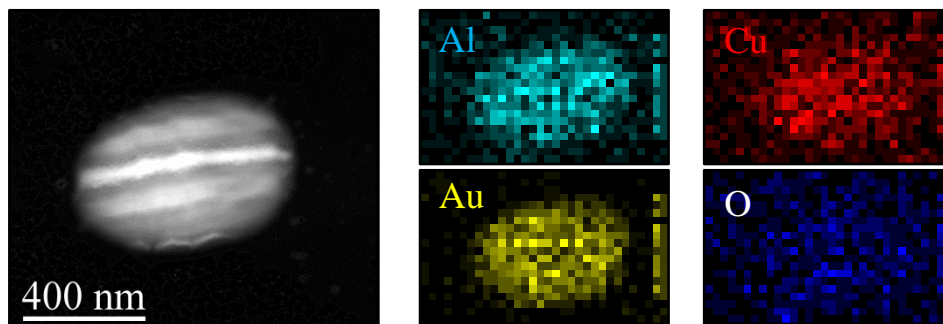


Figure 38: STEM image (left) and EDX maps of a particle. The maps suggest that the particle not only contains Al and Au, but also a considerable amount of Cu. The O signal is homogeneous over the scanned area.

The matrix in between the particles was also mapped but was too thin to lead to a reliable EDX signal. It appears to contain the same elements as the particles. The diffraction pattern consists of broad rings which are too few to be attributed to a certain material.

### *Discussion*

5 nm: The sputtered elements on the 5 nm thick samples appear to coexist as separate phases, in both the as-deposited and the heat treated state. This is rather unusual, as Au and Al are known to readily interdiffuse and form intermetallic phases [68]. The origin of the separation could be the short duration of the sputter deposition. The deposition rate of Au is very large compared to the one of Al, therefore the power applied on the Al target to obtain an Au:Al ratio of 1:2 had to be very high (350 W), while the one on the Au target was rather low (47 W). Hence, the overall sputter rate was very high and the duration of the deposition of the 5 nm thick sample consequently short with only 6 s. With a substrate rotation of 15 rpm, the sample would have only performed 1.5 rotations during the whole deposition. As the position of the Cu grid on the substrate holder was off-centre by roughly 2 cm, it is possible that an uneven coverage of the substrate was achieved, with the atoms of the two elements, arriving from different directions, condensing on slightly different parts of the substrate.

However, the reason why the elements are still separated after the heat treatment of 30 min at 350°C is not entirely clear. A possible explanation could be that the oxide layer that inevitably formed on the aluminium after it was taken from the deposition chamber prevented the interdiffusion of the elements.

10 nm: The behaviour of the 10 nm thick film is more easily explained. While the as-deposited sample with very small grains only leads to a diffraction signal of the intermetallic AuAl<sub>2</sub> phase, the overall atomic composition might be slightly higher in Au than the required 33 %. The heat

treatment then not only leads to a significant grain growth but also the precipitation of the second intermetallic phase, AuAl, which removes the excessive Au from the AuAl<sub>2</sub> grains.

50 nm: The as-deposited film shows a regular grain structure with slightly larger grains than the 10 nm thick film consisting only of the expected AuAl<sub>2</sub> phase. After the heat treatment, through cross-contamination with Cu from the substrate, a ternary phase has formed. Several different ternary intermetallic phases of Au, Al and Cu are known [34], but the identification would exceed the scope of this thesis. The contamination appears to be an isolated case, as none of the other samples contained copper.

The reflectivity measurements of the 50 nm film are not affected by the contamination, as the sample for the optical investigations was deposited on a glass substrate. While no information about its morphology could be obtained, its colour leads to the assumption that the binary, purple AuAl<sub>2</sub> was formed and is the predominant phase.

In conclusion, for AuAl<sub>2</sub> the film thickness that is required to obtain optical properties that correspond to the bulk is below 200 nm. The reflectivity curve of the 200 nm sample is shifted to slightly higher values than a 500 nm thick sample that was used for comparison. This could be due to the increased roughness or grain size of the thicker sample, which normally occurs when the sputter duration increases.

### 3.5 Comparison of thin films of different materials

The optical properties of thin films of four different materials, three pure elements and one intermetallic phase, were investigated. It was found that all materials were transparent at very thin film thickness and reached bulk properties within the investigated thickness range (5 nm to 200 nm). The required thickness for the optical properties to correspond to the bulk material is different for all materials. In Al and Pt the 50 nm thick films are already completely opaque and have a reflectivity that corresponds to the bulk materials. For Au a thickness of 100 nm and for AuAl<sub>2</sub> a thickness of 200 nm are required to fulfil the same criteria. The exact thickness value at which bulk properties were obtained could not be determined, as only a limited number of film thicknesses was investigated. Therefore, the lowest thickness that displays bulk properties is used as the critical value for the comparison.

Different properties were considered to be an influencing factor for the critical film thickness and are listed in Table 7. No connection can be made between the critical thickness and the atomic number  $Z$ , the electrical resistivity, the melting temperature and the density of the materials. However, a correlation is present to the number of conduction electrons, as can be observed in Figure 39. The number of conduction electrons  $n$  was calculated from the Hall coefficients of the respective metal by means of  $n=I/A \cdot e$ , with  $e$  being the electronic charge.

Table 7: List of inherent properties of the investigated materials

Material	Critical thickness	Z	Resistivity	T <sub>m</sub>	Density	# Conduction electrons
	[nm]	-	[μΩcm]	[°C]	[g/cm <sup>3</sup> ]	[m <sup>-3</sup> ]
Au	200	79	2.4	1064	19.3	8.72 * 10 <sup>28</sup> [69]
Pt	50	78	10.5	1768	21.45	2.71 * 10 <sup>29</sup> [69]
Al	50	13	2.8	660	2.7	1.84 * 10 <sup>29</sup> [69]
AuAl <sub>2</sub>	200	35	8	1060	7.73	4.00 * 10 <sup>28</sup> [60]



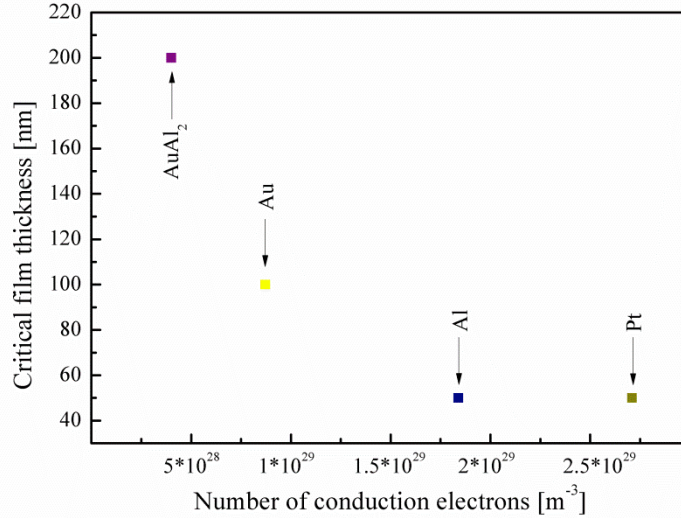


Figure 39: Correlation between the number of conduction electrons and the critical film thickness for the investigated materials.

It appears that materials with a lower number of conduction electrons require a higher film thickness to display optical properties that correspond to the bulk material. The conduction electrons are those who interact most strongly with the electromagnetic radiation, hence it is reasonable that their number would affect the reflectivity predominantly. To obtain the exact shape of the curve in Figure 39, the number of investigated materials would need to be increased. Unfortunately, a comparison with literature is difficult as the critical values were only roughly determined and might change when a different light source is employed.

The film formation at the initial stages of deposition and the percolation thickness of the materials were not investigated, but are more likely to be governed by the mobility of the atoms after precipitation on the substrate. This mobility depends on the melting temperature of the material, rather than its number of conduction electrons.

All investigated films had passed the percolation threshold, no separate islands were found in the TEM investigation, apart from the heat treated 50 nm thick  $\text{AuAl}_2$  sample, which due to the substrate contamination cannot be used for the comparison. No unusual optical effects were observed that would imply surface plasmon excitations, hence the films do not need to be treated from a colloidal point of view.

In conclusion and for further experiments it can be stated that the critical film thickness changes with the material but at thicknesses over 300 nm the optical properties of a bulk material are most probably achieved. Additionally, very short deposition times should be avoided to prevent inhomogeneous distributions of elements when two or more materials are co-deposited.



## 4. Colours due to electronic band structures

### 4.1 Au-Ag

#### *Results*

##### Macroscopic appearance and reflectivity

The thin film with a composition gradient of gold and silver across its surface shows a smooth colour transition, from yellow to a silver hue with a slightly yellow tinge (Figure 40). Composition measurements by EDX reveal that a range from 15 at.% silver at the left end to 55 at.% silver at the right end of the sample is covered.

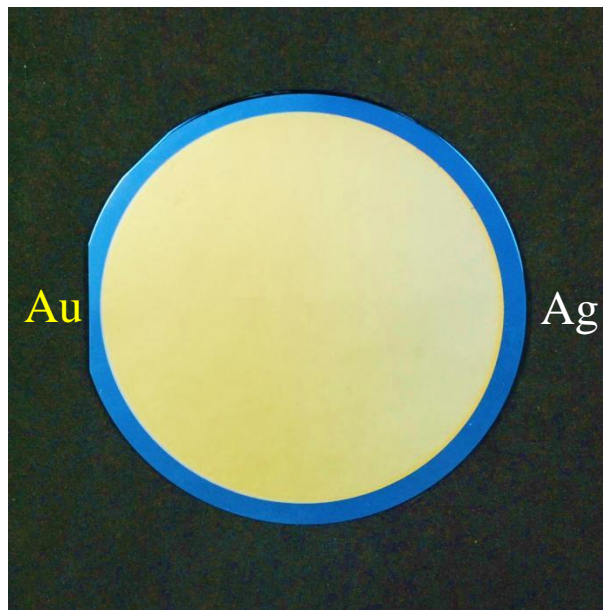


Figure 40: Three inch wafer with an Au-Ag composition gradient, ranging from 15 at.% Ag on the left to 55 at.% Ag on the right side of the sample. A smooth transition of the colour can be observed.

A similar transition can be observed on the homogeneous samples in Figure 41: the colour of the Au-Ag alloys with the lowest silver content is a bright yellow, similar to pure gold, and fades gradually as the Ag content increases. This corresponds well to literature ([70]) and is expected as the two metals form a solid solution independent of the composition of the alloy [71]. The exact contents of the samples, determined by EDX measurements, are listed in Table 8.

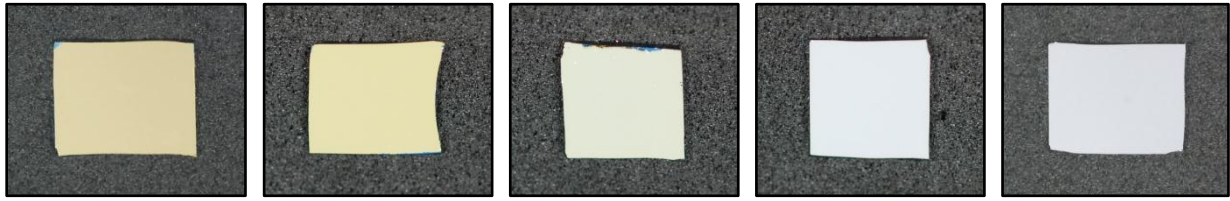


Figure 41: Images of the Au-Ag alloys (roughly 4 cm<sup>2</sup> in size) in the order of increasing Ag content: Au, Au84Ag16, Au55Ag45, Au23Ag77 and Ag (from left to right).

Table 8: Sample descriptions, compositions determined by EDX and film thickness determined by SEM

Sample name	Ag [at.%]	Au [at.%]	Thickness [nm]
Au	0	100	950
Au84Ag16	16	84	320
Au55Ag45	45	55	330
Au23Ag77	77	23	350
Ag	100	0	350

The reflectivity curves reflect the smooth colour transition in a continuous shift of the absorption edge (Figure 42). The inflexion point in the reflectivity was used as a measure of the position of the edge and was determined by measuring the position of the maximum in the first derivative of the curve (Table 9).

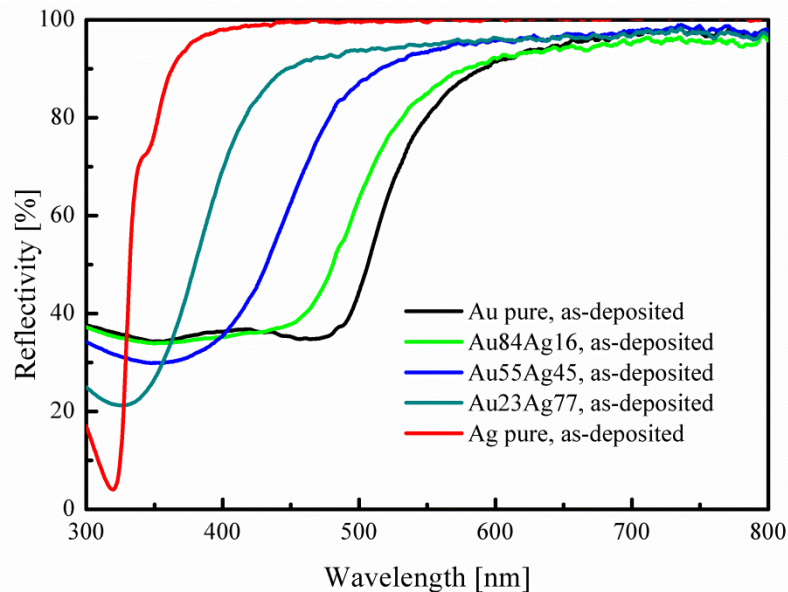


Figure 42: Comparison of the reflectivity of different Au-Ag alloys with pure elements. A shift of the position of the absorption edge can be observed with changing content.

Assuming the absorption edge changes linearly with the composition, it is possible to calculate its position for an arbitrary alloy with the help of only the values of pure gold and silver. The values thus calculated are plotted in Figure 43. They fit rather nicely to the measured values but

are slightly lower, a deviation that can be attributed to an uncertainty in the determination of the composition by EDX and the exact position of the absorption edge. Its influence on the colour is expected to be too small to be observed by the naked eye. The heat treatments of the samples, carried out for 5 h at 350°C, changes the reflectivity of the alloys only very slightly (Figure 44).

Table 9: Positions of the measured and calculated absorption edges, assuming a linear shift with the concentration

Sample	at.% Ag	Measurement [nm]	Calculation [nm]	Difference [nm]
Au	0	511		--
Au84Ag16	16	490	482	8
Au55Ag45	45	444	430	14
Au23Ag77	77	382	373	9
Ag	100	332		--

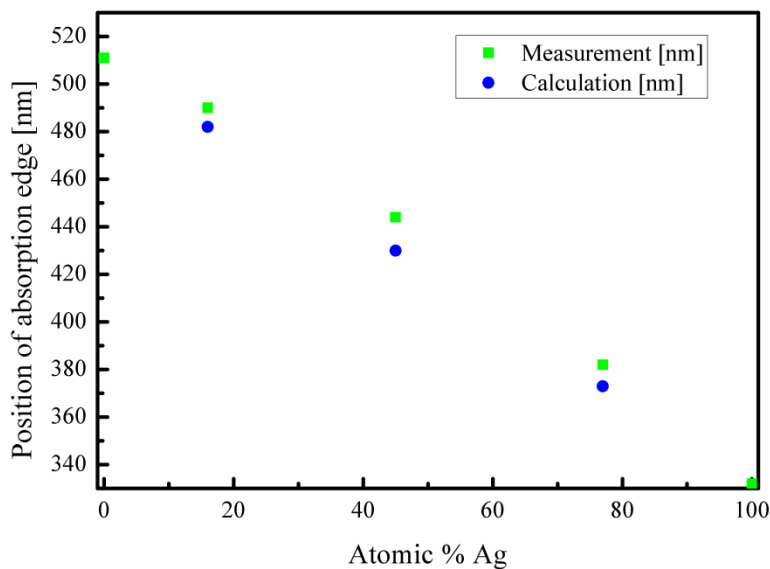


Figure 43: Measured and calculated positions of the absorption edge for Au-Ag alloys. The transition seems to occur linearly with the composition.

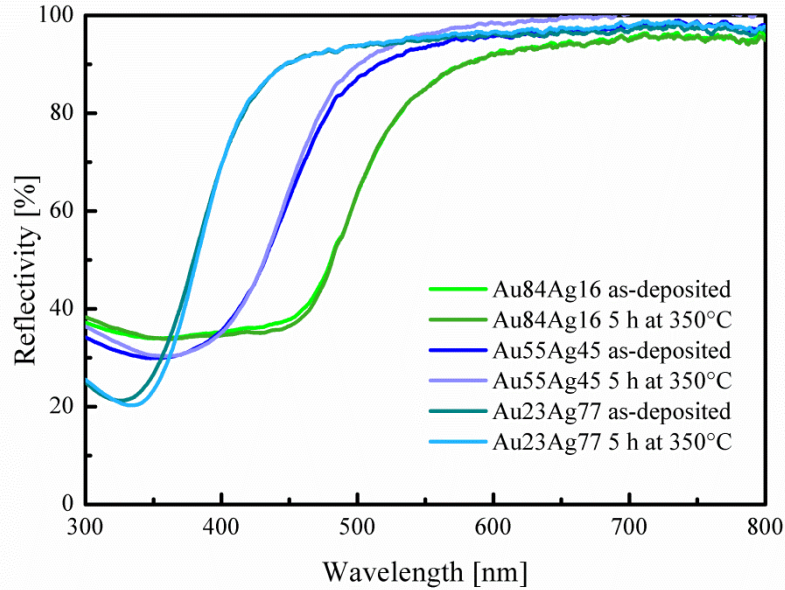


Figure 44: Reflectivity curves of as-deposited and heat treated samples (5 h at 350°C). No significant change of the reflectivity can be observed, indicating that the grain size does not have a major influence.

Figure 45 shows the CIE chromaticity diagram with the values of the different Au-Ag alloys marked. They are not located on a straight line between silver and gold but seem to describe a slight curve. More values would be required to make a certain statement about its exact progression. All calculated colour coordinates are listed in appendix C.

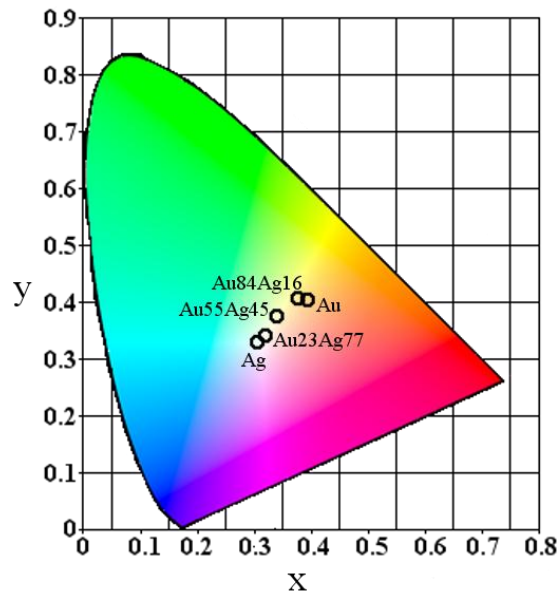


Figure 45: Chromaticity diagram with the x,y colour values of the Au-Ag alloys inserted. The colour shift is not linear from silver to gold but seems to describe a slightly curved path.

## Electrical resistivity

The change of the electrical resistivity with the composition corresponds rather well to bulk values found in literature [72, 73], where an increase of the values with increasing solute concentration is reported, peaking in the middle of the composition range and declining towards the pure elements. The heat treatments lead to a slight reduction of the resistivity in the samples with 16 at.% and 77 at.% silver (Table 10), most likely due to the grain growth that is taking place. The resistivity of the sample with 45 at.% silver remains the same after the heat treatment despite a considerable grain growth. Table 11 lists the grain sizes of all samples, measured from SEM BSE images. In Figure 46 the values of the heat treated samples are compared to literature values of bulk materials from Iyer ([73], black) and Crisp ([72], green) and fit quite nicely. They are slightly higher than the bulk values, which is usually the case for thin films, as the amount of scattering sites increases with decreasing thickness and the amount of defects in sputter-deposited films is generally rather high.

Table 10: Measured resistivity values of the as-deposited (AD) and heat treated samples (5 h at 350°C, HT)

Sample	Resistivity [ $\mu\Omega\text{cm}$ ]
Ag AD	2.22
Ag HT	1.89
Au84Ag16 AD	7.75
Au84Ag16 HT	7.73
Au55Ag45 AD	12.87
Au55Ag45 HT	12.91
Au23Ag77 AD	9.75
Au23Ag77 HT	9.95
Au AD	4.01
Au HT	3.11

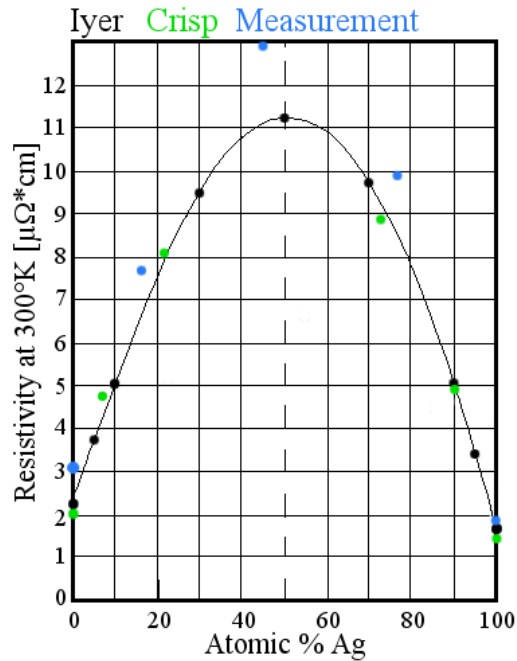


Figure 46: Comparison of the resistivity of heat treated Au-Ag alloys with literature values of bulk materials. The blue points are the measured values, the black points are from Iyer *et al.* [73] and the green points from Crisp *et al.* [72].

Table 11: Grain sizes of the Au-Ag alloys, as-deposited (AD) and heat treated for 5 h at 350°C (HT), determined from SEM BSE images

Sample	Grain size AD [nm]	Grain size HT [nm]
Au	112	154
Au84Ag16	55	85
Au55Ag45	61	152
Au23Ag77	58	401
Ag	88	542

### *Discussion*

The investigated properties of the gold-silver alloy thin films produced by means of magnetron sputter deposition are very similar to the ones of bulk alloys in literature, produced by conventional production techniques: Solid solutions are formed at all compositions and the optical and electrical properties change smoothly with composition.

The position of the absorption edge in the reflectivity curve varies linearly with the alloy composition. This could allow the prediction and accurate tailoring of an alloy with a specific colour when the reflectivity of the two pure elements is known, provided the alloy system forms a solid solution over the full composition range. Unfortunately, apart from Au-Ag and Au-Cu, there are no alloy systems forming solid solutions which are interesting from a colour point of view, as gold and copper are the only pure metals that display an inherent colour.

The reflectivity of the alloys barely changes during the heat treatment, indicating that the grain size has no influence on the optical properties, at least in the size range at hand. Heat treatments that are too long, or performed at too high temperatures could affect the reflectivity by an increase of the surface roughness, and thus a more diffuse scattering of the light. The (111) out-of-plane texture that usually develops on sputter-deposited gold and silver films [74, 75] does not appear to influence the reflectivity, which is to be expected given that all the alloys have a cubic crystal structure.

The change of the resistivity with the alloy composition also corresponds well to the bulk references, implying that the electric band structures are comparable. The heat treatment of most of the samples leads to a reduction of the resistivity which is probably due to grain growth and reduction of defects. Despite a significant increase in the grain size, the resistivity of the Au55Ag45 sample in the middle of the composition range does not change after the heat treatment. Other factors must be dominating the resistivity in this alloy, such as the scattering of electrons at impurity atoms or phonons.

The performed measurements provide an initial proof of concept for the comparability of sputtered thin film samples with conventionally produced bulk samples, certainly when dealing



with solid solutions. They suggest that it should be possible to upscale the materials produced in the course of this thesis without significant modifications.

## 4.2 Au-Al

### *Results*

#### Macroscopic appearance and reflectivity

Unlike the smooth colour change of the Au-Ag gradient sample the Au-Al thin film, shown in Figure 47, displays several sharp colour transitions across its surface. In the as-deposited state they have grey and brown colours of different shades and after a heat treatment for 5 h at 400°C certain areas obtain pink and purple colours. According to EDX the composition ranges from 46 at. % Al on the left side to 86 at. % Al on the right side of the wafer and does not change during the heat treatment. The stoichiometric composition of the intermetallic phases  $\text{AuAl}_2$  and  $\text{AuAl}$  are marked with an arrow. An intense purple line is visible, running vertically through the sample at the site of  $\text{AuAl}_2$ .

The additional colour transitions could have their origin in the morphology of the sample. As shown in Figure 48, the surface of the gradient wafer is not smooth but has a rough topography which changes along the sample. The features are often around 100 nm in size and arranged in a fairly regular manner. Therefore, they could interfere with light from the visible part of the spectrum. The origin of the surface topography is the deposition of the composition gradient, which takes place without rotation of the substrate. The atoms and clusters arrive at the substrate under a certain angle, and the mobility after condensation is probably not sufficient for a rearrangement and the formation of a densely packed film.

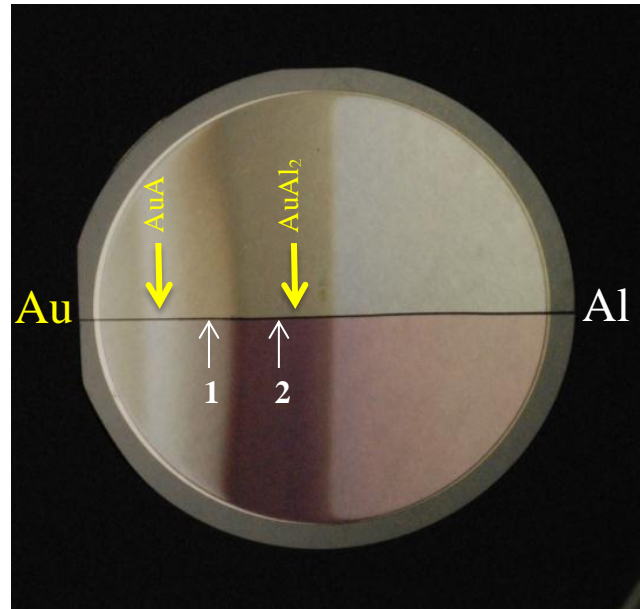


Figure 47: Sample with a composition gradient of Au and Al across the surface, going from 46 at.% on the left to 86 at.% Al on the right side. The bottom half of the wafer has been heat treated for 5 h at 400°C. Marked are the stoichiometric positions of  $\text{AuAl}_2$  and  $\text{AuAl}$  and the approximate positions where the SEM images 1 and 2 in Figure 48 were taken from.

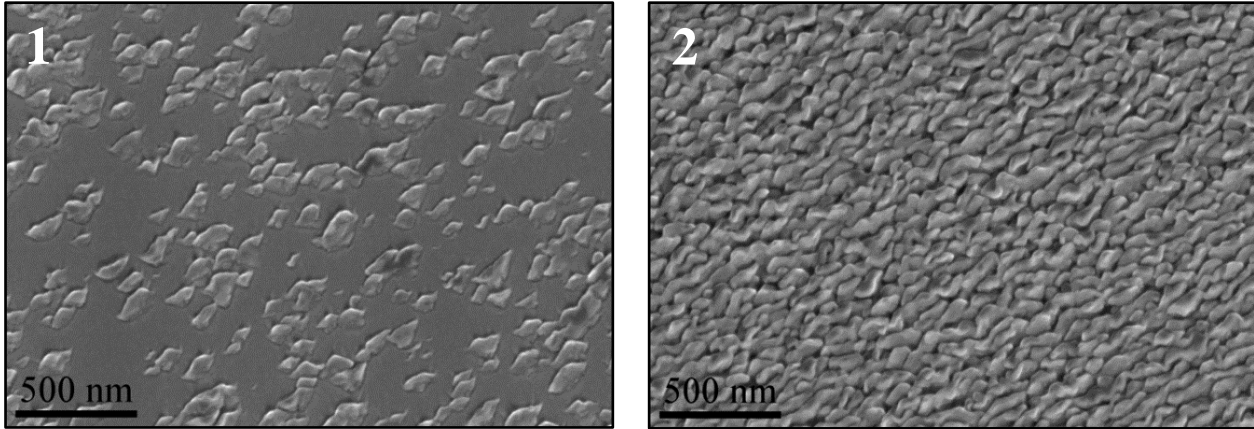


Figure 48: SEM SE images of the topography of the gradient wafer at two different locations along the surface. The feature size is in the range of 100 nm and could therefore interfere with light of wavelengths in the visible spectrum.

Similar to the gradient wafer, the samples with a homogeneous composition of 33 at.% Au and 67 at.% Al are not as intensely purple as one would expect from the literature, but initially have a grey or slightly pink colour. Already after 2 min of the heat treatment at 350°C a significant colour change can be observed (Figure 49, left). The reflectivity curve of the as-deposited sample has a shallow minimum at 540 nm (Figure 49, right). This minimum becomes steeper during the heat treatments while keeping its position roughly at the same energy. After 10 min the curve appears to have reached a stable position and does not change anymore for longer heat treatments.

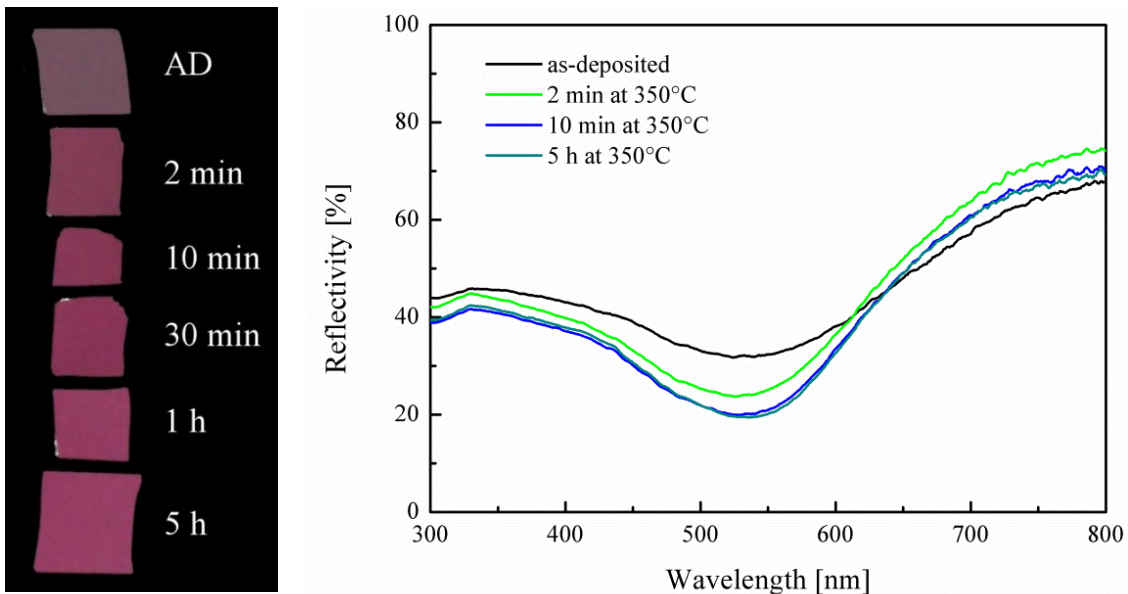


Figure 49: Images and reflection measurements of samples treated for different durations at 350°C (sample size between 1 cm<sup>2</sup> and 2 cm<sup>2</sup>). The minimum at 540 nm becomes increasingly pronounced while keeping its position. After 10 min a stable state seems achieved.

From literature it is assumed that the lack of colour is due to the high amount of defects in sputter-deposited thin films. If that is the case, reintroducing defects into the heat treated layer would remove the colour again. One possible way to do this is the irradiation of the film with high-energy ions. As can be seen in Figure 50, the colour of the samples is gradually removed when irradiated with  $\text{Au}^+$  ions, until it disappears completely at a fluence of  $5 \cdot 10^{15}$  ions/cm<sup>2</sup>. Again, this can be observed in the reflectivity curve, which becomes shallower with rising fluence (Figure 50, right). The curve of the sample irradiated with  $5 \cdot 10^{15}$  ions/cm<sup>2</sup> resembles the one of the as-deposited sample, with a slight shift of the minimum from 540 nm to 550 nm.

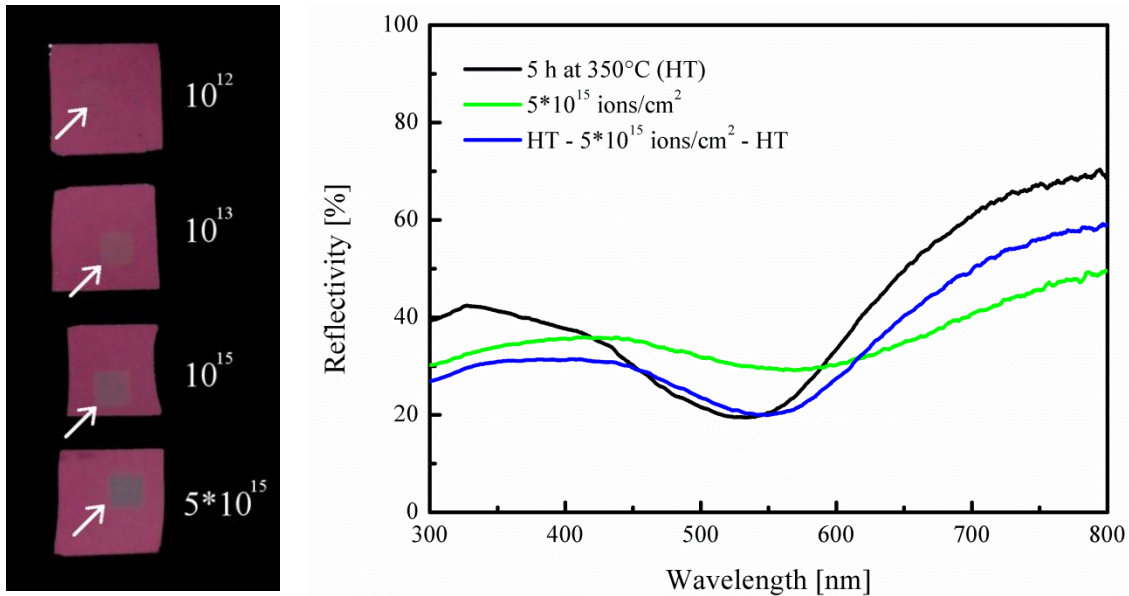


Figure 50: Images and reflection curves of the irradiated samples (the sample size is roughly 2 cm<sup>2</sup>, the irradiated area is 9 mm<sup>2</sup>). Irradiation with  $5 \cdot 10^{15}$  ions/cm<sup>2</sup> flattens the reflectivity curve and shifts the minimum to a lower value. The post-irradiation temperature treatment shifts the curve back to almost its initial position. The reflectivity at lowest and highest energies remains reduced, possibly due to the increased roughness.

After the second heat treatment the pronounced dip in the reflection curve is restored, however a slight shift of the minimum reflection and a reduction of the reflectivity at the high and low end of the visible spectrum is present. A visual inspection shows that the purple colour returns, but is slightly darker than before the irradiation (Figure 51, left). The irradiated sample on a glass substrate (Figure 51, right) confirms that the irradiation is effective throughout the whole film thickness and not just a surface effect, as the colour removal is also visible at the film/substrate interface.

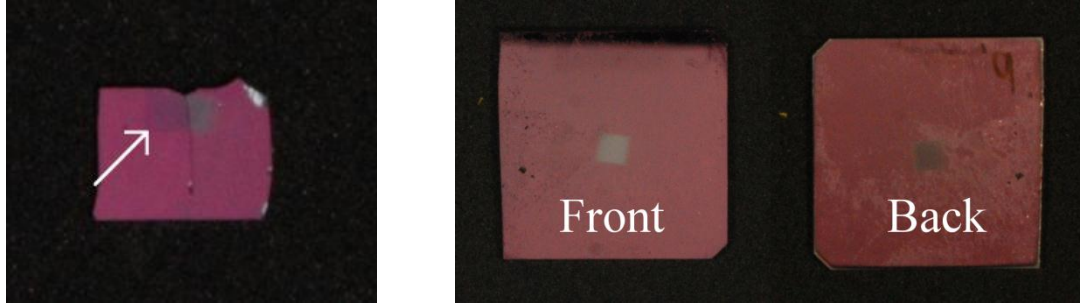


Figure 51: Left: Post-irradiation heat treated sample (arrow) in comparison with an irradiated one (sample size roughly  $2 \text{ cm}^2$ , the irradiated area is  $9 \text{ mm}^2$ ). Right: Thin film on  $\text{SiO}_2$  substrate (roughly  $4 \text{ cm}^2$ , the irradiated area is  $9 \text{ mm}^2$ ), irradiated with  $5 \cdot 10^{15}$  ions/ $\text{cm}^2$ , images are taken from the front and the back side.

The development of the colour coordinates  $x$  and  $y$  during heat treatments and irradiations is shown in Figure 52. All colour coordinates are listed in appendix C.

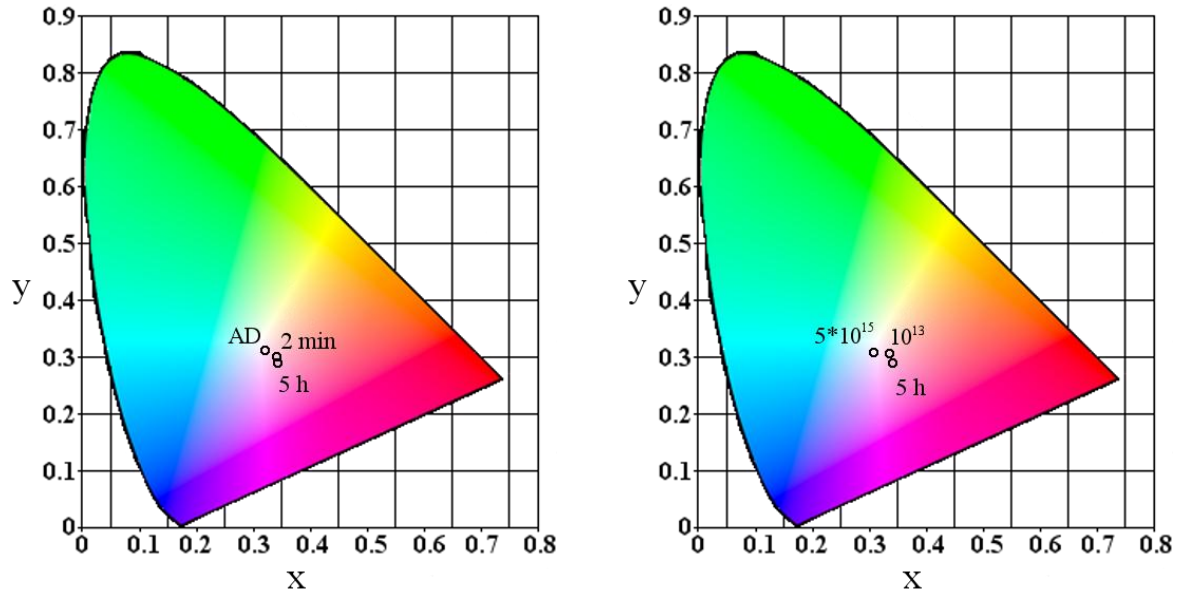


Figure 52: Colour development in the chromaticity diagram. Left: During a heat treatment at  $350^\circ\text{C}$ , right: with increasing fluence (in ions/ $\text{cm}^2$ , '5 h' marks the heat treated, not irradiated sample). Only selected samples are marked to improve the clarity.

SEM images of samples treated at  $350^\circ\text{C}$  for 30 min and longer display hillocks on the surface, an increasing amount with increasing treatment time. The sample treated for 5 h at  $350^\circ\text{C}$  contains dendrite-like precipitates (Figure 53, left). According to EDX, the precipitates consist of roughly 50 at.% Au and 50 at.% Al, the composition corresponding to the intermetallic, monoclinic AuAl phase. EDX measurements of the surrounding matrix suggest it still consists of the  $\text{AuAl}_2$  phase. After the irradiations and the post-irradiation heat treatment no significant changes are observed in the SEM images or the EDX measurements. As can be seen on the light



microscopy image of Figure 53 (right side), the colour of the matrix in the irradiated patch has become darker compared to the non-irradiated part of the same sample and the precipitates are coarser than in the surrounding area.

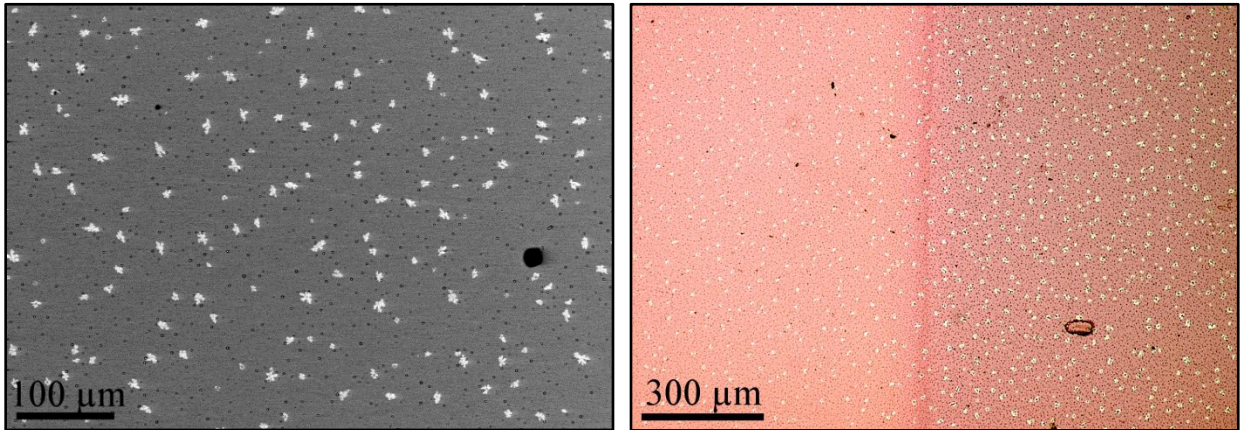


Figure 53: SEM BSE image (left) of a sample heat treated for 5 h at 350°C and an optical microscopy image (right) of a sample with a post-irradiation heat treatment. Bright precipitates of AuAl are visible in both images, and the colour of the irradiated patch is darker than the not irradiated part.

Interestingly, the surface topography does not change during the heat treatments, as can be seen in Figure 54, where the as-deposited sample is compared to the sample heat treated for 5 h at 350°C. A hillock has formed in the heat treated state but the grain-like features remain the same. This suggests that a very thin  $\text{Al}_2\text{O}_3$  film forms on top of the surface as soon as it comes into contact with air. Such films are usually amorphous [76] but do not change during the heat treatment while the underlying metal grains grow with time and temperature.

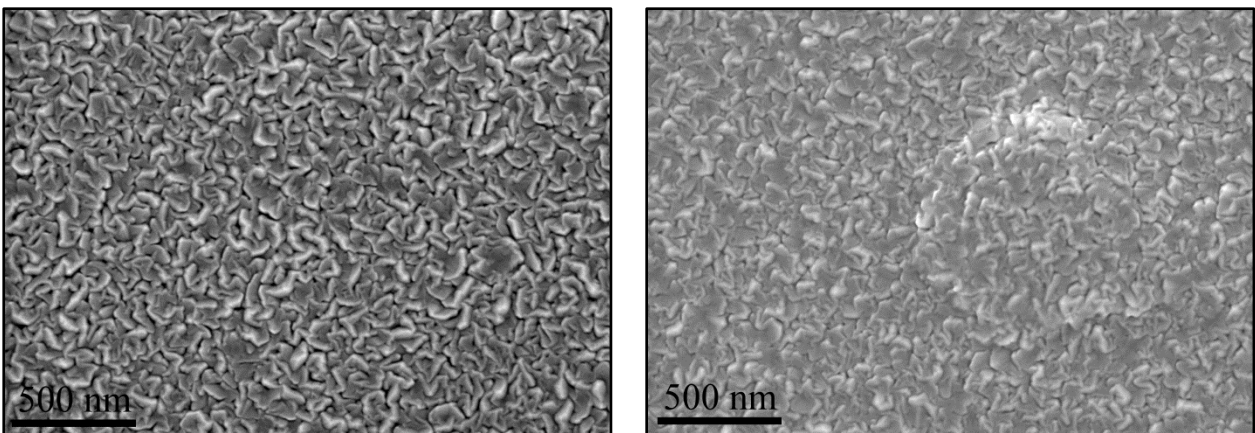


Figure 54: SEM SE images of an as-deposited (left) and heat treated for 5 h at 350°C (right) sample. Apart from the formation of hillocks, the surface topography remains the same, indicating that a thin oxide film has formed on the surface, which does not change during the heat treatment.

## X-Ray diffraction (XRD)

XRD measurements (Figure 55) show that the  $\text{AuAl}_2$  phase is already present in the as-deposited sample; no signal from a possible amorphous phase is detected. After the heat treatment the peaks become marginally sharper, which is probably due to an increase in grain size. In the irradiated sample and the sample with a post-irradiation heat treatment, minor peaks of the  $\text{AuAl}$  intermetallic phase are present. It was observed that the peak positions of the as-deposited sample are slightly below reference values for the unstrained lattice, while the heat treated sample shows values that are slightly above it, indicating a change in the stress state due to the heat treatment or a change in stoichiometry due to the precipitation of the second phase. A similar shift to lower values was apparent after the irradiation, which could again be reversed with the second heat treatment.

A rough estimation of the present stresses from the (3 1 1) reflex is shown in Table 12. From the difference of the measured lattice spacing  $d_{311}$  from the reference value the out-of-plane strain  $\varepsilon_z$  is calculated. Using a Young's modulus  $E$  of 85 GPa and a Poisson ratio  $\nu$  of 0.38 [77], the stress is calculated using  $\sigma_x = -\varepsilon_z * E / 2\nu$ . According to these calculations compressive stresses are present in the as-deposited and the irradiated sample, and are in both cases mostly removed during the heat treatment. However, the absolute values are not reliable, as they depend on the knowledge of a reference value, which is only available for bulk material. Additionally, there are influences of the measurement set-up which increase the uncertainty, as for instance the exact sample height during the measurement.

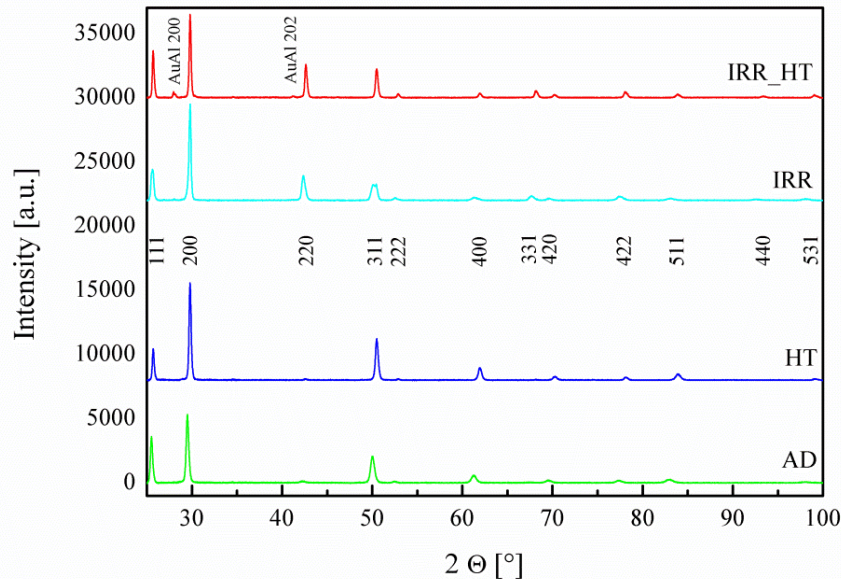


Figure 55: XRD spectra of an as-deposited (AD), a heat treated (HT, 5 h at  $350^\circ\text{C}$ ), an irradiated (IRR,  $5 * 10^{15}$  ions/ $\text{cm}^2$ ) and a post-irradiation heat treated sample (IRR\_HT). The as-deposited sample is already fully crystalline, consisting only of  $\text{AuAl}_2$ . The irradiated and post-irradiation heat treated samples show small peaks of  $\text{AuAl}$ .

Table 12: Measured lattice spacings, strains and stresses calculated by means of the deviation from an unstrained bulk reference

Sample	$d_{311}$ [Å]	$\epsilon_z$	$\sigma$ [MPa]
as-deposited	1.82347	0.0085	-949
5 h at 350°C	1.80745	-0.0003	34
$5 \cdot 10^{15}$ ions/cm <sup>2</sup>	1.82039	0.0068	-761
Post-irradiation HT	1.8074	-0.00033	37

No external reference value is required when the stress evaluation is performed using the  $\sin^2\psi$  method. Here, the strain calculated from the lattice spacing is plotted against the  $\sin^2\psi$  of the respective measurement. From the slope  $m$  of the resulting curve the stress can be calculated independent of a reference value, using  $\sigma = E \cdot m / (1-\nu)$ . An example of a  $\sin^2\psi$  plot is shown in Figure 56 for the as-deposited sample. Judging from the slope it can already be determined whether the stress is tensile (positive slope) or compressive (negative slope). The slopes and stress values obtained by this method for the as-deposited, the heat treated and the sample with a post-irradiation heat treatment are listed in Table 13. No  $\psi$ -scan was made of the irradiated sample before the second heat treatment, but as the peak positions from the measurement at  $\psi = 5^\circ$  are similar to the as-deposited sample, its stress state is assumed to be comparable. The differences to the first method are clear: while the heat treated samples were nearly stress-free, a considerable tensile stress is found by means of the  $\sin^2\psi$  method. It can be concluded that the reference value for the bulk material does not correspond to the lattice spacing of an unstrained thin film. Typical statistical errors for the  $\sin^2\psi$  method are on the order of several tens of MPa, consequently the major source of error will be the estimation of elastic constants.

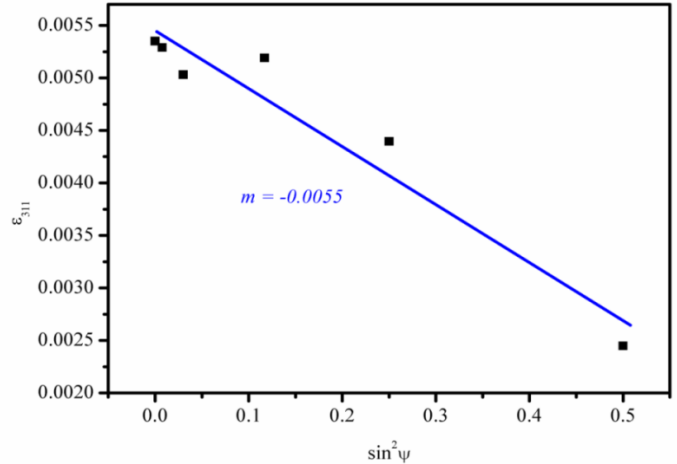


Figure 56:  $\sin^2\psi$  plot for the as-deposited sample. The slope is used to calculate the present stresses.

Table 13: Slopes of the fitted  $\sin^2\psi$  plots and the stresses calculated with this method

Sample	$m$	$\sigma$ [MPa]
as-deposited	-0.0055	-750
5 h at 350°C	0.0042	575
Post-irradiation HT	0.0032	439

## Microstructure studies

The TEM cross-section of the as-deposited sample (Figure 57, left) shows a columnar grain structure, with a coarsening of the grains towards the top of the film. This morphology is quite common for sputter-deposited metals [78]. After 5 h at 350°C the columnar structure is mostly preserved, with a coarsening of the grains taking place, mainly at the substrate-film interface (Figure 57, right). The average grain size increases slightly from 44 to 65 nm. After ion irradiation with a fluence of  $5 \cdot 10^{15}$  ions/cm<sup>2</sup> (Figure 58, left), the columnar structure has been replaced by equiaxed grains with sizes around 180 nm and a rather large size distribution. The STEM image (Figure 58, right) of the same sample shows cracks in the surface, which were not present before the irradiation. The grains of the sample with a post-irradiation heat treatment (not shown) have grown further, but resemble the structure of the irradiated sample. The average grain sizes are listed in Table 14. Diffraction patterns of all samples suggest that the film consists of AuAl<sub>2</sub> only, independent of the heat treatment or whether the sample had been irradiated or not. No AuAl was measured, probably because the FIB lamellae were cut from regions without precipitates.

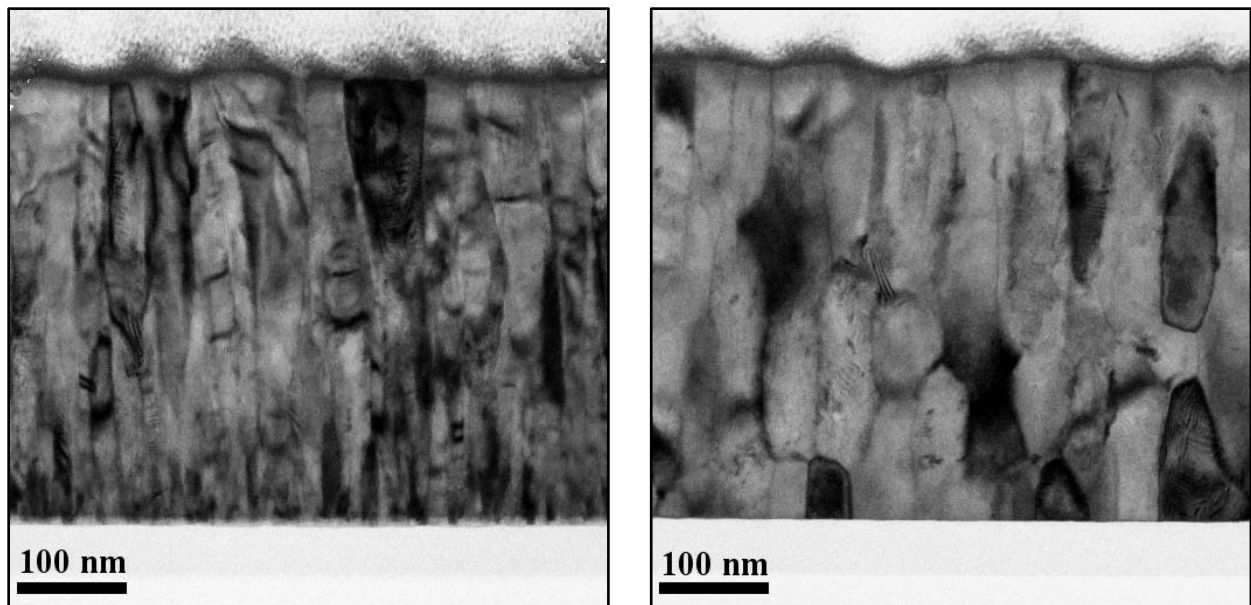


Figure 57: TEM BF images of a cross section of an as-deposited (left) and heat treated (right) sample (5 h at 350°C).

A grain growth takes place during the heat treatment, especially at the substrate-film interface the grains have coarsened.



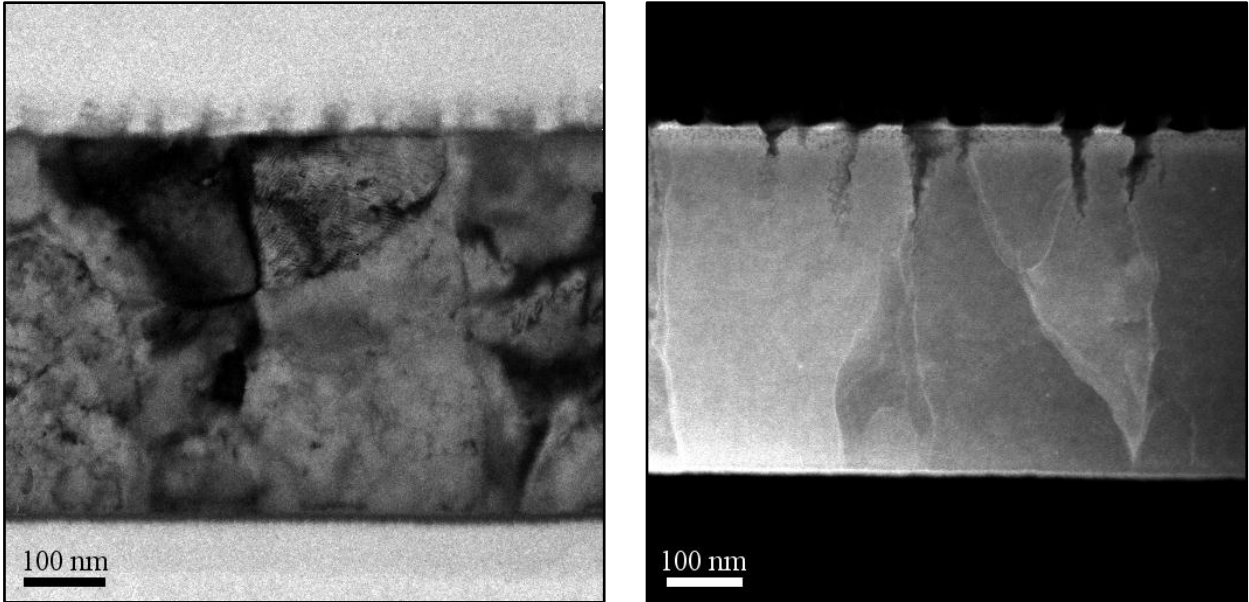


Figure 58: TEM images: BF of a cross section of an irradiated sample ( $5 \cdot 10^{15}$  ions/cm<sup>2</sup>) (left) and an STEM image of an irradiated sample ( $5 \cdot 10^{15}$  ions/cm<sup>2</sup>), showing large grains and surface cracks (right).

Table 14: Grain sizes of AuAl<sub>2</sub> samples after heat treatments and irradiation

Time [min]	Grain size [nm]
as-deposited	44
2	58
10	61
30	58
60	62
300	65
1440	67
300 + $5 \cdot 10^{15}$ ions/cm <sup>2</sup>	180
post-irradiation HT	250

### Electron backscatter diffraction (EBSD)

The out-of-plane grain orientation maps of the as-deposited (not shown) and the heat treated sample (Figure 59, left) show a preferential orientation of the grains along the (100) crystallographic direction, visible from the uniform red colour and the central peaks in the (100) pole figure. The black spaces are areas from which the crystal orientation could not be indexed,

probably due to surface roughness. In fcc metals with anisotropic elastic properties, a (100) texture is known to develop upon film growth in order to minimize the stored strain energy [78]. As the fluorite structure of  $\text{AuAl}_2$  is rather similar to fcc and a (100) texture is present in the as-deposited sample, it is assumed that the strain energy reduction is also the driving force behind the formation of the initial texture. After irradiation with  $5 \cdot 10^{15}$  ions/cm<sup>2</sup> (Figure 59, right) the texture has disappeared.

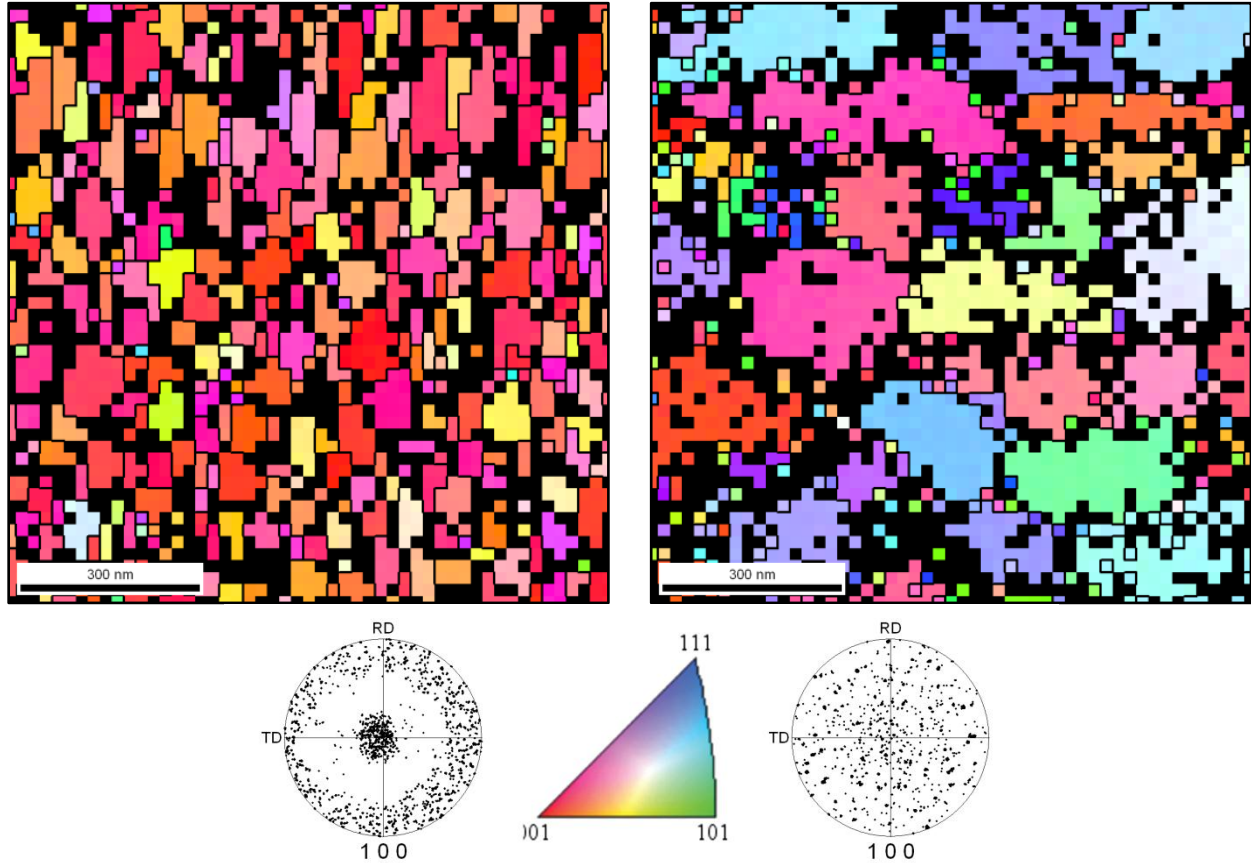


Figure 59: EBSD texture maps with corresponding pole figures and colour legend, left: 5 h at 350°C, right:  $5 \cdot 10^{15}$  ions/cm<sup>2</sup>. While the heat treated sample has a (100) out-of-plane texture, the grains in the irradiated sample are randomly oriented.

## Electrical resistivity

The measured resistivity value of the as-deposited sample (Figure 60, top left) is rather high compared to its modelled counterpart ( $33 \mu\Omega\text{cm}$  compared to  $17.7 \mu\Omega\text{cm}$ ), but declines exponentially during annealing and reaches a stable value after 5 h. The modelled values decrease less steadily, with the zigzag appearance in the early stages of the heat treatment, a result of small fluctuations in the grain size which lie within the accuracy of the measurement. The resistivity measurements of the irradiated samples on the other hand differ more and more strongly from the modelled values the higher the fluence becomes (Figure 60, bottom left).

While the modelled resistivity gets smaller due to the increase in grain size during irradiation, the measured values increase in an exponential-like manner. The measurement of the sample with a post-irradiation heat treatment (plotted in Figure 60, top left) decreases to the value of the fully annealed samples, while its modelled value is lower, due to the large grain size (around 250 nm). It is notable to mention that the modelled resistivity at this grain size approaches the resistivity value of the bulk material at  $8 \mu\Omega\text{cm}$ , suggesting that the choice of model parameters was reasonable. The reason for the discrepancies between the measurements and the model is in both cases believed to be point defects in the film. The standard deviation for all measurements is within the  $\text{n}\Omega\text{cm}$  range and is therefore not visible in the plots. The plots on the right side of Figure 60 show the same resistivity data, divided into the respective contributions of each scattering factor.

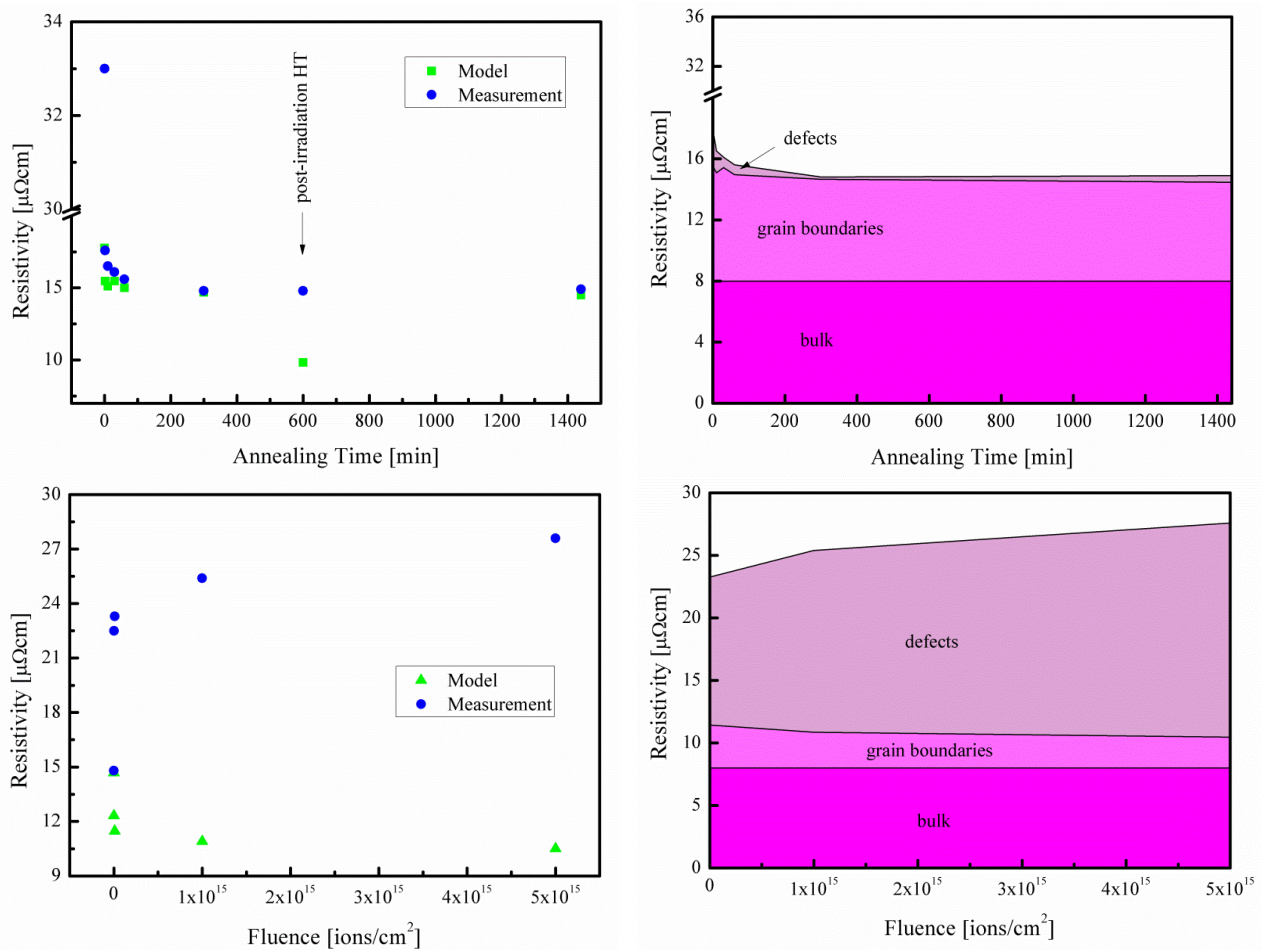


Figure 60: Measured and modelled resistivity of heat treated (top) and irradiated (bottom) samples. The standard deviation is in the  $\text{n}\Omega\text{cm}$  range; hence the error bars are not visible. The images on the right show the measured data, divided into their respective contributions to the resistivity.

From the obtained results and calculations, the defect concentration in the samples is calculated. As they have the strongest effect on the resistivity, it was assumed that vacancies were the only

defect present. In the literature, different methods have been found to measure the resistivity increase per atomic per cent vacancies  $\Delta c_{\text{vac}}/\text{at.}\%$ . DeSorbo [79] combined calorimetric studies and electrical resistivity measurements of gold samples containing vacancies from quenching from high temperatures and obtained a  $\Delta c_{\text{vac}}$  value of  $1.8 \mu\Omega\text{cm/at.}\%$ . Simmons and Balluffi [80, 81] compared the macroscopic length change and the change of the lattice constant while increasing the temperature, and with the help of simultaneous resistivity measurement obtained a  $\Delta c_{\text{vac}}$  value of  $3.6 \mu\Omega\text{cm/at.}\%$  for aluminium. As no  $\Delta c_{\text{vac}}$  value for in  $\text{AuAl}_2$  could be found in literature, we calculated the mean value from the constitutive elements and obtained  $\Delta c_{\text{vac}} = 3 \mu\Omega\text{cm/at.}\%$  vacancies. By dividing the resistivity difference between our measurements and corresponding model values by this value, the vacancy content of the respective samples was obtained and is plotted in Figure 61.

From the obtained defect concentration of the as-deposited sample, the average distance between vacancies  $L$  was estimated according to  $L = b/\sqrt[3]{c}$ , with  $b$  being the burgers vector along the (110) direction, and found to be 1.2 nm.

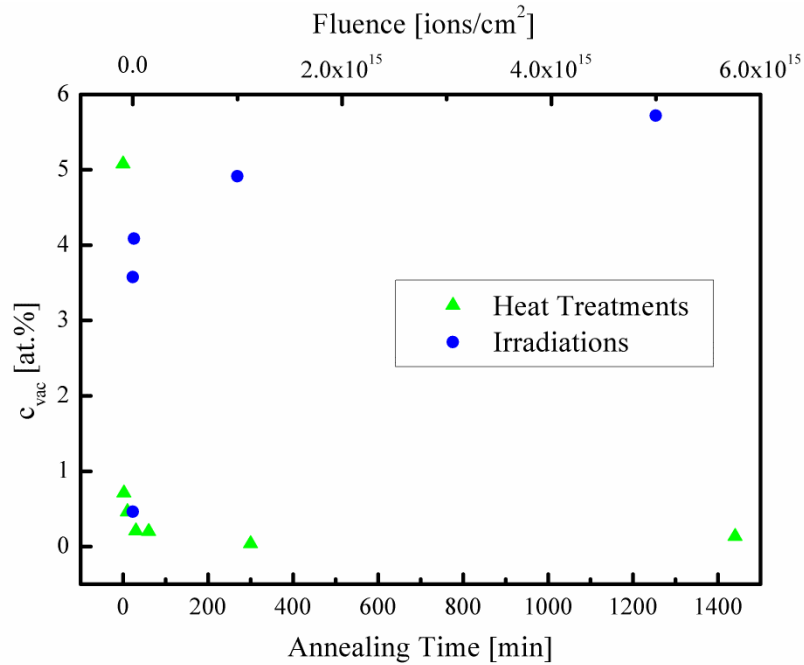


Figure 61: Development of defect concentrations during heat treatments and irradiations.

## *Discussion*

Unlike the Au-Ag gradient sample, the as-deposited Au-Al gradient wafer shows sharp, vertical transitions of grey and brown colours along its surface. This is not surprising, considering there is only little solubility of Al in Au, and none at all of Au in Al (compare the phase diagram in Figure 15 of the introduction). One could even assume that the transition lines correspond to the locations of intermetallic phases, however, according to EDX only two of them should be present on the sample. The additional colour transitions are due to changes in surface topography, which is rather rough due to the deposition without rotation of the substrate.

The expected purple colour is not present in as-deposited films, neither the gradient nor the homogeneous samples. A number of different phenomena could be the reason why, and will be discussed in the following.

*Absence of the coloured intermetallic phase:* It is well established that magnetron sputter deposition can lead to the formation of metastable phases and even to non-equilibrium phase compositions (e. g. [54]). Consequently, the simplest explanation for the absence of the characteristic purple colour would be the absence of the intermetallic phase AuAl<sub>2</sub>. However, X-ray and electron diffraction confirm the presence of the phase even in as-deposited films.

*Evolution of a surface layer:* In metals, due to strong interaction, only the first tens of nanometres are penetrated by the visible part of the electromagnetic spectrum (compare chapter 3). Thus, a surface layer alone could be responsible for the presence or absence of colour, by e.g. the presence of a transparent interference layer. In our case this can also be excluded, as the sample deposited on a transparent glass substrate shows the same annealing and irradiation behaviour on its front and back side. The thin surface layer, probably consisting of Al<sub>2</sub>O<sub>3</sub> does not seem to have an influence as it is present in the as-deposited as well as the heat treated samples and would be too thin to create interference colours.

*Solid solution effects - change in the Fermi level:* A classical way to change the colour of metals is the formation of solid solutions with an alloying element, observed for instance in white (Au-Pd) or rose (Au-Cu) gold alloys and brass (Cu-Zn). The number of valence electrons is altered and with it the position of the Fermi level. This changes the possible electron transitions and therefore the colour of the material. A slight shift away from the stoichiometric composition towards the gold-rich side could have the same effect on our thin films. Au atoms in solid solution of AuAl<sub>2</sub> occupying the lattice sites of Al atoms, could increase the Fermi energy and affect the electron transitions which lead to the selective absorption of light. The heat treatment, leading to the precipitation of the AuAl phase and thus removal of the excess Au atoms from the lattice, would in this case lead to the appearance of the purple colour. The precipitates themselves do not seem to affect the colour of the sample, as they only appear after a heat treatment of 30 min - the reflectivity however, remains stable after a heat treatment of only 10 min. Nevertheless, the composition of the deposited film is not very far from the stoichiometric

ratio and is therefore not expected to have a measureable impact. In addition, the ion irradiation only leads to a local mixing of atoms and hence should not be able to remove the colour again. The maximum increase of Au content due to the irradiation is 0.54 at.%, probably not sufficient to affect the colour.

*Macrostrains:* The effect of macrostrains on the colour was also considered. Compressive stresses are found in the as-deposited and the irradiated sample, as opposed to tensile stresses in both the heat treated sample and the sample with a post-irradiation heat treatment. However, the stresses are not very high and therefore assumed not to have an influence on the colour.

*Texture:* The loss of the film texture after the irradiation is possibly due to an amorphization of the material during the irradiation at low temperature [82-84]. The crystallization that takes place during reheating to room temperature is different from the grain growth and therefore the lack of texture is not unexpected. However, an influence of the texture on the colour can be excluded as the as-deposited and heat treated samples are both textured, but only one of them displays a colour.

*Defects and microstrains:* A further possibility is the presence of microstrains due to imperfections in the structure. Different types of defects can occur in a metallic film, such as grain boundaries, dislocations, voids or point defects, like interstitials or vacancies. They lead to a local distortion of the crystal lattice, which, if their number is high enough, can result in a smearing out of the band structure. This changes the possible electron transitions and hence the colour of the material. In the case of AuAl<sub>2</sub>, the grain size, while being rather small, increases only marginally during the heat treatment, indicating that the grain boundaries are not the colour-inhibiting factor. During the deposition of the intermetallic phase, the formation of dislocations is unlikely, as the mobility of the atoms in the intermetallic phase is not sufficient. No voids have been observed in the TEM images, which leaves point defects as the likely cause for the lack of colour in as-deposited layers of AuAl<sub>2</sub>. The mean distance between the defects, which for calculating purposes were assumed to be vacancies, is very small with  $\approx 1.2$  nm. This suggests that they are the controlling factor inhibiting the colour. Their annihilation during the heat treatments leads to the relaxation of the lattice spacings and the appearance of colour. During the bombardment with Au<sup>+</sup> ions, point defects are reintroduced. The fact that the grains grow further during this treatment supports the assumption that the lack of colour is not affected by the grain size. The second annealing removes the newly introduced defects and reinstates the colour. The only aspect stopping the process from being completely reversible are the small cracks that are created in the surface during irradiation and lead to a slight darkening of the colour.

Concluding, this is the only explanation for the missing colour that is in agreement with the entire range of experimental observations.

Resistivity measurements are highly sensitive to point defects and show strong differences between the samples. After the exclusion of all other known electron scattering contributions,

the residual difference was attributed to vacancies. This is justified by vacancies having the stronger influence on resistivity than dislocations, stacking faults and voids. In addition, the vacancy contribution to resistivity is experimentally well characterized. The resulting values are high compared to literature for pure metals [80] or semiconductors [85]; however, they are in the range of vacancy concentrations obtainable by quenching or irradiation of intermetallics [86]. The development of the vacancy concentration during irradiation seems to exponentially approach a limit of around 6 at.%. It is possible that when a certain fluence is reached, an equilibrium is established between the creation of new defects by atom collisions and the annihilation of defects due to the thermal spikes.

### 4.3 Pt-Al

#### *Results*

#### Macroscopic appearance and reflectivity

Similarly to the Au-Al gradient sample, the wafer with a composition gradient of Pt and Al displays a variation of grey colours after the deposition but a heat treatment of 1 h at 400°C reveals the expected yellow colour in a certain area of the wafer (Figure 62, bottom half of the wafer). The range of the coloured phase is much smaller in this case, corresponding to the limited stability range of the  $\text{PtAl}_2$  phase compared to  $\text{AuAl}_2$ . The alloy composition on the wafer ranges from 50 at. % Al on the left to 84 at.% on the right side, the stability of  $\text{PtAl}_2$  however only between 60 at.% and 72.5 at.% Al. The arrows mark the approximate position of the positions of the intermetallic phases  $\text{PtAl}$ ,  $\text{Pt}_2\text{Al}_3$ ,  $\text{PtAl}_2$ ,  $\text{Pt}_6\text{Al}_2$  and  $\text{Pt}_6\text{Al}_{21}$ .

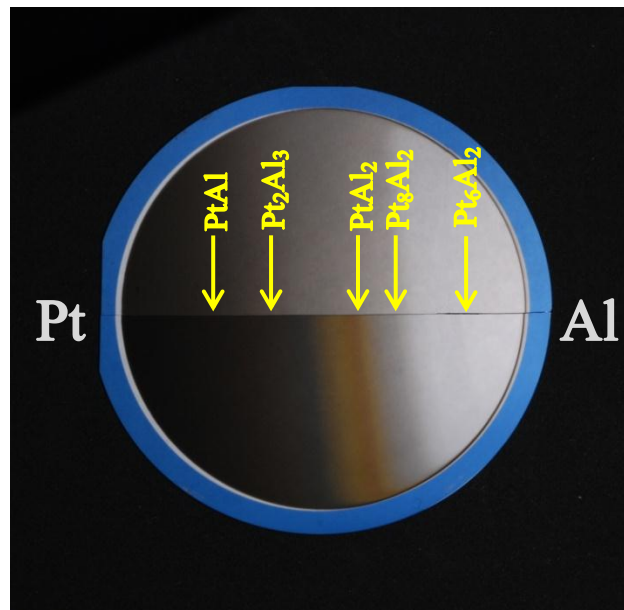


Figure 62: Sample with a composition gradient of Pt and Al across the surface, ranging from 50 at.% on the left to 84 at.% Al on the right side. The top half of the wafer is as-deposited, the bottom half has been heat treated for 1 h at 400°C.

Again, the homogeneous samples with the composition of the  $\text{PtAl}_2$  phase are grey in their as-deposited state (Figure 63); no shade of colour can be detected. Heat treatments of 30 min at 100°C and 200°C do not change the appearance of the samples; a temperature of 300°C is required to bring out the expected yellow colour. An increase of the treatment temperature to 350°C does not lead to a further intensification of the colour. To investigate whether a certain minimum temperature is required for the colour to appear and if a smooth transition from grey to coloured takes place, as was the case with the  $\text{AuAl}_2$  samples, heat treatments were carried out at 200°C for 1 h, 3 h, 6 h and 24 h. As can be seen in Figure 64, the reflectivity after 1 h



remains roughly the same as in the as-deposited state, but after 3 h a minimum begins to form in the curve around 400 nm. This minimum becomes intensified with increasing treatment time and after 24 h, the curve has the same shape as after a heat treatment of 30 min at 350°C. The latter sample has overall a slightly lower reflectivity, which could be due to an increase in the surface roughness during the heat treatment at higher temperatures.

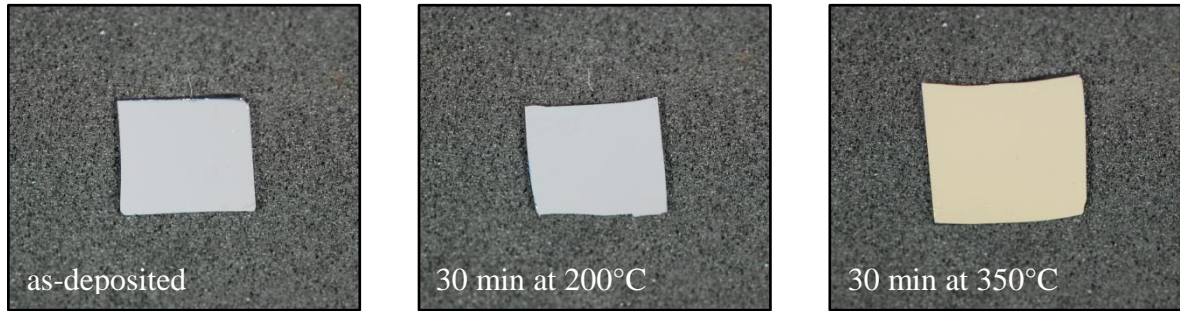


Figure 63: Images of homogeneous PtAl<sub>2</sub> samples after different heat treatments. The treatments for 30 min at 100°C and 200°C do not change the colour, temperatures of 300°C and 350°C for 30 min are required for the expected yellow. The size of the samples is roughly 2 cm<sup>2</sup>.

This position of the minimum in the reflectivity curve is roughly in agreement with the literature value at 410 nm [87], where the reflectivity of a polished bulk sample was measured.

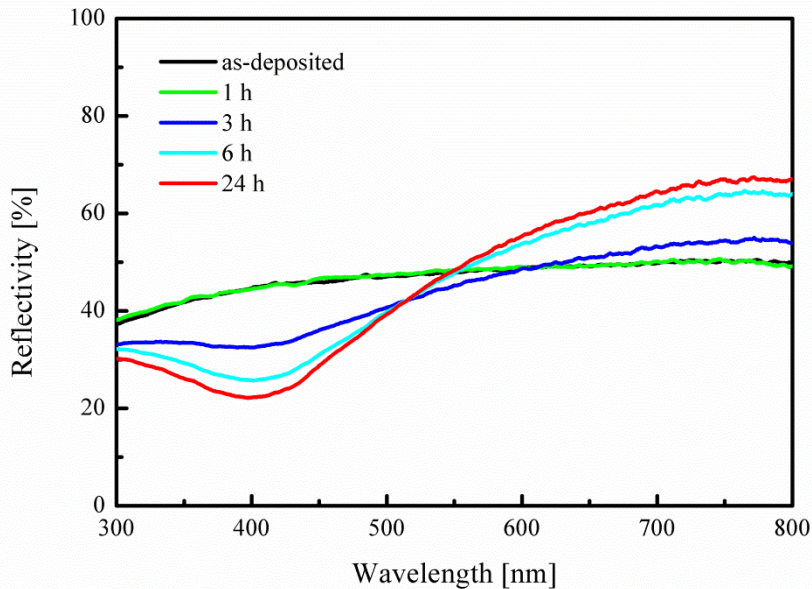


Figure 64: Reflectivity measurements of the homogeneous PtAl<sub>2</sub> samples in different heat treatment states. While a treatment for 1 h does not noticeably change the reflectivity curve, a dip starts to develop around 400 nm after 3 h and intensifies as the duration is increased until after 24 h its position remains stable.

## X-Ray diffraction (XRD)

The XRD spectra of the as-deposited sample, the one heat treated for 30 min at 100°C and at 200°C do not display sharp peaks, only a very broad hill around the position of the (220) peak, which resembles the pattern of an amorphous material (Figure 65). The treatment at 300°C finally leads to the formation of a crystalline PtAl<sub>2</sub> phase. All the expected peaks are present and their intensity distribution is very close to the bulk reference, suggesting that the film is not textured. The position of the peaks also fits rather well to the reference with an average shift of 0.1° to lower 2θ values. This would mean the d values are an average of 0.005 Å smaller than the reference. The peak broadening of the 220 reflex in the as-deposited sample was used to roughly estimate the size of the coherently scattering areas with the help of the Scherrer formula. The mean grain size was found to be about 17 Å.

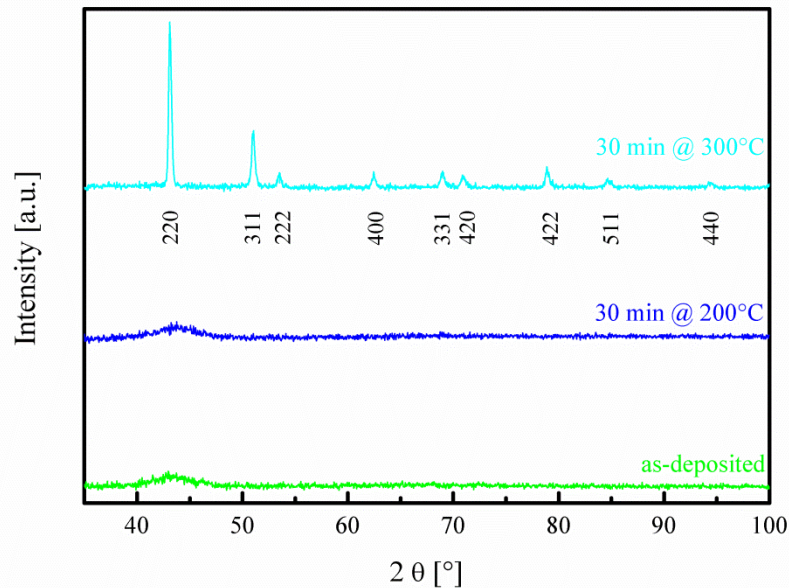


Figure 65: XRD measurements of PtAl<sub>2</sub> samples in different heat treatment states. The as-deposited spectrum only shows a single broad peak, which indicates an X-Ray amorphous material. Also after 30 min at 200°C no change is visible; sharp diffraction peaks only appear after a heat treatment of 30 min at 300°C.

## Microstructure studies

The diffraction pattern of the as-deposited sample displays several broad rings, an indication of very small crystallites in the nanometre scale rather than fully amorphous material (Figure 66, left). Their distances roughly correspond to the PtAl<sub>2</sub> phase, and the fact that the second ring, attributed to the (200) reflex, has a much stronger intensity than the first ring, the (111) reflex, also indicates the presence of the phase. This intensity distribution is also found in the bulk reference. The TEM BF images show extremely fine columns of about 20 nm in size, increasing towards the surface. Occasionally, the grain size at the surface reaches up to 90 nm, leading to a bubble-like topography on the surface (SEM image, insert Figure 66). It is questionable if the

columnar features correspond to the crystalline grains, as the broadness of the diffraction rings would suggest them to be smaller. Unfortunately, it was not possible to prepare the TEM lamella thin enough to perform high-resolution images. After a heat treatment of 30 min at 350°C, the grains have grown to sizes around 230 nm, with a rather broad size distribution (Figure 67). The very fine columns of the as-deposited sample are partially still recognisable within the large grains as very fine, bright lines, possibly a type of columnar porosity. Interestingly, the surface topography as observed in SEM does not change during the heat treatment, suggesting that here too; a thin, amorphous layer of  $\text{Al}_2\text{O}_3$  has formed, shielding the underlying metal from further oxidation.

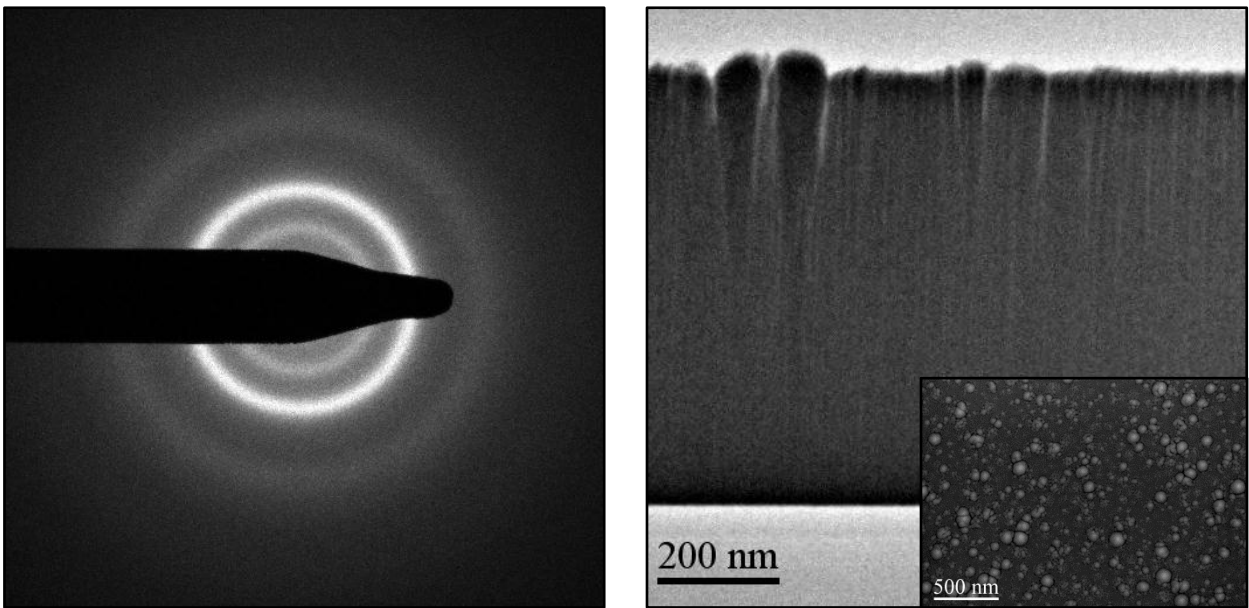


Figure 66: Diffraction pattern and TEM BF image of an as-deposited PtAl film. Broad rings in the diffraction pattern indicate a nanocrystalline morphology. Some of the very fine columns broaden into larger grains towards the film surface, leading to a bubble-like appearance of the topography (insert, SEM image).

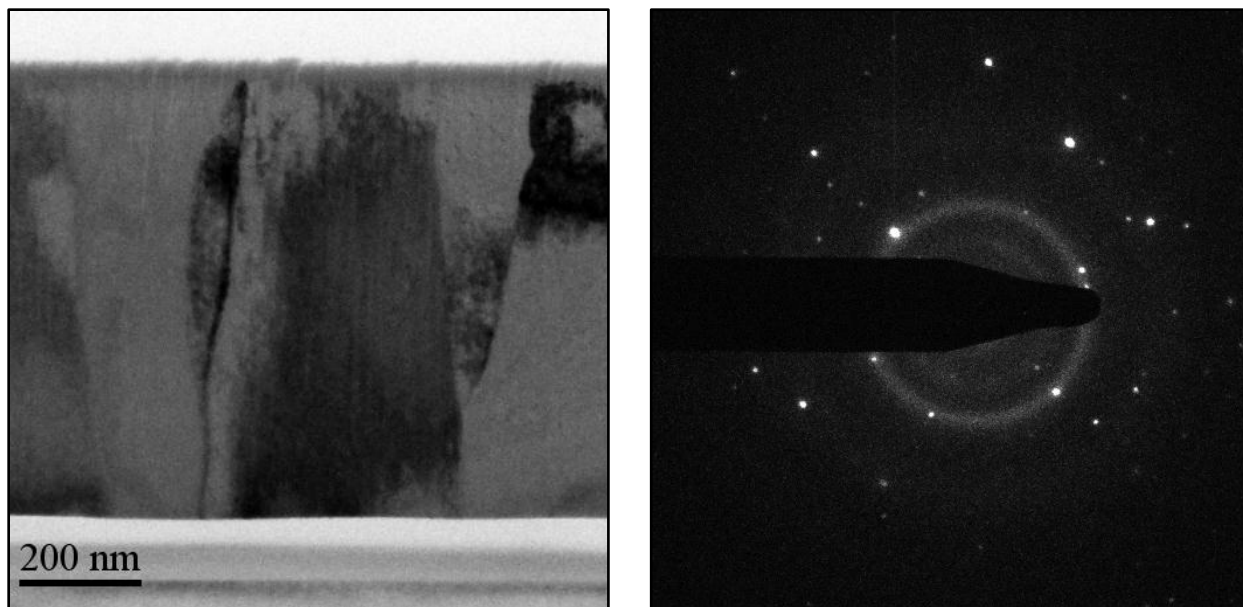


Figure 67: TEM BF and diffraction pattern of a  $\text{PtAl}_2$  sample heat treated for 30 min at  $350^\circ\text{C}$ . The fine columns have grown into rather large grains but are still detectable as fine bright lines. The diffraction reveals only reflexes belonging to the  $\text{PtAl}_2$  phase.

### Electrical resistivity

The electrical resistivity measurements of the  $\text{PtAl}_2$  samples nicely reflect the appearance of the colour. While the as-deposited sample and the ones with heat treatments of 0.5 h and 1 h at  $200^\circ\text{C}$  have very high resistivity values of close to  $400\ \mu\Omega\text{cm}$ , a reduction is measured for the sample annealed for 3 h to nearly half of that value ( $213\ \mu\Omega\text{cm}$ ). The duration of 6 h reduces the resistivity again to exactly  $100\ \mu\Omega\text{cm}$  and after 24 h it has gone down to  $53\ \mu\Omega\text{cm}$ . The sample that was heat treated for 30 min at  $350^\circ\text{C}$ , also inserted in Figure 68, has an even lower resistivity of roughly  $45\ \mu\Omega\text{cm}$ , but still lies quite far above the values for the  $\text{AuAl}_2$  samples, even in the as-deposited state. Unfortunately, no reference value could be found, either for bulk or for thin film samples. It is therefore not clear if the high resistivity has its origin in the nature of the material or if thin-film, defects or possibly grain size effects are at work. Most likely it is a combination of all factors.

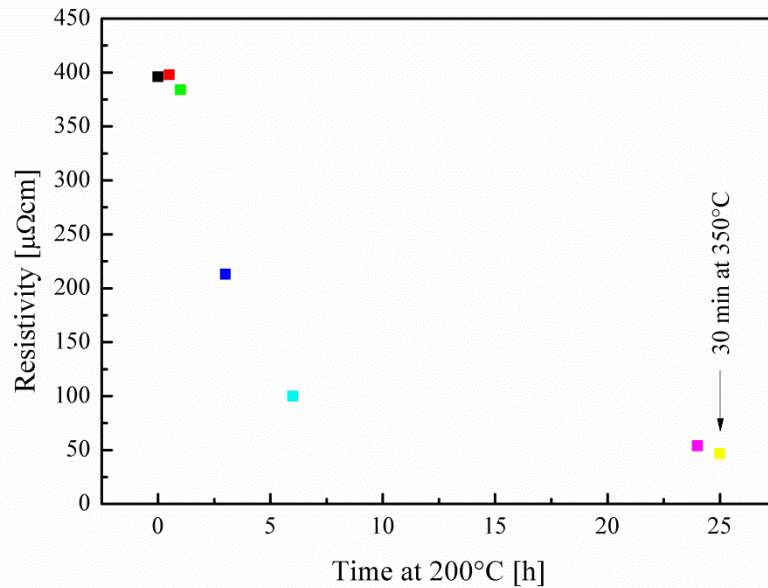


Figure 68: Measured resistivity values of differently treated PtAl<sub>2</sub> samples. The very high values of the as-deposited sample begin to drop only after 3 h at 200°C. After 24 h it has been reduced to nearly 1/10 of its initial value but remains rather high compared to the AuAl<sub>2</sub> samples.

### Discussion

As was the case in the as-deposited samples of the AuAl<sub>2</sub> phase, the PtAl<sub>2</sub> does not display the expected colour directly after the deposition. The experimental results for the two alloys are not identical and different phenomena could be the cause for the lack of colour. The same possibilities are discussed in the following.

*Absence of the coloured intermetallic phase:* Unlike in the previous case, the XRD spectrum implies that no long-range order is present in the as-deposited PtAl<sub>2</sub> sample. Despite being X-ray amorphous, the broad rings of the electron diffraction patterns suggest that the phase is structurally ordered, in a nanocrystalline state. The heat treatments lead to a full crystallisation of the material. Similar findings of a PtAl<sub>2</sub> phase lacking long-range order have been reported by Blanpain *et al.* [88], who performed a so-called *solid state amorphization* by interdiffusion of sequentially deposited, crystalline layers of platinum and aluminium at temperatures between 150°C and 220°C to form an amorphous, single-phased thin film. Above 270°C this film was then transformed into a fully crystalline layer of PtAl<sub>2</sub>. The diffraction patterns of the ‘amorphous’ alloy they report show the same broad rings that we obtained from our as-deposited samples, indicating that their material was also nanocrystalline.

The fact, that the phase is present in only a nanocrystalline state is likely to be the origin of the grey colour of the as-deposited samples. However, a lack of a long-range order does not necessarily lead to a lack of colour. For example, Schroers *et al.* [89] have produced a gold-based, bulk metallic glass which still displays a colour that is very close to the expected yellow of

crystalline gold. Hence, the glassy alloy still possesses a band structure with electron transitions at similar energies to a crystalline one.

*Evolution of a surface layer:* Again, the presence of a thin surface oxide layer is very likely, solely because the layer consists of 66 at. % aluminium, which instantly reacts with oxygen when in contact with air. Also the fact that the surface topography in the SEM SE images does not change during the heat treatment is an indication of such a layer. However, the film is very thin and not expected to influence the colour. Additionally, the colour appears after a heat treatment, which would not be explicable with this approach, as an elevated temperature only leads to a thickening of the film and not a removal, despite being carried out in vacuum. The formation of interference colours due to an oxide layer can also be excluded, as a layer thickness of at least  $\approx 100$  nm is required for interference to occur. An oxide layer of this thickness would be easily observable in the TEM.

*Solid solution effects - change in the Fermi level:* While the EDX measurements indicate that the sample exists of exactly 66.6 at.% Al and 33.3 at.% Pt, the uncertainty of the method allows for a deviation of up to 5 at.%, meaning that it is well possible that an excess amount of Pt or Al are accommodated within the structure of  $\text{PtAl}_2$ . This could lead to a shift of the Fermi level and a loss of the distinct interband transitions that cause the yellow colour. However, the solubility of Pt or Al in  $\text{PtAl}_2$  is not very large; therefore no big influence on the position of the Fermi level is expected. Additionally, no second phases were found after the heat treatment of the  $\text{PtAl}_2$  sample, neither in SEM BSE images, nor in the XRD spectra or electron diffraction. This suggests that the composition is not very far from the aimed-for Pt:Al ratio of 1:2. Thus, excessive amounts of either of the two elements are bound to be very small and are not expected to influence the colour.

*Macrostrains:* Unfortunately, the change in the macrostrains from the as-deposited, grey sample to the coloured ones could not be determined as the as-deposited sample does not display sharp peaks. The positions of the peaks in the yellow, heat treated sample fit rather nicely to the reference value, but as they are based on measurements of a bulk sample it is not possible make a certain statement.

*Texture:* No EBSD measurements were performed for the  $\text{PtAl}_2$  samples and XRD spectra were only taken at a single  $\psi$ -angle. The presence of all XRD peaks in the expected intensity distribution is an indicator for a not textured film, but no certain statements can be made. In either case, as the crystal structure is cubic, no effect of a possible texture on the colour is expected.

*Defects and microstrains:* As in the  $\text{AuAl}_2$  sample, the defects that locally strain the crystal lattice could be the reason for the grey colour of as-deposited  $\text{PtAl}_2$ . The grain size in this case is a lot smaller, with only  $\approx 1.7$  nm and an extensive grain growth has taken place during the heat treatments (to 230 nm). Unfortunately, with no modelling of the resistivity available, it is not

possible to make a clear distinction between the influence of the grain size and the defect concentration.

The reason for the lack of colour is probably a mixture of both the presence of a high defect concentration, paired with the very small grains of the phase, which together lead to a smearing out of the distinct band structure and thus a lack of colour.

There is a notable difference in the morphology of the samples of  $\text{AuAl}_2$  and  $\text{PtAl}_2$ , which in all likelihood is due to their different melting points. While  $\text{AuAl}_2$  melts at  $1060^\circ\text{C}$ , it requires  $1406^\circ\text{C}$  for the same to happen in  $\text{PtAl}_2$ . During sputter deposition, the melting point of a material strongly influences the mobility of the atoms after condensation. A certain mobility in the  $\text{AuAl}_2$  phase leads to the formation of defined grains, while the atoms in the  $\text{PtAl}_2$  phase are confined to a very small volume and unable to move. Other parameters that influence the mobility of the atoms, such as the sputter pressure or the substrate temperature, were the same for both samples.



## 4.4 Au-In

### *Results*

#### Macroscopic appearance and reflectivity

The AuIn<sub>2</sub> film already displays a shade of blue colour directly after the deposition (Figure 69), which is in contrast to the previously observed AuAl<sub>2</sub> and PtAl<sub>2</sub> samples. The heat treatments at 300°C for 30 min and 12 h do not seem to intensify or change the colour. A treatment for 1 h at a higher temperature of 400°C leads to a strong hillock formation and very dull appearance of the sample.

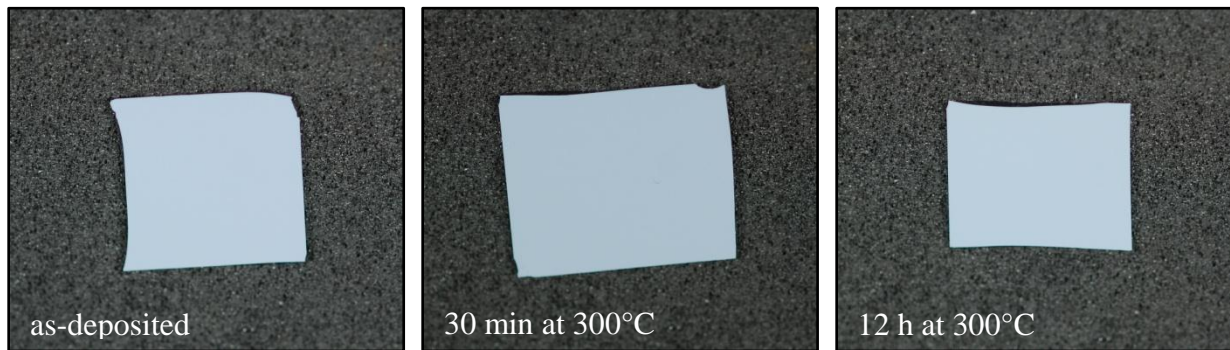


Figure 69: Images of AuIn<sub>2</sub> samples in different heat treatment states. No colour change can be observed. The sample size is roughly 2 cm<sup>2</sup>.

The reflectivity measurements reveal that the heat treatments do affect the reflectivity of AuIn<sub>2</sub>, however only very slightly (Figure 70). The minimum in the curve at 680 nm becomes marginally more pronounced than in the as-deposited state, also at the short-wavelength end of the spectrum the reflectivity is reduced. The curves of the two heat treated samples are almost exactly the same, indicating that the change that is brought on by the heat treatment happens rather quickly. The position and height of the local minimum and maximum are in good agreement with the literature [90].



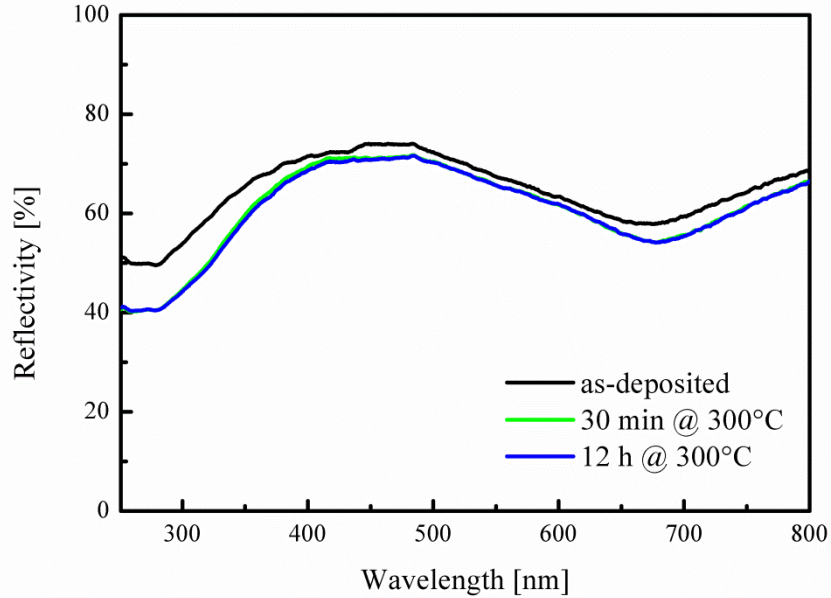


Figure 70: Reflectivity measurements of AuIn<sub>2</sub> samples in different heat treatment states, revealing that a very small change in the reflectivity occurs during the heat treatments.

### X-Ray diffraction (XRD)

The XRD measurements of the as-deposited and the sample heat treated for 12 h at 300°C (Figure 71) both indicate that they exist of only the blue AuIn<sub>2</sub> phase. The films appear to be slightly textured as not all the reference peaks are present. This texture becomes intensified during the heat treatment, as for example the (220) peak, which, according to the bulk reference is supposed to be the strongest reflex, loses intensity while the (311) peak increases. The positions of the peaks of the as-deposited sample fit rather nicely to the bulk reference with an average deviation of only 0.01°, but are shifted to slightly higher  $2\theta$  values in the heat treated one, increasing the difference of the peak position to the bulk reference to 0.2°, corresponding to a difference in the  $d$  value of 0.003 Å. This indicates a change of the stress state during the annealing but as no reference is available that corresponds to lattice constants of thin films, it is only possible to say that the stresses become more tensile.

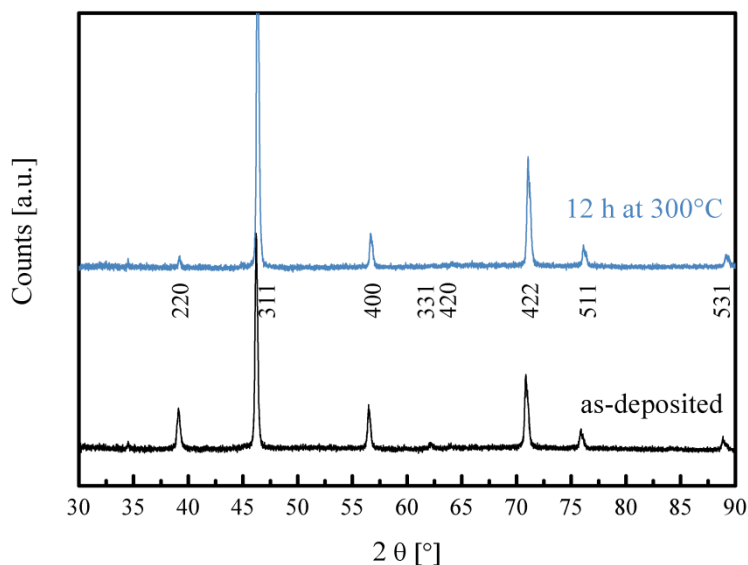


Figure 71: XRD spectra of the AuIn<sub>2</sub> layer, as-deposited (bottom) and heat treated for 12 h at 300°C (top). The intensity distribution of the peaks suggests that a slight texture is present in the films.

### Microstructure studies

The TEM images of the as-deposited lamella display a columnar grain structure, with grains that are roughly the same size throughout the thickness of the film (Figure 72, top left). Horizontal dark bands are visible, which go roughly parallel to the surface, possibly due to a bending contrast. At higher resolutions vacancy clusters become visible within the grains (Figure 72, bottom left), some of which are arranged in lines perpendicular to the surface. No possible explanation for this alignment could be found. After the heat treatment for 12 h at 300°C, the dark bands have disappeared and the grains have grown from initially around 38 nm to 106 nm, the columnar structure is still visible. The vacancy clusters have coarsened and are not linearly aligned anymore.

From the diffraction patterns (Figure 73) it has to be assumed that not only the expected AuIn<sub>2</sub> (marked in green) but also a certain amount of the binary AuIn phase (marked in orange) and In<sub>2</sub>O<sub>3</sub> is present in the as-deposited sample. After the heat treatment, the signal of the oxide remains, but no reflexes of AuIn are found. This suggests that the sample is not completely homogeneous and the lamella of the heat treated sample was cut from an area where no AuIn phase was present. The fact that no AuIn was found with XRD, where the scanned area is much larger, means that the volume of the phase is rather small. The same applies for the In<sub>2</sub>O<sub>3</sub>. Unlike the thermally grown oxide on aluminium, which is normally amorphous, indium oxide is known to be crystalline at lower temperatures [91]. It could have formed during the interrupted sputter deposition, which was necessary to keep the indium target from melting or during the storage of the samples in air.

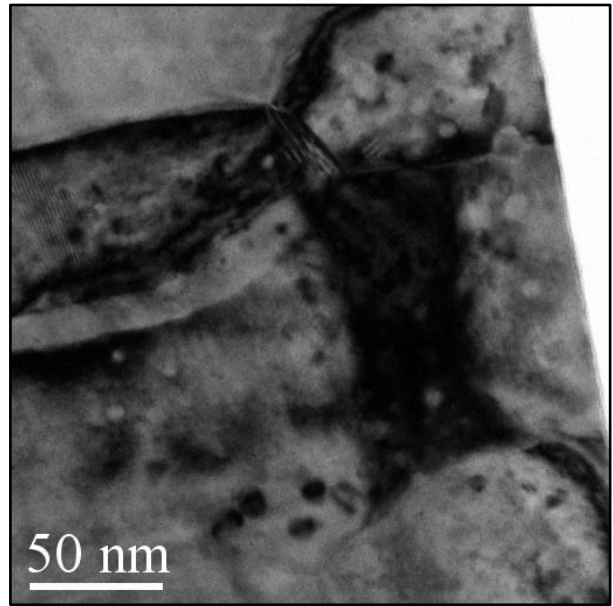
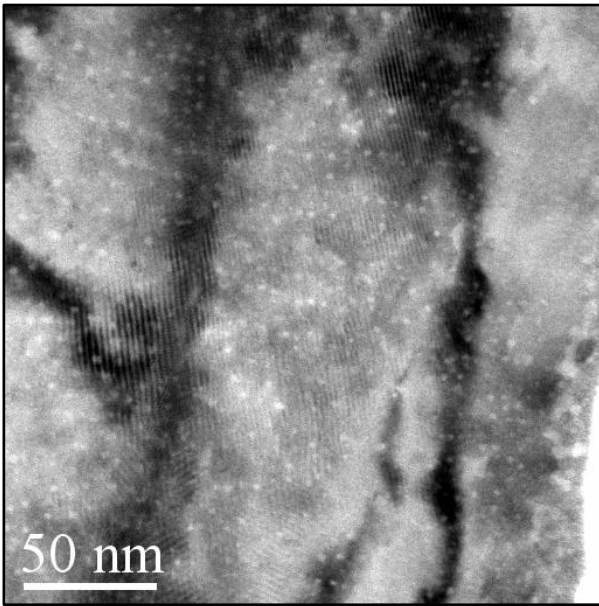
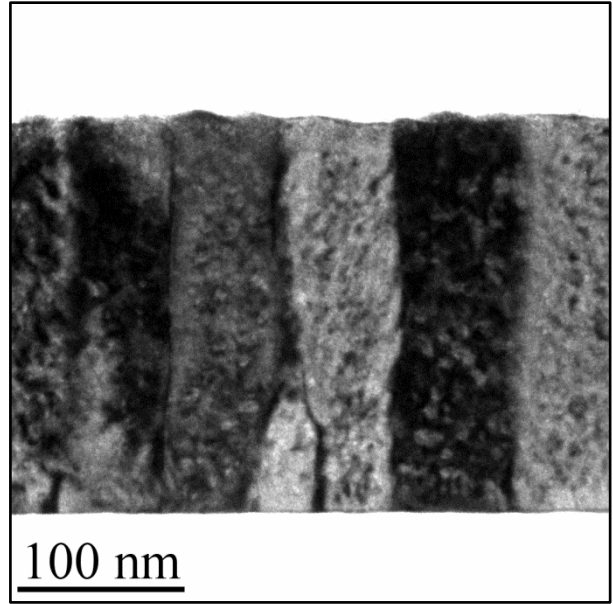
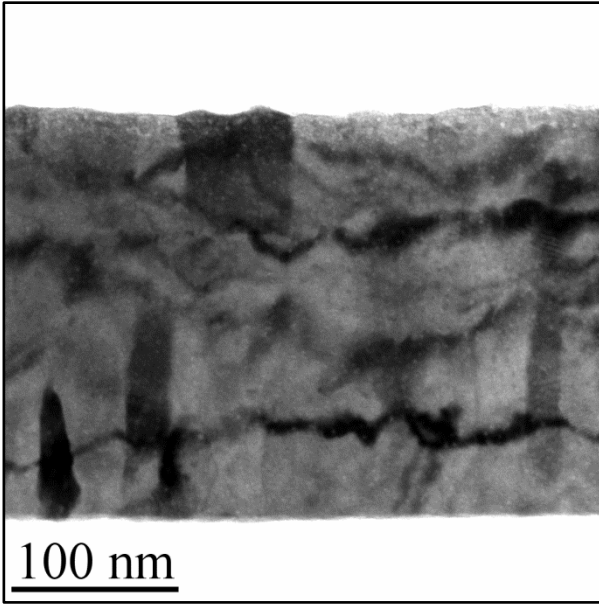


Figure 72: TEM BF images of an as-deposited (left, top and bottom) and heat treated (12 h at 300°C) sample (right, top and bottom). The initially rather small grains (38 nm) grow during the heat treatment to an average size of 106 nm. Vacancy clusters that initially seem to be arranged in lines perpendicular to the surface coarsen to form rather large voids.

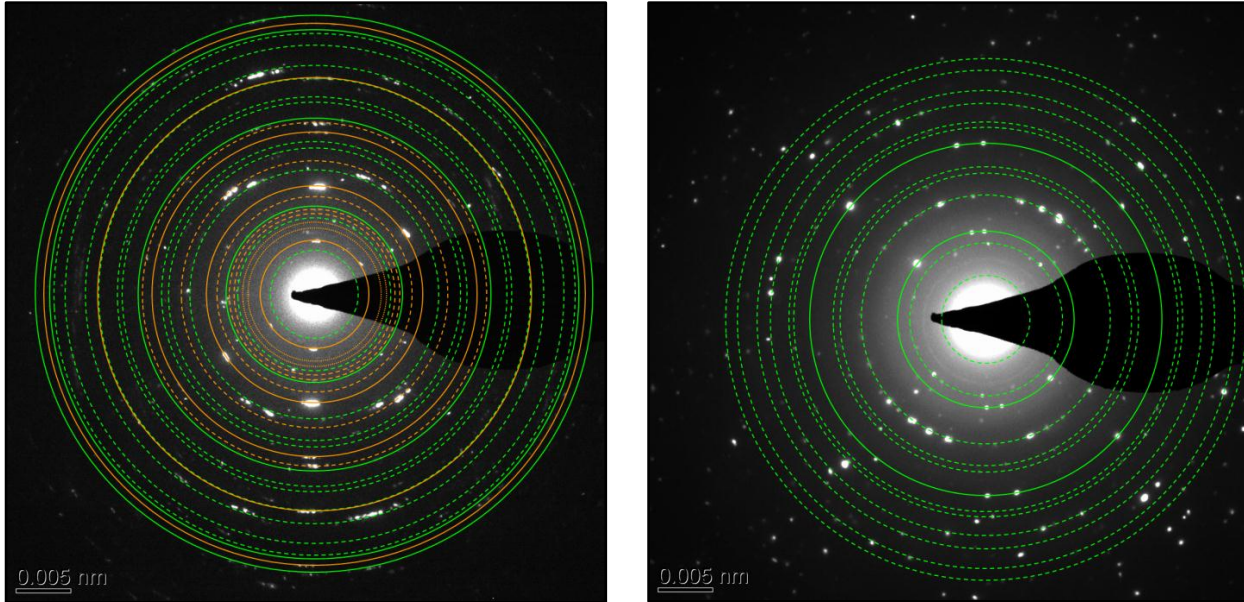


Figure 73: Diffraction pattern of the as-deposited (left) and heat treated (right)  $\text{AuIn}_2$  sample. Next to the expected reflexes from the  $\text{AuIn}_2$  phase (marked in green), the as-deposited sample also contains a clear signal from the  $\text{AuIn}$  intermetallic phase (marked in orange). As no such reflexes could be detected in the heat treated state, it has to be assumed that the original sample was not completely homogeneous and the two lamellae were cut from different regions. In both patterns a weak signal of  $\text{In}_2\text{O}_3$  was detected.

### Electrical resistivity

The resistivity in the as-deposited film (Figure 74) is with  $20.6 \mu\Omega\text{cm}$  rather high compared to the bulk reference of  $8 \mu\Omega\text{cm}$  [60]. The short heat treatment of 30 min at  $300^\circ\text{C}$  reduces it to around  $11 \mu\Omega\text{cm}$  where it remains even after 12 h of heat treatment at the same temperature. The modelled resistivity was calculated with grain sizes measured from TEM images for the as-deposited and the sample heat treated for 12 h at  $300^\circ\text{C}$ . No TEM images were available for the sample heat treated for 30 min at  $300^\circ\text{C}$ ; hence the grain size was roughly determined from SEM BSE images. Similar to the  $\text{AuAl}_2$  samples, the as-deposited measurement is far above the modelled one. Already after 30 min at  $300^\circ\text{C}$  the modelled and measured resistivity fit rather nicely. The values of the sample treated for 12 h at  $300^\circ\text{C}$  coincide, as the grain boundary reflection coefficient was adjusted to this value.

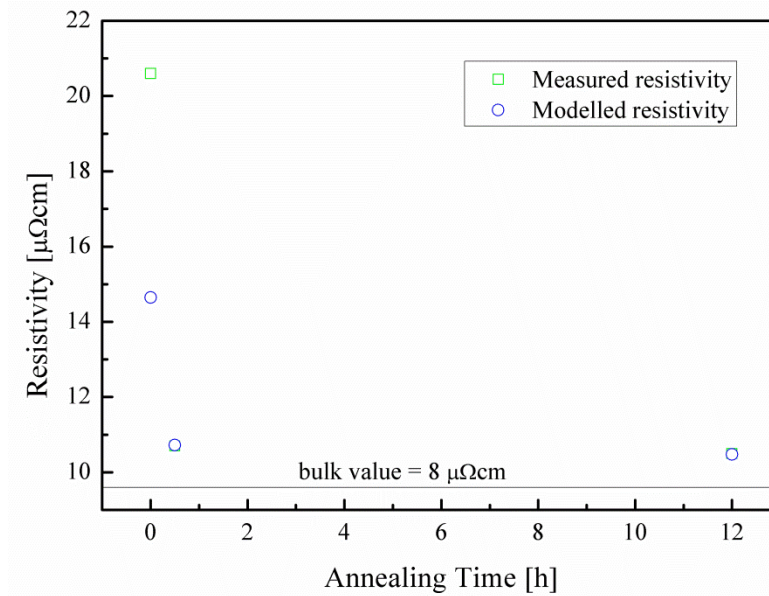


Figure 74: Measured and modelled resistivity values of the  $\text{AuIn}_2$  samples in different heat treatment states. While a clear difference between model and measurement is present in the as-deposited sample, they fit perfectly after a heat treatment of only 30 min at  $300^\circ\text{C}$ . The bulk resistivity at  $8 \mu\Omega\text{cm}$  is marked as horizontal line.

No reference value for a resistivity increase per atomic % of defects was found for In, but due to the similarities of the two phases, the same value of  $\Delta c_{\text{vac}} = 3 \mu\Omega\text{cm}/\text{at.}\%$  vacancies was assumed for  $\text{AuIn}_2$  as for  $\text{AuAl}_2$  and the vacancy concentration calculated accordingly (Figure 75).

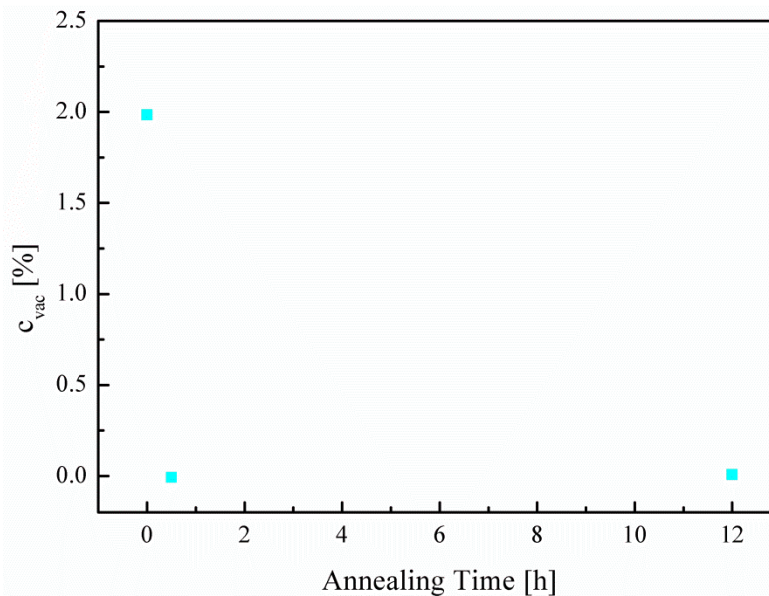


Figure 75: Calculated vacancy concentrations in the  $\text{AuIn}_2$  sample in different heat treatment states. Already after 30 min at  $300^\circ\text{C}$  all of the defects appear to be annihilated.

The vacancy concentration of the as-deposited sample is already considerably lower than in the  $\text{AuAl}_2$  sample and is reduced to nearly 0 % already after 30 min. After 12 h at  $300^\circ\text{C}$  the vacancy

concentration has gone down to zero, due to the initial assumptions for the calculations. Again the average distance between the vacancies was calculated and found to be 1.7 nm.

### *Discussion*

The AuIn<sub>2</sub> samples display the expected blue colour directly after the deposition and there is near to no change during the heat treatments. XRD and diffraction measurements confirm the presence of the AuIn<sub>2</sub> fluorite phase, and even though there are indications for a second intermetallic phase (the triclinic AuIn) phase and In<sub>2</sub>O<sub>3</sub>, neither of them are present in a large amount and do not appear to influence the macroscopic colour appearance of the samples.

The dissimilarity to the previous two cases is clearly that no heat treatment is required for the colour to appear. Nevertheless, the AuIn<sub>2</sub> films contain the same defects as the previously investigated alloys. The grain size in the as-deposited sample is comparable to AuAl<sub>2</sub> and clearly not a critical factor. Dislocations were not found in TEM investigations; however numerous closely spaced voids are present. Their average distance of roughly 5 nm is still larger than the mean distance between the vacancies, which was calculated to be 1.7 nm. The difference to the respective value in AuAl<sub>2</sub>, which was estimated to be 1.2 nm is very small, but the critical length might just be exceeded. The assumptions that were made for the calculations of the defect concentration could also be faulty, leading to values that differ from reality.

The melting point of the AuIn<sub>2</sub> phase is quite low at 539°C compared to AuAl<sub>2</sub> with 1060°C and PtAl<sub>2</sub> with 1406°C. Hence, the mobility of the atoms during the deposition is expected to be larger, enabling the structure to anneal defects to a certain degree while the deposition is ongoing. Again, the sputter pressure and substrate temperature, which could be the reason for an altered morphology of a film, are the same for all three investigated materials.

## 4.5 Comparison of AuAl<sub>2</sub>, PtAl<sub>2</sub> and AuIn<sub>2</sub>

Despite being structurally very similar, the experiments with the intermetallic phases AuAl<sub>2</sub>, PtAl<sub>2</sub> and AuIn<sub>2</sub> revealed certain differences, which are summarised in Table 15. As the deposition parameters, like the sputter pressure of 2 mTorr and the substrate temperature (RT), were identical, the differences have to be due to intrinsic materials properties.

The presence or absence of colour in as-deposited samples is controlled by crystal imperfections, or more precisely, the distance between them. The type of defect which is most closely spaced has the largest impact on the distortion of the lattice and the consequential change of the band structure. In the case of AuAl<sub>2</sub>, the predominant defects are vacancies, for PtAl<sub>2</sub> the distinction is difficult to make. Assuming the sample contains a similar amount of defects as AuAl<sub>2</sub>, the distance between the grain boundaries is only marginally larger than the spacing of the defects.

The reason for the different behaviour of the otherwise very similar materials is probably the melting temperature, which is quite different for all three and influences the mobility of the atoms during the deposition. When this mobility is very low, as for the case of PtAl<sub>2</sub>, it prevents grain growth during deposition and results in a nanocrystalline structure. A higher mobility, as found in AuIn<sub>2</sub>, leads to small but defined columnar grains and the removal of part of the vacancies, possibly by the formation of voids. This enables the display of colour directly after the deposition. In AuAl<sub>2</sub>, an intermediate melting temperature probably leads to a mobility that is high enough to form defined grains but not able to annihilate enough defects. These defects lead to a local distortion of the lattice and thus a change of the band structure. A changed band structure allows different electron transitions and inhibits the selective absorption of light.

Table 15: Comparison of measured properties of AuAl<sub>2</sub>, PtAl<sub>2</sub> and AuIn<sub>2</sub>

	<b>AuAl<sub>2</sub></b>	<b>PtAl<sub>2</sub></b>	<b>AuIn<sub>2</sub></b>
Colour in AD	no	no	yes
XRD phase AD	yes	'no'	yes
Grain size in AD	44 nm	1.7 nm	38 nm
Vacancy spacing in AD	1.2 nm	-	1.7 nm
Resistivity AD	4.4xbulk (35μΩcm)	- (400μΩcm)	2.5xbulk (20μΩcm)
Colour & phase in HT	yes	yes	yes
Melting T	1060°C	1406°C	539°C
T <sub>m</sub> pure elements	Au: 1064°C Al: 660°C	Pt: 1769°C	In: 157°C

That a small change of the crystal lattice can have such a large impact might be a little surprising, but seems justified when considering the example of quantum dots. The small particles of semiconductor material have lattice constants that increase as the particles become smaller, due to the increasing surface-to-volume ratio. The stretching of the lattice leads to an increase of the band gap and consequently changes the energy that is necessary for the electron transition, thus changing the colour.

However, metals are different from semiconductors, and as was already mentioned, amorphous and even liquid gold still seem to possess a band structure with similar transition energies and the same colour as the undisturbed bulk metal [89]. But unlike the colour of gold, which is due to the onset of transitions of electrons from the filled d-bands to energy states above the Fermi level, in the intermetallic phases  $\text{AuAl}_2$ ,  $\text{PtAl}_2$  and  $\text{AuIn}_2$  the colours are based on interband transitions from the Fermi level to higher states and the presence of a pseudo-gap in the density of states, which reduces the effectiveness of the absorption over a certain energy range. This behaviour is much closer to a semiconductor than a typical metal and the transitions are probably more sensitive to changes in the band structure.

Conclusively, sputter deposition might offer possibilities for the alloy production that are not obtained with conventional casting techniques, but at the same time it has to be kept in mind that the produced materials can be far from thermodynamic equilibrium and could display unforeseen features. For instance, the production of unexpected colour effects due to the film morphology, as has been seen in the gradient wafers of Au-Al and Pt-Al, or the lack of an expected colour due to an excess amount of defects in the structure, as was the case in the homogeneous samples of  $\text{AuAl}_2$  and  $\text{PtAl}_2$ .

Once one is aware of these issues, magnetron sputter deposition can be a useful and easy method to produce small amounts of highly diverse alloy compositions.

The results of the experiments on the  $\text{AuAl}_2$  phase in chapter 4.2 have recently been published [92].



## 4.6 Au-Pt-Al

### Results

#### Sample compositions

Seven homogeneous samples were produced with a constant aluminium content of roughly 66.6 at. % and varying ratios of gold and platinum. The compositions of the samples are listed in Table 16; the samples were named after their relative Au to Pt content, which are also marked in the Au-Pt phase diagram in Figure 76. Currently, no ternary phase diagram of Au, Pt and Al is available. The Al content of 66.6 at.% was not obtained in any of the samples, but the deviations are not large and lie within the accuracy of EDX.

Table 16: (Au/Pt)Al<sub>2</sub> sample compositions according to EDX

Sample	Name	Al [at. %]	Au [at.%]	Pt [at.%]
1	Au89Pt11	64	32	4
2	Au86Pt14	65	30	5
3	Au71Pt29	65	25	10
4	Au61Pt39	69	19	12
5	Au44Pt56	66	15	19
6	Au43Pt57	69	13	18
7	Au26Pt74	69	8	23

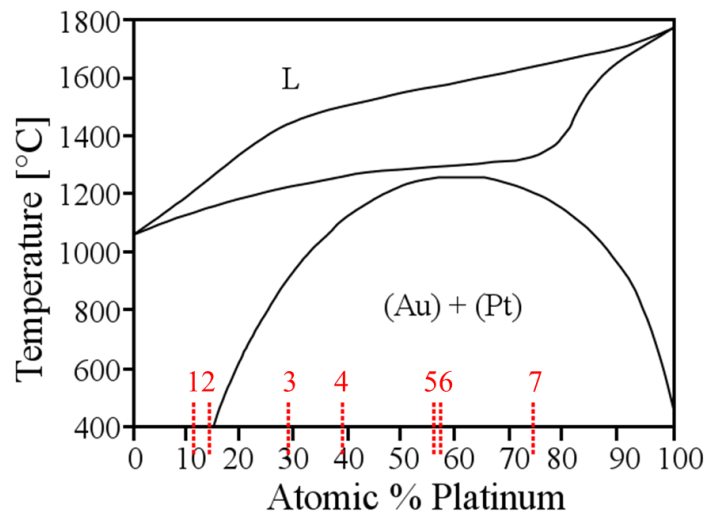


Figure 76: Au-Pt phase diagram indicating the relative compositions of Au to Pt of all samples.

## Macroscopic appearance and reflectivity

All of the samples display a grey colour in the as-deposited state, some of them with a very slight tinge of purple. After a heat treatment for 30 min at 350°C different colours appear, changing with composition (Figure 77). As the amount of platinum in the alloy increases, the colour of the heat treated samples change from purple to a rusty, then a peachy colour, and becomes more and more yellow as the composition of  $\text{PtAl}_2$  is approached. While the differences between samples Au61Pt39 to Au43Pt57 are barely visible by eye, the reflectivity changes steadily (Figure 78). The reflectivity curves do not only differ in the position of the minimum, but also the overall reflectivity, which is probably a consequence of the varying roughness of the samples. The exact position of the local minimum was determined by calculating the first derivative of the reflectivity curve and measuring its zero point. When plotting the obtained values against the platinum content (relative to the gold content), a linear shift of the position of the minimum is obtained (Figure 79).

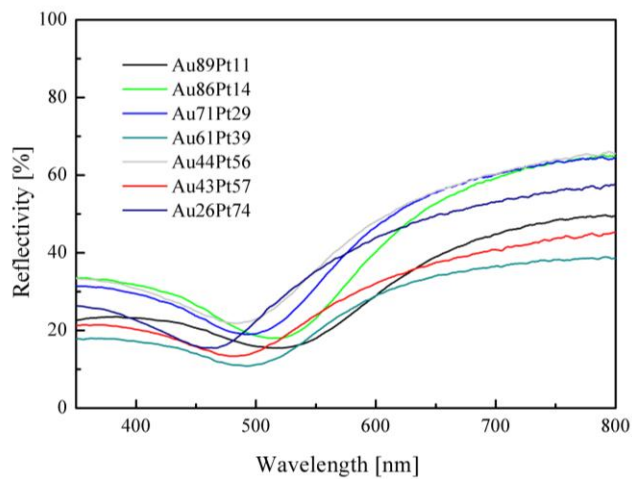


Figure 78: Reflectivity curves of the ternary (Au/Pt) $\text{Al}_x$  alloys.

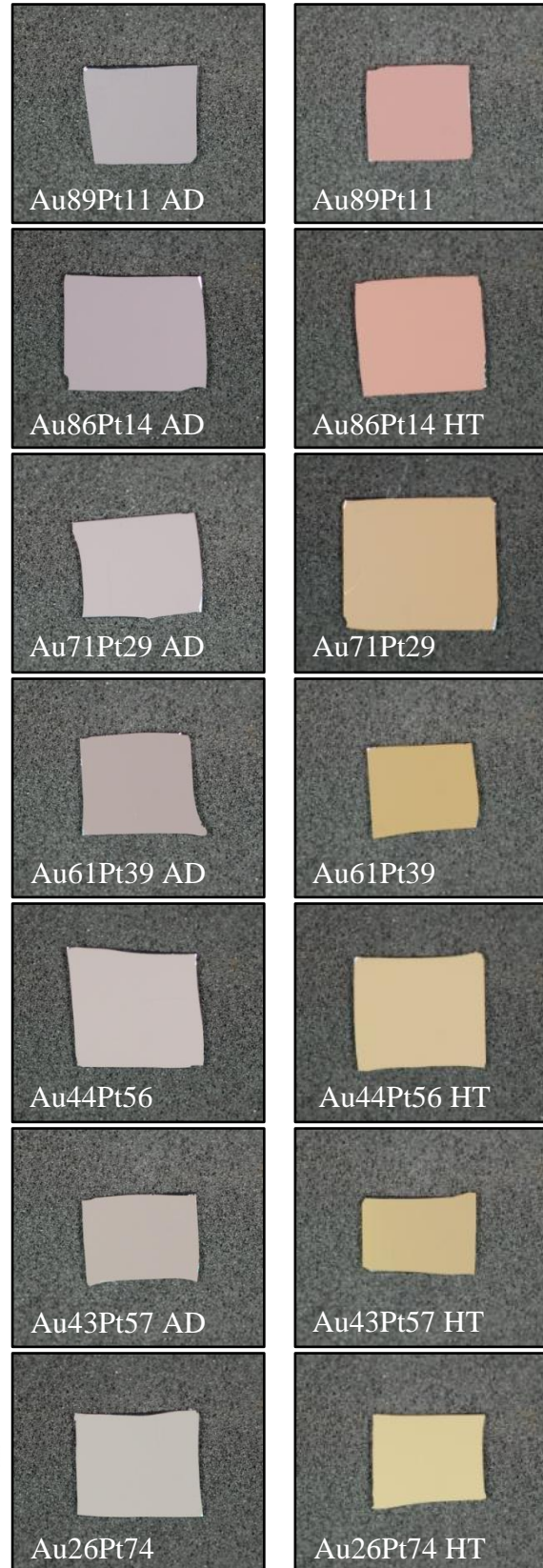


Figure 77: Images of ternary (Au/Pt) $\text{Al}_x$  samples, as-deposited (AD, left) and heat treated (HT, right).

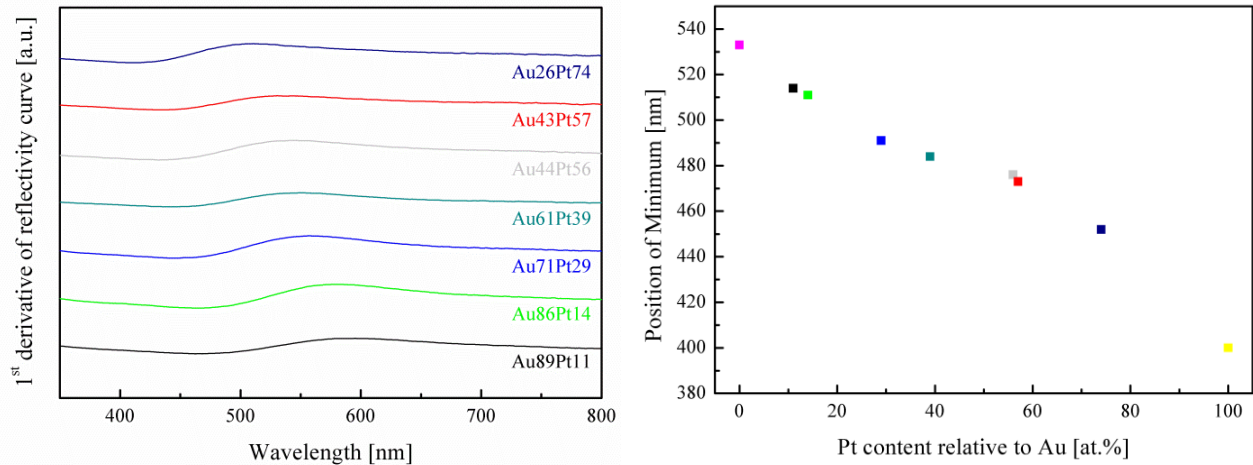


Figure 79: First derivative of the reflectivity curves of the ternary (Au/Pt)Al<sub>2</sub> alloys (left) and the therefrom determined positions of the minima of the reflectivity curves (right).

The colour coordinates of the samples shift along a curved path from the purple of AuAl<sub>2</sub> to the yellow of PtAl<sub>2</sub> (Figure 80), making a prediction of the colour for an alloy with an arbitrary Au to Pt ratio difficult. As was expected from their appearance, some of the alloys lie very close to each other and for a better visibility only a section of the chromaticity diagram is shown. The colour coordinates for all samples are listed in appendix C.

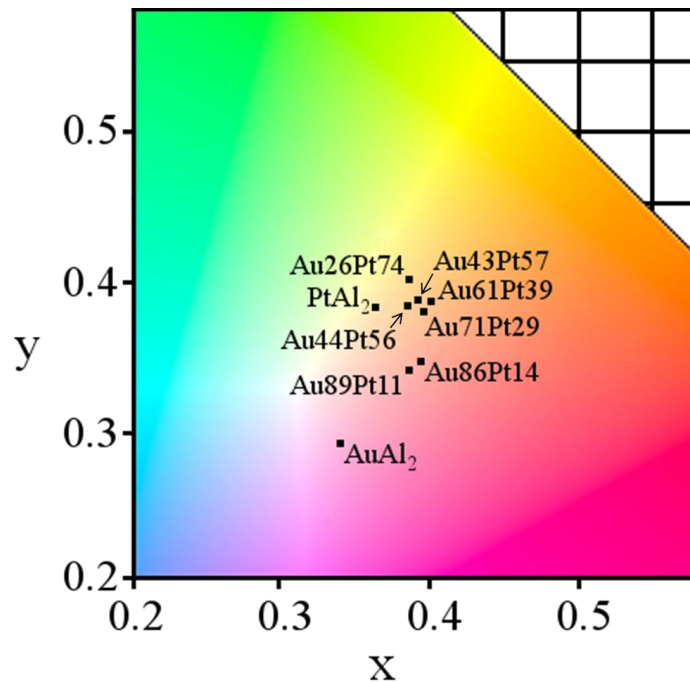


Figure 80: Section of the chromaticity diagram showing the positions of the ternary (Au/Pt)Al<sub>2</sub> samples, along with the coordinates of pure AuAl<sub>2</sub> and PtAl<sub>2</sub>.

## Scanning electron microscopy (SEM)

The surface topography of the ternary samples varies with their composition and the argon pressure that was maintained during the deposition. A low Pt content seems to favour a rather round shape of the grains, as for example in sample Au<sub>89</sub>Pt<sub>11</sub> (Figure 81, left). With an increasing amount of Pt the structure becomes more faceted, as observed in sample Au<sub>43</sub>Pt<sub>57</sub> (Figure 81, right). The grain size is around 50 nm for both examples.

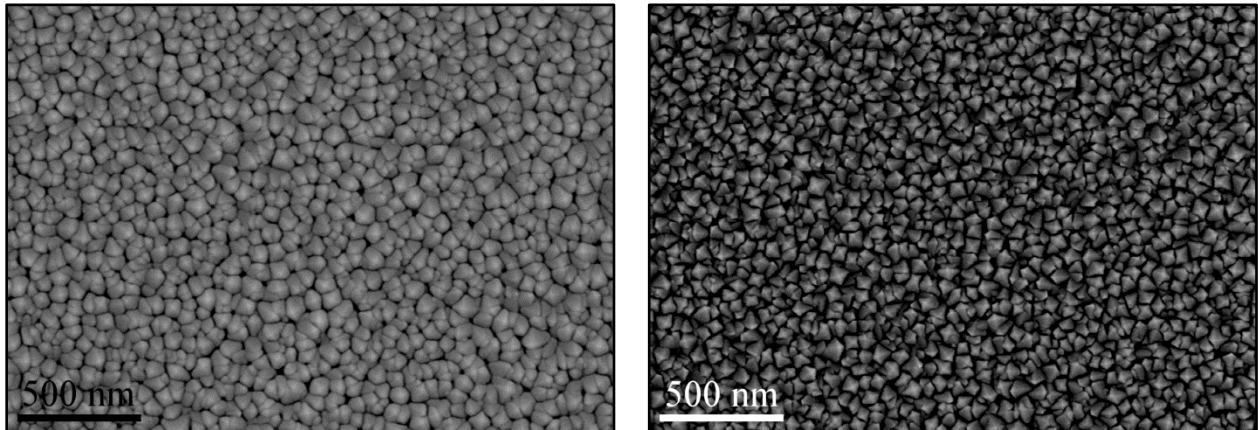


Figure 81: Comparison of the topography of sample Au<sub>89</sub>Pt<sub>11</sub> (left) and sample Au<sub>43</sub>Pt<sub>57</sub> (right). While a low Pt content seems to lead to grains with a round shape, faceted grains are formed when it increases.

A higher argon pressure during the deposition seems to result in grain structures that are more loosely packed than when deposited at lower pressure, as can be observed in the comparison between samples Au<sub>44</sub>Pt<sub>56</sub> and Au<sub>43</sub>Pt<sub>57</sub> in Figure 82. The two samples have nearly the same composition, but were deposited at different argon pressures (5 mTorr and 10 mTorr, respectively).

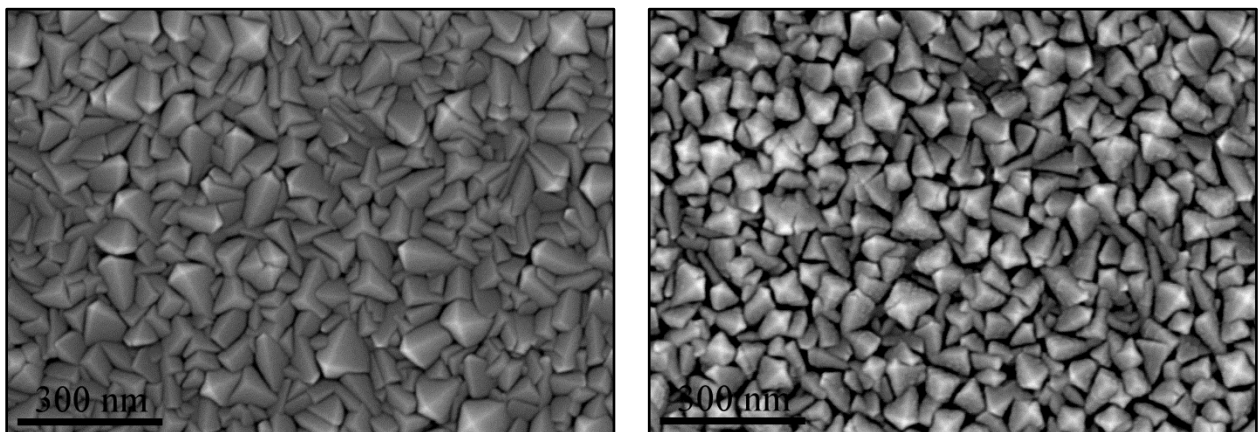


Figure 82: SEM SE images of sample Au<sub>44</sub>Pt<sub>56</sub> (left) and Au<sub>43</sub>Pt<sub>57</sub> (right) in the as-deposited state, with nearly the same composition but deposited at different argon pressures (5 mTorr and 10 mTorr, respectively).

The topography of sample Au26Pt74 looks different from the others, with large, faceted grains that seem to be embedded in a matrix of very fine, globular grains (Figure 83). From images taken with the BSE detector the two different grain shapes seem to have the same composition.

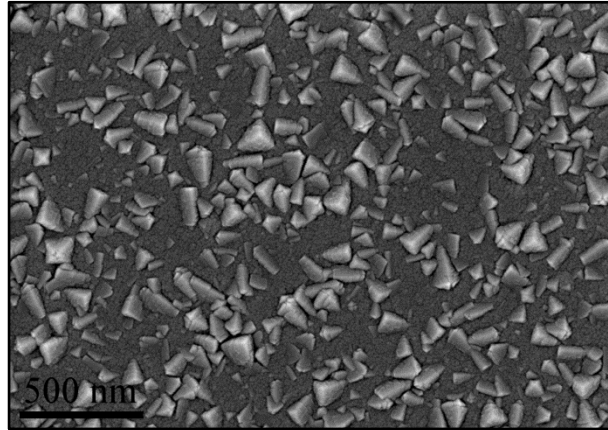


Figure 83: Topography of sample Au26Pt74, where large grains seem to stick out of a matrix of very fine, globular grains.

When viewed with the BSE detector, it becomes obvious that in some samples a second phase is present after the heat treatment, as for example in sample Au86Pt14, shown in Figure 84. EDX measurements reveal that the dark surroundings still have roughly the same composition as the as-deposited sample, with a slight increase in Al content. The bright areas are enriched with Au, in certain places up to nearly 50 at. %, while the Pt is strongly reduced. The composition of the second phase suggests that the monoclinic AuAl phase has precipitated during the heat treatments. Two of the seven samples, namely sample Au86Pt14 and Au71Pt29, were found to be two-phased. The other 5 samples do not display a second phase after the heat treatment for 30 min and were additionally heat treated for 24 h at 350°C, to investigate their stability. No second phases could be observed after the longer heat treatment either. However, the resolution power of the SEM might not be sufficient to image them and other techniques are required to clarify the matter.

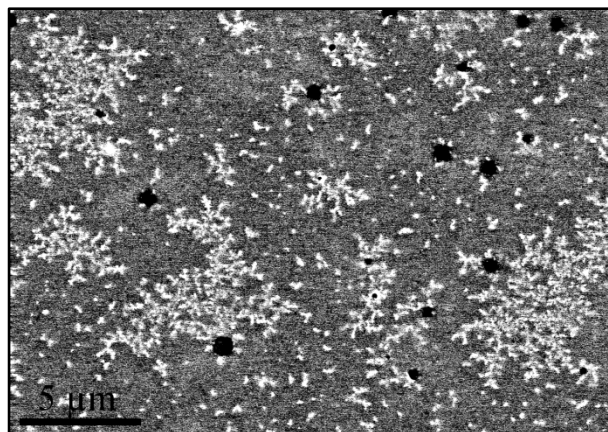


Figure 84: SEM BSE image of sample Au86Pt14 after the heat treatment, clearly revealing that the thin film consists of more than one phase.



## X-Ray diffraction (XRD)

In their as-deposited state, all samples display only reflexes of the fluorite phase (Table 17). The peak position does not exactly match with either the  $\text{AuAl}_2$  or the  $\text{PtAl}_2$  reference, which could be due to different factors: First, sputter-deposited films are normally under a certain amount of internal stress, as was already observed for the binary alloys in the previous section. This stress is due to the production method and can be tensile or compressive, depending on the material, the substrate and the deposition parameters. As a consequence, the lattice parameters change to longer or shorter values. Second, the reference values are derived from bulk material, which is known to have lattice constants different from thin films and third, if a ternary phase is present, its lattice parameters are expected to be somewhere in between the two pure phases.

There is a trend visible, which shows a shift of the measured peak positions, and hence the lattice spacings, from closer to the  $\text{AuAl}_2$  reference towards the  $\text{PtAl}_2$  reference with increasing Pt content of the sample. Figure 85 shows the reduction of the  $d_{200}$  spacing with increasing platinum content for the as-deposited and heat treated samples. Both show a roughly linear dependence. Between the as-deposited and heat treated specimen of the same composition a reduction of the  $d_{200}$  spacing is visible. This is probably due to a change in the stress state during the heat treatment. Again, due to the lack of a reference for thin films, it can only be concluded that the stresses become more tensile, but nothing about their absolute value.

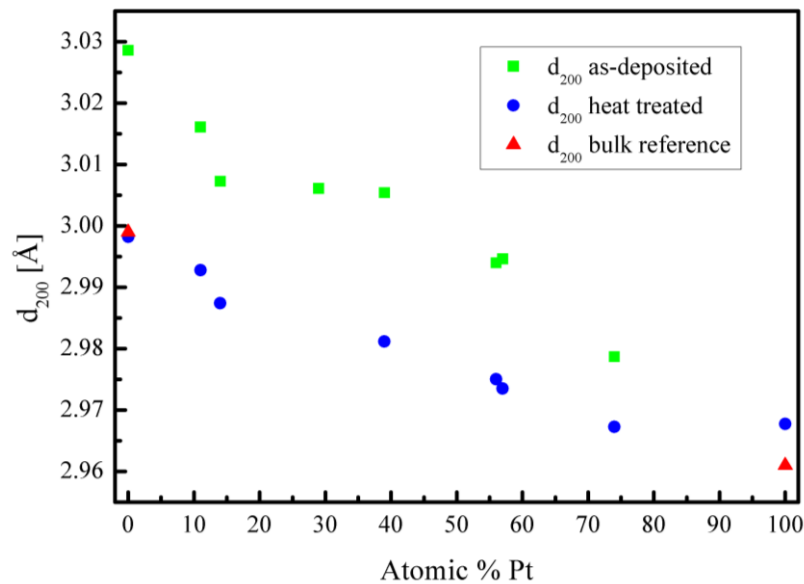


Figure 85: Dependence of the  $d_{200}$  value on the Pt content. A roughly linear progression of the curve is visible for both, the as-deposited and the heat treated samples, indicating that the size of the unit cell approaches the one of  $\text{PtAl}_2$ . The reduction of  $d_{200}$  due to the heat treatments is probably due to a change in the stress state of the samples.

Table 17: Phases found in the different samples in both the as-deposited (AD) and heat treated (HT) state

Sample #	Phases AD	Phases HT
Au89Pt11	fluorite	fluorite, Al or Au, weak AuAl
Au86Pt14	fluorite	fluorite, strong AuAl
Au71Pt29	fluorite	fluorite, strong AuAl, Pt, Al
Au61Pt39	fluorite	fluorite
Au44Pt56	fluorite	fluorite
Au43Pt57	fluorite	fluorite
Au26Pt74	fluorite	fluorite

Some of the heat treated samples display peaks from phases other than the fluorite structure, as listed in Table 17. Figure 86 shows the exemplary XRD spectra in the as-deposited and heat treated state of the Au89Pt11 and Au71Pt39 samples. The heat treated spectrum of sample Au89Pt11 displays a rather strong reflex at  $38^\circ$  which could be the (111) peak of either pure gold or aluminium. From the EDX measurement it is more likely that pure Au is present than Al, however, its occurrence is rather unusual, as the excess amount of gold in the film is only small and should be even more reduced by the formation of the intermetallic AuAl phase. Also in sample Au86Pt14 and Au71Pt29, which are two-phased in the heat treated state, the additional phase is the monoclinic AuAl, as was previously the case in the binary Au-Al samples. Sample Au61Pt39 only shows peaks that belong to the fluorite phase, independent of whether the sample is in the as-deposited or heat treated state.

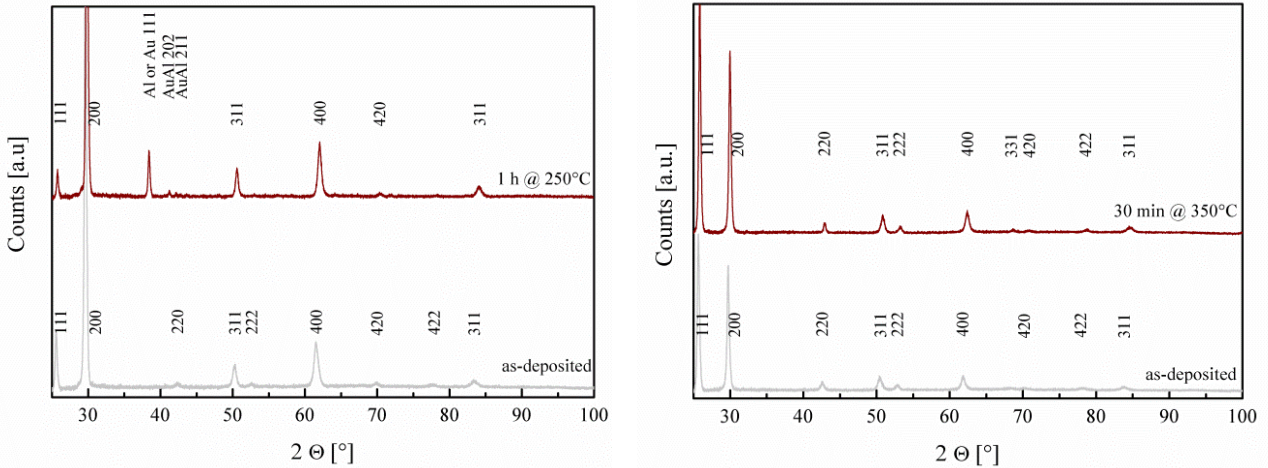


Figure 86: XRD spectra of sample Au89Pt11 (left) and sample Au61Pt39 (right) in the as-deposited and heat treated state. While both samples only display peaks from the fluorite structure in the as-deposited state, in sample Au89Pt11 a strong Al signal and two peaks from the AuAl are measured.

The XRD spectra of sample Au<sub>26</sub>Pt<sub>74</sub> in Figure 87 are different from the others in-so-far as the as-deposited sample shows few sharp, crystalline reflexes superimposed on an amorphous-looking background. After the heat treatment, the sample is fully crystalline, displaying only peaks of the fluorite phase. A similar appearance had been found for the pure PtAl<sub>2</sub> phase, which was fully X-ray amorphous in the as-deposited state. The XRD spectra of the samples not shown here are found in appendix D.

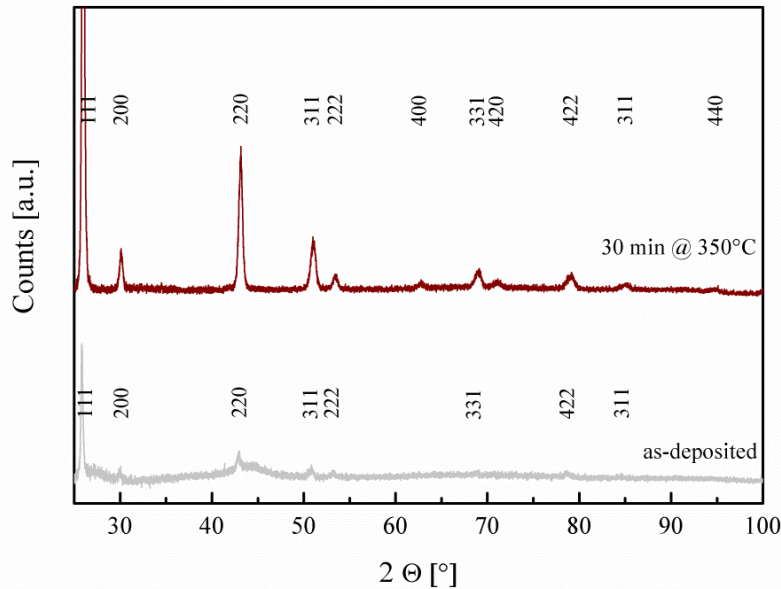


Figure 87: XRD spectra of sample Au<sub>26</sub>Pt<sub>74</sub>. In the as-deposited spectrum (bottom) small crystalline peaks are superimposed on an amorphous-looking background. After the heat treatment (top) the sample is fully crystalline.

### Transmission electron microscopy (TEM)

As is very often the case in sputter-deposited films, the cross-sectional TEM BF images display a columnar grain structure, with rather fine grains at the bottom, which coarsen towards the film surface. Even more clearly than from the topography images in the SEM, differences in the film structures are visible between samples deposited at lower and higher pressure (Figure 88). While the grains in sample Au<sub>44</sub>Pt<sub>56</sub>, sputtered at 5 mTorr are densely packed throughout the whole layer, sample Au<sub>43</sub>Pt<sub>57</sub>, sputtered at 10 mTorr, consists of needle-shaped grains that are dense at the very bottom of the layer, but rather loosely packed further up. A higher argon pressure during the deposition leads to a larger number of collisions of atoms on their way from the target to the substrate. Consequently, they lose energy and thus their mobility after condensation is reduced [93]. Notable is also the serrated shape of the grains in sample Au<sub>43</sub>Pt<sub>57</sub>, which is in contrast to the straight grain boundaries of sample Au<sub>44</sub>Pt<sub>56</sub>. The heat treatment of the dense sample Au<sub>44</sub>Pt<sub>56</sub> leads to a small grain growth that is equal throughout the whole film (Figure 90). In the porous part of sample Au<sub>43</sub>Pt<sub>57</sub> no grain growth is observed, a coarsening of the grains only occurs in the dense bottom layer. It is possible that the elongated pores between the individual grains prevent them from growing.



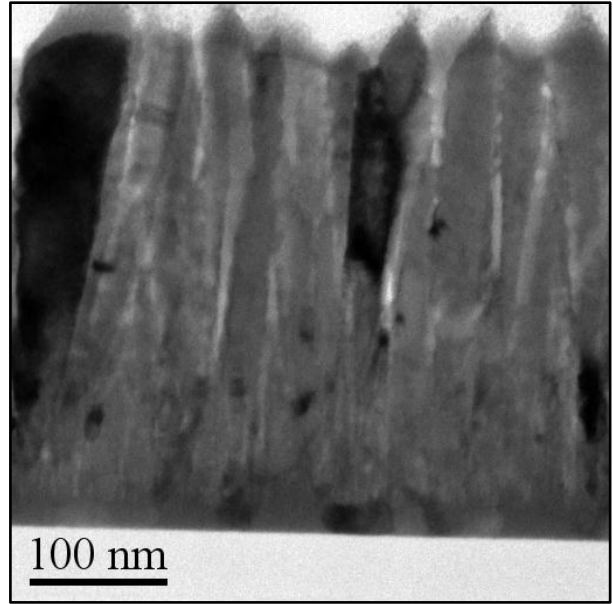
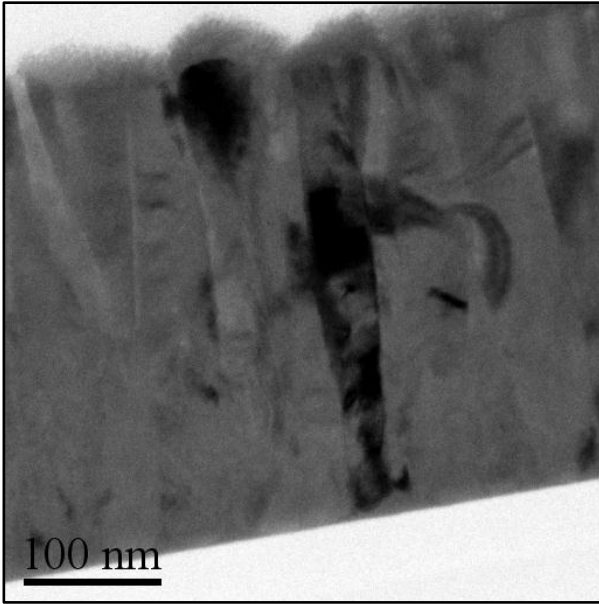


Figure 88: Cross-sectional TEM BF images of samples Au44Pt56 (left) and Au43Pt57 (right) in the as-deposited state. While the grain structure of sample Au44Pt56, sputtered a 5 mTorr argon pressure is very dense, there are elongated voids visible between the grains of sample Au43Pt57, sputtered at 10 mTorr.

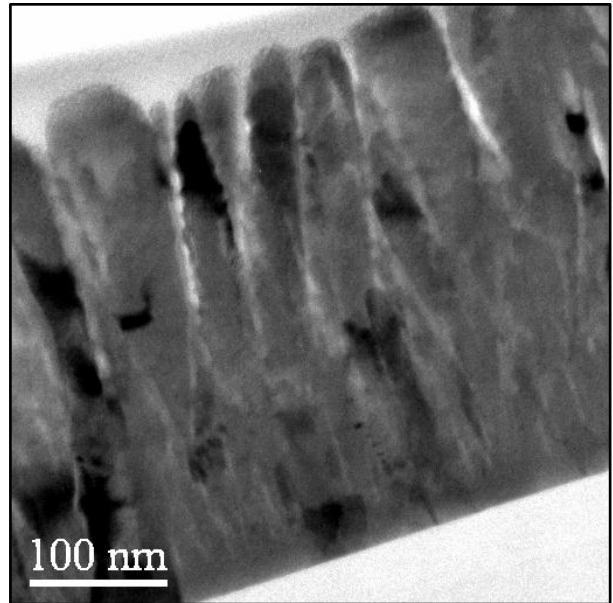
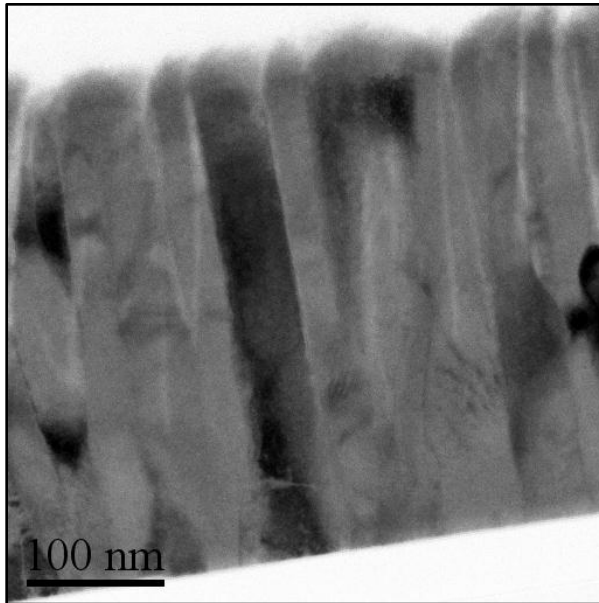


Figure 89: Cross-sectional TEM BF images of samples Au44Pt56 (left) and Au43Pt57 (right) after a heat treatment of 30 min at 350°C. A slight but even grain growth has taken place in the dense sample Au44Pt56, while the voids in sample Au43Pt57 prevented the upper part of the grains from growing.

TEM images of all samples are listed in appendix E and look very similar when deposited at the same pressure, apart from the sample with the highest Pt-content, Au<sub>26</sub>Pt<sub>74</sub>. As was already observed in the pure PtAl<sub>2</sub> sample, it consists of very fine, columnar grains in the as-deposited state, that in some places become rather large towards the surface (Figure 90). After the heat treatment, larger grains have formed but the initial grain structure is still visible as fine, bright lines. The diffraction patterns (Figure 90, inserts) show a similar picture to the XRD results: In the as-deposited state it consists of broad rings with few distinct reflexes, indicating that the main component has a nanocrystalline structure, which surrounds few larger crystallites. This corresponds nicely to the TEM BF images. The diffraction spots as well as the approximate position of the broad rings correspond to the fluorite reference. After the heat treatment the broad rings have disappeared and discrete spots are present, which can as well be attributed to the fluorite phase.

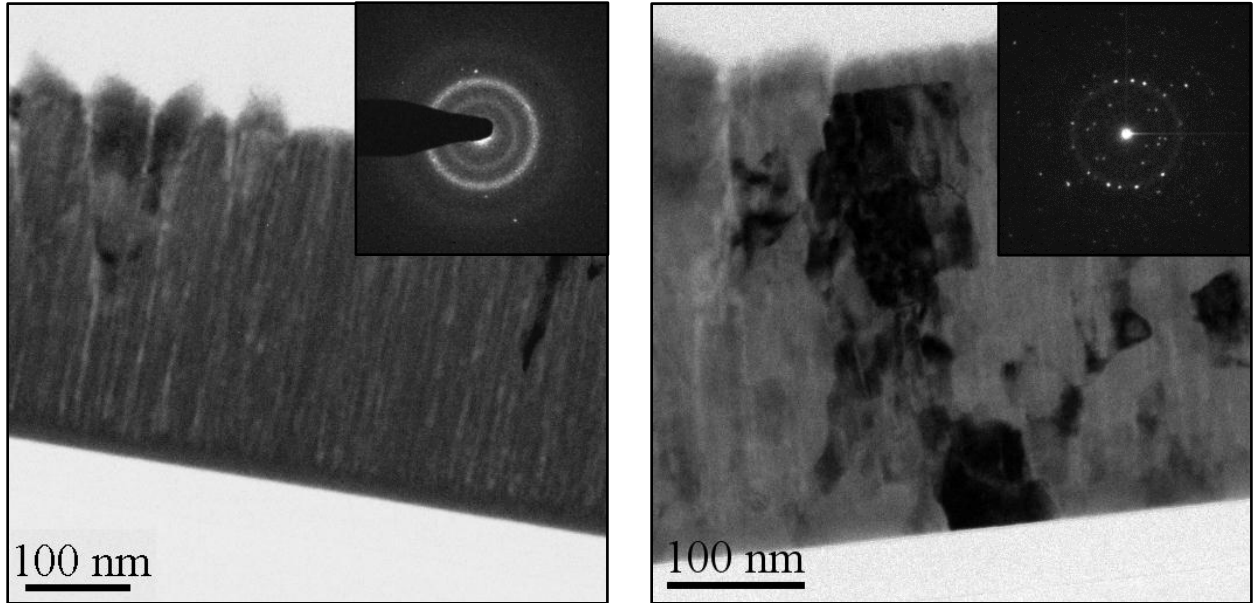


Figure 90: TEM BF images of sample Au<sub>26</sub>Pt<sub>74</sub> in the as-deposited (left) and heat treated state (right). The initially very small grains grow during the heat treatment and the rather broad diffraction rings turn into a distinct pattern.

The diffraction patterns in general confirm the results from the XRD measurements. While the as-deposited samples only have reflexes that belong to the fluorite phase, several partially strong spots from the AuAl phase are found in the heat treated state of samples Au86Pt14 and Au71Pt29 (Figure 91). In sample Au89Pt11 no reflexes of Au or Al were visible. To gain further information about the localised crystal structure, high-resolution images were taken from all samples except sample Au26Pt74 in the as-deposited state. A computer program (Digital Micrograph, Gatan Inc., USA) was used to Fourier-transform the images into diffraction patterns, which could then be used for determination of the crystal structure of single grains. An example, taken from the heat treated sample Au86Pt14, is shown in Figure 92.

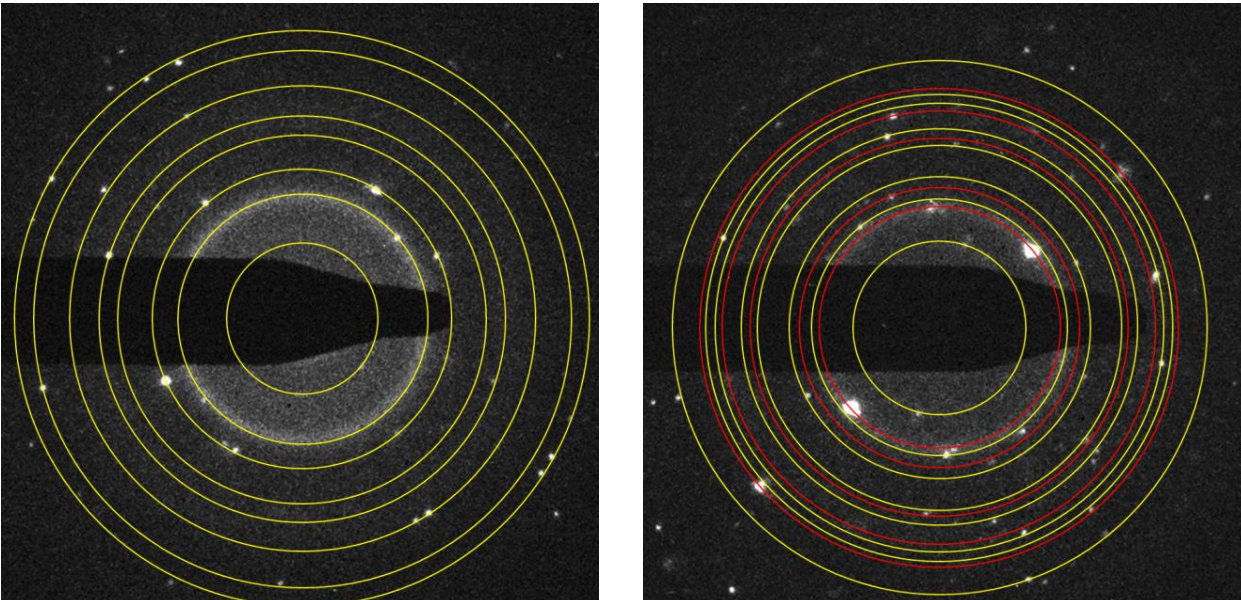


Figure 91: Diffraction patterns of sample Au86Pt14 in the as-deposited (left) and the heat treated state (right). The yellow lines belong to the AuAl<sub>2</sub> phase, the red lines to the AuAl phase.

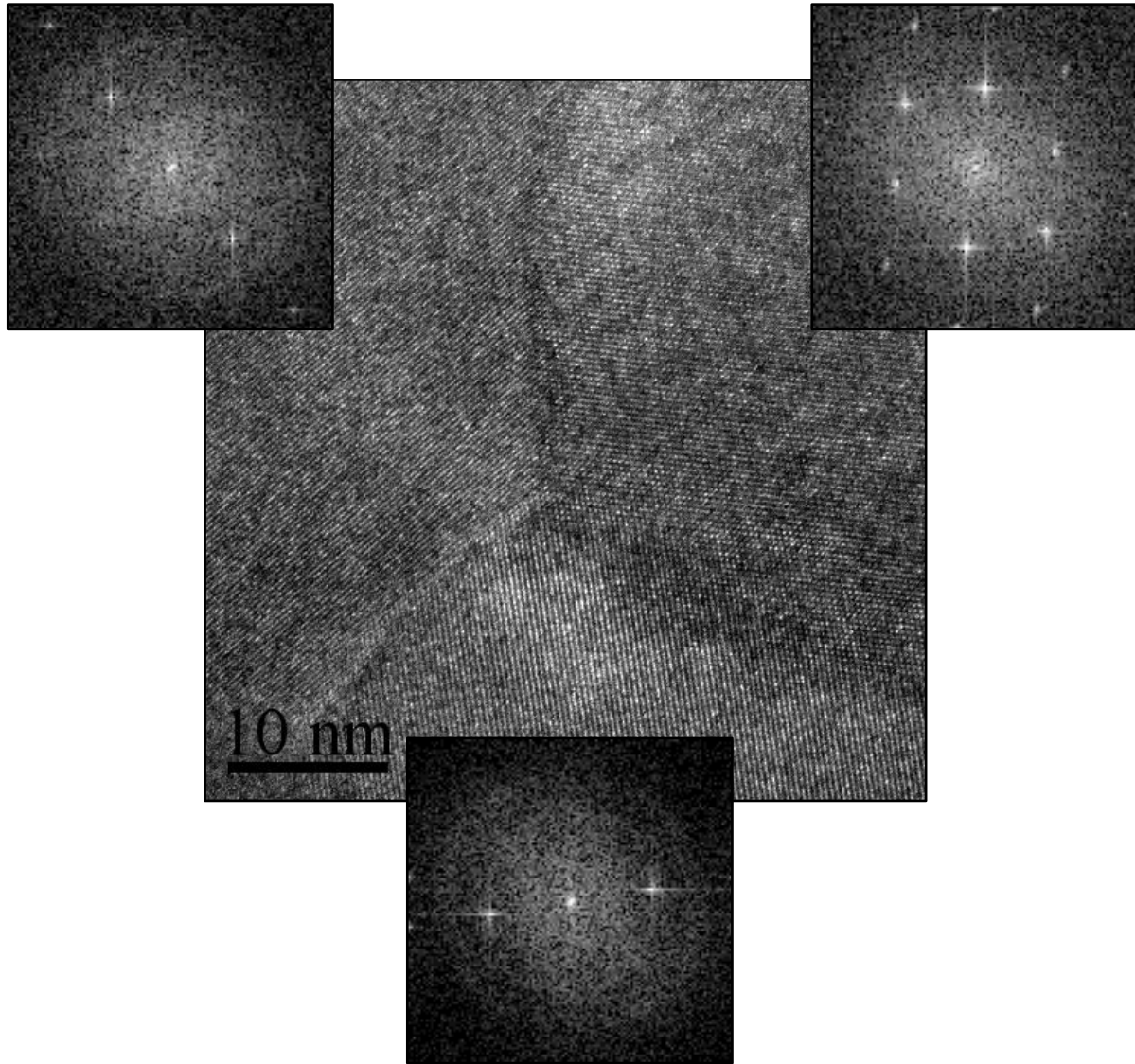


Figure 92: Example of a high-resolution TEM image of sample Au<sub>86</sub>Pt<sub>14</sub> in the heat treated state and the calculated FFT images of the respective grains.

To confirm that the samples in which no second phase was found with either XRD or electron diffraction were really consisting of a single phase, EDX mappings were performed. As an example the results for sample Au<sub>43</sub>Pt<sub>57</sub> are shown in Figure 93, while the maps for the other samples are found in appendix F. The elemental maps of sample Au<sub>89</sub>Pt<sub>11</sub>, where in the XRD measurement a signal of pure Au was found, show that a thin layer of about 50 nm at the bottom of the film is enriched in Au and Pt. This gives a possible explanation why no signal of pure Au or Al was found in the diffraction pattern: to avoid the strong signal of the Si substrate, the patterns were taken from slightly higher up in the film. The maps of samples Au<sub>61</sub>Pt<sub>39</sub>, Au<sub>44</sub>Pt<sub>56</sub>, Au<sub>43</sub>Pt<sub>57</sub> and Au<sub>26</sub>Pt<sub>74</sub> confirmed that the elements in the films are homogeneously distributed, meaning that the layers consist of a single phase.

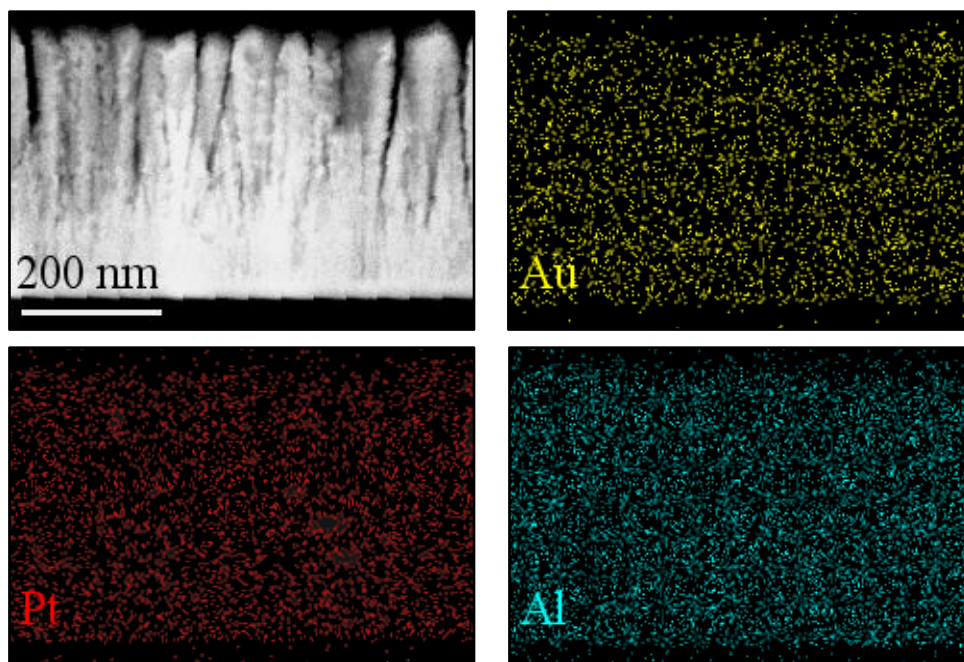


Figure 93: STEM image and EDX maps of sample Au<sub>43</sub>Pt<sub>57</sub> in the heat treated state. The distribution of the three elements Au, Pt and Al seems homogeneous throughout the whole film.

### Discussion

Unsurprisingly, the as-deposited samples of all investigated alloys did not display a colour and required a heat treatment to do so. The mobility of the atoms is expected to be intermediate of the two binary phases, which also explains why sample Au<sub>26</sub>Pt<sub>74</sub>, with the highest Pt content, contains a certain amount of X-ray amorphous phase. Figure 94 shows an interpolation of the melting temperatures of the ternary alloys, assuming  $T_m$  varies linearly with the composition. For the homogeneous samples, this assumption is feasible as the Au and Pt atoms are expected to be distributed ‘solid-solution-like’ within the fluorite lattice spaces. Even for the samples in which a second phase precipitated, the thus calculated values could fit reasonably well, as the matrix still consists of the ternary phase.

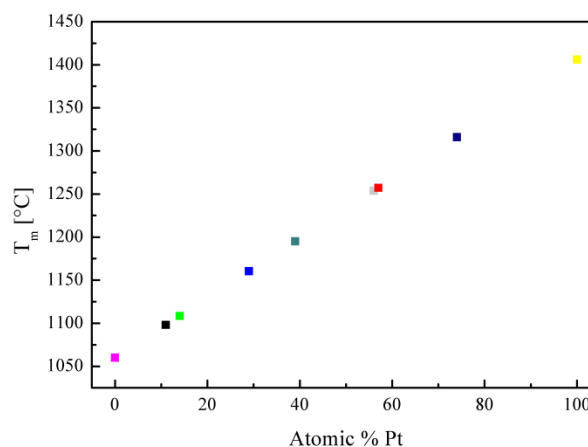


Figure 94: Melting point of the ternary (Au/Pt)Al<sub>2</sub> alloys, assuming  $T_m$  increases linearly with the composition.

The reflectivity, and along with it the colour, of the heat treated ternary (Au/Pt)Al<sub>2</sub> alloys changes smoothly with the modification of the Au:Pt ratio. This could be due to two different reasons: First, a mixture of binary phases is present and the resulting colour is a mixture between the purple of AuAl<sub>2</sub> and PtAl<sub>2</sub>, as was found by Klotz [41] and Fischer-Bühner [39].



Second, ternary phases have formed with the same crystal structure as the two binary phases, and therefore similar band structures. The difference in the number of valence electrons then shifts the position of the Fermi level and thus the onset of interband transitions, which lead to the specific absorption of light of a certain wavelength range. The linear shift of the minimum in the reflectivity curve could be the consequence of either possibility.

XRD measurements show that in certain samples, namely the Au-rich ones, a second phase is present. It is mostly the binary AuAl phase, which is grey, and does not have a large influence on the overall colour, as was seen in the binary AuAl<sub>2</sub> samples. However, the lattice distances of AuAl<sub>2</sub> and PtAl<sub>2</sub> are very similar (0.5997 nm and 0.591 nm, respectively), which means it is possible that two phases are present, but the technique is not sensitive enough to resolve them. However, none of the peaks displays even an indication of a shoulder, which suggests that the samples consist of only one phase. This is supported by the SEM BSE images, which only show a second phase in samples Au86Pt14 and Au71Pt29. No second phase is visible in the images of sample Au89Pt11 despite the presence of a second phase in the XRD spectrum, which could mean that the Au-enriched phase is distributed as an even layer at the interface to the substrate across the whole sample.

TEM results also support that a ternary phase is present – not only in the homogeneous samples, but also the ones where a second phase precipitated. A segregation of the binary AuAl<sub>2</sub> and PtAl<sub>2</sub> phases was not observed in any of the samples.

The microstructure seems to have an influence on the overall reflectivity, as can be seen in Figure 95, where samples Au44Pt56 and Au43Pt57 are directly compared. The shape of the two curves is very similar, sample Au43Pt57 is only slightly shifted towards lower reflectivities. This is due to the rougher surface of the sample, which leads to a more diffuse reflection than the smooth surface of sample Au44Pt56. The observed colour is not affected by the pressure difference, which, after all is only 5 mTorr. Higher differences could lead to significantly different grain structures, possibly even different phases and might therefore have a larger impact on the films and their colour.

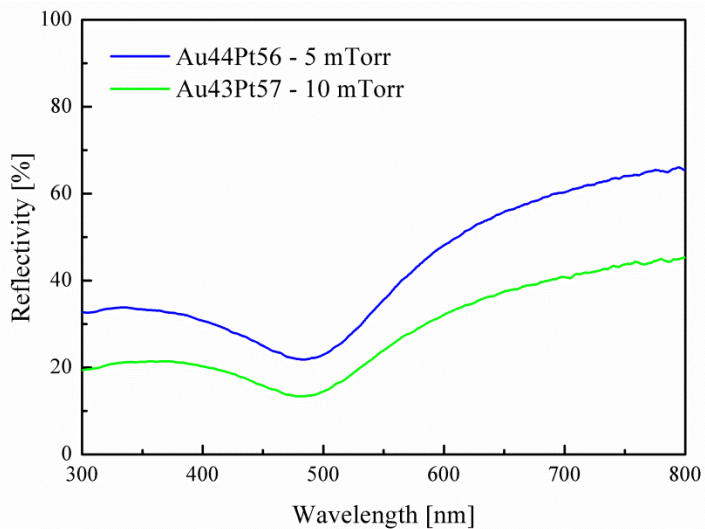


Figure 95: Direct comparison between samples Au44Pt56 and Au43Pt57, which have nearly the same composition but have been sputtered at different pressures (5 mTorr and 10 mTorr).

The production of the intermetallic phases with different techniques could prove to be challenging. When using casting methods, the slow cooling of the melt leads to the formation of thermodynamically stable phases and it has been shown that there is very little solubility of the two intermetallic phases [39, 41]. A different possibility to obtain metastable materials is the quenching of a melt, leading to X-ray amorphous metallic glasses, however no literature has been found on the glass formability of either AuAl<sub>2</sub> or PtAl<sub>2</sub>.

Mechanical properties were not investigated in the course of this thesis, but are assumed to be rather poor. The binary phases have a very high hardness (2.55 GPa for AuAl<sub>2</sub> [41] and 8.74 GPa for PtAl<sub>2</sub> [87]), which comes hand in hand with a high brittleness. The ternary alloys are expected to have a comparable, if not higher hardness. For an application as thin film emphasis should be put on the formation of dense layers by keeping the deposition pressure low or possibly heating the substrate during the deposition. For the latter approach, care would have to be taken to work in very good vacuum, as a trial deposition of AuAl<sub>2</sub> at elevated temperatures (300°C) led to a strong oxidation of the aluminium in the film, despite an initial chamber pressure of below 10<sup>-6</sup> mTorr (10<sup>-7</sup> Pa).

In conclusion, it was possible to produce ternary phases consisting of Au, Pt and Al, with a constant Al ratio of approximately 66.6 at.% and varying amounts of Au and Pt. The fluorite crystal structure of the binary intermetallic phases is maintained with lattice parameters that lie in between the two binaries. The colour of the phases can be shifted between the purple of pure AuAl<sub>2</sub> and the yellow of PtAl<sub>2</sub> by simply adjusting the ratio of Au to Pt.





## 5. Final discussion and conclusions

The optical properties of thin metal layers produced by means of magnetron sputter deposition were investigated. One of the aims was to determine a critical film thickness, which was defined as the thickness at which the optical properties correspond to those of the respective bulk material. Different materials were investigated and a correlation between the electron density of the material and the critical film thickness was established.

Furthermore, different alloys which are known to display special colours as bulk materials were investigated as thin films, at layer thicknesses well above the critical value. It became clear that the upscaling of alloys developed as sputter-deposited thin films to bulk presents certain difficulties. Depending on the material, the properties are affected to varying degrees, and not all properties are influenced to the same extent.

The optical properties seem to be the ones which are easiest to coincide with the bulk properties, provided the critical film thickness has been reached and the roughness of the film is not too high. Some materials require a heat treatment to reduce the amount of defects in the structure, but subsequently easily obtain the same reflectivity as the bulk material. When the mobility of the atoms during the deposition is high enough, as for example in the solid solutions of Au and Ag, optical bulk properties can even be present directly after the deposition.

In contrast, the electrical properties, such as the resistivity, are not only rather different in the as-deposited state of the films, but deviate from the bulk properties even after extended heat treatments. The influence of grain boundaries, surface and interfaces which interfere with the motion of the conduction electrons is too high. Heat treatments can only alter this to a certain degree. Exceptions are again the Au-Ag alloys, which have values that are reasonably close to the bulk references. The grain sizes of those alloys are larger than those obtained in any of the intermetallic phases; the reason for it is again the higher mobility of the atoms.

Mechanical properties were not investigated in the presented work. However, from literature it is known that the strength of pure metals increases as the grains become smaller [94]. This is due to the constrained motion of dislocations due to the small grain size (*Hall-Petch effect*), the usually high dislocation density, and possible oxide layers on the surface that confine the dislocations. In intermetallic phases, which are conventionally very brittle, the reduction of the grain size can enhance the ductility by increasing the probability of grain boundary sliding [95]. However, this theory applies to microstructures with globular grains and probably has only limited validity with respect to sputter-deposited films, which normally have columnar grain structures.

The predominant factor determining size effects of materials in small dimensions appears to be the species of imperfections with the smallest length scale. Different properties display varying sensitivities towards them. Compared with other characteristics, the optical properties of a material appear to be rather insensitive and disturbances of the crystal lattice need to be very

closely spaced for them to be influenced. In terms of alloy development with the focus on colour, this is of course very favourable. Nevertheless, for an application as bulk materials, not only the optical, but also the mechanical properties need to be at an acceptable level and for this second requirement the upscaling from thin films could prove to be more difficult.

The successful production of ternary intermetallic (Au/Pt)Al<sub>2</sub> phases was accomplished, which displayed varying colours between the purple of AuAl<sub>2</sub> and the yellow of PtAl<sub>2</sub>, depending on their Au to Pt ratio. While the stability of the phases appeared persistent during the investigated time and temperature scales, they are clearly not in an equilibrium state. It is assumed that the further away from equilibrium state a thin film is, the more difficult the upscaling to larger dimension will turn out to be. As has been tried in different experiments, the cast production of the ternary phases is not possible [39, 41].

From the experiments carried out during the course of this thesis, the following conclusions can be made:

- Sputter deposition is a useful tool for the production of numerous different samples with a low material consumption. Especially when dealing with precious metals, this reduces the production costs drastically.
- The film thickness at which a material obtains its optical properties that are equal to the bulk is material dependent and connected with the density of conduction electrons.
- The mobility of the atoms during the deposition also determines the grain size and defect density in the produced film, which in turn influence the formation of the band structure and the display of colour.
- Heat treatments annihilate the microstructure defects to an extent that the optical properties correspond to the bulk material; however the electrical properties remain influenced by grain boundaries and surfaces. As the film thickness often governs the lateral size of the grains, an extension of the heat treatment probably might not be able to lead to the same properties as the bulk materials either.
- It is possible to produce ternary (Au/Pt)Al<sub>2</sub> phases by means of magnetron sputter deposition. Their colour can be shifted from the purple AuAl<sub>2</sub> to the yellow PtAl<sub>2</sub> and is linearly dependent on the composition.

For the upscaling of the optical properties from thin films to bulk materials certain factors need to be considered.

- Is the thickness of the film higher than the critical value and thus do the optical properties correspond to the bulk material?
- For gradient samples: Is the surface roughness small enough to prevent additional colour effects due to the interference of light at regular structures in the same size-range?

The low atom mobility during deposition can lead to issues with intermetallic phases or metals with a high melting point, such as refractory metals.

- Does the microstructure contain an excessive amount of defects that could intervene with the formation of a band structure and the display of colour?
- Are the produced materials in a state that is close to equilibrium and therefore allow a production with conventional methods?

If these points are taken account for, magnetron sputter deposition can be employed as valuable tool for the alloy development of bulk metals, at only small material effort.



## 6. Outlook

### 6.1 Layer thickness dependence of colour

To be able to exactly determine the critical thickness of a material, two experimental factors would have to be improved: First, the light source used for the determination of the transparency needs to be clearly defined. For instance, a UV/Vis photo spectrometer with the option of transmission measurements could be used. Second, the amount of investigated film thicknesses needs to be increased. The performed measurements are an indication in which thickness range the critical values lie and can be used as a basis for further experiments.

For the investigation of alloys at very small film thicknesses, an alloy target could be used for the deposition to avoid a separation of elements even at very low sputter times. However, the preferential sputtering of one element compared to the other might affect the exact composition of the film and would have to be accounted for.

### 6.2 Colours due to electronic band structures

The production of the ternary (Au/Pt)Al<sub>2</sub> phases by conventional casting techniques is not feasible, as the thus manufactured materials are much closer to an equilibrium state than the sputter-deposited ones. Other techniques could be employed, which also result in materials that are similarly far from equilibrium, for example techniques that are used in the production of metallic glasses, such as splat quenching or melt spinning.

The colour of the produced (Au/Pt)Al<sub>2</sub> alloys allows a shifting of the colour between the purple of AuAl<sub>2</sub> and the yellow of PtAl<sub>2</sub>. The minimum in the reflection curve moves from  $\approx 530$  nm (2.3 eV) in the purple to  $\approx 400$  nm (3.1 eV) in the yellow phase. Colours that lay outside this range are not available and for their production different materials would be required.

To create a metal with for example a green shade of colour, the reflectivity around 530 nm would have to be rather high and at all other wavelengths rather low, as shown in the schematic of Figure 96. Hence, a band structure with a pseudo-gap around that energy range would result in a green colour. To ensure that the reflectivity at the low-energy end of the spectrum remains low, the interband transitions would have to set in at energies that are in the infrared range of the spectrum, where generally the reflection is governed by the intraband transitions of the conduction electrons. Refractory metals, such as Ta would fulfil this requirement but the production of a pseudo-gap at the correct energy could prove to be challenging.

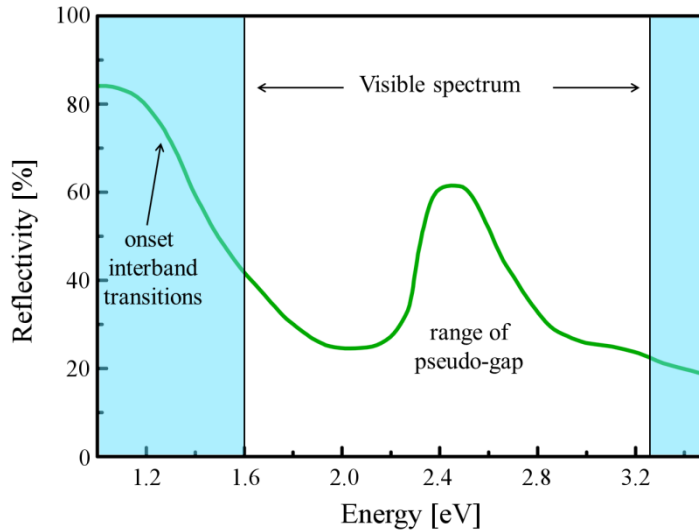


Figure 96: Hypothetical reflectivity curve of a green metal. The interband transitions would have to set in at energies in the infrared part of the spectrum to ensure the reflectivity is already low at the low-energy end of the visible spectrum. A pseudo-gap in the density of states around 2.33 eV (530 nm) would lead to the increase of the reflectivity over the range of green wavelengths.

A different approach to obtain a specific colour is a two-phased microstructure. By subtractive mixing of two components with different colours, a third one is produced. This is the mechanism by which the samples in the work of Klotz *et al.* [41] and Fischer-Bühner *et al.* [39]

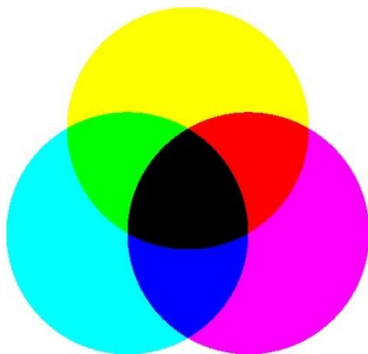


Figure 97: Subtractive colour mixing using the primary colours cyan, magenta and yellow.

obtained their colours. The alloys consisted of a mixture of purple  $\text{AuAl}_2$  and blue  $\text{AuIn}_2$  phases and displayed intermediate colours, depending on the relative phase content. Subtractive colour mixing is based on the primary colours cyan, magenta and yellow. Based on those three, theoretically any colour can be matched. Starting with the blue colour of  $\text{AuIn}_2$  (which could pass as cyan), the purple of  $\text{AuAl}_2$  (similar to magenta) and the yellow of  $\text{PtAl}_2$  (or possibly Au), all of those primary colours are available and in theory a mixture of those phases could produce any desired colour. To obtain green, an equal amount of  $\text{AuIn}_2$  and  $\text{PtAl}_2$  phase would be required to coexist in a mixture,

with the size of the individual phases too small to be resolved by the human eye. While the casting of such a material could be difficult due to the formation of ternary or binary phases that do not display the desired colour, the powder-metallurgical preparation could be feasible, as the two phases have very little solubility within each other.

The field of colour research in metals is not only highly interesting; it is also far from being exhausted. The correlation between a crystal structure, its electron density and the resulting band structure which decides what electron transitions are possible requires further effort but might enable the exact tailoring of optical properties in metals. In addition to the design of coloured alloys and intermetallic phases, the mechanical properties of the materials are a challenging topic that will require ample research. While the development might take some time, it is possible to imagine that at some point in the future gold is not only famous in its yellow, red and white version, but available in blue, green or black colours.





## 7. References

- [1] Campbell NA, Reece JB. *Biology*. San Francisco: Benjamin Cummings, 2002.
- [2] Nassau K. *The Physics and Chemistry of Color*: John Wiley & Sons, Inc., 2001.
- [3] Finger E. *Naturwissenschaften* 1995;**82**:570.
- [4] Ashcroft NW, Mermin ND. *Solid State Physics*: Thomson Learning, Inc., 1976.
- [5] Monin J, Boutry G-A. *Physical Review B* 1974;**9**:1309.
- [6] Ehrenreich H. *IEEE Spectrum* 1965;**2**:162.
- [7] Ehrenreich H, Philipp HR, Segall B. *Physical Review* 1963;**132**:1918.
- [8] <http://www.microlabgallery.com/gallery/NewtonsRings.aspx>. Newton's Rings Interference Colors: 17.01.2013.
- [9] Newton I. *Opticks*. London, 1704.
- [10] Evans U. *Journal of the Society of Chemical Industry* 1926;**45**:211.
- [11] Pfaff G, Kniess H, Reynders P. Multilayered interference pigments. Office USPaT: 6,656,259, 2003.
- [12] Parker AR, Martini N. *Optics & Laser Technology* 2006;**38**:315.
- [13] [en.wikipedia.org/wiki/Munsell](http://en.wikipedia.org/wiki/Munsell). Munsell color system: 15.03.2013.
- [14] <http://munsell.com/>. Munsell Color: 27.04.2013.
- [15] *Encyclopaedia Britannica, Inc.*, 1996.
- [16] Guild C. *Philosophical Transactions of the Royal Society A* 1932;**230**:149.
- [17] Wright WD. *Transactions of the Optical Society* 1929;**30**:141.
- [18] [http://en.wikipedia.org/wiki/CIE\\_1931\\_color\\_space](http://en.wikipedia.org/wiki/CIE_1931_color_space). CIE 1931 color space: 15.03.2013.
- [19] Bouma PJ. *Physical Aspects of Colour*. Eindhoven: Philips, 1971.
- [20] CIE. *Standard Practice for Computing the Colors of Objects by Using the CIE System*: ASTM International E308-06b.
- [21] Pascale D. *A Review of RGB Color Spaces*. The Babel Color Company, 2003.
- [22] [http://www.nma.org/pdf/gold/gold\\_history.pdf](http://www.nma.org/pdf/gold/gold_history.pdf). The History of Gold: 22.01.2013.
- [23] [www.gold.org/about\\_gold/story\\_of\\_gold/heritage](http://www.gold.org/about_gold/story_of_gold/heritage). About gold - Heritage: 22.01.2013.
- [24] <http://oldestcoins.reidgold.com/>. Beginning with the Lydian Lion - World's Oldest Coins: 27.04.2013.
- [25] <http://www.onlygold.com/tutorialpages/historyfs.htm>. A brief history of gold: 22.01.2013.
- [26] Grimwade M. *Introduction to Precious Metals*. Brunswick: Brynmorgen Press, 2009.
- [27] [en.wikipedia.org/wiki/Gold](http://en.wikipedia.org/wiki/Gold). Gold: 22.01.2013.
- [28] Kean WF, Forestier F, Kssam Y, et al. *Seminars in Arthritis and Rheumatism* 1985;**14**:180.
- [29] [www.ediblegold.com/ediblegoldhistory.asp](http://www.ediblegold.com/ediblegoldhistory.asp). Edible Gold and Silver Leaf Facts: 22.01.2013.
- [30] [www.orogoldcosmetics.com/about](http://www.orogoldcosmetics.com/about). Gold benefits: 22.01.2013.
- [31] McDonald AS, Sistare GH. *Gold bulletin* 1978;**11**:66.
- [32] Raynor GV. *Gold Bulletin* 1976;**9**:12.
- [33] Corti CW. Blue, black and purple! The special colours of gold. *International Jewellery Symposium*. St. Petersburg, 2006.
- [34] Bhatia V, Levey F, Kealley C, et al. *Gold Bulletin* 2009;**42**:201.
- [35] Wolff IM, Cortie MB. *Gold Bulletin* 1994;**27**:44.
- [36] Roberts-Austen W. *Proceedings of the Royal Society of London* 1892;**50**:367.
- [37] Hsu L-S, Guo G-Y, Denlinger J, et al. *Journal of Physics and Chemistry of Solids* 2001;**62**:1047.

- [38] Keast VJ, Birt K, Koch CT, et al. Applied Physics Letters 2011;**99**:1.
- [39] Fischer-Bühner J, Basso A, Poliero M. Gold Bulletin 2010;**43**:11.
- [40] Supansomboon S, Maarooof A, Cortie M. Gold Bulletin 2008;**41**:296.
- [41] Klotz U. Gold Bulletin 2010;**43**:4.
- [42] Philipp H. Phys. Stat. Sol (A) 1982;**69**:547.
- [43] Mitterer C, Lenhart H, Mayrhofer P, et al. Intermetallics 2004;**12**:579.
- [44] Steinemann SG, Wolf W, Podloucky R. Colour and Optical Properties. In: Westbrook JH, Fleischer RL, editors. Intermetallic Compounds - Principles and Practice, vol. 3. John Wiley & Sons Ltd, 2002.
- [45] Hsu L-S. Modern Physics Letters B 1993;**8**:1297.
- [46] Richter K. Kolloid-Zeitschrift 1932;**61**:208.
- [47] Kraft O, Gruber PA, Mönig R, et al. Annual Review of Materials Research 2010;**40**:293.
- [48] Fuchs K. Mathematical Proceedings of the Cambridge Philosophical Society 1938;**34**:100.
- [49] Coutts TJ. Thin Solid Films 1970;**7**:77.
- [50] Underwood S, Mulvaney P. Langmuir 1994;**10**:3427.
- [51] Sun Y, Xia Y. Analyst 2003;**128**:686.
- [52] Norrman S, Andersson T, Granqvist CG, et al. Physical Review B 1978;**18**:674.
- [53] Kaiser N. Applied Optics 2002;**41**:3053.
- [54] Borgia C, Scharowsky T, Furrer A, et al. Acta Materialia 2011;**59**:386.
- [55] Keçik D. The optical properties of gold and its alloys: an *ab-initio* approach from DFT to MBPT. Paus-Scherrer-Institute, Materials Science and Simulations. Villingen: École Polytechnic Fédérale de Lausanne, Institute of Materials, 2012.
- [56] Kats MA, Blanchard R, Genevet P, et al. Nature Materials 2012;**12**:1.
- [57] Filmetrics. Refractive Index Database
- [58] Van der Pauw LJ. Philips Research Reports 1958;**13**:1.
- [59] Camacho J, Oliva A. Microelectronics Journal 2005;**36**:555.
- [60] Jan J-P, Pearson W. Philosophical Magazine 1963;**8**:279.
- [61] Hering E, Martin R, Stohrer M. Physik für Ingenieure: Springer, 2002.
- [62] Welzel U, Ligot J, Lamparter P, et al. Journal of Applied Crystallography 2005;**38**:1.
- [63] Sennett RS, Scott GD. Journal of the Optical Society of America 1950;**40**:203.
- [64] Shiraishi T, Hisatsune K, Tanaka Y, et al. Gold Bulletin 2001;**34**:129.
- [65] Yu AY-C, Spicer WE. Physical Review 1968;**171**:834.
- [66] Gils SV, Dimogerontakis T, Buytaer G, et al. Journal of Applied Physics 2005;**98**:1.
- [67] Murr LE. Acta Metallurgica 1973;**21**:791.
- [68] Campisano SU, Foti G, Rimini E, et al. Philosophical Magazine 2006;**31**:903.
- [69] Schulz WW, Allen PB, Trivedi N. Physical Review B 1992;**45**:10886.
- [70] Wessel PR. Physical Review 1963;**132**:2062.
- [71] Okamoto H, Massalski TB. Bulletin of Alloy Phase Diagrams 1983;**4**:30.
- [72] Crisp RS, Rungis J. Philosophical Magazine 1970;**22**:217.
- [73] Iyer VK, Asimow RM. Journal of the less-common metals 1966;**13**:18.
- [74] Dietiker M, Olliges S, Schinhammer M, et al. Acta Materialia 2009;**57**:4009.
- [75] Seita M, Pecnik C, Frank S, et al. Acta Materialia 2010;**58**:6513.
- [76] Jona F. Journal of Physics and Chemistry of Solids 1967;**28**:2155.
- [77] Wu HY, Chen YH, Deng CR, et al. Journal of Alloys and Compounds 2012;**528**:115.
- [78] Thompson C. Annual Review of Materials Science 2000;**30**:159.
- [79] DeSorbo W. Physical Review B 1960;**117**:444.

- [80] Simmons R, Balluffi R. *Physical Review* 1960;**117**:62.
- [81] Simmons R, Balluffi R. *Physical Review* 1960;**117**:52.
- [82] Heinz B, Ziemann P. *Nuclear Instruments and Methods in Physics Research* 1997;**132**:589.
- [83] Schmid A, Ziemann P. *Nuclear Instruments and Methods in Physics Research* 1985;**8**:581.
- [84] Ziemann P, Miehle W, Plewnia A. *Nuclear Instruments and Methods in Physics Research* 1993;**81**:370.
- [85] Swanson M, Parsons J, Hoelke C. *Radiation Effects* 1971;**9**:249.
- [86] Chang Y, Pike L, Liu C, et al. *Intermetallics* 1993;**1**:107.
- [87] Hurly J, Wedepohl PT. *Journal of Materials Science* 1993;**28**:5648.
- [88] Blanpain B, Allen LH, Legresy J-M, et al. *Physical Review B* 1989;**39**:13067.
- [89] Schroers J, Lohwongwatana B, Johnson WL, et al. *Applied Physics Letters* 2005;**87**:1.
- [90] Vishnubhatla SS, Jan J-P. *Philosophical Magazine* 1967;**16**:45.
- [91] Das VD, Kirupavathy S, Damodare L, et al. *Journal of Applied Physics* 1996;**79**:8521.
- [92] Furrer A, Seita M, Spolenak R. *Acta Materialia* 2013;**61**:2874.
- [93] Thornton JA. *Journal of Vacuum Science and Technology A* 1986;**4**:3059.
- [94] Nix WD. *Metallurgical Transactions A* 1988;**20A**:1989.
- [95] Siegel RW, Fougere GE. *Nanostructured Materials* 1995;**6**:205.
- [96] Dietiker M, Buzzi S, Pigozzi G, et al. *Acta Materialia* 2011;**59**:2180.
- [97] Mook WM, Nowak JD, Perrey CR, et al. *Physical Review B* 2007;**75**:1.



## 8. Appendices

### Appendix A - Sputter parameters for the sample production

#### *Chapter 3 - Film thickness dependence of colour*

Sample name	Power [W]	Pressure [mTorr]	Magnetron tilt [°]	Time [min]	Substrate
Au 5	100	5	0	0.2	SiO <sub>2</sub> glass, Si wafer piece, Cu grid
Au 10	100	5	0	0.4	SiO <sub>2</sub> glass, Si wafer piece, Cu grid
Au 50	100	5	0	1.7	SiO <sub>2</sub> glass, Si wafer piece, Cu grid
Au 100	100	5	0	3.5	SiO <sub>2</sub> glass, Si wafer piece
Au 200	100	5	0	6.9	SiO <sub>2</sub> glass, Si wafer piece
Au 300	100	5	0	10.4	SiO <sub>2</sub> glass, Si wafer piece

Sample name	Power [W]	Pressure [mTorr]	Magnetron tilt [°]	Time [min]	Substrate
Al 5	200	5	0	0.4	SiO <sub>2</sub> glass, Si wafer piece, Cu grid
Al 10	200	5	0	0.7	SiO <sub>2</sub> glass, Si wafer piece, Cu grid
Al 50	200	5	0	3.7	SiO <sub>2</sub> glass, Si wafer piece, Cu grid
Al 100	200	5	0	7.4	SiO <sub>2</sub> glass, Si wafer piece
Al 200	200	5	0	14.7	SiO <sub>2</sub> glass, Si wafer piece

Sample name	Power [W]	Pressure [mTorr]	Magnetron tilt [°]	Time [min]	Substrate
Pt 5	50	5	0	0.9	SiO <sub>2</sub> glass, Si wafer piece, Cu grid
Pt 10	50	5	0	1.8	SiO <sub>2</sub> glass, Si wafer piece, Cu grid
Pt 50	50	5	0	8.8	SiO <sub>2</sub> glass, Si wafer piece, Cu grid
Pt 100	50	5	0	17.5	SiO <sub>2</sub> glass, Si wafer piece
Pt 200	50	5	0	35.1	SiO <sub>2</sub> glass, Si wafer piece

Sample name	Power Au [W]	Power Al [W]	Pressure [mTorr]	Magnetron tilt Au [°]	Magnetron tilt Al [°]	Time [min]	Substrate
AuAl <sub>2</sub> 5	47	350	5	3	3	0.1	SiO <sub>2</sub> glass, Si wafer piece, Cu grid
AuAl <sub>2</sub> 10	47	350	5	3	3	0.25	SiO <sub>2</sub> glass, Si wafer piece, Cu grid
AuAl <sub>2</sub> 50	47	350	5	3	3	1.2	SiO <sub>2</sub> glass, Si wafer piece, Cu grid
AuAl <sub>2</sub> 100	47	350	5	3	3	2.3	SiO <sub>2</sub> glass, Si wafer piece
AuAl <sub>2</sub> 200	47	350	5	3	3	4.6	SiO <sub>2</sub> glass, Si wafer piece

*Chapter 4 - Colours due to electronic band structures*

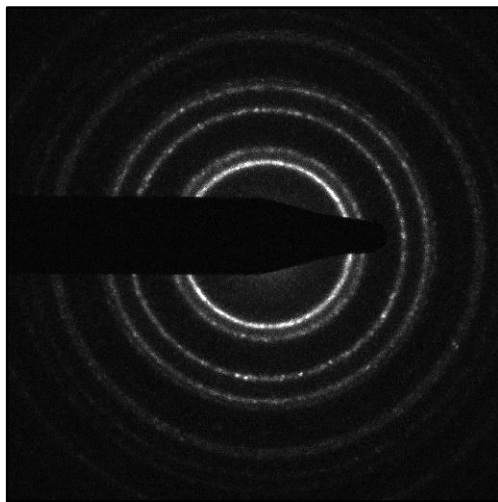
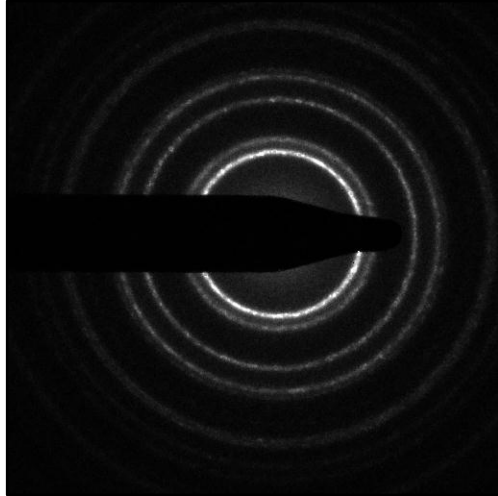
Sample name	Power Au [W]	Power Ag [W]	Pressure [mTorr]	Magnetron tilt Au [°]	Magnetron tilt Ag [°]	Time [min]	Substrate
Au - Ag	240	174	2	0	0	5	Si-SiO <sub>2</sub> -Si <sub>3</sub> N <sub>4</sub> wafer
Au	300	-	2	0	-	15	Si-SiO <sub>2</sub> -Si <sub>3</sub> N <sub>4</sub> wafer
Au <sub>84</sub> Ag <sub>16</sub>	180	39	2	0	0	5	Si-SiO <sub>2</sub> -Si <sub>3</sub> N <sub>4</sub> wafer
Au <sub>55</sub> Ag <sub>45</sub>	112	98	2	0	0	5	Si-SiO <sub>2</sub> -Si <sub>3</sub> N <sub>4</sub> wafer
Au <sub>26</sub> Ag <sub>74</sub>	45	156	2	0	0	5	Si-SiO <sub>2</sub> -Si <sub>3</sub> N <sub>4</sub> wafer
Ag	-	200	5	-	0	5	Si-SiO <sub>2</sub> -Si <sub>3</sub> N <sub>4</sub> wafer

Sample name	Power 1 [W]	Power 2 [W]	Pressure [mTorr]	Magnetron tilt 1 [°]	Magnetron tilt 2 [°]	Time [min]	Substrate
Au-Al gradient	60 (Au)	250 (Al)	2	15 (Au)	0 (Al)	10	Si-SiO <sub>2</sub> -Si <sub>3</sub> N <sub>4</sub> wafer
AuAl <sub>2</sub>	35 (Au)	350 (Al)	5	3 (Au)	3 (Al)	15	Si-SiO <sub>2</sub> -Si <sub>3</sub> N <sub>4</sub> wafer
Pt-Al gradient	200 (Pt)	400 (Al)	2	0 (Pt)	0 (Al)	10	Si-SiO <sub>2</sub> -Si <sub>3</sub> N <sub>4</sub> wafer
PtAl <sub>2</sub>	170 (Pt)	390 (Al)	2	15 (Pt)	5 (Al)	15	Si-SiO <sub>2</sub> -Si <sub>3</sub> N <sub>4</sub> wafer
AuIn <sub>2</sub>	15 (Au)	45 (In)	2	15 (Au)	0 (In)	30	Si-SiO <sub>2</sub> -Si <sub>3</sub> N <sub>4</sub> wafer

Sample name	Power 1 [W]	Power 2 [W]	Power 3 [W]	Pressure [mTorr]	Magnetron tilt 1 [°]	Magnetron tilt 2 [°]	Magnetron tilt 3 [°]	Time [min]	Substrate
	Au	Al	Pt		Au	Al	Pt		
Au89Pt11	80	400	35	5	0	5	10	10	Si-SiO <sub>2</sub> -Si <sub>3</sub> N <sub>4</sub> wafer
Au86Pt14	35	351	30	5	0	5	10	10	Si-SiO <sub>2</sub> -Si <sub>3</sub> N <sub>4</sub> wafer
Au71Pt29	29	351	50	5	0	5	10	10	Si-SiO <sub>2</sub> wafer
Au61Pt39	25	400	50	10	0	5	10	10	Si-SiO <sub>2</sub> wafer
Au44Pt56	19	351	80	5	0	5	10	10	Si-SiO <sub>2</sub> wafer
Au43Pt57	18	400	70	10	0	5	10	10	Si-SiO <sub>2</sub> wafer
Au26Pt74	13	400	85	10	0	5	10	6	Si-SiO <sub>2</sub> wafer

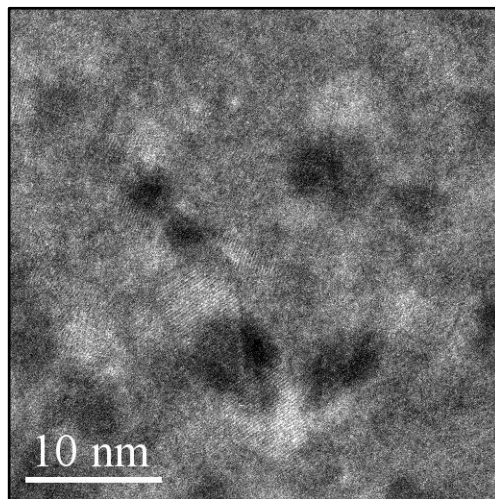
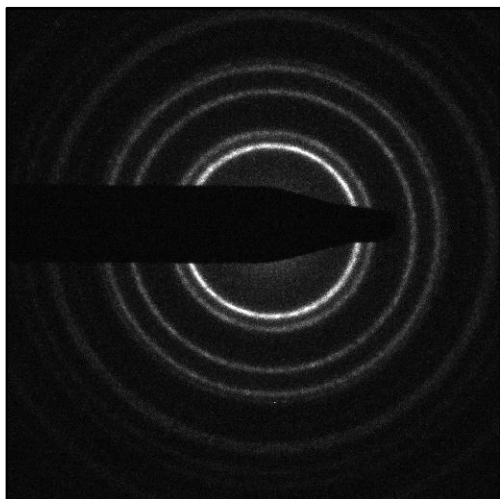
## Appendix B - Diffraction patterns and high resolution images of thin films

Au: Diffraction pattern of a 5 nm (top) and 10 nm thick (bottom) Au layer. The rings become slightly sharper and individual reflexes become visible in the thicker sample.

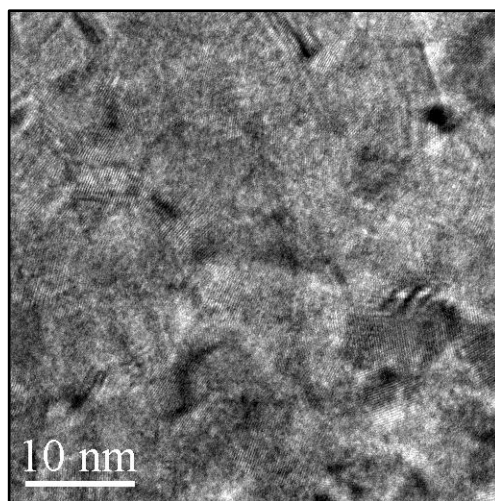




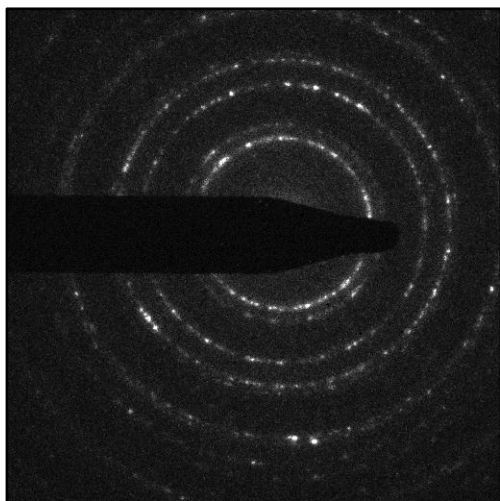
Pt: Diffraction patterns (left) and high resolution images (right) of Pt layers with 5 nm (top), 10 nm (middle) and 50 nm (bottom). The continuous rings, an evidence of very small grains, break up into single spots when the grain size increases with the film thickness.



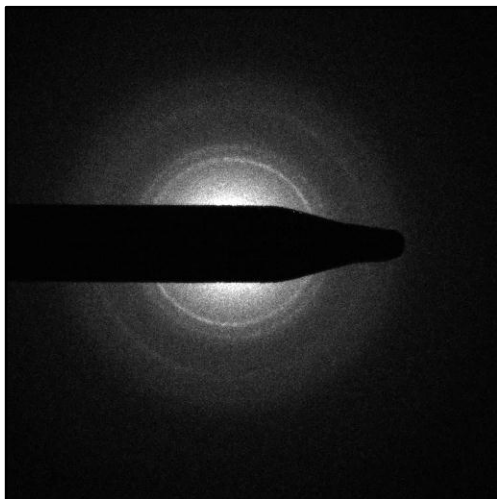
*n.a.*



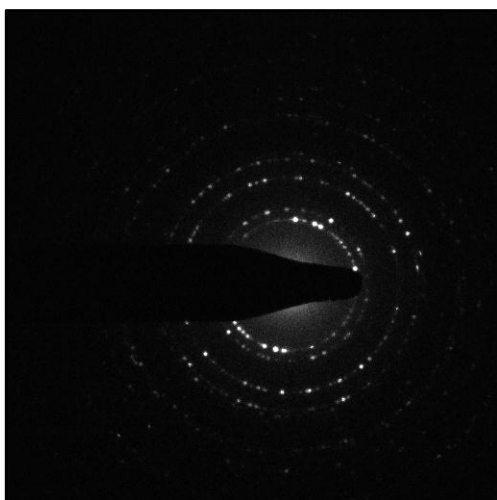
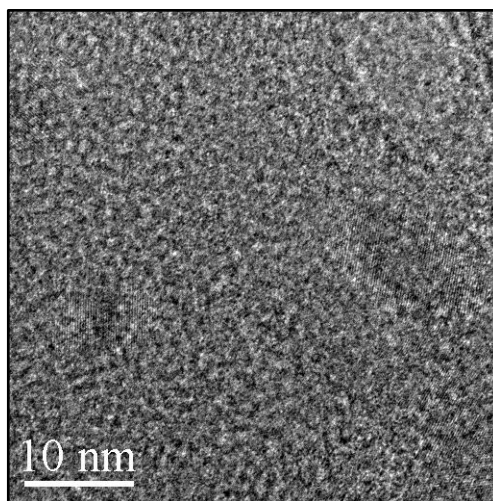
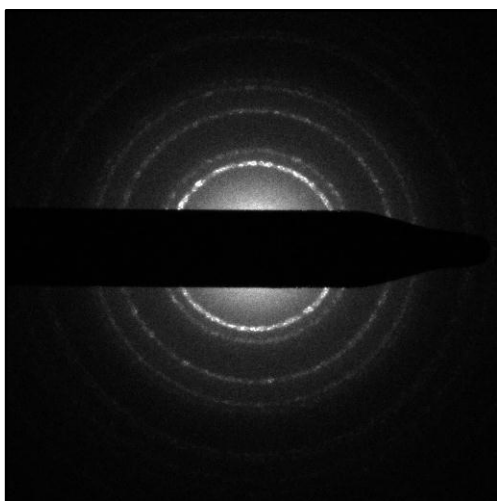
*n.a.*



Al: Diffraction patterns (left) and high resolution images (right) of Al layers with 5 nm (top), 10 nm (middle) and 50 nm (bottom). The initially slightly broadened rings become sharper with increasing film thickness and eventually, in the 50 nm sample are discrete spots (the diffraction pattern of the 50 nm thick sample has been taken with a different camera length).

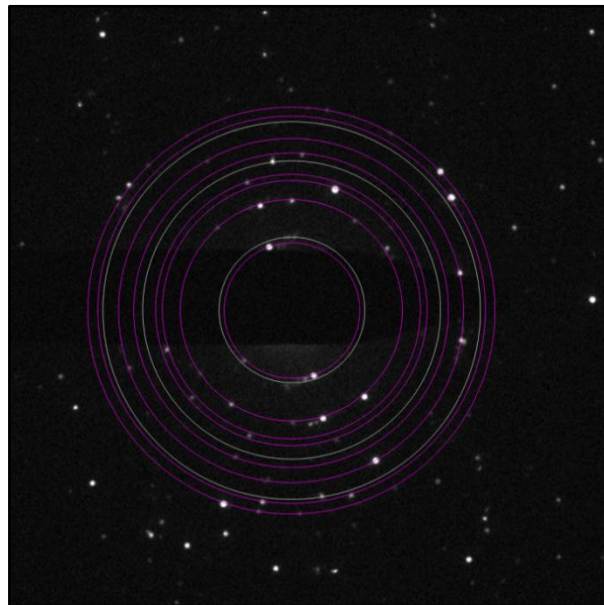
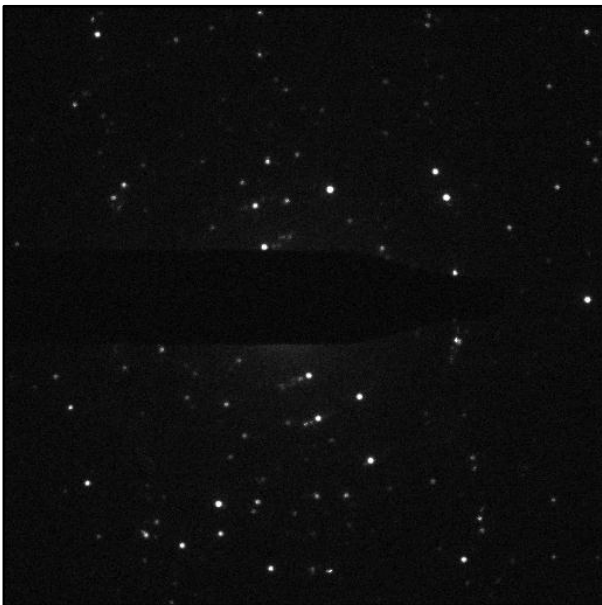


*n.a.*



*n.a.*

AuAl<sub>2</sub>: Diffraction pattern of the heat treated, 10 nm thick AuAl<sub>2</sub> film. In the indexed image (right) the reflexes of the AuAl<sub>2</sub> phase are marked in purple, the ones of the AuAl in grey.



## Appendix C – Calculated colour coordinates

Au-Ag alloys, as-deposited (AD) and heat treated for 5 h at 350°C (HT)

	X	Y	Z	x	y	z	L*	a*	b*
Au	76.46	78.63	39.9	0.39	0.40	0.20	91.07	3.53	41.48
Au84Ag16 AD	77.94	84.19	44.26	0.38	0.41	0.21	93.53	-4.12	40.7
Au84Ag16 HT	76.62	82.56	41.47	0.38	0.41	0.21	92.82	-3.7	42.64
Au55Ag45 AD	83.87	92.03	69.89	0.34	0.37	0.28	96.83	-6.77	22.01
Au55Ag45 HT	81.72	89.87	64.05	0.35	0.38	0.27	95.94	-7.07	25.42
Au23Ag77 AD	89.88	95.04	96.9	0.32	0.34	0.34	98.05	-0.82	4.26
Au23Ag77 HT	88.29	93.54	92.13	0.32	0.34	0.34	97.45	-1.13	6.43
Ag AD	95.05	99.95	108.30	0.31	0.33	0.36	99.98	0.09	0.32

AuAl<sub>3</sub>, heat treatments

	X	Y	Z	x	y	z	L*	a*	b*
as-deposited	34.42	32.59	39.24	0.32	0.31	0.37	63.83	12.32	-4.69
2min at 350°C	33.66	29.17	35.54	0.34	0.3	0.36	60.93	22.15	-5.07
10min at 350°C	29.42	25.19	30.98	0.34	0.29	0.36	57.26	22.44	-5.23
30min at 350°C	29.46	25.11	30.88	0.34	0.29	0.36	57.19	22.94	-5.22
1h at 350°C	30.19	25.55	31.94	0.34	0.29	0.36	57.61	23.88	-5.99
5h at 350°C	32.80	27.80	34.97	0.34	0.29	0.37	59.71	24.40	-6.43

AuAl<sub>3</sub>, irradiations

	X	Y	Z	x	y	z	L*	a*	b*
10 <sup>12</sup> ions/cm <sup>3</sup>	30.96	27.16	33.20	0.34	0.30	0.36	59.12	20.22	-5.10
10 <sup>13</sup> ions/cm <sup>3</sup>	31.01	28.80	33.43	0.33	0.31	0.36	60.61	14.02	-2.84
5*10 <sup>13</sup> ions/cm <sup>3</sup>	33.73	31.48	37.53	0.33	0.31	0.37	62.91	13.84	-4.17
10 <sup>15</sup> ions/cm <sup>3</sup>	28.33	27.33	33.02	0.32	0.31	0.37	59.28	9.52	-4.57
5*10 <sup>15</sup> ions/cm <sup>3</sup>	30.00	30.52	37.88	0.30	0.31	0.38	62.10	3.80	-6.01
5*10 <sup>15</sup> ions/cm <sup>3</sup> + 5h at 350°C	26.08	23.57	31.46	0.32	0.29	0.39	55.65	16.07	-8.68

PtAl<sub>2</sub>, heat treatments

	X	Y	Z	x	y	z	L*	a*	b*
as-deposited	45.77	48.06	50.26	0.32	0.33	0.35	74.86	0.26	2.09
30 min at 300°C	41.73	43.83	45.12	0.32	0.34	0.35	72.12	0.21	2.82
1 h at 300°C	45.92	48.31	50.58	0.32	0.33	0.35	75.02	0.02	2.03
3 h at 300°C	43.40	45.33	39.75	0.34	0.35	0.31	73.11	0.94	10.69
6 h at 300°C	46.21	48.01	34.87	0.36	0.37	0.27	74.83	1.65	19.77
24 h at 300°C	46.95	48.77	32.67	0.37	0.38	0.25	75.31	1.67	23.54
30 min at 350°C	51.32	53.49	35.73	0.37	0.38	0.25	78.16	1.28	24.41

AuIn<sub>2</sub>, heat treatments

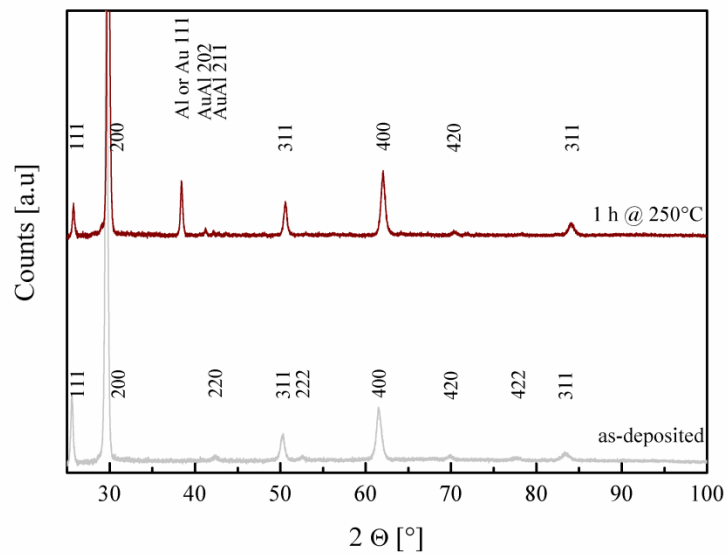
	X	Y	Z	x	y	z	L*	a*	b*
as-deposited	60.99	65.30	78.14	0.30	0.32	0.38	84.64	-2.52	-5.54
30 min at 300°C	59.61	64.28	76.33	0.30	0.32	0.38	84.11	-3.54	-5.06
12 h at 300°C	58.92	63.57	74.39	0.30	0.32	0.38	83.74	-3.58	-4.18

(Au/Pt)Al<sub>2</sub> alloys

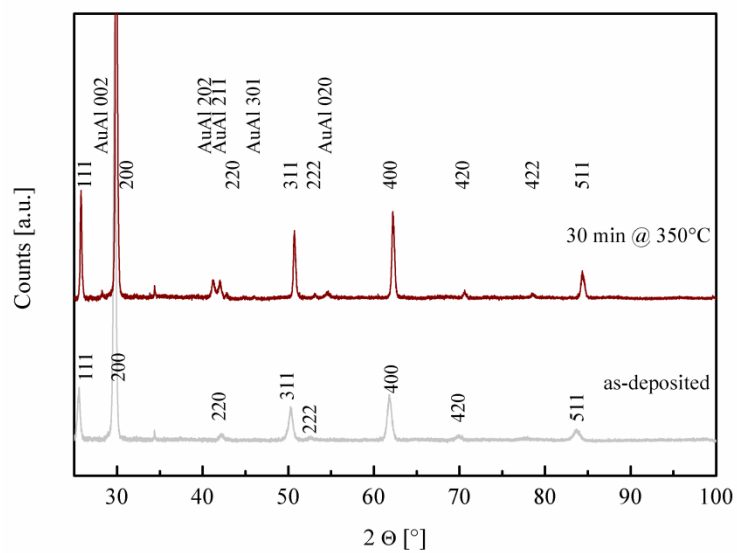
	X	Y	Z	x	y	z	L*	a*	b*
AuAl <sub>2</sub>	30.05	25.26	32.33	0.34	0.29	0.37	57.33	24.54	-6.99
Au89Pt11	27.42	24.34	19.21	0.39	0.34	0.27	56.43	18.21	12.71
Au86Pt14	37.53	33.10	24.50	0.39	0.35	0.26	64.24	20.96	16.70
Au71Pt29	41.23	39.21	23.19	0.40	0.38	0.22	68.90	12.57	26.94
Au61Pt39	25.67	25.00	13.29	0.40	0.39	0.21	57.08	8.22	26.78
Au44Pt56	43.18	42.96	25.70	0.39	0.38	0.23	71.52	7.12	27.30
Au43Pt57	28.71	28.72	16.11	0.39	0.39	0.22	60.54	5.60	26.19
Au26Pt74	38.45	40.01	20.91	0.39	0.40	0.21	69.47	1.37	31.99
PtAl <sub>2</sub>	48.80	50.78	33.60	0.37	0.38	0.25	76.54	1.49	24.41

Appendix D - XRD spectra of ternary alloys

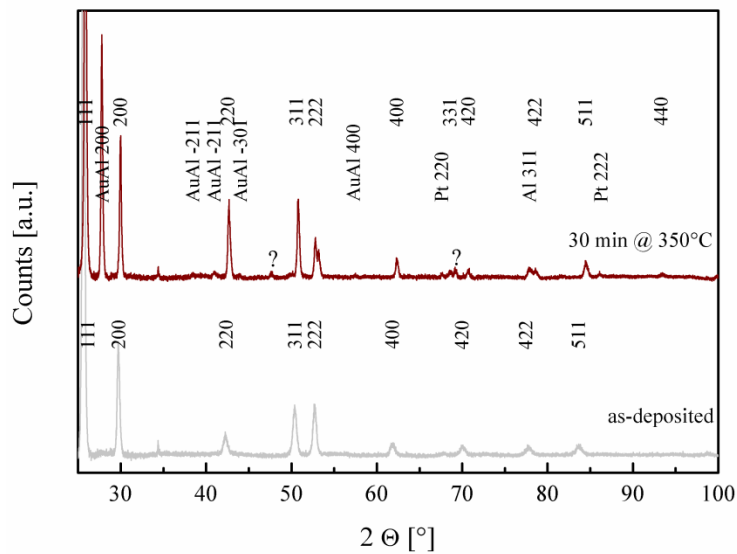
Au89Pt11



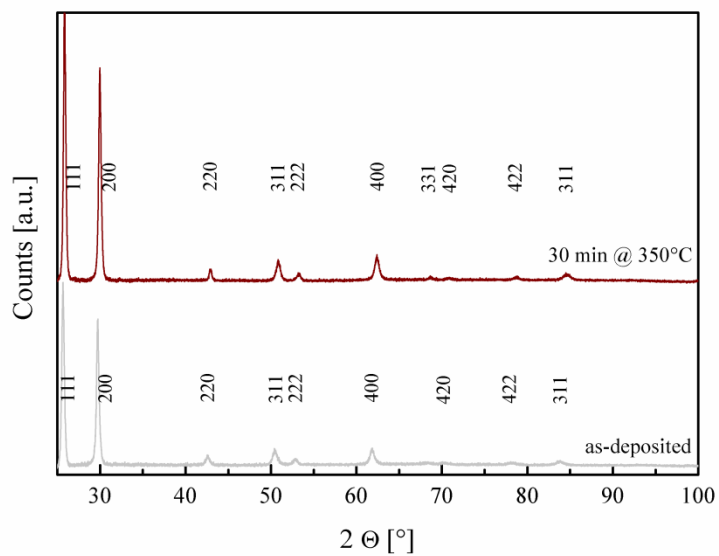
Au86Pt14



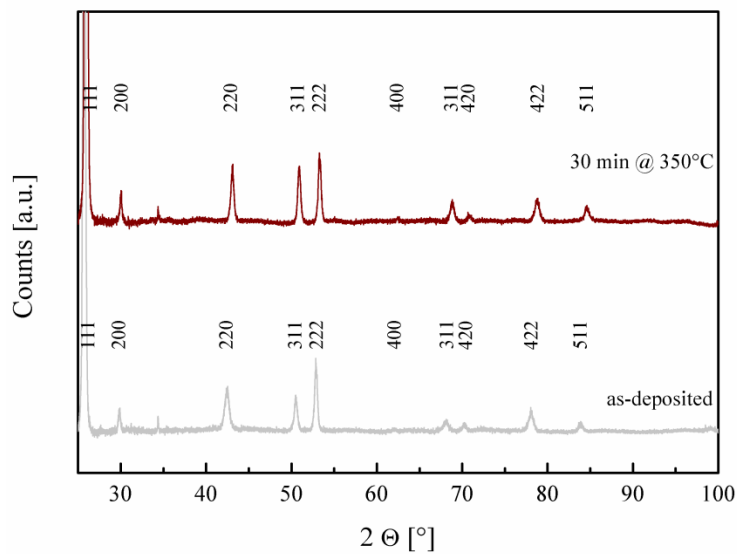
Au71Pt29



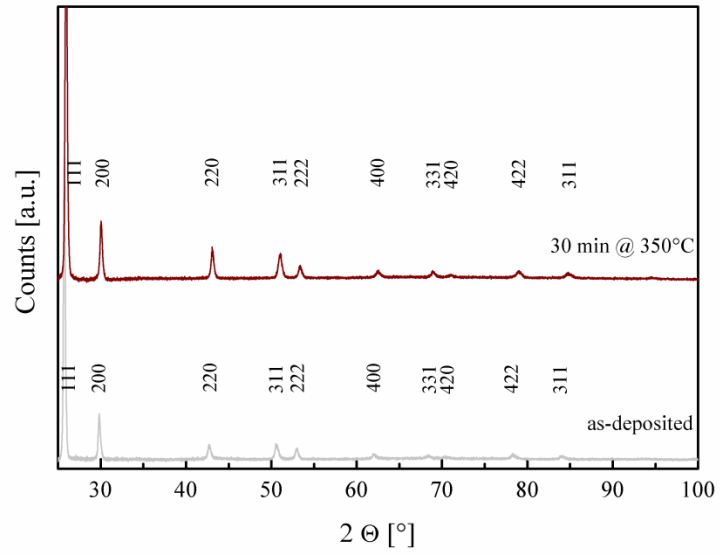
Au61Pt39



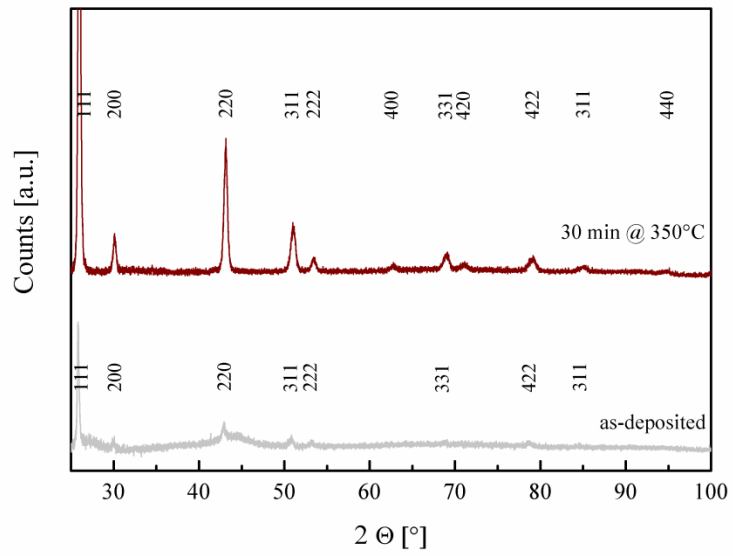
Au44Pt56



Au<sub>43</sub>Pt<sub>57</sub>



Au<sub>26</sub>Pt<sub>74</sub>

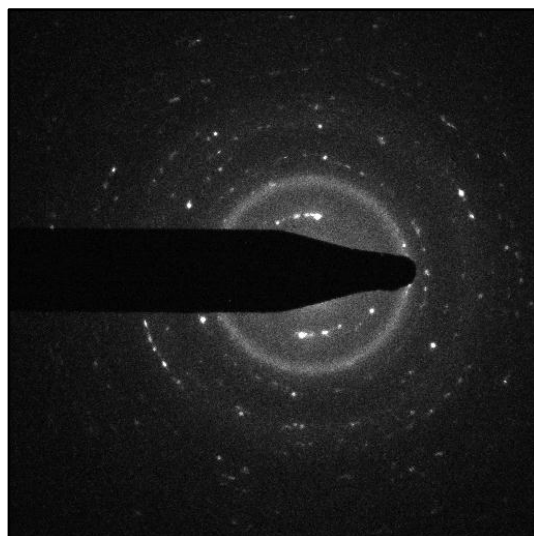
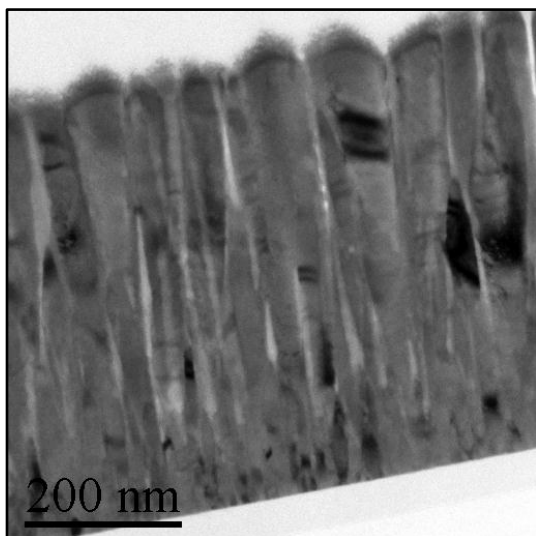




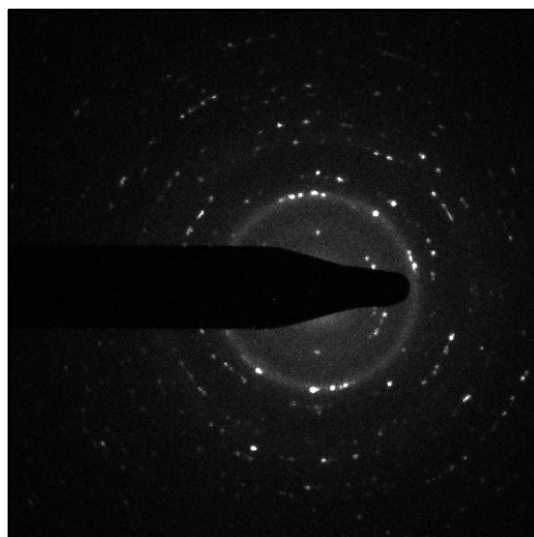
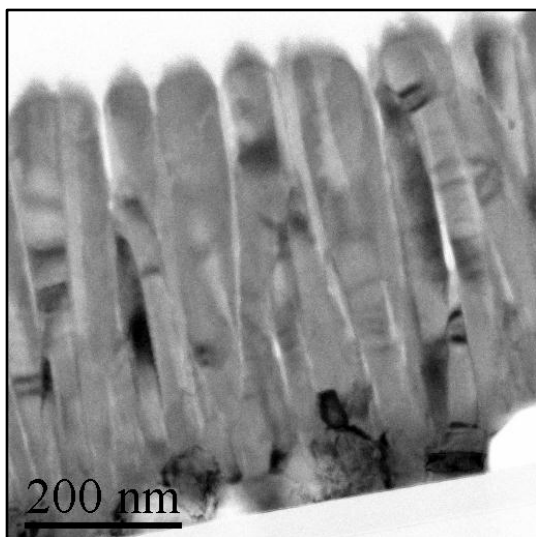
Appendix E - TEM BF images and diffraction patterns of the (Au/Pt)Al<sub>2</sub> alloys

*Au89Pt11*

as-deposited

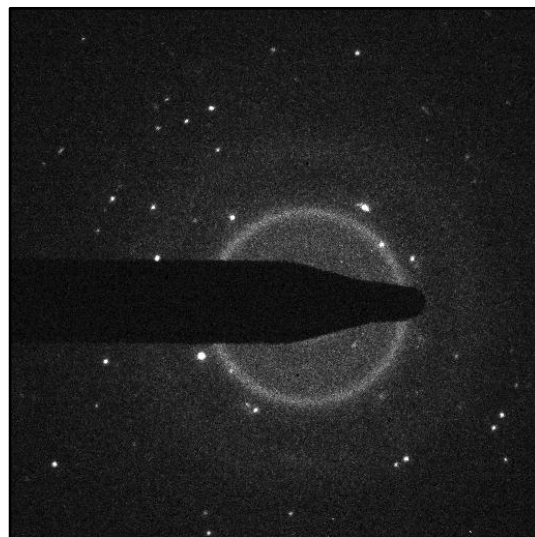
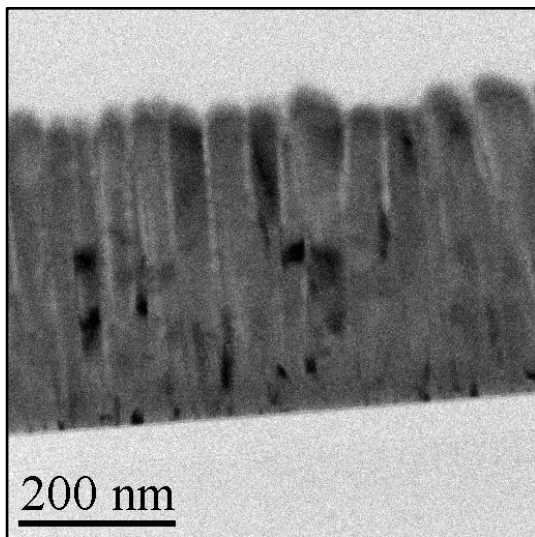


1 h at 250°C

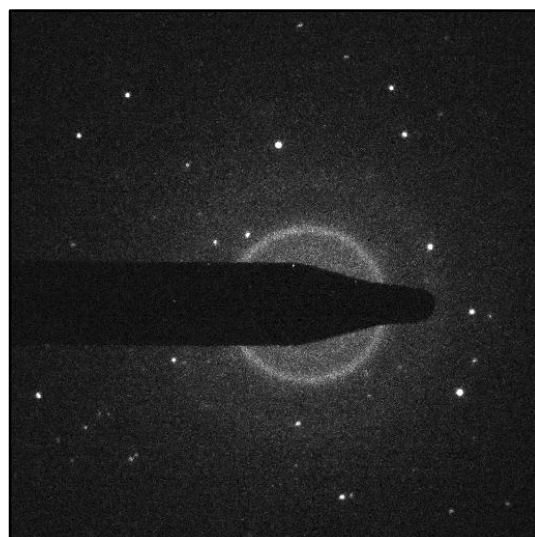
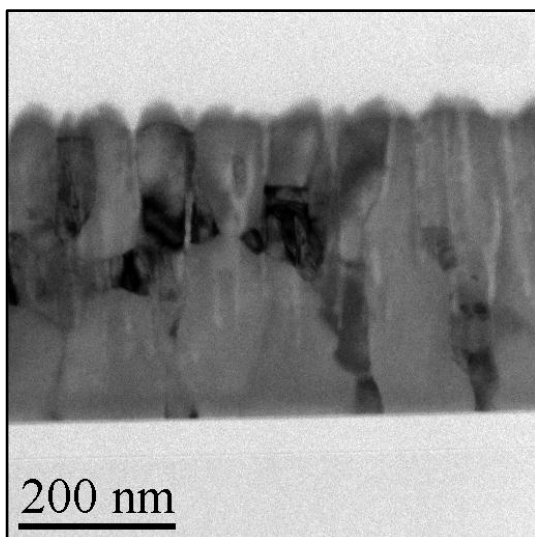


*Au86Pt14*

as-deposited

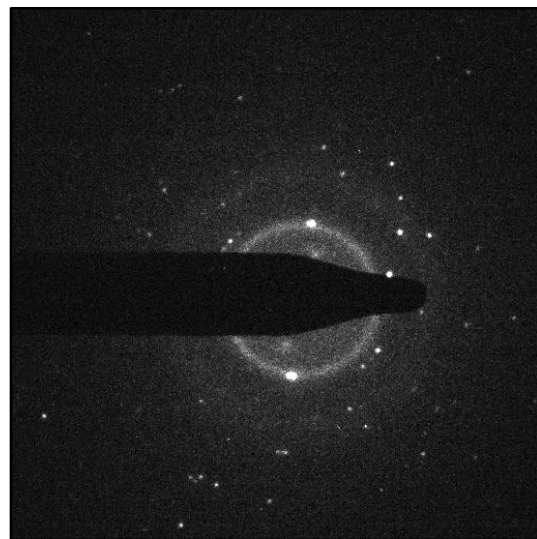
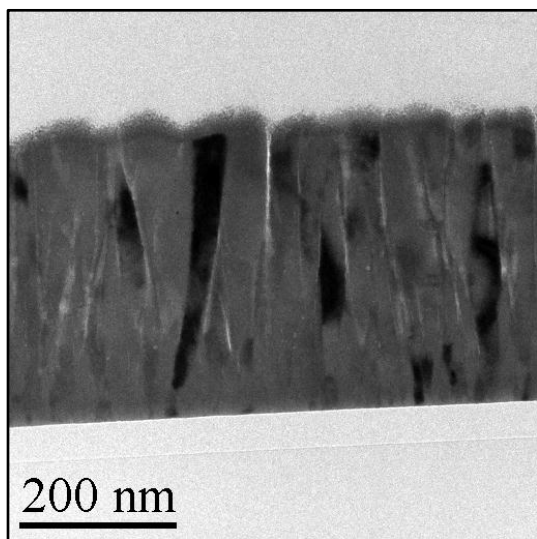


30 min at 350°C

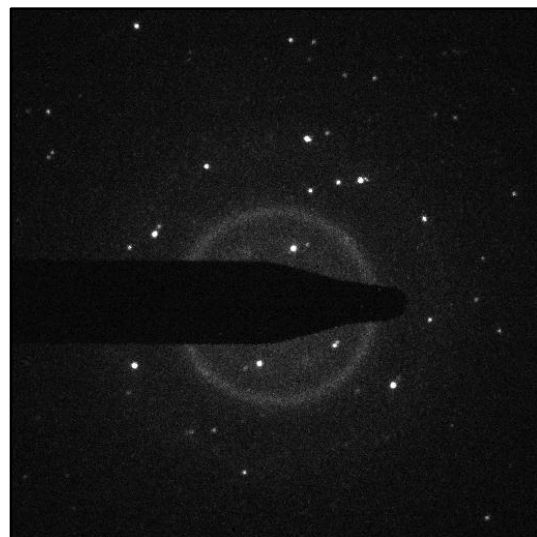
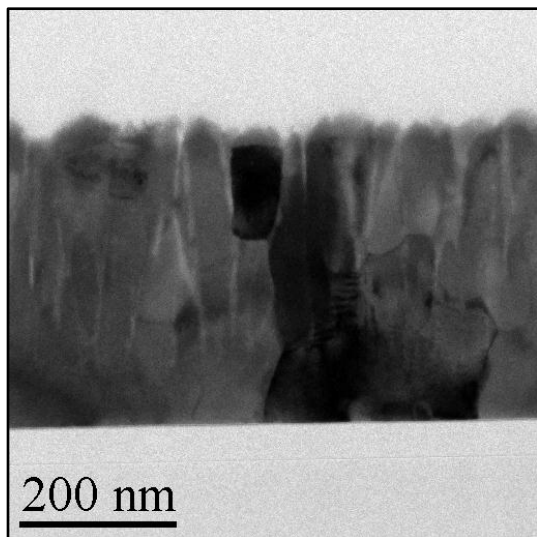


*Au71Pt29*

as-deposited

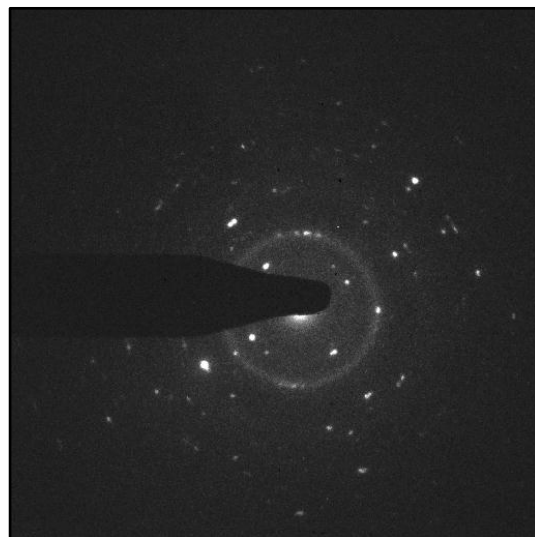
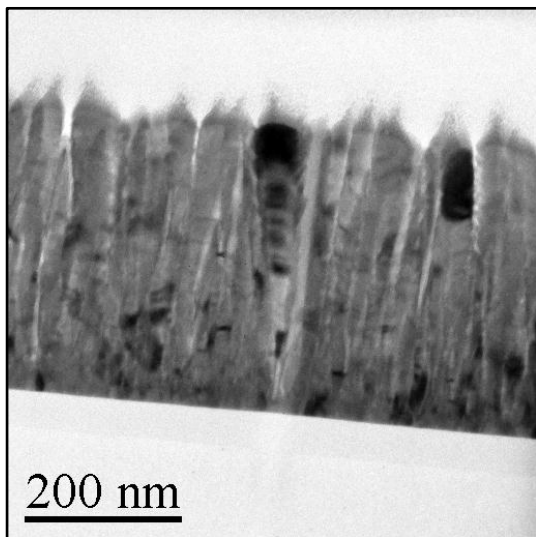


30 min at 350°C

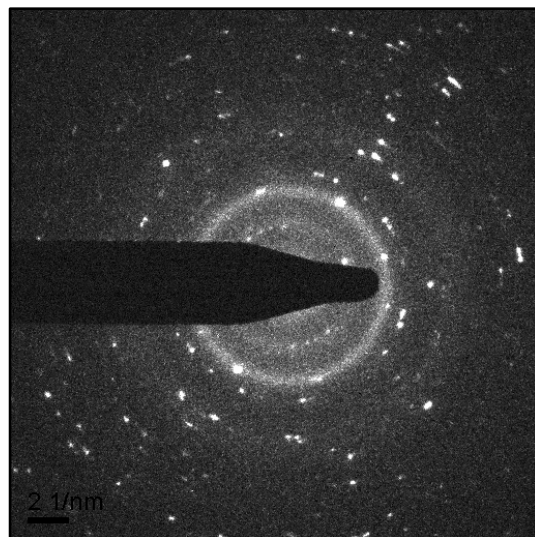
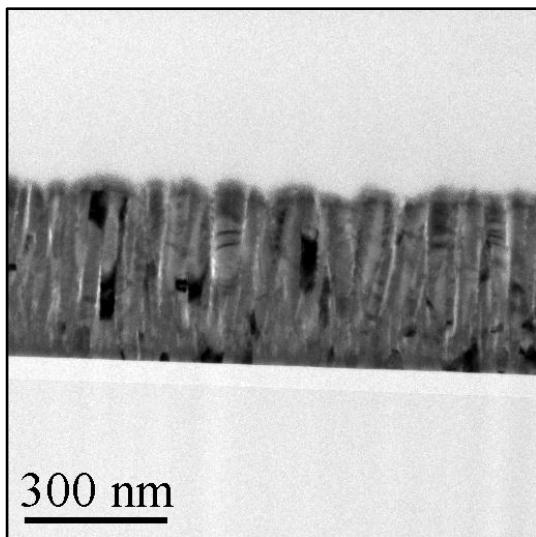


*Au61Pt39*

as-deposited

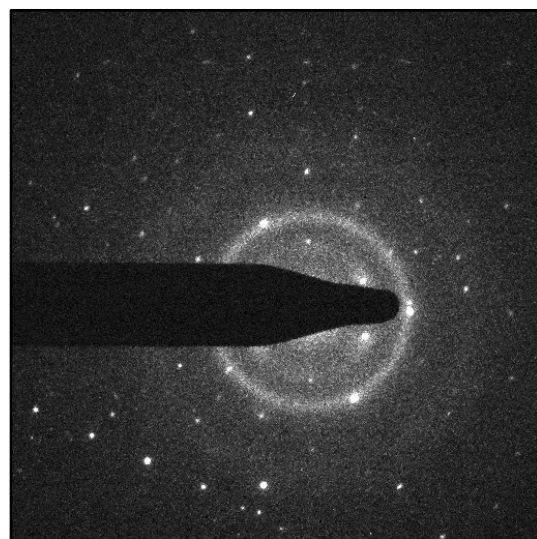
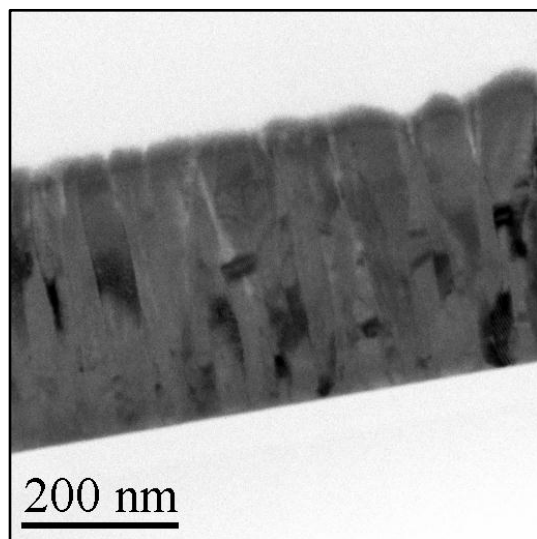


30 min at 350°C

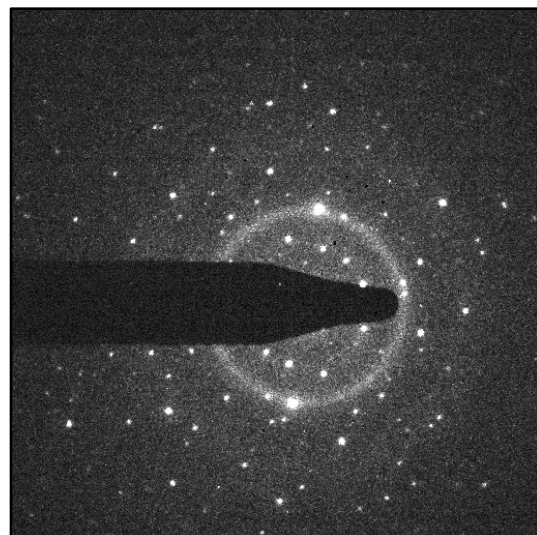
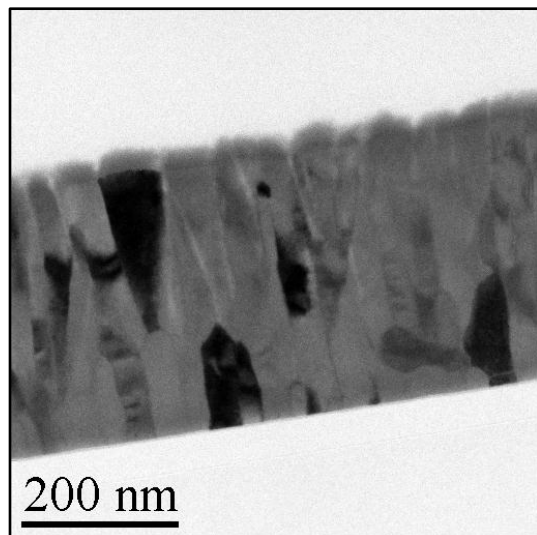


*Au44Pt56*

as-deposited

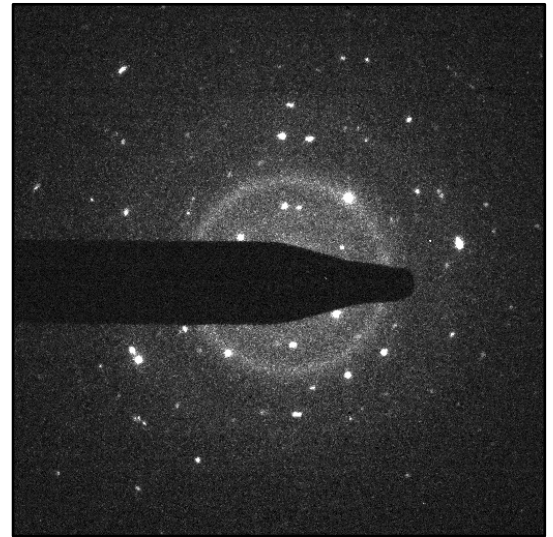
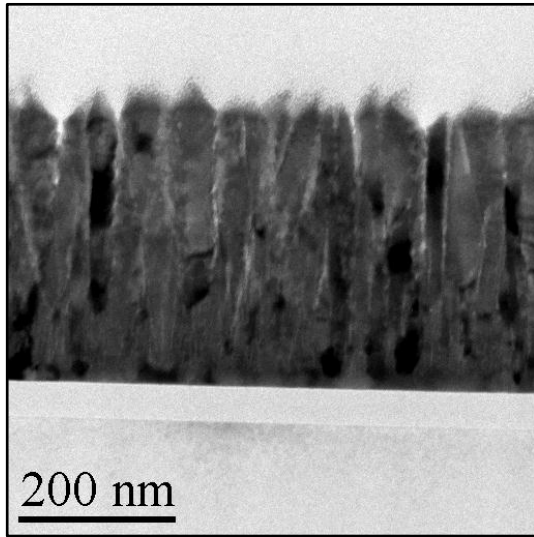


30 min at 350°C

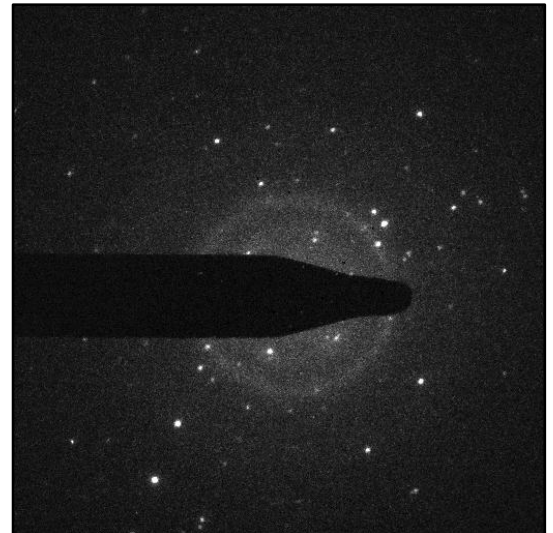
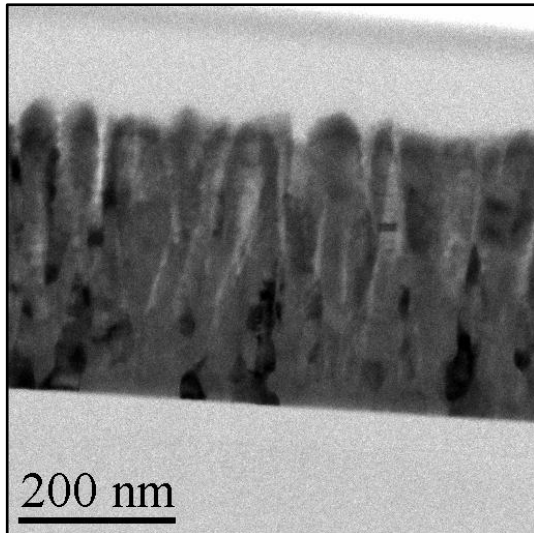


*Au<sub>43</sub>Pt<sub>57</sub>*

as-deposited



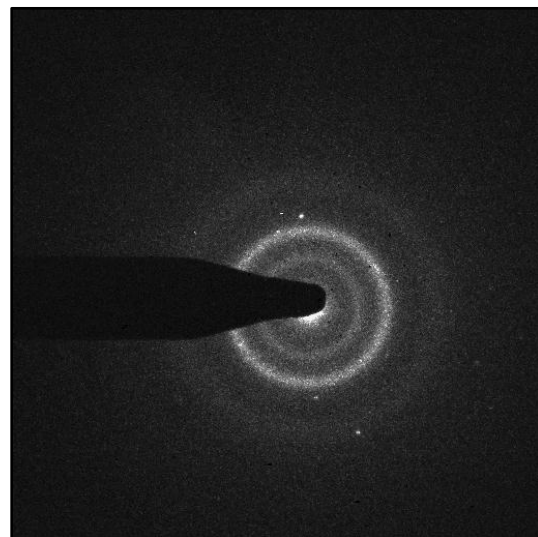
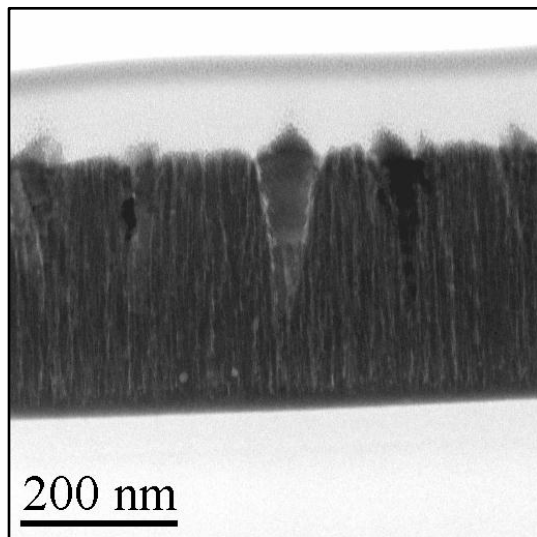
30 min at 350°C



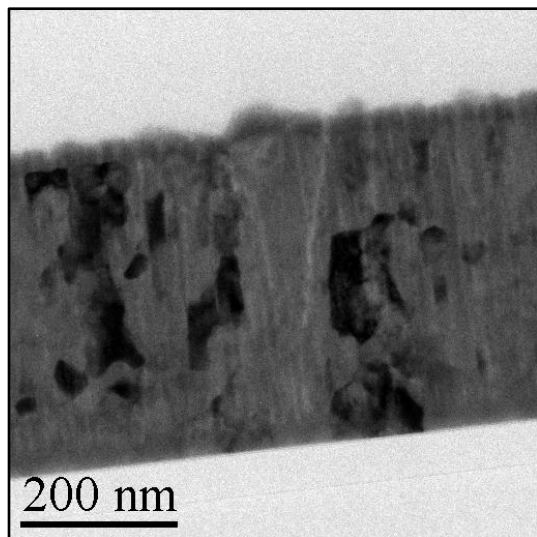


*Au<sub>26</sub>Pt<sub>74</sub>*

as-deposited

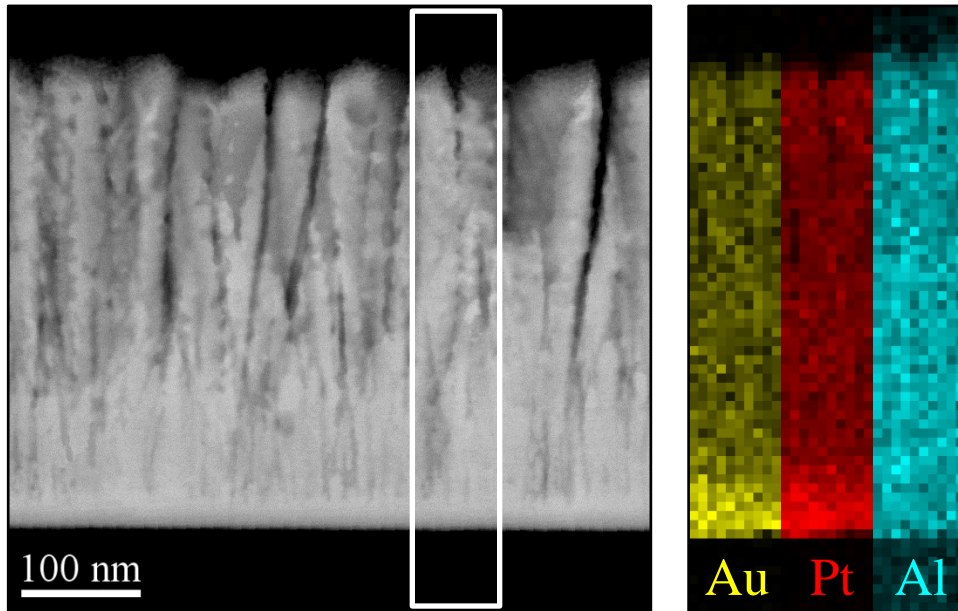


30 min at 350°C

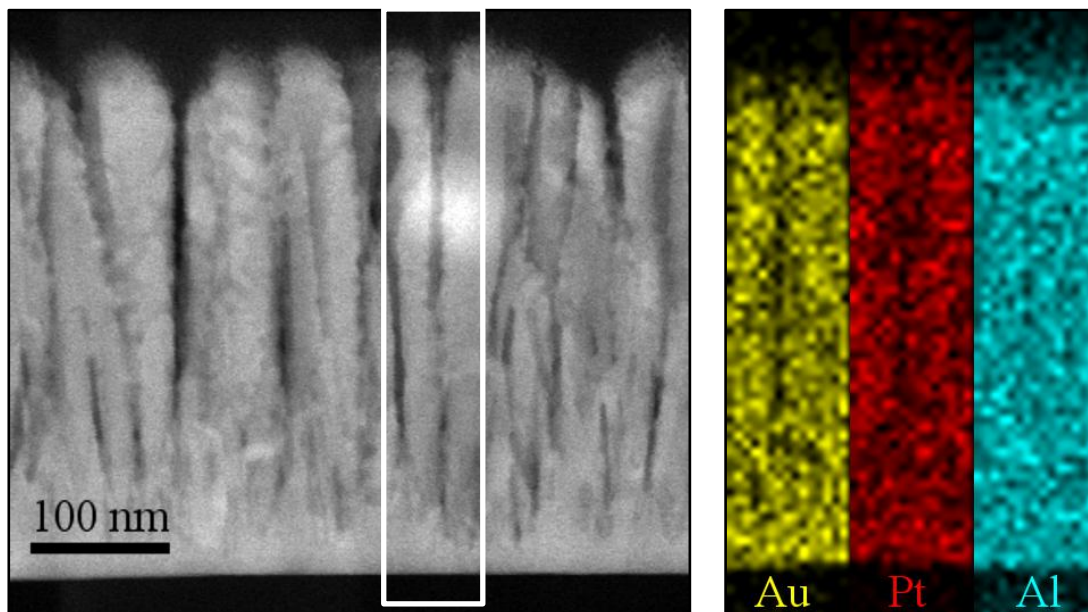


## Appendix F - EDX Maps of selected samples

Au89Pt11: The white box in the STEM image (left) marks the location where the mapping was performed. It can be seen that at the bottom of the film, a thin layer is enriched with Au and possibly Pt.

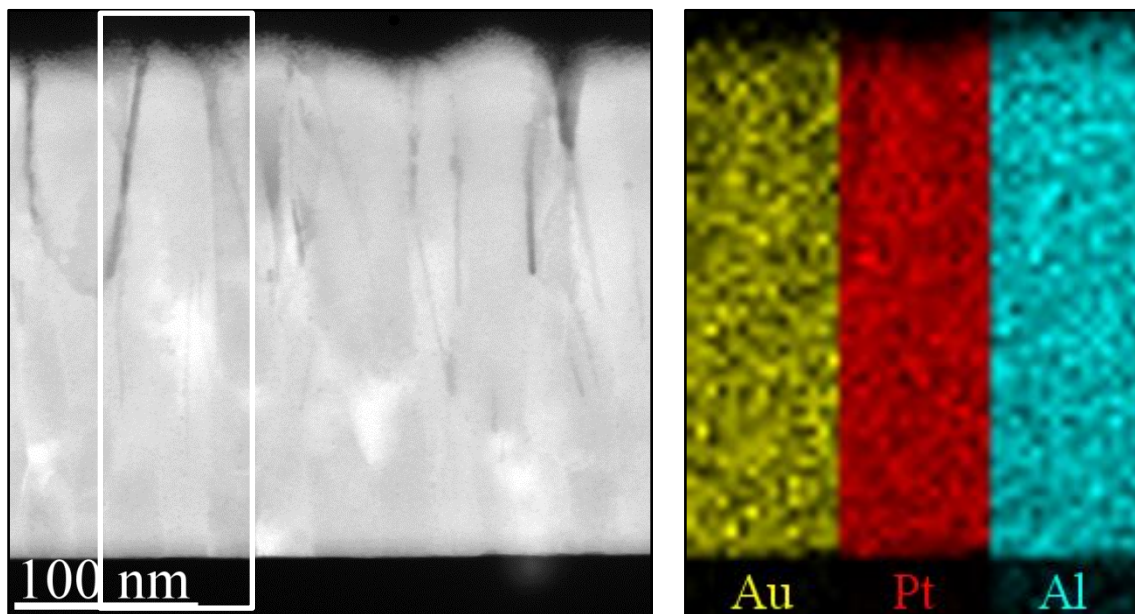


Au61Pt39: The white box in the STEM image (left) marks the location where the mapping was performed. The three elements Au, Pt and Al appear to be evenly distributed in the film.

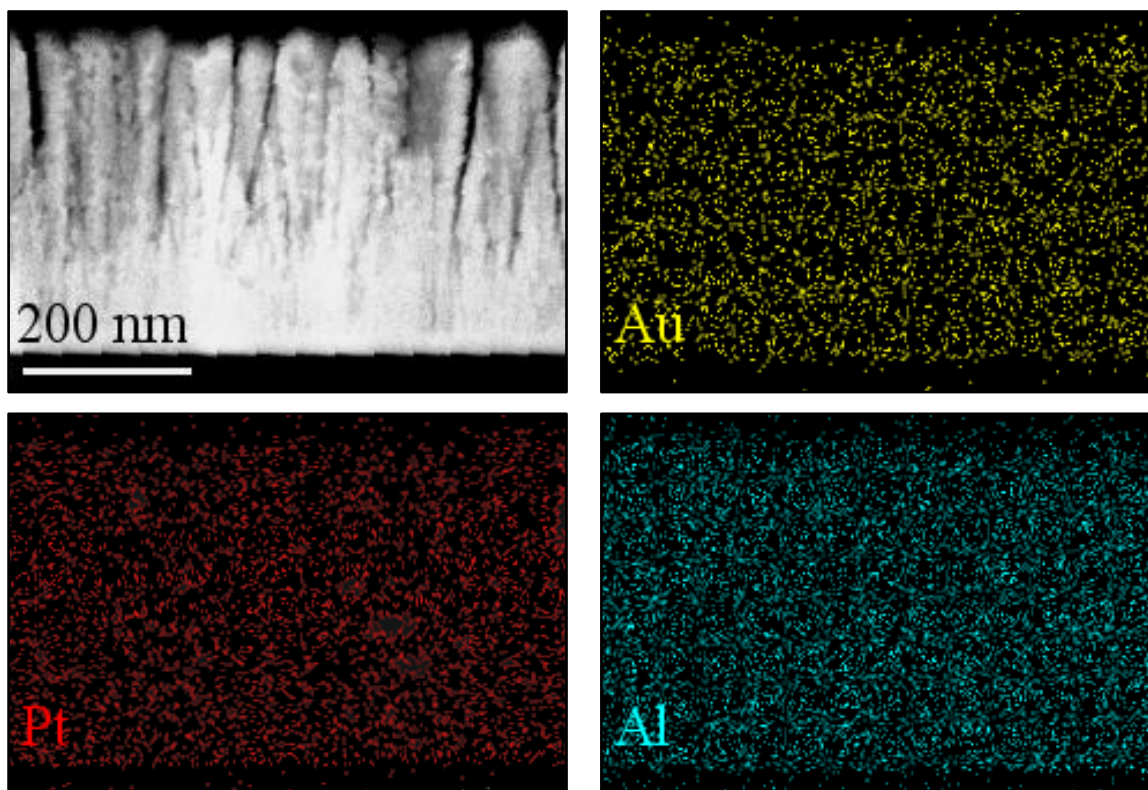




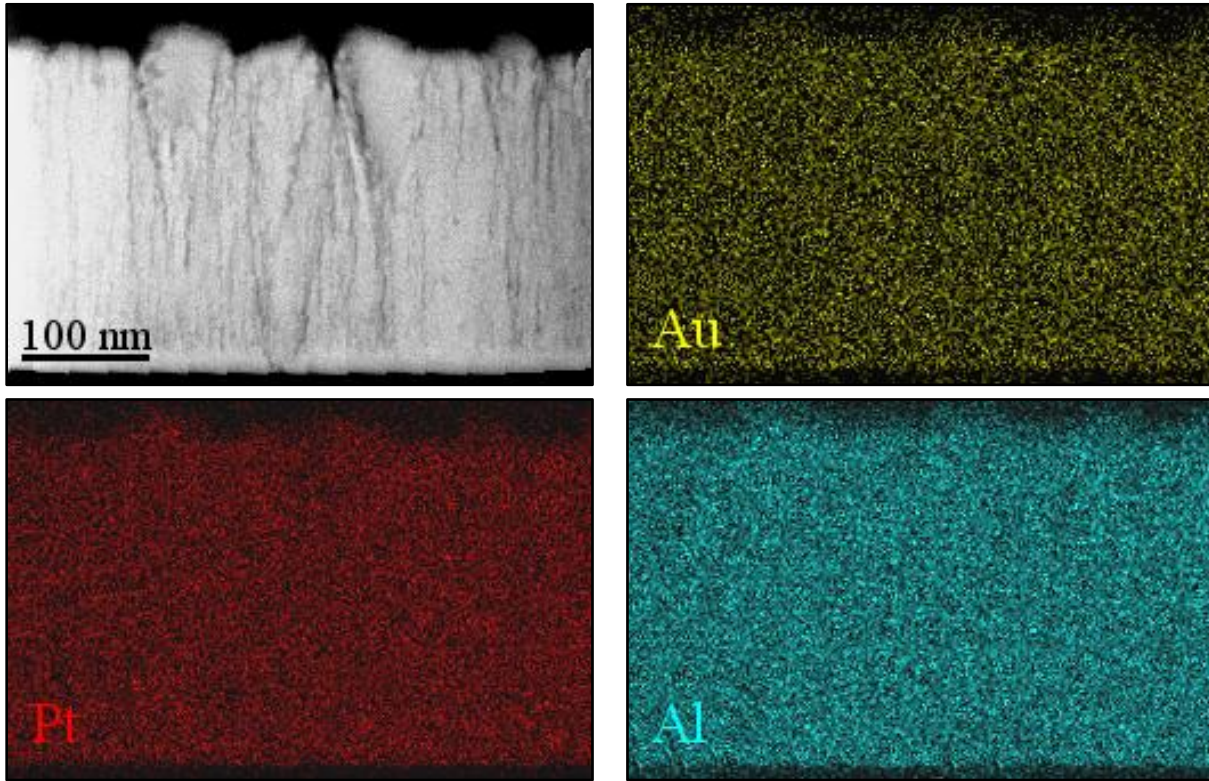
Au<sub>44</sub>Pt<sub>56</sub>: The white box in the STEM image (left) marks the location where the mapping was performed. The three elements Au, Pt and Al appear to be evenly distributed in the film.



Au<sub>43</sub>Pt<sub>57</sub>: The EDX mapping was performed over the STEM image (top left) and suggests that all investigated elements are distributed evenly over the whole film thickness.



Au<sub>26</sub>Pt<sub>74</sub>: The EDX mapping was performed over the STEM image (top left) and suggests that all investigated elements are distributed evenly over the whole film thickness.



## Appendix G - Additional Experiments

### 1. Layer deposition to produce ternary phases

#### *Experimental*

An alternative approach to the simultaneous deposition of Au, Pt and Al was made by producing layered samples. A first layer of Al was deposited on a Si wafer with (100) orientation, with a thickness of roughly 200 nm. On top, a layer of Au and Pt was co-deposited with aimed-for thickness of about 100 nm. Two different ratios of Au to Pt were deposited, one with roughly 4 at.% Pt and a second one with around 43 at.% Pt (with respect to Au). A heat treatment was then performed for 5 h and 72 h at 400°C in argon, to lead to an interdiffusion of the two layers and the formation of a ternary phase. Additional to reflectivity measurements and XRD investigations, FIB-prepared cross sections of as-deposited samples, and samples heat treated for 5 h at 400°C were examined in TEM.

#### *Results*

##### Macroscopic evaluation and reflectivity

In the as-deposited state the  $(\text{Au}_{96}\text{Pt}_4)\text{Al}_2$  sample displays a yellow-grey colour, produced by the gold-rich transparent top layer and the underlying, grey aluminium. The  $(\text{Au}_{57}\text{Pt}_{43})\text{Al}_2$  sample is a pale grey. After the heat treatment at 400°C for 5 h, a peachy colour is visible on the  $(\text{Au}_{96}\text{Pt}_4)\text{Al}_2$  sample, and a grey shade can be seen on the  $(\text{Au}_{57}\text{Pt}_{43})\text{Al}_2$  sample.

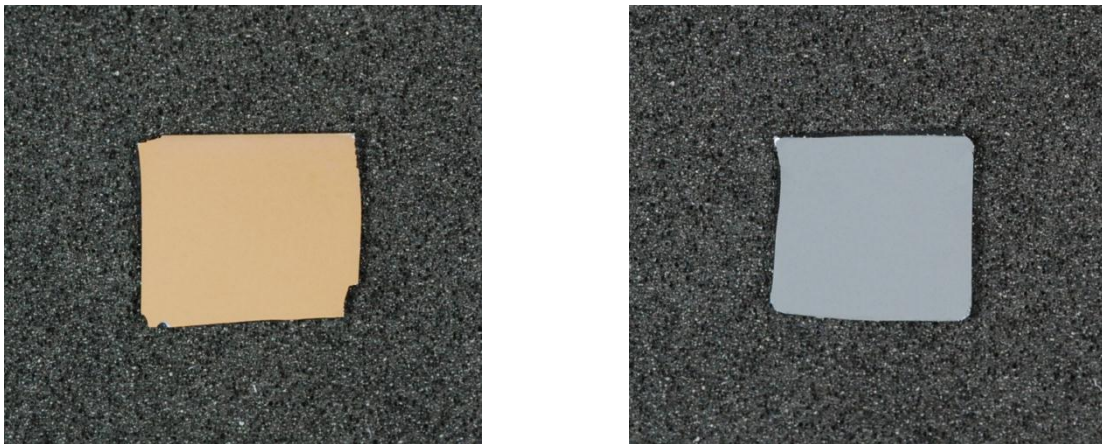


Figure 98: Images of the heat treated (5 h at 400°C), layered samples  $(\text{Au}_{96}\text{Pt}_4)\text{Al}_2$  (left) and  $(\text{Au}_{57}\text{Pt}_{42})\text{Al}_2$  (right).



The reflectivity curve of the as-deposited  $(\text{Au}_{96}\text{Pt}_4)\text{Al}_2$  sample shows a smooth decline with a shallow dip around 500 nm. In the sample heat treated for 5 h at 400°C a clear minimum is visible around 480 nm, which remains stable even when the heat treatment time is increased to 72 h. The reflectivity curve of  $(\text{Au}_{57}\text{Pt}_{43})\text{Al}_2$  also declines very smoothly and resembles the curve of pure platinum, in chapter 3.2. After the heat treatment the overall reflectivity is strongly reduced and a small bump around 480 nm is visible.

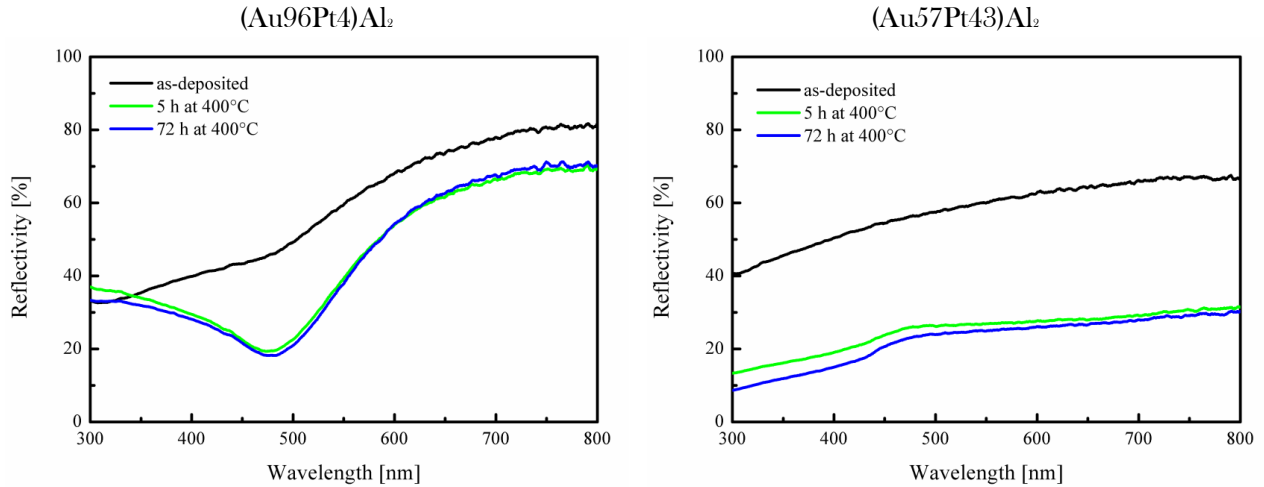


Figure 99: Reflectivity curve of the as-deposited and heat treated  $(\text{Au}_{96}\text{Pt}_4)\text{Al}_2$  (left) and  $(\text{Au}_{57}\text{Pt}_{43})\text{Al}_2$  (right). The initially rather shallow curve on the left obtains a clear dip around 480 nm, while the curve on the right has a strongly reduced overall reflectivity and a small bump around 480 nm.

### X-ray diffraction

In the XRD spectrum of the as-deposited  $(\text{Au}_{96}\text{Pt}_4)\text{Al}_2$  sample, the majority of the present peaks belong to the fluorite  $\text{AuAl}_2$  structure (Figure 100). One small peak could be attributed to pure Al. Also in the  $(\text{Au}_{57}\text{Pt}_{43})\text{Al}_2$  sample, most strong peaks belong to the fluorite phase ( $\text{PtAl}_2$  was taken as reference). Several reflexes were found that could be matched to the  $\text{Al}_3\text{Pt}_2$  intermetallic phase.

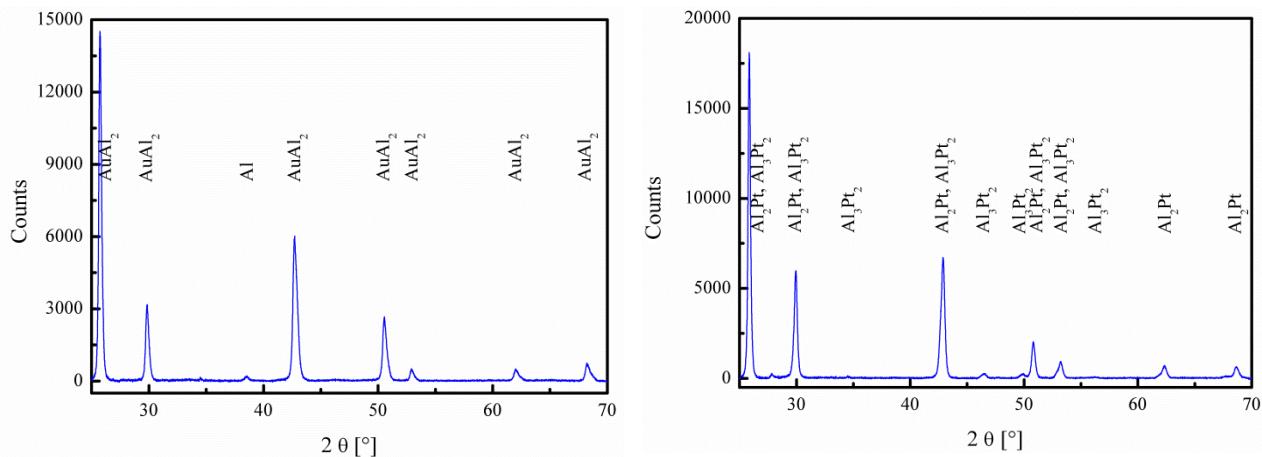


Figure 100: XRD spectra of the  $(\text{Au}96\text{Pt}4)\text{Al}_2$  and  $(\text{Au}57\text{Pt}43)\text{Al}_2$  sample in the heat treated state. In the  $(\text{Au}96\text{Pt}4)\text{Al}_2$  sample mainly reflexes from the fluorite  $\text{AuAl}_2$  structure are found, with one small peak from pure Al. The  $(\text{Au}57\text{Pt}43)\text{Al}_2$  sample contains next to the fluorite phase ( $\text{PtAl}_2$  taken as reference) weak reflexes from the  $\text{Al}_3\text{Pt}_2$  phase.

### Microstructure investigations

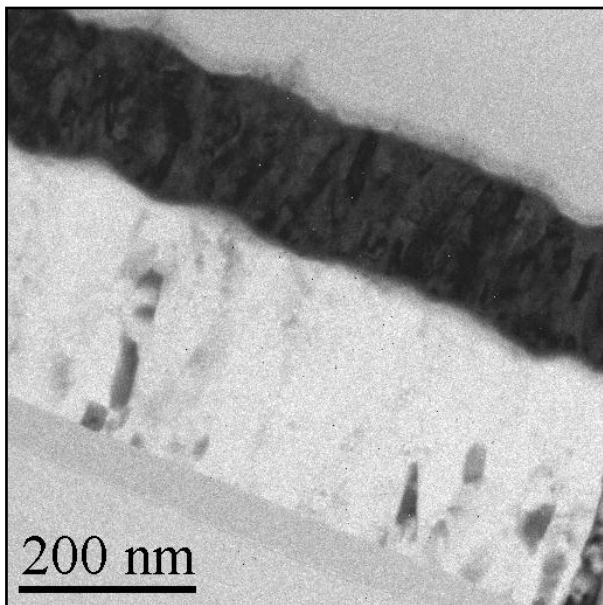


Figure 101: TEM BF image of the cross-section through the as-deposited  $(\text{Au}57\text{Pt}43)\text{Al}_2$  sample. The bright Al layer at the bottom can be clearly distinguished from the dark Au/Pt film on top.

In the TEM cross sections of the as-deposited samples the layered structure can clearly be observed (Figure 101). The bright columnar layer of Al with a thickness of roughly 200 nm is clearly separated from the dark (Au/Pt) top layer, with a thickness around 100 nm. An interdiffusion between the two layers does not appear to have taken place yet. After the heat treatment for 5 h at 400°C the columnar structure has disappeared in both samples (Figure 102). Equiaxed grains of sizes between 50 nm and 100 nm are visible. At the bottom of sample  $(\text{Au}96\text{Pt}4)\text{Al}_2$  a thin, bright layer is present, probably consisting of Al that did not react during the heat treatment. On the top a thin layer that is slightly darker can be seen.

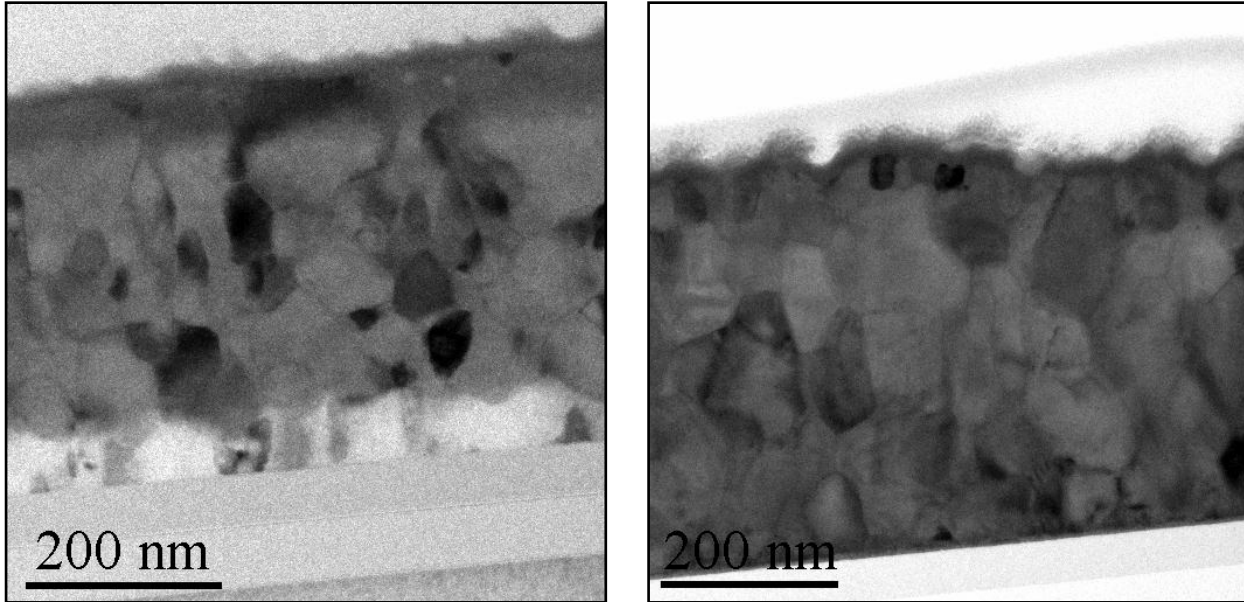


Figure 102: TEM BF images of the heat treated (5 h at 400°C) layers of (Au96Pt4)Al<sub>2</sub> and (Au57Pt43)Al<sub>2</sub>. The columnar structure has disappeared, and small, equiaxed grains of sizes between 50 nm and 100 nm are visible. In the image of the (Au96Pt4)Al<sub>2</sub> sample a thin layer of unreacted Al is visible. Also a darker surface layer is present.

To obtain information about the chemical composition of the films, EDX mappings were performed on the heat treated FIB lamellae of both samples. The bright layer that was observed in the (Au96Pt4)Al<sub>2</sub> sample appears to consist of pure Al as both, the Pt and the Au signal become very weak in this region (Figure 103). A surface layer that is enriched with Pt is present in both, the (Au96Pt4)Al<sub>2</sub> and the (Au57Pt43)Al<sub>2</sub> sample (Figure 104). While the Au signal is reduced in that area, the Al appears to remain the same.



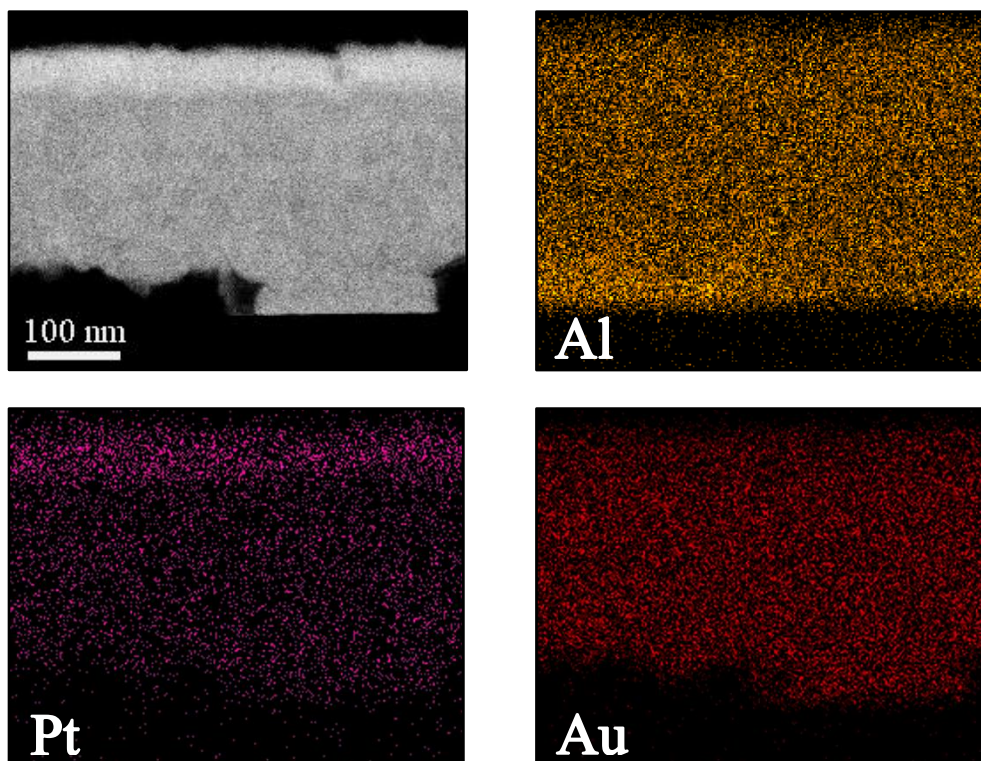


Figure 103: EDX maps of the  $(\text{Au}_{96}\text{Pt}_4)\text{Al}$  sample. The areas that appeared brighter in the BF images seem to consist of pure Al, as both the Pt and the Au signal are very weak in those areas. A layer with a high Pt content appears to be present on the surface, where the Au signal is slightly weaker but the Al signal remains constant.

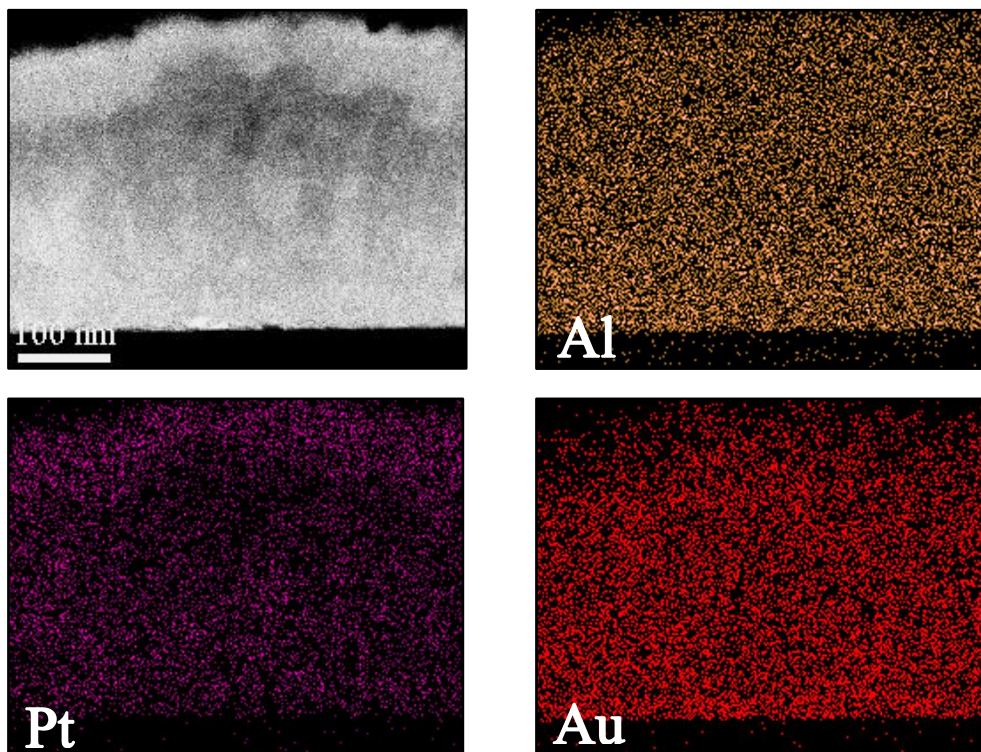


Figure 104: EDX mappings of the  $(\text{Au}_{57}\text{Pt}_{43})\text{Al}_2$  sample. A thin layer enriched in Pt appears to be present on the surface. The Au signal becomes weaker in that zone while the Al signal remains constant.

As both samples still appear to have a layer structure even after the heat treatment, a thickness gradient was introduced by polishing away part of the film at a shallow angle. In both cases more than one layer appears before the substrate is visible (the blue colour is due to the  $\text{Si}_3\text{N}_4$  diffusion barrier). The  $(\text{Au}96\text{Pt}4)\text{Al}_2$  sample reveals an intense purple layer under the peachy surface, clearly the  $\text{AuAl}_2$  phase, probably with a certain amount of Pt. Underneath the purple layer a very thin, white film is visible, possibly consisting of pure Al that did not react during the heat treatment. The blue-grey surface of the  $(\text{Au}57\text{Pt}43)\text{Al}_2$  sample covers a peachy bottom layer. It seems likely that the top consists of the  $\text{Pt}_2\text{Al}_3$  intermetallic phase, while the bottom, coloured layer has the fluorite phase, with a certain ratio of Au to Pt.



Figure 105: Heat treated samples  $(\text{Au}96\text{Pt}4)\text{Al}_2$  and  $(\text{Au}57\text{Pt}43)\text{Al}_2$ , with a thickness gradient introduced by polishing away part of the surface. In both samples differently coloured layers appear, before the substrate (blue) becomes visible.

### *Discussion*

The production of homogeneous, ternary thin films from initially separate layers was not successful. While the production of ternary phases was achieved, several differently composed layers coexist. The exact determination of their composition was not accomplished, as EDX measurements have a penetration depth that exceeds the film thickness. Interestingly, the grains of the heat treated layers are globular, which could be beneficial for the mechanical properties. It is possible that homogeneous films could be obtained if the thickness of the initially sputtered, individual layers was reduced.



## 2. Mechanical properties of small intermetallic particles

### *Experimental*

A 3 inch wafer (Si-SiO<sub>2</sub>-Si<sub>3</sub>N<sub>4</sub>) with a composition gradient between Al and Au had been deposited and heat treated for 2 h at 700°C in argon. As a consequence, there was no continuous film on the surface, but separate particles which appeared to consist of the intermetallic AuAl<sub>2</sub> phase. Twelve particles was selected with a shape close to circular and compressed by means of a nanoindenter (TriboIndenter, Hysitron), equipped with a flat punch tip (diameter 5 μm) and the dependence of the measured hardness correlated to the particle size. EBSD measurements were performed to investigate whether the particles were single crystalline and had a preferential orientation.

### *Results*

#### Light and scanning electron microscopy (SEM)

The light microscopy image in Figure 106 shows that the formerly continuous film consists of separate particles, dispersed on the blue substrate. In parts, a bright phase can be seen in between the particles, possibly elemental Al.

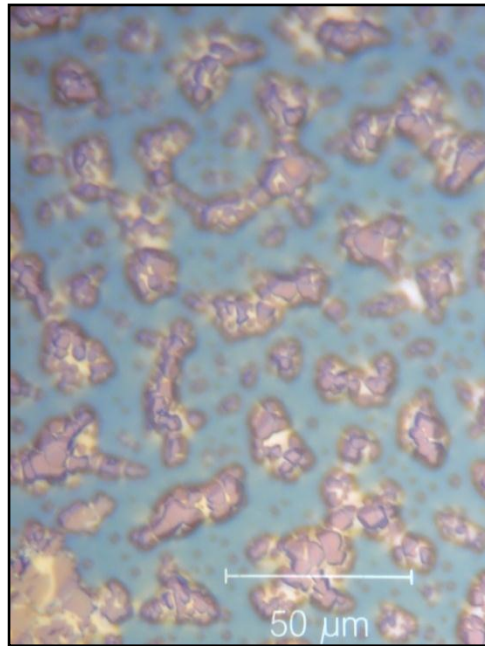


Figure 106: Light microscopy image of the surface of the heat treated wafer. Separate particles with an intense purple colour are visible on the blue substrate. In parts, a white phase is visible, possibly Al.

The SEM images of the sample show the same as the light microscopy. EDX measurements confirm that the particles consist of  $\text{AuAl}_2$  and suggest that the matrix around them contains mostly Al.

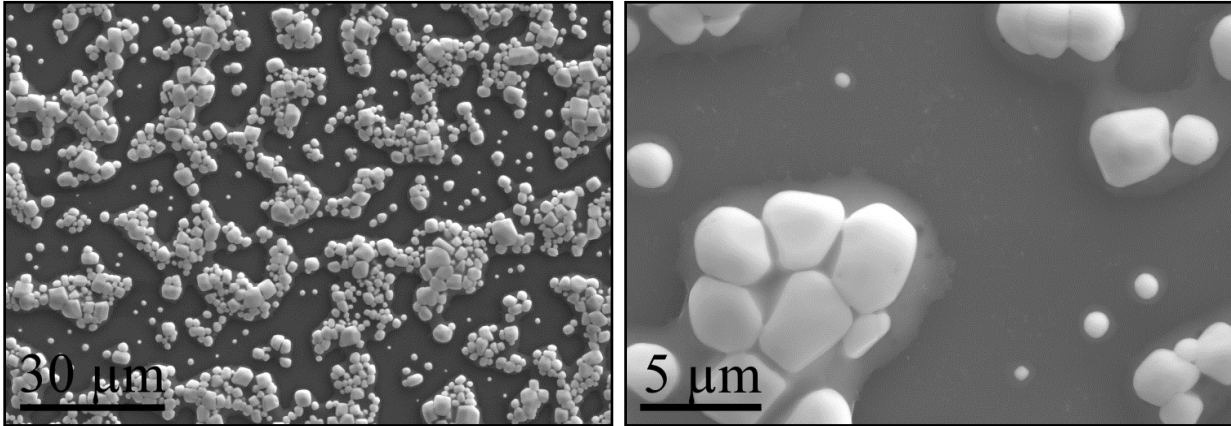


Figure 107: SEM images of the  $\text{AuAl}_2$  particles. A thin film surrounds the groups of particles, probably consisting of aluminium.

#### Electron backscatter diffraction (EBSD)

From the EBSD data in Figure 108 it appears that the individual particles are single crystalline, as the corresponding colour chart only displays one orientation per particle. The orientation of the particles with respect to the substrate and each other seems to be rather random, possibly with a tendency to a (100) out of plane texture, as suggested by the pole figure in Figure 109.

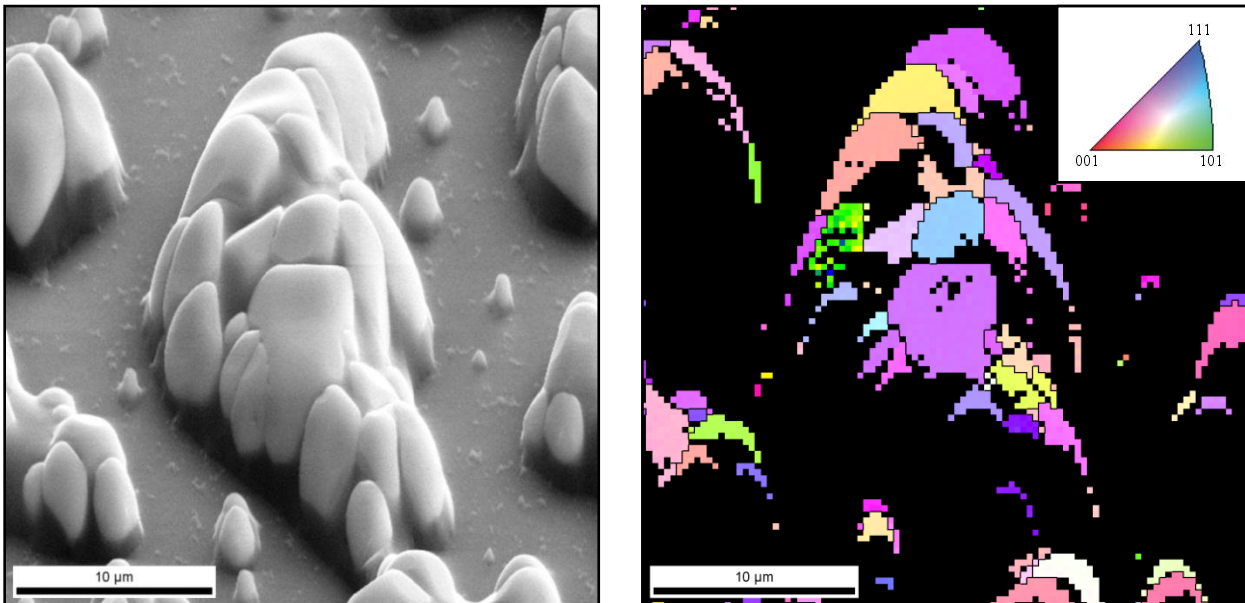


Figure 108: SEM image and corresponding colour chart of a group of particles. It appears that each of them is single crystalline and rather randomly oriented.

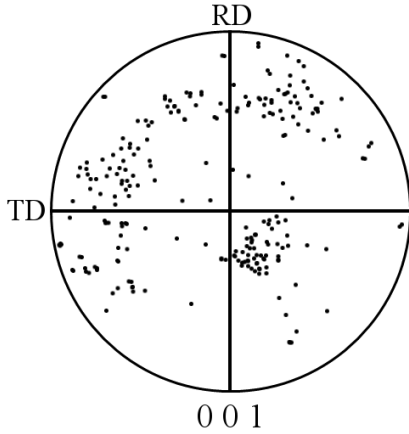


Figure 109: Pole figure indicating that the particles have a slight (100) out-of-plane texture.

### Mechanical testing

Figure 110 shows an example of a load-displacement curve of a particle. Clearly seen is the position of a so-called *pop-in* in the curve at a load shortly above 1500  $\mu\text{N}$ . Until that point, the deformation of the particle occurs elastically. When a certain limit is reached, a dislocation burst leads to a sudden jump in the displacement. The origin of a dislocation burst can be the reaching of the load required for dislocation motion, or if no initial dislocations are present, the load necessary for the activation of a dislocation source.

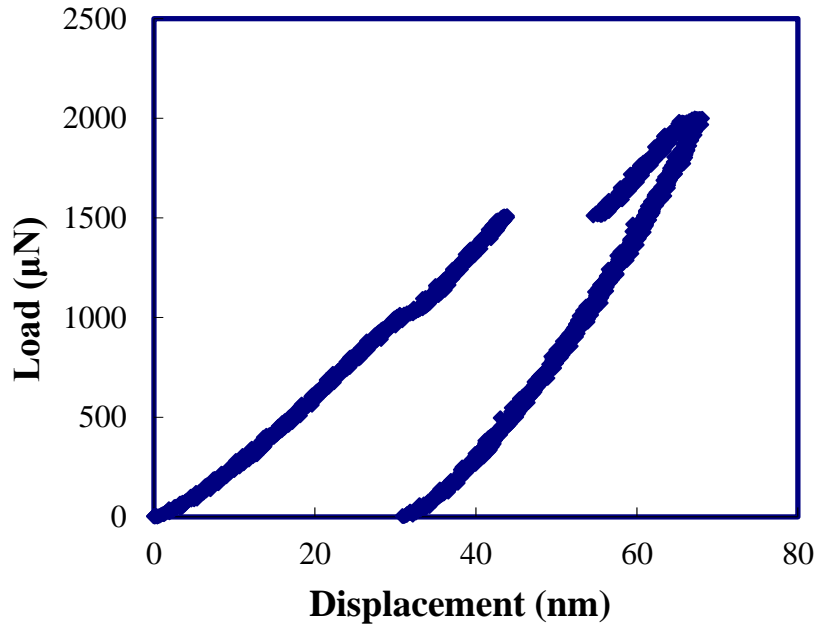


Figure 110: Example of a load-displacement curve of an AuAl<sub>3</sub> particle.

The required load  $L$  for the dislocation burst to occur was measured for all particles and were, together with their lateral dimension  $A$ , used to calculate the yield strength of the particles, using  $\sigma_y = L/A$ . The correlation between the yield strength and the particle radius is shown in Figure 111. Once the particles are smaller than a certain limit, which appears to be around 400 nm, the yield strength  $\sigma_y$  begins to increase remarkably.

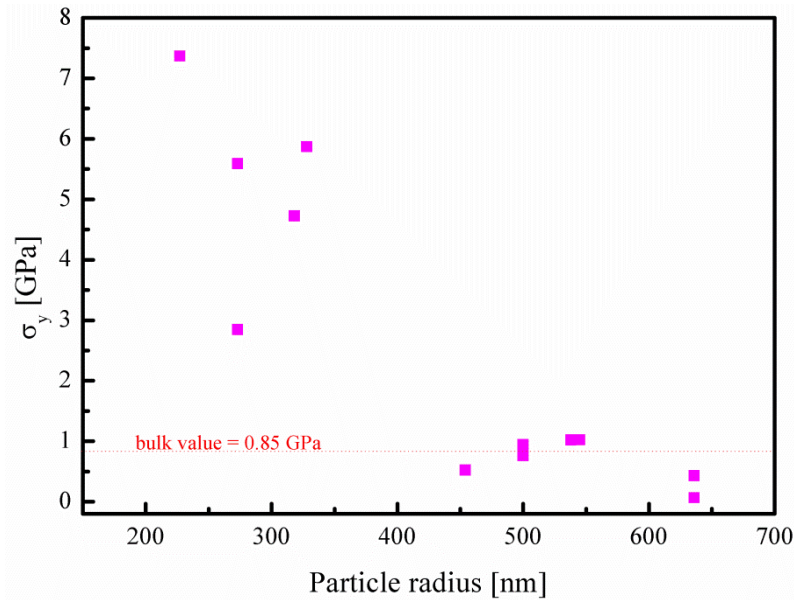


Figure 111: Yield strength dependence on the size of the particles. As the particles become smaller, the yield stress increases, as predicted by literature.

### *Discussion*

The mechanical properties of small particles consisting of an intermetallic phase were investigated and it was found that the yield strength increases with the particle size. The size effect that had previously been observed for pure materials, for example Au [96] or Si [97] hence is as well applicable to the intermetallic phase AuAl<sub>2</sub>.





## 9. Curriculum Vitae

### Personal Information

<i>Name</i>	Angela Furrer
<i>Address</i>	Binzmühlestrasse 52, 8050 Zürich
<i>Email</i>	angela.furrer@gmail.com
<i>Phone number</i>	+41 76 461 15 80
<i>Birthday</i>	23 <sup>rd</sup> of October 1983
<i>Hometown</i>	Aesch, LU

### Education

Oct. 2008 - Aug. 2013	Doctor in Materials Science at ETH Zurich, Laboratory for Nanometallurgy, Title: <i>Colours in thin metallic films based on precious metals and their intermetallic phases</i>
Apr. 2006 - Oct. 2007	Master of Materials Science at ETH Zurich, Title Master Thesis: <i>The influence of surface- and heat treatments and plastic deformation on the corrosion behaviour of the magnesium alloy WE43</i>
Oct. 2002 - July 2005	Bachelor of Materials Science at ETH Zurich
Aug. 1998 - July 2002	High School at Kantonsschule Kollegium Schwyz, SZ

## Work Experience

Dec. 2007 – May 2008	Scientific employee at the Laboratory of Metal Physics and Technology, ETH Zurich
Apr. 2006 – July 2006	Scientific assistant at the Laboratory of Metal Physics and Technology, ETH Zurich
Nov. 2005 – Feb. 2006	Internship at Contraves Space AG, Zurich, Department of Development and Technology
July 2005 – Sept. 2005	Internship at the University of Manchester, School of Physics and Astronomy, Manchester, England
Aug. 2002 – Sept. 2002	Workshop training at Victorinox AG, Ibach

## Publications

### *Journal Articles*

Angela Furrer, Matteo Seita, Ralph Spolenak: *The effects of defects in purple AuAl<sub>3</sub> thin films*. Acta Materialia **61** (2013), 2874-2883.

Cesare Borgia, Thorsten Scharowsky, Angela Furrer, Christian Solenthaler, Ralph Spolenak: *A combinatorial study on the influence of elemental composition and heat treatment on the phase composition, microstructure and mechanical properties of Ni-W alloy thin films*. Acta Materialia **59** (2011), 386-399.

Petra Gunde, Angela Furrer, Anja C. Hänzi, P. Schmutz, Peter J. Uggowitzer: *The influence of heat treatment and plastic deformation on the bio-degradation of a Mg-Y-RE alloy*. Journal of Biomedical Materials Research Part A **92** (2010), 409-418.

Dirk I. Uhlenhaut, Angela Furrer, Peter J. Uggowitzer, Jörg F. Löffler: *Corrosion properties of glassy Mg<sub>70</sub>Al<sub>15</sub>Ga<sub>15</sub> in 0.1 M NaCl solution*. Intermetallics **17** (2008), 811-817.

### *Oral Presentations*

CCMX Summer School, Lausanne, Aug. 2010: *Applications of Nanoindentation Measurements*.

MRC Graduate Symposium, ETH Zurich, June 2012: *The effects of defects on purple AuAl<sub>3</sub>*.



### *Poster Presentations*

Gold 2012 conference, Tokyo, Japan, Sept. 2012: *The effects of defects on purple AuAl<sub>2</sub>*.

MRC Graduate Symposium, ETH Zurich, June 2011: *Colours and Microstructure of AuAl<sub>2</sub> and AuIn<sub>2</sub> thin films*.

MRC Graduate Symposium, ETH Zurich, June 2010: *Colours in the Au-Pt-Al system*.

### **Experimental Techniques**

Scanning Electron Microscopy (SEM)

Focussed Ion Beam (FIB)

Transmission Electron Microscopy (TEM)

Nanoindentations

Magnetron Sputter Deposition

### **Various**

Languages German (Mother tongue)

English (fluent, CAE)

French (good, DELF 1)

Russian (basics)

### **Personal Engagements**

Member of the Local committee of IAESTE (International Association for the Exchange of Students for Technical Experience) between 2006 and 2011, member of the board in 2006 and 2007

Scout leader between 1998 and 2007

### **Personal Interests**

Dancing, Cooking, Hurling (Irish Team Sport), Violin, Running

## References

Prof. Ralph Spolenak, ETH Zurich

[ralph.spolenak@mat.ethz.ch](mailto:ralph.spolenak@mat.ethz.ch)

+41 44 632 25 90

Prof. Peter J. Uggowitzer, ETH Zurich

[peter.uggowitzer@mat.ethz.ch](mailto:peter.uggowitzer@mat.ethz.ch)

+41 44 632 25 54

Dr. Patrik Schmutz, Empa Dubendorf

[patrik.schmutz@empa.ch](mailto:patrik.schmutz@empa.ch)

+41 44 823 48 45

